Dante M. L. Horemans

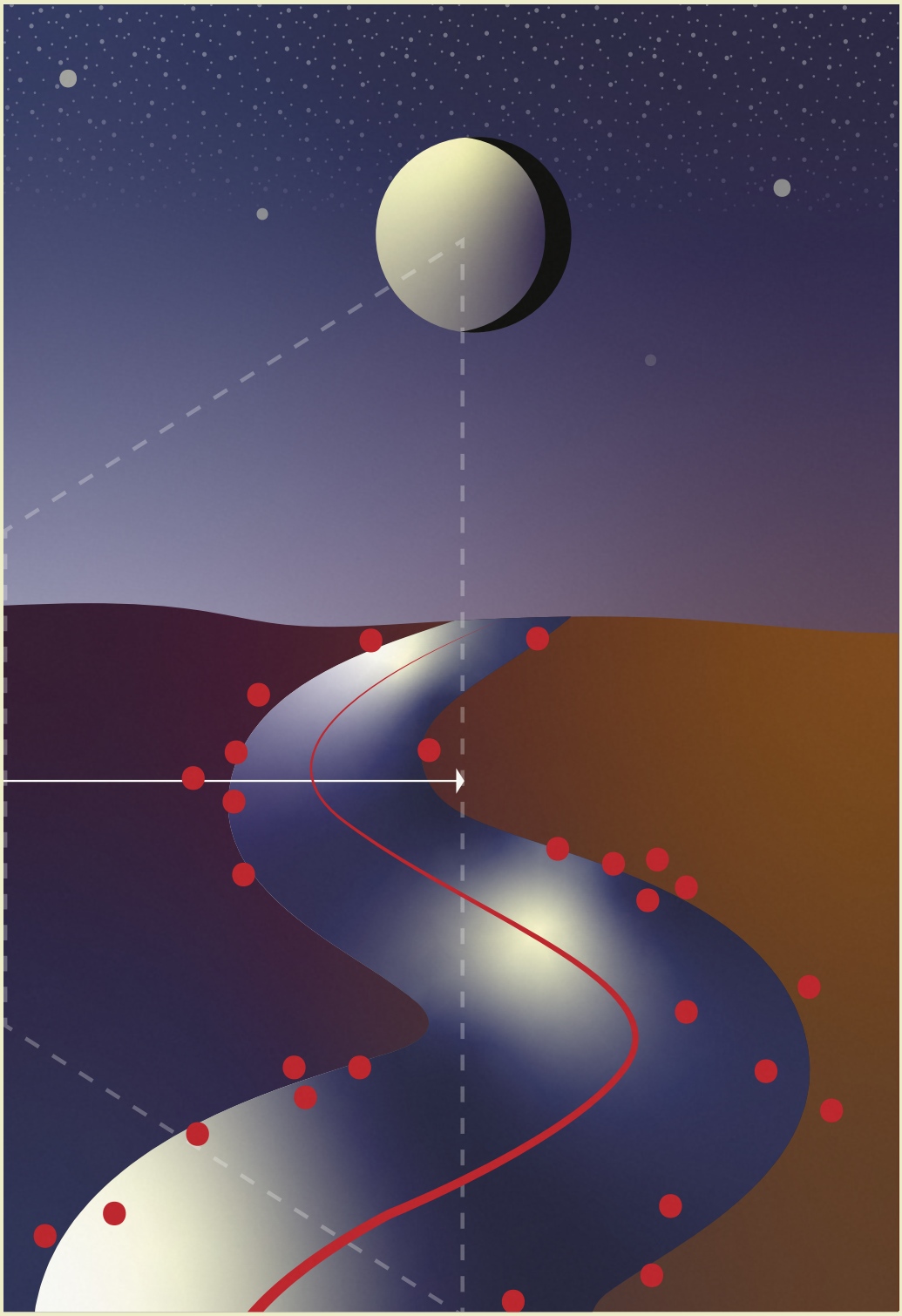

UNRAVELING THE COUPLED LARGE-SCALE SUSPENDED SEDIMENT AND PHYTOPLANKTON DYNAMICS IN A TURBID AND TIDE-DOMINATED ESTUARY

Faculty of Science

Department of Biology

Unraveling the coupled large-scale suspended sediment and phytoplankton dynamics in a turbid and tide-dominated estuary

Het ontraadselen van de gekoppelde grootschalige dynamiek van zwevend sediment en fytoplankton in een troebel en getijde-gedomineerd estuarium

Proefschrift voorgelegd tot het behalen van de graad van
Doctor in de Wetenschappen: Biologie
aan de Universiteit Antwerpen te verdedigen door

Dante M. L. Horemans

Prof. Dr. Patrick Meire
Dr. Ir. Tom J. S. Cox

Antwerpen, 2022

Members of the doctoral committee:

Prof. Dr. Patrick Meire	University of Antwerp, promotor
Dr. Ir. Tom J. S. Cox	University of Antwerp, co-promotor

Independent members:

Prof. Dr. Ir. Filip J. R. Meysman	University of Antwerp, chairman
Prof. Dr. Stefan Van Dongen	University of Antwerp
Prof. Dr. Stijn Temmerman	University of Antwerp

External members:

Prof. Dr. Henk M. Schuttelaars	Delft University of Technology
Dr. Michael Fettweis	Royal Belgian Institute of Natural Sciences

Internal defense: 1 December 2021
Public defense: 12 January 2022

The Ph.D. candidate (1S36518N) was an SB Ph.D. fellow, financially supported by the Research Foundation - Flanders (FWO).

Cover: Laura van Evelingen
Printed by: Reprography University of Antwerp
ISBN: 9789057287244
Deposit number: D/2021/12.293/44

Contents

Summary vii

Samenvatting xi

Chapter 1: introduction 1
1.1 Why study sediment and phytoplankton dynamics in estuaries? 2
1.2 The link between SPM and phytoplankton dynamics 3
1.3 Introduction to the Scheldt estuary 4
1.4 Approach and research questions 7
1.4.1 Monitoring campaigns in the Scheldt estuary 7
1.4.2 A suitable model: extending the iFlow model 7
1.4.3 Research questions and outline 9
List of symbols 11

Chapter 2: the impact of flocculation on the large-scale SPM dynamics 19
2.1 Introduction 20
2.2 Model 22
2.2.1 iFlow 22
2.2.2 Flocculation model 24
2.2.3 Ordering of the flocculation model 26
2.2.4 Impact of flocculation on net sediment transport 28
2.2.5 Solution method 29
2.3 The Scheldt: observations and calibration 29
2.3.1 The Scheldt 30
2.3.2 OMES data 30
2.3.3 Calibration 34
2.4 Results 35
2.4.1 Impact of flocculation on large-scale suspended sediment distribution 36
2.4.2 Impact of flocculation on net sediment transport 38
2.4.3 Sensitivity analysis of floc break-up parameter k_B and total freshwater discharge Q 38
2.5 Discussion 42
2.5.1 Indications of spatial and temporal variations of the settling velocity in the Scheldt estuary 42
2.5.2 Flocculation resulting in land-inward net sediment transport . . . 43
2.5.3 The potential impact of flocculation on sediment transport in the Scheldt estuary 43
2.5.4 Parameter variations in the Lagrangian flocculation model 45
2.6 Conclusions 45
List of symbols 46
Appendix 2.A: salinity dependence 49

Appendix 2.B: sediment equations with ordering . . . 50
Appendix 2.C: scaling analysis and perturbation theory . . . 53
Appendix 2.D: calculation of tidal components of w_s . . . 55
2.D.1 Pole $\zeta = 0$ . . . 57
2.D.2 Poles $\zeta = \pm\zeta_{k_1}$ . . . 57
Appendix 2.E: phase requirements for land-inward sediment transport due to flocculation . . . 59

Chapter 3: the impact of temporal variability in phytoplankton on SPM dynamics 67
3.1 Introduction . . . 68
3.2 Material and methods . . . 70
3.2.1 Study area . . . 70
3.2.2 In situ observations . . . 72
3.2.3 Model and model experiments . . . 73
3.3 Results . . . 76
3.3.1 Seasonality in the in situ observations . . . 76
3.3.2 Seasonality in the model experiments . . . 80
3.3.3 Sensitivity analysis of the modeled SPM concentration to D_p and n_f 84
3.4 Discussion . . . 84
3.4.1 Model performance and reverse engineering approach . . . 84
3.4.2 Biotic seasonality in floc size in the Scheldt estuary . . . 86
3.5 Conclusions . . . 87
List of symbols . . . 87
Appendix 3.A: floc size using various averaging methods . . . 89
Appendix 3.B: salinity profile . . . 89
Appendix 3.C: shear rate in the flocculation model . . . 90
Appendix 3.D: perturbation approach for $n_f \neq 2$ . . . 91
Appendix 3.E: primary particle size and density . . . 93

Chapter 4: the impact of temporal variability in SPM on phytoplankton 101
4.1 Introduction . . . 102
4.2 Material and methods . . . 104
4.2.1 Phytoplankton model . . . 104
4.2.2 Moment approximation . . . 106
4.2.3 Application 1: time-averaged GPP . . . 108
4.2.4 Application 2: phytoplankton bloom . . . 112
4.3 Results . . . 115
4.3.1 Moment approximation: the mfun functions . . . 115
4.3.2 Application 1: time-averaged GPP . . . 118
4.3.3 Application 2: phytoplankton bloom . . . 120
4.4 Discussion . . . 122
4.4.1 The impact of temporal variability on phytoplankton growth . . . 122
4.4.2 Implications of our findings for modelers and experimental scientists 123
4.4.3 Non-local processes and temporal variability in phytoplankton characteristics affecting the phytoplankton dynamics . . . 124
4.5 Conclusions . . . 125

List of symbols . . . 126
Appendix 4.A: analytical solution of DAP . . . 128
Appendix 4.B: application of a Taylor expansion to Λ: definition of the mfun functions . . . 128
Appendix 4.C: solution of phytoplankton biomass concentration . . . 129
Appendix 4.D: application 2: calibration of the amplitudes and phases . . . 132
Appendix 4.E: time integration of $\Lambda(t)$ . . . 132
Appendix 4.F: the impact of temporal variability in light climate on the onset of a phytoplankton bloom . . . 136

Chapter 5: applying the sediment transport - phytoplankton model: the disappearance of phytoplankton blooms in spring in the brackish region in the Scheldt estuary 143
5.1 Introduction . . . 144
5.2 Material and methods . . . 146
5.2.1 Study area . . . 146
5.2.2 In situ observations . . . 147
5.2.3 Model set-up . . . 149
5.3 Results . . . 156
5.3.1 Evolution of Chl-a and corresponding environmental conditions of the in situ observations . . . 156
5.3.2 Evolution of Chl-a studied using model experiments . . . 159
5.4 Discussion . . . 163
5.4.1 Suggested importance of grazing and phytoplankton community characteristics . . . 163
5.4.2 Model limitations . . . 165
5.5 Conclusions . . . 166
List of symbols . . . 166
Appendix 5.A: salinity profile . . . 168
Appendix 5.B: temperature dependence of $\mu_{\max}$ . . . 168
Appendix 5.C: SPM distribution . . . 169
Appendix 5.D: sediment-induced light extinction coefficient . . . 170
Appendix 5.E: evolution in discharge, salinity intrusion, and photosynthetic parameters . . . 172
Appendix 5.F: sensitivity study of model parameters . . . 175

Chapter 6: conclusions 185
6.1 Conclusions for our research questions . . . 186
6.2 General conclusion . . . 189
6.3 Implication for the Scheldt estuary . . . 189
6.3.1 Management . . . 189
6.3.2 Holistic approach . . . 190
6.3.3 Monitoring . . . 190
6.4 Opportunities for further research . . . 190
6.4.1 Application to other estuarine systems . . . 190
6.4.2 Alternative model applications . . . 191
6.4.3 The link between TEP, stickiness, and Chl-a . . . 191

6.4.4 Refinement of the boundary conditions 192
6.4.5 Explicitly resolve the zooplankton dynamics 192
6.4.6 Experimental validation of the calibrated model parameters 192

Model and data availability **197**

Acknowledgments **199**

List of publications **201**

Summary

Estuaries often show regions in which suspended particulate matter (SPM) and/or phytoplankton accumulate. Predicting the location of these regions and the corresponding magnitude of the SPM and phytoplankton concentration is of great importance for managing the estuary; it may prevent the system from evolving towards a (hyper-)turbid state, a condition in which phytoplankton growth is very limited. Such an evolution may have drastic consequences for the ecological state of the estuary as phytoplankton forms the basis of the food chain.

To predict the location and magnitude corresponding to accumulation of SPM and phytoplankton, we have to understand the interconnection between SPM and phytoplankton concentration. On the one hand, SPM is often a limiting factor for estuarine phytoplankton growth by deteriorating the light climate and thereby limiting photosynthesis. On the other hand, various authors showed that phytoplankton may determine the SPM concentration by, for example, the excretion of sticky substances. These substances may impact flocculation and thereby the settling velocity and dynamics of SPM flocs. Additionally, they may stabilize the bed and thus change the erosion properties, which also affects the SPM concentration by adjusting the sediment flux from the bed. While most literature focuses on the small-scale impact of biological flocculants on the formation of larger aggregates and erosion properties of the bed, its influence on the SPM profiles on the large spatial- and temporal scale is still largely unknown.

In this thesis, we study the interconnection of SPM and phytoplankton on the large temporal- and spatial scale, applied to a turbid, tide-dominated, and nutrient-rich estuary, being the Scheldt estuary. To this end, we combine a model approach and analysis of multi-annual observations covering the entire domain of the Scheldt estuary.

We first study the impact of flocculation on the formation of estuarine turbidity maxima (ETM), which are regions in which the concentration of SPM is larger than landward and seaward of these regions. To this end, an idealized, width-averaged hydro-sediment transport model is utilized and extended by a flocculation model. The model is applied to the Scheldt estuary in winter conditions. We show that spatial and temporal variations in settling velocity due to flocculation may promote land-inward sediment transport and result in additional ETM. They are essential to capture the observed magnitude of the SPM concentrations and their dependence on river discharge.

Secondly, to study the importance of biotically-induced seasonality in flocculation and erosion on seasonality in ETM formation, the same model framework is applied to both a winter and summer case in the Scheldt estuary. By calibrating the model to multi-annual, in situ turbidity observations, we show that we do not require seasonality

in biotically-affected flocculation and erosion parameters to reproduce the seasonality in ETM formation. Our findings are supported by multi-annual, in situ observations in turbidity, floc size, Chlorophyll-a (cf. phytoplankton abundance), and sticky substances excreted by phytoplankton; the abiotic observations show seasonality, while seasonality in the sticky substances is absent on the estuary scale.

Thirdly, before moving towards a fully operational phytoplankton-sediment transport model, we study the impact of temporal variability in factors affecting phytoplankton growth through light availability. These factors are solar irradiance at the water surface, exponential light extinction in the water column, and water depth (cf. ratio between euphotic/mixing depth). This study is important because, within our model approach, we aim to reduce computation time as it enables an extensive sensitivity analysis. We thus want to know whether we may neglect temporal variability in these factors and, if not, how we can correct for the introduced error by excluding this temporal variability. To this end, we construct a conceptual model and apply it to the Scheldt estuary. Here, we show that our conceptual model correctly predicts the magnitude and sign of the introduced error. Moreover, we demonstrate that variability in solar irradiance has the largest impact on time-averaged primary production (PP) in dynamic equilibrium, resulting in a 30 % decrease compared to time-invariant PP. Furthermore, temporal variability in solar irradiance may significantly decrease unbound exponential phytoplankton growth and may delay the onset of a phytoplankton bloom by $\sim$ 2 weeks.

Finally, we combine our previous results to construct a phytoplankton-sediment transport model. To show its applicability, we apply the model to investigate the multi-annual evolution of the estuary-scale phytoplankton distribution in spring in the Scheldt estuary. More specifically, we study what change in factors affecting phytoplankton growth may have dominantly contributed to the appearance and disappearance of a spring phytoplankton bloom in the Scheldt estuary between 2004-2018. Our results suggest that the observed change in SPM alone cannot explain the multi-annual evolution in phytoplankton blooms in spring. Instead, a change in phytoplankton mortality rate and the corresponding grazing by zooplankton and phytoplankton community characteristics may have significantly contributed to this multi-annual estuary-scale evolution.

To conclude, we combined a model approach and analysis of multi-annual observations in the Scheldt estuary to study the coupled SPM-phytoplankton dynamics on a large spatial- and temporal scale. First, we extended a hydro-sediment transport model by a flocculation model and showed that flocculation might significantly impact the estuary-scale SPM distribution. Next, we applied the model to study the impact of biotically-induced flocculation and erosion on the estuary-scale seasonality in the SPM distribution. Here, we showed that biotically-induced seasonality in flocculation and erosion only has a minor impact on the seasonality in SPM on the estuary scale; seasonality in freshwater discharge might explain the observed seasonality in SPM. Next, before constructing a fully operational phytoplankton-sediment transport model, we constructed a conceptual model to assess the relative impact of temporal variability in light climate (cf. SPM) on phytoplankton growth. We found that temporal variability in light climate may drastically reduce the time-averaged PP and exponential phytoplankton growth and delay the onset of a spring bloom by $\sim$ 2 weeks. Last, we combined our previous results to show that

a multi-annual change in mortality rate, and not in the SPM alone, may explain the observed multi-annual evolution in phytoplankton blooms in spring in the Scheldt estuary. Although we applied our modeling framework to the Scheldt estuary, it can also be applied to other turbid, tide-dominated, and nutrient-rich estuaries for which our assumptions are valid.

Hier gaan over het tij
de maan, de wind en wij

Leeflang, Ed

Samenvatting

Estuaria vertonen regelmatig regio's waarin gesuspendeerd sediment (SPM) en fytoplankton accumuleert. Voor het beheer van het estuarium is het belangrijk om de locaties van dergelijke regio's te voorspellen en de bijhorende magnitude van de SPM en fytoplankton concentratie; zo kan men immers voorkomen dat het systeem evolueert naar een hypertroebele toestand, een conditie waarin fytoplankton zeer gelimiteerd is. Een dergelijke evolutie kan drastische gevolgen hebben voor de ecologische waarde van het estuarium aangezien fytoplankton de basis vormt van de voedselketen.

Om de locatie te voorspellen waar SPM en fytoplankton accumuleert en de bijhorende concentraties dient het verband tussen SPM en fytoplankton begrepen te worden. Aan de ene kan is SPM vaak limiterend voor fytoplankton groei aangezien SPM zorgt voor een verslechtering van het lichtklimaat en daarmee de fotosynthese bemoeilijkt. Aan de andere kant toonden verschillende auteurs aan dat fytoplankton de SPM-concentratie kan bepalen door bijvoorbeeld de uitscheiding van plakkerige substanties. Deze substanties hebben immers een invloed op het vlokvormingsproces en bepalen daarmee de valsnelheid en dynamiek van SPM vlokken. Daarbovenop kunnen ze de bodem stabiliseren en zo de erosie eigenschappen aanpassen, wat dan weer een impact heeft op de sediment flux afkomstig van de bodem. Terwijl de meeste literatuur focust op de impact van biologische flocculanten op de vorming van grotere vlokken en op de bodemeigenschappen op kleine schaal, is de invloed op grote spatiale en temporele schaal nog voornamelijk onbekend terrein.

In deze thesis bestuderen we het verband tussen SPM en fytoplankton op grotere temporele en spatiale schaal, toegepast op een troebel, getijde-gedomineerd en nutriëntrijk estuarium, zijnde het Schelde estuarium. Om dit te bekomen combineren we een model aanpak en analyse van meerjaarlijkse observaties die het gehele domein van het Schelde estuarium omvatten.

Ten eerste bestuderen we de impact van vlokvorming op het ontstaan van estuariene turbiditeitsmaxima (ETM). Dit zijn regio's waarin de SPM-concentraties groter zijn dan land en zeewaarts van deze regio's. Met dit als doel gebruiken we een geïdealiseerd breedtegemiddeld hydro- en sediment transport model. Het model wordt uitgebreid en toegepast op het Schelde estuarium in winter condities. We tonen aan dat spatiale en temporele variaties in de valsnelheid ten gevolge van vlokvorming kunnen resulteren in landinwaarts sediment transport en het ontstaan van extra ETM. Bovendien zijn deze variaties essentieel om de geobserveerd magnitude van de SPM-concentraties en bijhorende afhankelijkheid van rivierafvoer te modeleren.

Ten tweede bepalen we de bijdrage van seizoenaliteit in vlokvorming en erosie met

een biotische oorsprong aan seizoenaliteit in het vormen van ETM. Hiervoor passen we dezelfde modelaanpak toe op zowel een winter als zomer geval in het Schelde estuarium. Door het model te kalibreren aan meerjaarlijkse in situ turbiditeitsobservaties tonen we aan dat seizoenaliteit in parameters gelinkt aan vlokvorming en erosie met een biotische oorsprong niet noodzakelijk is om de seizoenaliteit in de ETM-dynamiek te verklaren. Onze bevindingen worden bevestigd door meerjaarlijkse in situ observaties van turbiditeit, vlokgrootte, Chlorophyll-a (cf. fytoplankton aanwezigheid) en plakkerige substanties uitgescheiden door fytoplankton; terwijl abiotische observaties een seizoenaal patroon vertonen, zien we dit niet in de observaties van de plakkerige substanties op estuariene schaal.

Ten derde bestuderen we de impact van temporele variaties in lichtklimaat op fytoplankton groei alvorens we overgaan op een uitgebreid fytoplankton en sediment transport model. Hier focussen we op variaties in lichtinstraling aan het wateroppervlak, exponentiële licht-extinctie in de waterkolom en waterdiepte (cf. ratio tussen eufotische- en mengdiepte). Deze studie is belangrijk aangezien we in onze modelaanpak de rekentijd zo veel als mogelijk trachten te beperken om zo een uitgebreide gevoeligheidsanalyse mogelijk te maken. We wensen dus te bepalen of we bovengenoemde temporele variaties al dan niet mogen verwaarlozen. Als dit niet kan, wensen we te bepalen welke correcties we kunnen opleggen om de geïntroduceerde fout te beperken. Om dit te doen stellen we een conceptueel model op en passen we dit model opnieuw toe op het Schelde estuarium. We tonen aan dat ons conceptueel model de magnitude en het teken (i.e., afname of toename) van de geïntroduceerde fout juist voorspelt. Bovendien laten we zien dat variabiliteit in lichtinstraling aan het wateroppervlak de grootste impact heeft op tijdsgemiddelde primaire productie (PP). Het resulteert in een vermindering van tijdgemiddelde PP van ongeveer 30 %, zorgt voor een significante vertraging van fytoplankton in exponentiële groei en kan resulteren in het uitstellen van een fytoplankton voorjaarsbloei met twee weken.

Ten slotte combineren we al onze eerdere resultaten om een uitgebreid fytoplankton-sediment transport model op te stellen. Om de toepasbaarheid van dit model aan te tonen, gebruiken we dit model om de meerjaarlijkse evolutie van de fytoplankton verdeling op estuariene schaal in het Schelde estuarium te bestuderen. Meerbepaald bekijken we welke verandering in factoren die fytoplankton groei beïnvloeden een belangrijke voetdruk zou kunnen hebben op het ontstaan en verdwijnen van een fytoplankton voorjaarsbloei in het Schelde estuarium in 2004-2018. Onze resultaten suggereren dat de geobserveerde verandering in SPM niet voldoende is om de meerjaarlijkse evolutie in voorjaarsbloei te verklaren. Daartegenover, een verandering in sterfte van fytoplankton en daaraan gelinkte begrazing door zoöplankton en de soorteneigenschappen van het fytoplankton zouden wel eens een belangrijke verklaring kunnen zijn voor deze meerjaarlijkse evolutie op estuariene schaal.

Samengevat, we hebben een modelaanpak en analyse van meerjaarlijkse observaties in het Schelde estuarium gecombineerd om de gekoppelde SPM en fytoplankton dynamica te bestuderen op grote spatiale en temporale schaal. Ten eerste hebben we een hydro-sediment transport model uitgebreid met een vlokvormingsmodel. We hebben aangetoond dat vlokvorming een belangrijke impact kan hebben op de SPM-verdeling op estuariene schaal. Vervolgens hebben we het model toegepast om zo de invloed van vlokvorming

en erosie met biotische oorsprong op seizoenaliteit in de SPM-verdeling op estuariene schaal te bestuderen. Hier toonden we aan dat biotische-geïnduceerde seizoenaliteit in vlokvorming en erosie slechts een beperkte impact heeft op seizoenaliteit in SPM op estuariene schaal. Seizoenaliteit in rivierafvoer kan grotendeels de geobserveerde seizoenaliteit in de SPM-verdeling verklaren. Vervolgens hebben we een conceptueel model opgesteld om de relatieve impact van temporele variabiliteit in lichtklimaat (cf. SPM) op fytoplankton groei te bepalen. We vonden dat temporale variabiliteit in lichtinstraling aan het wateroppervlak de tijdsgemiddelde PP en fytoplankton in exponentiële groei drastisch kan verlagen. Bovendien kan het resulteren in het uitstellen van een fytoplankton bloei met twee weken. Ten slotte hebben we al onze eerdere resultaten samengenomen om aan te tonen dat een meerjaarlijkse verandering in mortaliteit van fytoplankton, en niet enkel SPM, de geobserveerde meerjaarlijkse evolutie in de voorjaarsbloei van fytoplankton in het Schelde estuarium kan verklaren. De toepassing van onze modelaanpak is niet beperkt tot het Schelde estuarium. Het model kan ook toegepast worden op andere troebele getijde-gedomineerde en nutriëntrijke estuaria.

Hier gaan over het tij
de maan, de wind en wij

Leeflang, Ed

Chapter 1

Introduction

1.1 Why study sediment and phytoplankton dynamics in estuaries?

The term estuary originates from the Latin adjective *austuarium*, meaning tidal (Fairbridge, 1980); as defined by Dionne (1963), *An estuary is an inlet of the sea reaching into a river valley as far as the upper limit of tidal rise, usually being divisible into three sectors: (a) a marine or lower estuary, in free connection with the open sea; (b) a middle estuary, subject to strong salt and freshwater mixing; and (c) an upper or fluvial estuary, characterized by freshwater but subject to daily tidal action.*

The specific features of estuaries make them valuable from multiple perspectives. Being the interconnection between land and sea makes estuaries often densely populated. Consequently, estuaries are necessary for flood protection as they reduce the tidal wave energy in the land-ward direction. They are also crucial for the economy through, for example, food production, water regulation, and wastewater treatment (Costanza et al., 1997). Furthermore, estuaries form unique habitats (Davidson et al., 1991) and thereby are essential to maintain biodiversity from an ecological perspective.

In many estuaries, we have two crucial indicators regarding their ecological condition: primary production of phytoplankton and the suspended particulate matter (SPM) concentration. The reason is that first of all, phytoplankton forms the base of the estuarine pelagic food web (Brett and Müller-Navarra, 1997; Sobczak et al., 2005; Falkowski, 2012). Additionally, the fact that estuaries are often turbid and SPM may significantly deteriorate the light climate in the water column (Wofsy, 1983) makes the SPM concentration an important limiting factor for phytoplankton growth (Sverdrup, 1953; Colijn, 1982; Cloern, 1987) compared to other limiting factors such as nutrient limitation and grazing.

In the past, specific anthropogenic measures had drastic consequences on both the phytoplankton and SPM concentration. For example, the Ems estuary evolved towards hyper-turbid conditions after deepening the system, prohibiting primary production of phytoplankton, the base of the estuarine food web, and even impeding navigation because of increased friction force (Winterwerp and Wang, 2013; Winterwerp et al., 2013). Another example, the notable increase in wastewater treatment capacity in the Scheldt estuary around 2006 resulted in significantly higher oxygen concentrations and intense phytoplankton blooms (Maris and Meire, 2017).

To summarize, why study sediment and phytoplankton dynamics in estuaries? Estuaries are unique systems with substantial economic value and are essential to maintain biodiversity and ensure flood protection. However, they are under continued anthropogenic pressure. To assess the impact of specific management measures on phytoplankton and SPM dynamics, often two crucial factors for a good ecological state of an estuary, insight into the fundamental functioning of the SPM and phytoplankton dynamics and their interconnection is required.

1.2 The link between SPM and phytoplankton dynamics

This section briefly introduces the complex interconnection between SPM and phytoplankton dynamics we focus on in this thesis (Fig. 1.1). To reduce complexity, we mainly study the SPM and phytoplankton dynamics on the estuary scale. Here, regions with locally elevated phytoplankton and SPM concentrations are particularly interesting.

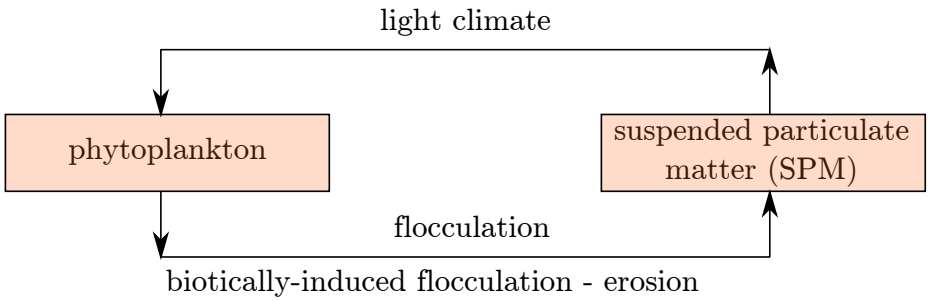

Figure 1.1: Illustration of the interconnection between SPM and phytoplankton studied in this thesis. SPM limits phytoplankton growth by deteriorating the light climate in the water column. Phytoplankton may affect the SPM dynamics by altering the erosion properties of the bed, floc size density and structure of flocs, and by excreting sticky substances which stimulate flocculation of SPM.

Focusing on phytoplankton, such elevated concentrations result from a complex interplay between physical, transport-related processes and chemical-biotic factors that determine net local phytoplankton growth. Such processes include water temperature (Eppley, 1972), river flushing (Filardo and Dunstan, 1985; Liu and de Swart, 2015), salinity (Lucas et al., 1998), phytoplankton grazing (Alpine and Cloern, 1992; Lionard et al., 2005), nutrients (Tilman et al., 1982; Cira et al., 2016), and the light climate in the water column (Sverdrup, 1953; Desmit et al., 2005).

The light climate in the water column is determined by the SPM concentration, especially in turbid estuaries (Wofsy, 1983). To understand the phytoplankton dynamics, we thus have to study the SPM dynamics.

The SPM dynamics also result from complex interactions of various sediment transport mechanisms. Examples of such transport mechanisms are, amongst others, related to tidal asymmetries in water motion, water density gradients, and transport mechanisms related to temporal variability in settling velocity of SPM [see, for example, Burchard et al. (2018) for a review]. One mechanism resulting in temporal and spatial variability of settling velocity is flocculation. Flocculation results in the aggregation and break-up

of cohesive SPM, including both organic and mineral solids, thus changing the density, floc size, and settling velocity.

The fact that the flocculation process impacts the SPM dynamics has important consequences. Many authors showed that the presence of biota might have a significant impact on the flocculation process. Biotic characteristics that influence flocculation are, for example, sticky biotic substances excreted by phytoplankton and the organic content of SPM. The organic content directly alters the differential density and structure of flocs (Kranenburg, 1994; van Leussen, 1994; Fall et al., 2021), which affects the averaged floc size (Mietta et al., 2009), floc strength and collision efficiency (Winterwerp and van Kesteren, 2004), and floc break-up (Alldredge et al., 1990). Finally, in situ observations show a correlation between Chlorophyll-a (Chl-a), which is an indicator for phytoplankton abundance, and flocculation efficiency (Verney et al., 2009), and sticky biotic substances excreted by phytoplankton [i.e., Transparent Exopolymer Particles (TEP)] and floc strength (Fettweis et al., 2014).

Besides the flocculation process, biotic factors may also impact the erosion properties of the sediment bed, which also affects the SPM dynamics. On the one hand, various authors found that phytoplankton activity, which typically peaks in spring and summer, often stabilizes the sediment bed (Frostick and McCave, 1979) and induces the formation of bedforms (Malarkey et al., 2015) by, for example, the excretion of extracellular polymeric substances (EPS), of which TEP are a particulate form (Passow, 2002), and which bind the sediment together (Stal, 2010). On the other hand, the subsequent grazing of phytoplankton by bioturbatory macroheterotrophs may increase the erodibility (Paterson and Black, 1999).

To summarize, both the SPM and phytoplankton dynamics are complex and coupled. On the one hand, the SPM concentrations impact phytoplankton growth by deteriorating the turbidity of the water column, especially in turbid estuaries. On the other hand, phytoplankton may affect SPM dynamics by altering the erosion properties of the bed and flocculation characteristics.

1.3 Introduction to the Scheldt estuary

Depending on the domain of interest, estuaries can be classified based on, for example, their physiography (e.g., shallow, funnel-shaped), hydrodynamics (e.g., freshwater discharge, tidal range), climate (e.g., tropical, non-tropical), and biological condition (nutrient-rich, light-limited for phytoplankton growth) (Fairbridge, 1980).

This thesis focuses on shallow, tide-dominated systems, which are systems in which the tidal energy is large compared to the freshwater discharge. Consequently, the system can be considered to be well-mixed. This assumption allows us to approximate the vertical distribution of salinity and phytoplankton as homogeneous. Moreover, we assume that the system is nutrient-rich and light-limited, allowing us to neglect nutrient limitation. These

assumptions result in a drastic simplification of the dynamics. This is recommended given the complexity of phytoplankton and SPM dynamics, as demonstrated in the previous section.

An example of an estuary for which these assumptions are valid is the Scheldt estuary (Belgium, Netherlands). The Scheldt estuary is the system we focus on in this thesis. In each chapter, we apply our theoretical results to this estuary. However, our theoretical results are not limited to the Scheldt estuary but are also applicable to other systems with similar characteristics. In the following, we briefly introduce the Scheldt estuary by focusing on the features of interest in this thesis.

The Scheldt estuary is an approximately 160 km long, funnel-shaped estuary (Fig. 1.2). It flows through Belgium into the North Sea near Vlissingen (Netherlands). Because of its relatively small freshwater discharge, the Scheldt estuary can be considered a tide-dominated and well-mixed estuary (Baeyens et al., 1997; Meire et al., 2005). The total time-averaged freshwater discharge over the years 2015-2018 shows distinct seasonality and equals 40 $m^3\ s^{-1}$, 174 $m^3\ s^{-1}$, and 72 $m^3\ s^{-1}$ in summer (Jun.-Aug.), winter (Jan.-Mar.), and spring (Apr.-May), respectively. The main tributaries of the Scheldt estuary are the Rupel and the Dender. The Upper Sea Scheldt boundary (i.e., the upstream boundary of the Scheldt estuary), the Rupel, and the Dender are responsible for 16.4, 77.2, and 6.4 % of the total river discharge in summer, 35.4, 53.1, and 11.5 % in winter, and 27.1, 63.3, and 9.6 % in spring, respectively (Waterinfo.be, 2019, deducted from gauge stations at the upstream boundary *zes57a-1066*, at the Dender tributary *den02a-1066*, and downstream from the Rupel tributary *zes29f-1066* assuming conservation of mass). The dissolved nitrogen, phosphorous, and silicate concentrations in spring range from 0.1 mmol L^{-1}, 0.001 mmol L^{-1}, and 0.005 mmol L^{-1} at the seaside boundary to 0.4 mmol L^{-1}, 0.007 mmol L^{-1}, and 0.13 mmol L^{-1} at the upstream boundary, respectively. These concentrations are at least one order of magnitude larger than the half-saturation constants at which we expect nutrient depletion (Billen and Garnier, 1997; Lancelot et al., 2005; Arndt et al., 2011; Naithani et al., 2016).

The maintenance of the navigation channel to the port of Antwerp (first four red dots from the Dutch-Belgian border in Fig. 1.2) requires intensive dredging activities. To minimize the risk of flooding by altering the total volume of the estuary, the dredged material is often dumped back into the Scheldt estuary. This dumping comes with significantly higher SPM loads (10^6 ton $year^{-1}$) than the fluvial input of SPM (Dijkstra et al., 2019b). At the main dumping locations at km 73 and 78 from the mouth, the time-averaged dumped material between 2001-2015 corresponds to a high SPM input of approximately 60 and 100 kg s^{-1}, respectively. Consequently, these dumping activities impact the SPM concentration locally, which was confirmed by a multivariate regression analysis of SPM observations between 1996-2016. This analysis showed that the SPM concentrations at the dumping sites are dominantly correlated to dumping activities (IMDC, 2016). The yearly fluvial input of SPM at the upstream boundary and tributaries is of the order of 10^4-10^5 ton $year^{-1}$ (Plancke et al., 2017; Dijkstra et al., 2019b).

The Scheldt estuary is an interesting example in view of the interplay between phytoplankton, SPM, and other factors. Firstly, the flocculation process, which links phyto-

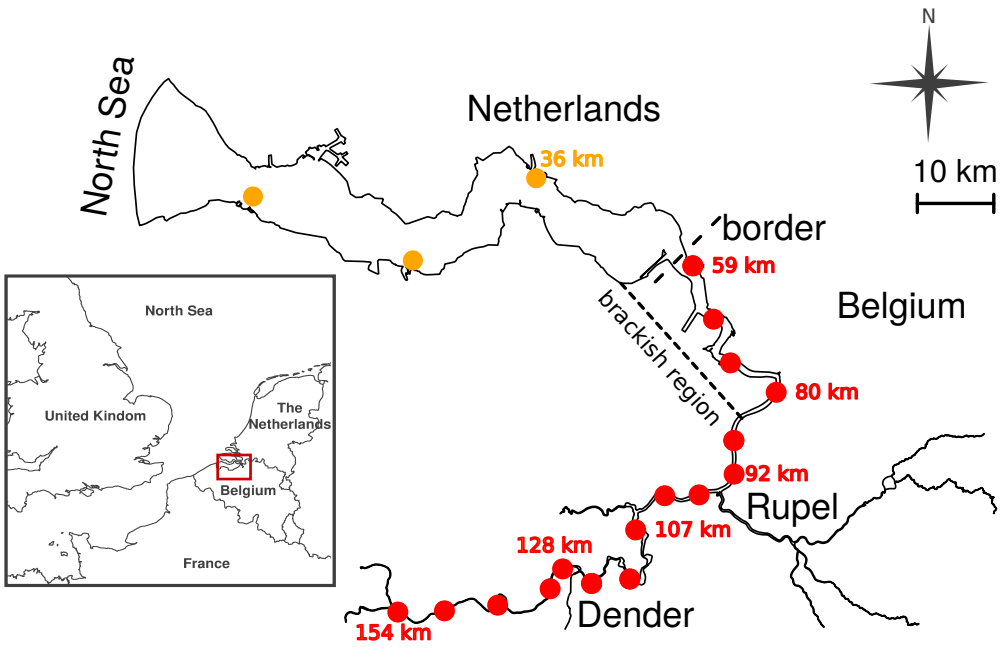

Figure 1.2: The Scheldt estuary and its two main tributaries (Rupel and Dender). The red dots represent the locations where monthly and biweekly turbidity and floc size profiles were measured in the frame of the OMES environmental monitoring program. The orange dots depict the sites corresponding to the observations conducted by Rijkswaterstaat.

plankton to SPM, is important in the Scheldt estuary (Peters, 1972; Gourgue et al., 2013). Moreover, Cox et al. (2019) reported a long-term estuary-scale change in SPM dynamics in the Scheldt estuary. From 2009 onwards, a change in the estuarine turbidity maximum dynamics and an overall increase in SPM concentration was observed, reaching typical SPM concentration at the water surface of ~ 100 mg L^{-1}, which may significantly limit photosynthesis (Wofsy, 1983). Simultaneously, the water quality in the Scheldt estuary improved drastically mainly because of a significant increase in wastewater treatment capacity in Brussels around 2006 (Brion et al., 2015). This resulted in increasing oxygen concentrations and changes in the zooplankton community and abundance. More specifically, calanoid copepods, in casu *Eurytemora affinis*, dominated in the downstream brackish region and were quasi absent in the freshwater region at the beginning of the observations in 1996. Next, they gradually developed more upstream to also become dominant there from 2009 (Appeltans, 2003; Mialet et al., 2010, 2011; Chambord et al., 2016). This could affect the phytoplankton abundance through grazing. These changes in the SPM dynamics and zooplankton abundance coincide with long-term changes in phytoplankton dynamics, such as the appearance and disappearance of a phytoplankton spring bloom in the brackish region. From 2004 until 2007, we observed almost no spring bloom in the brackish region. Such a spring bloom was consistently observed between 2008-2014 but disappeared after 2015.

1.4 Approach and research questions

In this thesis, we combine two approaches to study the SPM and phytoplankton dynamics in the Scheldt estuary. Firstly, we analyze long-term in situ observations in the Scheldt estuary. Secondly, we develop a model to study the interconnection between SPM and phytoplankton dynamics. To show the applicability of our model approach, we apply our model to the multi-annual observations in the Scheldt estuary. The following sections introduce the monitoring campaigns resulting in the multi-annual observations and the model approach.

1.4.1 Monitoring campaigns in the Scheldt estuary

Both the Belgian and Dutch part of the Scheldt estuary have been monitored intensively over the last two decades. In the Belgian region, various variables, including Chl-a (cf. phytoplankton), SPM, salinity, and phytoplankton characteristics, such as the maximum photosynthetic production rate and growth efficiency, have been measured within the multi-annual OMES (Dutch: "Onderzoek Milieu Effecten Sigmaplan") monitoring campaign (Maris and Meire, 2017), independently of the tidal phase and spring-neap tide biweekly or monthly at 16 fixed stations (see Fig. 1.2). In the Dutch region, we use biweekly or monthly observations of Chl-a and SPM by Rijkswaterstaat at three stations in the main channel (see Fig. 1.2). For a detailed methodological description, we refer the reader to the OMES reports (Maris and Meire, 2017) and the website of Rijkswaterstaat (Rijkswaterstaat, 2020).

1.4.2 A suitable model: extending the iFlow model

The model we use is the process-based, width-averaged, idealized model known as iFlow (Dijkstra et al., 2017). The model solves the width-averaged shallow water equations in tide-dominated estuaries by neglecting the effects of Coriolis and assuming that density variability is small compared to the average density, allowing for the Boussinesq approximation. The hydrodynamics are forced at the upstream boundary and two main tributaries by a fixed water inflow and at the mouth by a tidal signal. These equations and corresponding boundary conditions result in the dynamics of the water level elevations, horizontal- and vertical water velocity. For a detailed description, we refer the reader to Chernetsky et al. (2010) and Dijkstra et al. (2017). Following Warner et al. (2005), the longitudinal salinity profile is implemented as a tide- and depth-independent profile. This assumption is consistent with the Scheldt estuary being a well-mixed estuary (Baeyens et al., 1997; Meire et al., 2005). The SPM and phytoplankton dynamics are resolved using the SPM and phytoplankton mass balance equations in equilibrium conditions. For completeness and because these dynamics form the basis of this thesis, we repeat the latter equations and corresponding boundary conditions. The width-averaged sediment mass balance equation and related boundary conditions read as (Chernetsky et al., 2010;

Dijkstra et al., 2017)

$$\partial_t c + u\partial_x c + w\partial_z c - \partial_z(w_s c + K_\nu \partial_z c) - \frac{1}{B}\partial_x(BK_h\partial_x c) = 0, \tag{1.1}$$

$$\begin{cases} w_s c + \partial_z(K_\nu c) = 0, & \text{at the water surface (no flux),} \\ w_s c + K_\nu \partial_z c = D - E, & \text{at the bed (flux equals } D - E\text{),} \end{cases} \tag{1.2}$$

in which t represents time, x and z are the coordinates in longitudinal and vertical direction, c is the suspended sediment concentration, u and w are the water velocity in the x- and z-direction, w_s is the settling velocity, B is the time-invariant width of the Scheldt estuary, K_ν is the constant vertical eddy diffusivity coefficient, K_h the constant horizontal diffusivity coefficient and D and E are the deposition and erosion of sediment defined as

$$D = w_s c, \tag{1.3}$$

$$E = M|\tau_b|f(a), \tag{1.4}$$

where M is the constant erosion parameter, τ_b is the shear stress at the bed, and $f(a)$ is the erodibility.

The phytoplankton model consists of a dynamic model that describes the spatial and tidal evolution of phytoplankton concentration and corresponding nutrients nitrogen and phosphorous (Dijkstra et al., 2019a). We do not focus on the equation for the nutrient dynamics because the Scheldt estuary can be considered a nutrient-rich system, as mentioned above. The model consists of a single-phytoplankton class and thus does not differentiate between diatoms and non-diatoms. Consequently, Si-dynamics and salinity stress are not included, and phytoplankton characteristics are assumed constant in the system. The width-averaged equation for the phytoplankton concentration P and corresponding boundary conditions read (Dijkstra et al., 2019a)

$$\underbrace{\partial_t P + u\partial_x P + (w - w_P)\partial_z P - \partial_z(K_\nu\partial_z P) - \frac{1}{B}\partial_x(BK_h\partial_x P)}_{\text{advection-diffusion}} = \underbrace{(\mu - m)P}_{\text{balance between local growth and mortality}}, \tag{1.5}$$

$$\begin{cases} w_P P + K_\nu \partial_z P = 0, & \text{at the bed and water surface (no flux),} \\ \left\langle \frac{1}{H+\zeta} \int_{-H}^{\zeta} P dz \right\rangle = P_{\text{sea}}, & \text{at the seaside boundary (constant concentration),} \\ B\left\langle \int_{-H}^{\zeta} (uP - K_h\partial_x P)dz \right\rangle = QP, & \text{at the upstream boundary (constant influx),} \end{cases} \tag{1.6}$$

in which w_P is the constant settling velocity of phytoplankton cells, $\langle\cdot\rangle$ denotes averaging over a long time scale (i.e., larger than a tide or day), ζ and time-invariant $-H$ are the z-coordinates of the water surface and bed, P_{sea} is the constant phytoplankton concentration at the seaside boundary, QP is the constant influx of phytoplankton at the upstream boundary, and μ and m are the growth and (constant) mortality rate of phytoplankton.

The model only focuses on the estuary-scale hydro-, SPM, and phytoplankton dynamics by approximating the estuary's bathymetry and width by smooth profiles. The model resolves the tidal and subtidal water motion and cohesive SPM concentration and provides approximate solutions of the complex and non-linear set of equations for hydro and SPM dynamics using a scaling and perturbation approach. This approach simplifies the interpretation of the results, allows us to focus on individual processes, and drastically decreases computation time, enabling an extensive sensitivity analysis. For the technical details, we refer the reader to Chernetsky et al. (2010), Dijkstra et al. (2017), and Dijkstra et al. (2019a).

In this thesis, we implement three major extensions to the iFlow model. Firstly, we extend the iFlow model by a flocculation model to resolve flocculation of cohesive sediment, which forms an important link between phytoplankton and SPM. Here, we also apply a scaling and perturbation approach following Chernetsky et al. (2010) and Dijkstra et al. (2017). Secondly, we use an alternative approximated light limitation function for local phytoplankton growth [cf. μ in Eq. (1.5)]. This alternative allows us to further decrease the computational cost and include the impact of temporal variability in water depth on phytoplankton productivity, which is important in shallow regions. Thirdly, we consider two phytoplankton groups (i.e., freshwater and marine diatoms), thereby implementing salinity stress. Additionally, we make the mortality rate dependent on two (meso)zooplankton groups: calanoids and non-calanoids.

1.4.3 Research questions and outline

The extended model combined with the long-term observations in the Scheldt estuary is used to answer the main research questions, which we present in this section. Each research question corresponds to a Chapter. The outline of this thesis is illustrated in Fig. 1.3.

- What is the impact of flocculation on the large-scale SPM dynamics?

In Chapter 2, we determine whether flocculation can change the estuary-scale SPM distribution. To this end, we extend the iFlow model by a flocculation model and apply the model to a winter case in the Scheldt estuary.

- Can we detect a seasonal biotic impact on the SPM dynamics through flocculation and erosion?

Assuming a strong biotic impact on flocculation and erosion and knowing that biota typically show strong seasonal behavior, we expect to detect seasonality in biotically-induced flocculation and erosion. In Chapter 3, we estimate the impact of biota on the seasonality of the sediment distribution through flocculation and erosion on the seasonal and estuary scale using the results from Chapter 2. This insight is crucial when constructing a

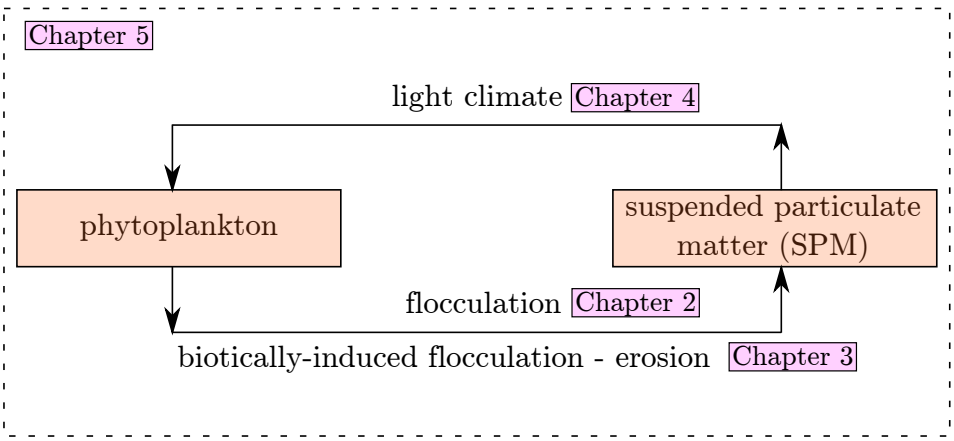

Figure 1.3: Illustration of the interconnection between SPM and phytoplankton studied in this thesis and corresponding chapters. SPM limits phytoplankton growth by deteriorating the light climate in the water column. Phytoplankton may affect SPM dynamics by altering the floc size and structure of flocs and excreting sticky substances that stimulate flocculation of SPM. In Chapter 2, we study the impact of flocculation on SPM. In Chapter 3, we focus on the importance of biotically-induced flocculation on SPM. In Chapter 4, we study the impact of temporal variability in light climate (cf. SPM) on phytoplankton. We combine all results and study a specific case regarding phytoplankton-SPM dynamics in the Scheldt estuary in Chapter 5.

coupled sediment transport - phytoplankton model; sediment transport - phytoplankton models are typically divided between physical and biotic models that are not coupled. This chapter is thus essential to determine whether this division is a fair approximation.

- Can we construct a model to easily assess the relative impact of temporal fluctuations in SPM on phytoplankton growth?

Before proceeding to a fully complex phytoplankton-SPM model, we develop a tool to locally study the impact of temporal variability in light climate on primary production in Chapter 4 without solving the complex SPM dynamics explicitly. The tool allows us to determine the relative impact of temporal variability in the SPM dynamics without a priori assumptions regarding these dynamics. We aim to know whether we may neglect temporal variability in these parameters and, if not, how we can correct for the introduced error by excluding this temporal variability. We again apply the tool to the Scheldt estuary.

- Can we link the disappearance of the spring bloom in the brackish region in the

Scheldt estuary between 2004-2018 to multi-annual changes of processes impacting phytoplankton growth and their corresponding model parameters?

In Chapter 5, we combine all the previous results from Chapters 2, 3, and 4 to construct a sediment transport - phytoplankton model. To show its applicability, we again apply the model to the Scheldt estuary. We focus on the appearance and consequent disappearance of phytoplankton blooms in spring in the brackish region in the Scheldt estuary in the last two decades, which we introduced at the end of Section 1.3.

List of symbols

Latin

a	Availability of easily erodible fine sediment at the sediment bed
B	Width of the estuary
c	Suspended sediment concentration
D	Deposition flux of suspended sediment
E	Erosion flux of sediment from the sediment bed
$f(a)$	Erodibility
H	Magnitude of the z-coordinate of the river bed
K_h	Horizontal diffusivity coefficient
K_ν	Vertical eddy diffusivity coefficient
M	Erosion parameter
m	Mortality rate of phytoplankton
P	Phytoplankton concentration
P_{sea}	Phytoplankton concentration at the seaside boundary
QP	Influx of phytoplankton at the upstream boundary
t	Time
u	Water flow velocity in the longitudinal dimension
w	Water flow velocity in the vertical dimension
w_P	Settling velocity of phytoplankton cells
w_s	Settling velocity of suspended sediment
x	Spatial coordinate in the longitudinal dimension
z	Spatial coordinate in the vertical dimension

Greek

ζ	z-coordinate of the water surface
μ	Growth rate of phytoplankton
τ_b	Shear stress at the river bed

Bibliography

Alldredge, A. L., Granata, T. C., Gotschalk, C. C., and Dickey, T. D. (1990). The physical strength of marine snow and its implications for particle disaggregation in the ocean. *LIMNOLOGY AND OCEANOGRAPHY*, 35(7):1415–1428.

Alpine, A. E. and Cloern, J. E. (1992). Trophic interactions and direct physical effects control phytoplankton biomass and production in an estuary. *Limnology and Oceanography*, 37(5):946–955.

Appeltans, W. (2003). Zooplankton in the Schelde estuary (Belgium/The Netherlands). The distribution of Eurytemora affinis: effect of oxygen? *Journal of Plankton Research*, 25(11):1441–1445.

Arndt, S., Lacroix, G., Gypens, N., Regnier, P., and Lancelot, C. (2011). Nutrient dynamics and phytoplankton development along an estuary-coastal zone continuum: A model study. *Journal of Marine Systems*, 84(3-4):49–66.

Baeyens, W., Van Eck, B., Lambert, C., Wollast, R., and Goeyens, L. (1997). General description of the Scheldt estuary. *Hydrobiologia*, 366(1-3):1–14.

Billen, G. and Garnier, J. (1997). The Phison River plume: Coastal eutrophication in response to changes in land use and water management in the watershed. *Aquatic Microbial Ecology*, 13(1):3–17.

Brett, M. T. and Müller-Navarra, D. C. (1997). The role of highly unsaturated fatty acids in aquatic foodweb processes. *Freshwater Biology*, 38(3):483–499.

Brion, N., Verbanck, M. A., Bauwens, W., Elskens, M., Chen, M., and Servais, P. (2015). Assessing the impacts of wastewater treatment implementation on the water quality of a small urban river over the past 40 years. *Environmental Science and Pollution Research*, 22(16):12720–12736.

Burchard, H., Schuttelaars, H. M., and Ralston, D. K. (2018). Sediment Trapping in Estuaries. *Annual Review of Marine Science*, 10(1):371–395.

Chambord, S., Maris, T., Colas, F., Van Engeland, T., Sossou, A. C., Azémar, F., Le Coz, M., Cox, T., Buisson, L., Souissi, S., Meire, P., and Tackx, M. (2016). Mesozooplankton affinities in a recovering freshwater estuary. *Estuarine, Coastal and Shelf Science*, 177:47–59.

Chernetsky, A. S., Schuttelaars, H. M., and Talke, S. A. (2010). The effect of tidal asymmetry and temporal settling lag on sediment trapping in tidal estuaries. *Ocean Dynamics*, 60(5):1219–1241.

Cira, E. K., Paerl, H. W., and Wetz, M. S. (2016). Effects of Nitrogen Availability and Form on Phytoplankton Growth in a Eutrophied Estuary (Neuse River Estuary, NC, USA). *PLOS ONE*, 11(8).

Cloern, J. E. (1987). Turbidity as a control on phytoplankton biomass and productivity in estuaries. *Continental Shelf Research*, 7(11-12):1367–1381.

Colijn, F. (1982). Light absorption in the waters of the Ems-Dollard estuary and its consequences for the growth of phytoplankton and microphytobenthos. *Netherlands Journal of Sea Research*, 15(2):196–216.

Costanza, R., D'Arge, R., De Groot, R., Farber, S., Grasso, M., Hannon, B., Limburg, K., Naeem, S., O'Neill, R. V., Paruelo, J., Raskin, R. G., Sutton, P., and Van Den Belt, M. (1997). The value of the world's ecosystem services and natural capital. *Nature*, 387(6630):253–260.

Cox, T. J. S., Maris, T., Van Engeland, T., Soetaert, K., and Meire, P. (2019). Critical transitions in suspended sediment dynamics in a temperate meso-tidal estuary. *Scientific Reports*, 9(1):12745.

Davidson, N. C., Laffoley, D. d., Doody, J. P., Way, L. S., Gordon, J., Key, R., Drake, C. M., Pienkowski, M. W., Mitchell, R., and Duf, K. L. (1991). Nature Conservation and Estuaries in Great Britain. Nature Conservancy Council, Peterborough.

Desmit, X., Vanderborght, J. P., Regnier, P., and Wollast, R. (2005). Control of phytoplankton production by physical forcing in a strongly tidal, well-mixed estuary. *Biogeosciences*, 2(2):205–218.

Dijkstra, Y. M., Brouwer, R. L., Schuttelaars, H. M., and Schramkowski, G. P. (2017). The iFlow modelling framework v2.4: a modular idealized process-based model for flow and transport in estuaries. *Geoscientific Model Development*, 10(7):2691–2713.

Dijkstra, Y. M., Chant, R. J., and Reinfelder, J. R. (2019a). Factors Controlling Seasonal Phytoplankton Dynamics in the Delaware River Estuary: an Idealized Model Study. *Estuaries and Coasts*, 42(7):1839–1857.

Dijkstra, Y. M., Schuttelaars, H. M., and Schramkowski, G. P. (2019b). Can the Scheldt River Estuary become hyperturbid? A model analysis of suspended sediment concentrations and transport in response to channel deepening. *Ocean Dynamics*, 69(7):809–827.

Dionne, J. C. (1963). Towards a more adequate definition of the st. lawrence estuary. *Zeitschr. f. Geomorph.*, 7:36–44.

Eppley, R. W. (1972). Temperature and phytoplankton growth in the sea. *Fish. bull*, 70(4):1063–1085.

Fairbridge, R. W. (1980). The estuary: its definition and geodynamic cycle. In Olausson, E. and Cato, I., editors, *Chemistry and biogeochemistry of estuaries*, chapter 1, pages 1–35. Wiley Interscience, Chichester.

Falkowski, P. (2012). Ocean science: The power of plankton. *Nature*, 483(7387):S17–S20.

Fall, K. A., Friedrichs, C. T., Massey, G. M., Bowers, D. G., and Smith, S. J. (2021). The Importance of Organic Content to Fractal Floc Properties in Estuarine Surface Waters: Insights From Video, LISST, and Pump Sampling. *Journal of Geophysical Research: Oceans*, 126(1):e2020JC016787.

Fettweis, M., Baeye, M., Van der Zande, D., Van den Eynde, D., and Lee, B. J. (2014). Seasonality of floc strength in the southern North Sea. *Journal of Geophysical Research-Oceans*, 119(3):1911–1926.

Filardo, M. J. and Dunstan, W. M. (1985). Hydrodynamic control of phytoplankton in low salinity waters of the James River estuary, Virginia, U.S.A. *Estuarine, Coastal and Shelf Science*, 21(5):653–667.

Frostick, L. E. and McCave, I. N. (1979). Seasonal shifts of sediment within an estuary mediated by algal growth. *Estuarine and Coastal Marine Science*, 9(5):569–576.

Gourgue, O., Baeyens, W., Chen, M. S., de Brauwere, A., de Brye, B., Deleersnijder, E., Elskens, M., and Legat, V. (2013). A depth-averaged two-dimensional sediment transport model for environmental studies in the Scheldt Estuary and tidal river network. *Journal of Marine Systems*, 128:27–39.

IMDC (2016). Monitoringprogramma Flexibel Storten. Multivariate analyse van metingen van sedimentconcentratie in de Zeeschelde. WL Reports I /RA/11353/15.228/THL, IMDC, Antwerpen.

Kranenburg, C. (1994). The Fractal Structure of Cohesive Sediment Aggregates. *Estuarine, Coastal and Shelf Science*, 39(5):451–460.

Lancelot, C., Spitz, Y., Gypens, N., Ruddick, K., Becquevort, S., Rousseau, V., Lacroix, G., and Billen, G. (2005). Modelling diatom and Phaeocystis blooms and nutrient cycles in the Southern Bight of the North Sea: The MIRO model. *Marine Ecology Progress Series*, 289(June 2014):63–78.

Lionard, M., Azémar, F., Boulêtreau, S., Muylaert, K., Tackx, M., and Vyverman, W. (2005). Grazing by meso- and microzooplankton on phytoplankton in the upper reaches of the Schelde estuary (Belgium/The Netherlands). *Estuarine, Coastal and Shelf Science*, 64(4):764–774.

Liu, B. and de Swart, H. E. (2015). Impact of river discharge on phytoplankton bloom dynamics in eutrophic estuaries: A model study. *Journal of Marine Systems*, 152:64–74.

Lucas, L. V., Cloern, J. E., Koseff, J. R., Monismith, S. G., and Thompson, J. K. (1998). Does the Sverdrup critical depth model explain bloom dynamics in estuaries? *Journal of Marine Research*, 56(2):375–415.

Malarkey, J., Baas, J. H., Hope, J. A., Aspden, R. J., Parsons, D. R., Peakall, J., Paterson, D. M., Schindler, R. J., Ye, L., Lichtman, I. D., Bass, S. J., Davies, A. G., Manning, A. J., and Thorne, P. D. (2015). The pervasive role of biological cohesion in bedform development. *Nature Communications*, 6(1):1–6.

Maris, T. and Meire, P. (2017). Omes rapport 2016. Onderzoek naar de gevolgen van het Sigmaplan, baggeractiviteiten en havenuitbreiding in de Zeeschelde op het milieu. Technical Report Report Ecosystem Management Research Group ECOBE, 017-R206, University of Antwerp, Antwerp, Belgium.

Meire, P., Ysebaert, T., Van Damme, S., Van den Bergh, E., Maris, T., and Struyf, E. (2005). The Scheldt estuary: a description of a changing ecosystem. *Hydrobiologia*, 540(1-3):1–11.

Mialet, B., Azémar, F., Maris, T., Sossou, C., Ruiz, P., Lionard, M., Van Damme, S., Lecerf, A., Muylaert, K., Toumi, N., Meire, P., and Tackx, M. (2010). Spatial spring distribution of the copepod Eurytemora affinis (Copepoda, Calanoida) in a restoring estuary, the Scheldt (Belgium). *Estuarine, Coastal and Shelf Science*, 88(1):116–124.

Mialet, B., Gouzou, J., Azémar, F., Maris, T., Sossou, C., Toumi, N., Van Damme, S., Meire, P., and Tackx, M. (2011). Response of zooplankton to improving water quality in the Scheldt estuary (Belgium). *Estuarine, Coastal and Shelf Science*, 93(1):47–57.

Mietta, F., Chassagne, C., Manning, A. J., and Winterwerp, J. C. (2009). Influence of shear rate, organic matter content, pH and salinity on mud flocculation. *Ocean Dynamics*, 59(5):751–763.

Naithani, J., de Brye, B., Buyze, E., Vyverman, W., Legat, V., and Deleersnijder, E. (2016). An ecological model for the Scheldt estuary and tidal rivers ecosystem: spatial and temporal variability of plankton. *Hydrobiologia*, 775(1):51–67.

Passow, U. (2002). Transparent exopolymer particles (TEP) in aquatic environments. *Progress in Oceanography*, 55(3-4):287–333.

Paterson, D. and Black, K. (1999). Water flow, sediment dynamics and benthic ecology. *Advances in Ecological Research*, 29:155–193. This volume: 'Estuaries'. ISBN for this volume: 978-0-12-013929-3.

Peters, J. J. (1972). Transports de sédiments dans l'estuaire de l'Escaut. Technical report, Flanders Hydraulics Research.

Plancke, Y., Van De Moortel, I., Hertogs, R., Vereecken, H., Vos, G., Verdoodt, N., Meire, D., Deschamps, M., and Mostaert, F. (2017). Monitoring Effecten Ontwikkelingsschets (MONEOS) - Jaarboek monitoring 2016: Deelrapport 6 - Factual data rapportage van monitoring waterbeweging en fysische parameters in de Zeeschelde in 2016. WL Reports 12_070_6, Flanders Hydraulics Research, Antwerpen.

Rijkswaterstaat (2020). Rijkswaterstaat official website.

Sobczak, W. V., Cloern, J. E., Jassby, A. D., Cole, B. E., Schraga, T. S., and Arnsberg, A. (2005). Detritus fuels ecosystem metabolism but not metazoan food webs in San Francisco estuary's freshwater Delta. *Estuaries*, 28(1):124–137.

Stal, L. J. (2010). Microphytobenthos as a biogeomorphological force in intertidal sediment stabilization. *Ecological Engineering*, 36(2):236–245.

Sverdrup, H. U. (1953). On Conditions for the Vernal Blooming of Phytoplankton. *ICES Journal of Marine Science*, 18(3):287–295.

Tilman, D., Kilham, S. S., and Kilham, P. (1982). Phytoplankton Community Ecology: The Role of Limiting Nutrients. *Annual Review of Ecology and Systematics*, 13(1):349–372.

van Leussen, W. (1994). *Estuarine macroflocs and their role in fine-grained sediment transport.* PhD thesis, Utrecht University, Utrecht.

Verney, R., Lafite, R., and Brun-Cottan, J. C. (2009). Flocculation potential of estuarine particles: The importance of environmental factors and of the spatial and seasonal variability of suspended particulate matter. *Estuaries and Coasts*, 32(4):678–693.

Warner, J. C., Geyer, W. R., and Lerczak, J. A. (2005). Numerical modeling of an estuary: A comprehensive skill assessment. *Journal of Geophysical Research: Oceans*, 110(C5):1–13.

Waterinfo.be (cited 2019). Measurements and predictions of Waterinfo.be [data]. [Available online at `https://www.waterinfo.be/`].

Winterwerp, J. C. and van Kesteren, W. G. M. (2004). *Introduction to the physics of cohesive sediment in the marine environment*, volume 56. Elsevier Science, Amsterdam, The Netherlands, 1st edition.

Winterwerp, J. C. and Wang, Z. B. (2013). Man-induced regime shifts in small estuaries—I: theory. *Ocean Dynamics*, 63(11-12):1279–1292.

Winterwerp, J. C., Wang, Z. B., van Braeckel, A., van Holland, G., and Kösters, F. (2013). Man-induced regime shifts in small estuaries—II: a comparison of rivers. *Ocean Dynamics*, 63(11-12):1293–1306.

Wofsy, S. C. (1983). A simple model to predict extinction coefficients and phytoplankton biomass in eutrophic waters. *Limnology and Oceanography*, 28(6):1144–1155.

Chapter 2

The impact of flocculation on the large-scale SPM dynamics

Horemans, D. M. L., Dijkstra, Y. M., Schuttelaars, H. M., Meire, P., & Cox, T. J. S. (2020). Unraveling the Essential Effects of Flocculation on Large-Scale Sediment Transport Patterns in a Tide-Dominated Estuary, *Journal of Physical Oceanography*, 50(7), 1957-1981. https://doi.org/10.1175/JPO-D-19-0232.1

Abstract

Sediment transport in estuaries and the formation of estuarine turbidity maxima (ETM) highly depend on the ability of suspended particulate matter (SPM) to flocculate into larger aggregates. While most literature focuses on the small-scale impact of biological flocculants on the formation of larger aggregates, the influence of the flocculation process on large-scale estuarine SPM profiles is still largely unknown. In this paper, we study the impact of flocculation of SPM on the formation of ETM. For this, a semianalytical width-integrated model called iFlow is utilized and extended by a flocculation model. Starting from a complex one-class flocculation model, we show that flocculation may be described as a linear relation between settling velocity and suspended sediment concentration to capture its leading-order effect on the ETM formation. The model is applied to a winter case in the Scheldt Estuary (Belgium, Netherlands) and calibrated to a unique, long-term, two-dimensional set of turbidity (cf. SPM) observations. First, model results with and without the effect of flocculation are compared, showing that the spatial and temporal variations of the settling velocity due to flocculation are essential to reproduce the observed magnitude of the suspended sediment concentrations and its dependence on river discharge. Second, flocculation results in tidally averaged land-inward sediment transport. Third, we conduct a sensitivity analysis of the freshwater discharge and floc break-up parameter, which shows that flocculation can cause additional estuarine turbidity maxima and can prevent flushing of the ETM for high freshwater inflow.

2.1 Introduction

Estuaries often contain regions in which the concentration of suspended particulate matter (SPM) is larger than landward and seaward of these regions. These regions are called estuarine turbidity maxima (ETM) and are caused by fine sediments being trapped as a result of the complex interactions of the water motion and sediment dynamics. Examples of such transport mechanisms are, amongst others, related to tidal asymmetries in water motion, water density gradients, and transport mechanisms related to temporal variability in settling velocity of SPM (see Burchard et al. (2018) for a recent review). One mechanism resulting in temporal and spatial variability of settling velocity is flocculation. Flocculation results in the aggregation and break-up of cohesive SPM, thus changing the floc size and hence the settling velocity.

Two main classes of models describing flocculation can be distinguished, the Lagrangian flocculation (LF) models and the population balance equation (PBE) models (Lai et al., 2018). PBE flocculation models typically consist of multiple discrete size classes and compute the evolution of the number of flocs within each class over time (Smoluchowski, 1918; Verney et al., 2011). Although PBE models can calculate the evolution of particle size distribution over time, they come with high computational costs. In contrast, the LF models are dynamic models that resolve the dynamics of particle size and settling velocity by computing a balance between floc aggregation and floc break-

up (Winterwerp, 2002). Floc aggregation and break-up are implemented using empirical formulations, which depend on both abiotic and biotic factors (Dyer, 1989; van Leussen, 1994; Lai et al., 2018).

A first important abiotic factor that impacts flocculation is the suspended sediment concentration. Both in situ measurements (Pejrup and Mikkelsen, 2010) and laboratory experiments (Tran et al., 2018) show that floc size typically increases with increased suspended sediment concentration. Another important abiotic driver is turbulence, which both promotes aggregation through enhanced mixing and break-up by increasing the shear stresses on the flocs. Turbulence promoting break-up is observed in various estuaries such as the Yangtze estuary (Guo et al., 2017) and the Scheldt estuary (Manning et al., 2007; Schwarz et al., 2017). Also, laboratory experiments show that turbulence can decrease the averaged floc size (Mietta et al., 2009). A third abiotic environmental condition that impacts flocculation is salinity. Edzwald et al. (1974) conducted laboratory experiments in which they showed that salinity promotes aggregation of clay particles and very little salt ($\sim$ 5 ppt) is already sufficient to reach a maximum impact of salinity on flocculation. In contrast, Eisma et al. (1980) and Verney et al. (2009) found that salt flocculation is not a crucial factor in the Rhine estuary and Seine estuary, respectively. Biotic characteristics that impact flocculation are the organic content that directly alters the differential density and structure of flocs (Kranenburg, 1994; van Leussen, 1994). Furthermore, organic content impacts, for example, the floc strength and collision efficiency (Winterwerp and van Kesteren, 2004), averaged floc size (Mietta et al., 2009), and floc break-up (Alldredge et al., 1990). Finally, in situ observations show a correlation between Chlorophyll-a and flocculation efficiency (Verney et al., 2009) and sticky biotic substances (i.e., Transparent Exopolymer Particles) and floc strength (Fettweis et al., 2014).

Although temporal and spatial variations in settling velocity, which is related to floc size, are recognized as potentially important mechanisms for sediment trapping, most models for estuarine sediment transport use either a constant settling velocity or empirical flocculation relationships. Only a few studies included full floc dynamics in a sediment transport model (Ditschke and Markofsky, 2008; Xu et al., 2010; Sherwood et al., 2018; Shen et al., 2018), but the importance of flocculation on sediment transport mechanisms can not be clearly identified from these model results.

This study aims to model and gain an understanding of the impact of varying settling velocity on large-scale sediment transport and the corresponding development of ETM. As a first step, we consider estuaries in which the suspended sediment concentration is lower than 1 g L^{-1}, allowing us to focus on flocculation process and neglect hindered settling effects, which also result in a temporally and spatially varying settling velocity.

To be able to gain an understanding of the underlying mechanisms that result in sediment trapping and quantify the relative importance of flocculation on ETM formation, we extend the width-averaged, hydrodynamics and sediment transport model known as 'iFlow' (Dijkstra et al., 2017) to include flocculation processes. The iFlow model is specifically geared toward gaining an understanding of the water motion, sediment transport, and trapping in tidally dominated estuaries and allows for extensive sensitivity analysis. The model is extended with the one-class LF model of Winterwerp (2002), in which the

impact on flocculation of suspended sediment concentration, turbulent shear, and floc size and structure are directly parameterized in the floc aggregation and break-up terms. Other effects, such as salinity and biotic factors, are indirectly included by fitting to observations.

We apply the extended iFlow model to the Scheldt estuary. The Scheldt estuary is located in Belgium and the Netherlands and debouches into the North Sea. Being a well-documented estuary (Meire et al., 2005), there have been intensive monitoring campaigns (Maris and Meire, 2016) and modeling experiments. Moreover, the iFlow model without flocculation has already successfully been applied to the Scheldt estuary (Brouwer et al., 2018; Dijkstra et al., 2019a). The flocculation process is expected to be important in the Scheldt estuary (Peters, 1972; Gourgue et al., 2013).

In this paper, we extend the iFlow model to include the effect of flocculation in Section 2.2. In Section 2.3, we calibrate the model to a unique, long-term turbidity (cf. SPM) dataset of the Scheldt estuary. In Section 2.4, we apply the coupled flocculation-sediment transport model to the Scheldt estuary and study the effect of flocculation on the large-scale sediment distribution and the underlying sediment transport mechanisms.

2.2 Model

In this section, we first present the sediment transport model (i.e., iFlow) and flocculation model of Winterwerp (2002). Next, we use scaling and perturbation methods to simplify the coupling of the two models. Then, we describe the theoretical impact of flocculation on sediment transport. Last, we introduce the (numerical) implementation of our model.

2.2.1 iFlow

The iFlow model (Dijkstra et al., 2017) was developed to obtain the width-averaged water motion, sediment transport, and trapping in a tidally dominated estuarine system by solving the width-averaged shallow water equations, suspended sediment concentration equation, and a dynamic equation for the erodibility of the bed (Brouwer et al., 2018). The water motion is assumed to be forced by an M2 and M4 tidal signal at the mouth, while a river discharge is prescribed at the upstream tributaries. It is assumed that the M2 tidal signal dominates over the M4 and riverine signals. We decompose the water motion into a longitudinal and vertical velocity component, denoted by u and w. The suspended sediment concentration follows from an advection-diffusion equation and is forced by a constant suspended sediment concentration at the mouth and prescribed inflow of sediment at the upstream tributaries. The bathymetry and width are approximated by smooth polynomials, thereby neglecting the impact of small-scale gradients, as illustrated in Fig. 2.1. A diagnostic longitudinal salinity gradient is prescribed, consisting of a depth- and time-independent sigmoid function.

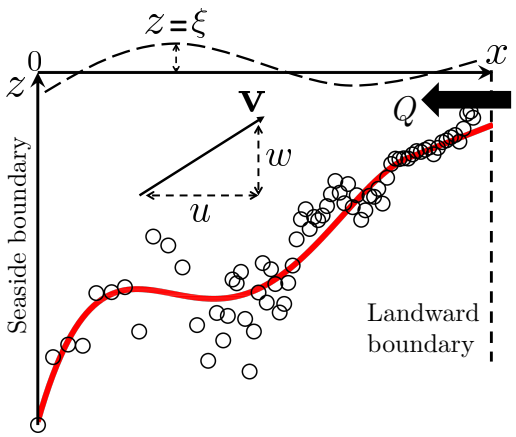

Figure 2.1: Illustration of the geometry of the iFlow model. The bathymetry (circles) is smoothed by a polynomial function (red graph). The water surface elevation ξ is assumed to be small (order ϵ) compared to the water depth. The water motion is forced by a tidal signal at the mouth and constant total river discharge Q. We decompose the water motion $\mathbf{v}$ into a longitudinal and vertical velocity components, denoted by u and w.

By assuming that the dynamics consist of strong tidal signals beside a subtidal part, the iFlow model solves the problem in frequency space for subtidal, M2, and M4 components. The water surface elevation is assumed small compared to the subtidal water depth, resulting in a small dimensionless parameter, given by the ratio of water surface elevation and water depth. Using a scaling procedure and relating the various dimensionless numbers to this small parameter allows for identifying the relative importance of individual processes (e.g., river, tide, density forcing, advection). Next, a perturbation approach is employed to solve the equations at different order. For further details on the iFlow model, we refer the reader to Dijkstra et al. (2017).

Using this information and truncating frequencies larger than M4 (i.e., M6, M8, etc. are neglected and, hence, not discussed), the leading-order water motion u^0 and suspended sediment concentration c^0 consist of an M2 tidal signal and subtidal and M4 tidal components, respectively (Chernetsky et al., 2010; Dijkstra et al., 2017), denoted by u^{02} and c^{00}, c^{04} (in which the first superscript denotes the order and the second one denotes the frequency) and defined as

$$u^0(x,z,t) = \mathrm{Re}\Big[\underbrace{\hat{u}^{02}(x,z)e^{i\omega_{M_2}t}}_{\text{M2 tidal signal } u^{02}}\Big] \text{and} \tag{2.1}$$

$$c^0(x,z,t) = \mathrm{Re}\Big[\underbrace{\hat{c}^{00}(x,z)}_{\text{subtidal } c^{00}} + \underbrace{\hat{c}^{04}(x,z)e^{2i\omega_{M_2}t}}_{\text{M4 tidal signal } c^{04}}\Big], \tag{2.2}$$

with x and z being the longitudinal and vertical coordinates and t being the time. At first order, the water motion u^1 and suspended sediment concentration c^1 consist of a subtidal and M4 tidal signal and an M2 tidal signal, respectively (Chernetsky et al., 2010; Dijkstra

et al., 2017), denoted by u^{10}, u^{14}, and c^{12} and defined as

$$u^1(x,z,t) = \mathrm{Re}\Bigg[\underbrace{\hat{u}^{10}(x,z)}_{\text{subtidal } u^{10}} + \underbrace{\hat{u}^{14}(x,z)e^{2i\omega_{M_2}t}}_{\text{M4 tidal signal } u^{14}} \Bigg] \text{and} \tag{2.3}$$

$$c^1(x,z,t) = \mathrm{Re}\Bigg[\underbrace{\hat{c}^{12}(x,z)e^{i\omega_{M_2}t}}_{\text{M2 tidal signal } c^{12}} \Bigg]. \tag{2.4}$$

The net sediment transport $\mathcal{T}$, i.e., the sediment transport averaged over a tidal period (denoted by angle brackets), is given by the sum of the advective and diffusive sediment transport integrated over the cross section:

$$\begin{aligned}
\mathcal{T} &= \left\langle B \int_{-H}^{R+\xi} uc - K_h(\partial_x c)dz \right\rangle \\
&\approx \left\langle B \int_{-H}^{R} \underbrace{u^0c^0 + u^1c^0 + u^0c^1}_{uc \text{ upto first order}} - K_h(\partial_x c)dz + u^0c^0\xi^0 \Big|_{z=R} \right\rangle \\
&= \left\langle B \int_{-H}^{R} \underbrace{u^{10}c^{00} + u^{14}c^{04}}_{u^1c^0} + \underbrace{u^{02}c^{12}}_{u^0c^1} - K_h(\partial_x c)dz + u^0c^0\xi^0 \Big|_{z=R} \right\rangle,
\end{aligned} \tag{2.5}$$

where B is the local channel width, R is the reference level of the water surface elevation, $H(x)$ is the magnitude of the local z-coordinate of the river bed, and K_h is the horizontal eddy diffusivity coefficient. Moreover, we used that only subtidal-subtidal, M2-M2, and M4-M4 tidal interaction terms result in net sediment transport, which is a direct result of the orthogonality of the complex exponential functions.

In iFlow, parameters such as the total freshwater discharge Q, horizontal eddy diffusivity coefficient K_h, and settling velocity w_s^0, are usually prescribed as constant parameters [although this is not needed, see Dijkstra et al. (2017)], allowing for a quick solution procedure. To include flocculation in the model, the settling velocity w_s has to be coupled to the suspended sediment concentration c, which makes the model nonlinear, requiring an iterative solution procedure (see Section 2.2.5).

2.2.2 Flocculation model

The Winterwerp flocculation model employed in this paper reads (Winterwerp, 2002) as

$$\begin{aligned}
&\partial_t N + \partial_x[uN] + \partial_z[(w - w_s)N] - \partial_x[K_h\partial_x N] - \partial_z[K_v\partial_z N] \\
&\quad = \underbrace{-k_A' G D_f^3 N^2}_{\text{aggregation}} + \underbrace{k_B G^{3/2}(D_f - D_p)D_f N}_{\text{break-up}},
\end{aligned} \tag{2.6}$$

where N is the number of flocs per unit volume, w_s is the settling velocity, K_ν is the vertical eddy diffusivity coefficient, G is the shear rate, D_f and D_p are the floc and primary

particle size, and k'_A and k_B are the empirical aggregation and break-up parameters. To acquire Eq. (2.6), we assumed a fractal dimension $n_f = 2$ and we set model calibration parameters $q = 0.5$ and $p = 1$, following Winterwerp (2002).

The aggregation parameter k'_A and break-up parameter k_B define the efficiency of the flocculation process and represent the intrinsic flocculation kinetics of the system of interest. Laboratory flocculation experiments show that floc kinetics depend, amongst others, on salinity (Peters, 1972; Edzwald et al., 1974). To include a salinity dependence in our model, we allow the flocculation kinetics to depend on the depth- and tidally averaged salinity profile, resulting in k'_A and k_B being functions of the longitudinal coordinate x. In Section 2.2.3, we show that net sediment transport only depends on the ratio of k'_A and k_B and not on the individual parameters. From the experiments carried out by Edzwald et al. (1974), we therefore postulate the following dependence of the ratio of k'_A and k_B on salinity S:

$$\frac{k'_A}{k_B} \sim \left\{ 1 + S_1 \left[1 + \tanh(S(x) - S_2) \right] \right\}, \tag{2.7}$$

with S_1 and S_2 being empirical parameters that are calibrated to a salinity $S(x)$ dataset. For more details, the reader is referred to Appendix 2.A.

Following Pejrup and Mikkelsen (2010), the shear rate G reads as

$$G(x, \tilde{z}_1) = \sqrt{\frac{\langle u_* \rangle^3 (1 - \tilde{z}_1)}{\nu H \kappa' \tilde{z}_1}}, \tag{2.8}$$

where κ' is the Von Karman constant, ν is the kinematic viscosity, $\tilde{z}_1 = z_1/H$ is the relative water depth, and $\langle u_* \rangle$ is the subtidal friction velocity:

$$\langle u_* \rangle(x) = \frac{\kappa'}{\ln \frac{z_1(x)}{s_{f_0}}} \langle \left| u^{02}(x, z_1) + u^{10}_{\text{riv.}}(x, z_1) \right| \rangle, \tag{2.9}$$

where z_1 is the distance in the logarithmic layer above the bed, s_{f_0} is the bed roughness coefficient, u^0 is the leading-order, longitudinal flow velocity [see Eq. (2.1)], and $u^{10}_{\text{riv.}}$ is the subtidal, first-order, longitudinal, river-induced flow velocity [see Eq. (2.3)]. For simplicity, we only consider the impact of subtidal shear velocity u_* at leading order. The first-order, subtidal, riverine contribution is also included (i.e., u^{10}_{river}) because this constituent is dominant at the upstream border. Apart from neglecting tidal variations of G, we also approximate G by its value at $z_1 = H/2$ and use this $G(x, \tilde{z}_1 = 1/2)$ as a proxy for the whole water column. Working with a depth-averaged value of G instead of a midpoint value has no major impact on our results and conclusion because vertical variations in G are relatively small (typically < 10 % in our case study) in the logarithmic layer. Although turbulence is an important driver of flocculation, we do not focus on this variable in our case study because we assume a tide-dominated system with low stratification. This results in a shear rate that has a similar order of magnitude within the ETM.

The Winterwerp model depends on both the number of flocs per unit volume N, floc size D_f, and settling velocity w_s. These three variables are not independent. We

Table 2.1: Definition of β, κ, τ and γ, along with their units.

variable	definition	units
γ	$18\mu g^{-1}(\rho_s - \rho_w)^{-1}$	m s
β	$\frac{1}{18\mu f_s}\frac{\rho_s-\rho_w}{\rho_s}\frac{g}{\sqrt{G}}\frac{k'_A}{k_B}$	$\mathrm{m^4\ s^{-1}\ kg^{-1}}$
κ	$\frac{k_B}{k'_A}D_p^2 f_s \rho_s \sqrt{G}$	$\mathrm{kg\ m^{-3}}$
τ	$\left(\frac{\rho_s-\rho_w}{18\mu}gD_p\right)^2 k_B^{-1}G^{-3/2}$	$\mathrm{m^2\ s^{-1}}$

rewrite Eq. (2.6) such that it solely depends on the settling velocity w_s. First, we express the number of flocs per unit volume N in terms of the floc size D_f (Kranenburg, 1994; Winterwerp and van Kesteren, 2004):

$$N = \frac{1}{f_s}\frac{c}{\rho_s}\frac{1}{D_p D_f^2}, \tag{2.10}$$

with f_s being the floc shape factor and ρ_s the floc density.

Next, to obtain an equation for the settling velocity, we use the generalized Stokes formulation to translate floc size D_f to settling velocity w_s (Winterwerp and van Kesteren, 2004):

$$w_s = \frac{\rho_s - \rho_w}{18\mu} g D_p D_f, \tag{2.11}$$

where ρ_w is the water density, g is the gravitational acceleration, and μ is the viscosity of water. We assumed spherical flocs ($f_s = \pi/6$), a fractal dimension $n_f = 2$, and that the floc Reynolds number $\mathrm{Re}_f = w_s D_f/\nu \ll 1$.

Combination of Eqs. (2.6), (2.10), and (2.11) gives a differential equation for w_s that results in the evolution of w_s over time and space:

$$\begin{aligned}\partial_t c w_s^{-2} + \partial_x[u c w_s^{-2}] + \partial_z[(w - w_s) c w_s^{-2}] - \partial_x[K_h \partial_x c w_s^{-2}] \\ - \partial_z[K_v \partial_z c w_s^{-2}] \\ = \gamma w_s^{-1} c G \Big[\underbrace{-k'_A c D_p^{-2} f_s^{-1} \rho_s^{-1}}_{\text{aggregation}} + \underbrace{k_B G^{1/2}(\gamma D_p^{-2} w_s - 1)}_{\text{break-up}} \Big],\end{aligned} \tag{2.12}$$

where γ is defined in Table 2.1. In the following section, we approximate this equation and write the settling velocity w_s as an explicit function of the suspended sediment concentration c.

2.2.3 Ordering of the flocculation model

We apply scaling and perturbation analysis to the Winterwerp flocculation model shown in Eq. (2.12) to gain more insight into this highly complex equation. We refer the reader to Appendices 2.B, 2.C, and 2.D for the derivation.

2.2.3.1 Leading order

At leading order, the flocculation model reduces to the balance between floc aggregation and floc break-up:

$$0 = \underbrace{-k'_A c^0 D_p^{-2} f_s^{-1} \rho_s^{-1}}_{\text{aggregation}} + \underbrace{k_B G^{1/2} (\gamma D_p^{-2} w_s^0 - 1)}_{\text{break-up}}. \tag{2.13}$$

This can be interpreted as if the flocculation process is instantaneous and local: there is no inertia and transport. As a result, the settling velocity scales linearly with the suspended sediment concentration:

$$w_s^0 = \beta(c^0 + \kappa), \tag{2.14}$$

where β and κ are defined in Table 2.1 and depend on several parameters including the shear rate and ratio between k'_A and k_B. Using the definitions of β and κ (Table 2.1), we see that the $\beta\kappa$ term equals the settling velocity $w_{s,\min.}$ corresponding to the settling velocity of primary particles. Indeed, it equals the Stokes formulation for massive ($n_f = 3$) primary particles with primary particle size D_p. This ensures that for $c \to 0$, $w_s^0 \to w_{s,\min.}$. Moreover, our leading-order result in Eq. (2.14) is equivalent to the equilibrium floc size D_e presented in Winterwerp (2002):

$$D_e = D_p + \frac{k'_A c}{k_B \sqrt{(G)}}. \tag{2.15}$$

The positive correlation of w_s with suspended sediment concentration in the leading-order result complies with observations. Indeed, Pejrup and Mikkelsen (2010), assuming a power relationship between settling velocity and suspended sediment concentration, found exponents ranging between 0.47 and 2.9 with an average of 1.29, using 18 different tidal systems based on real measurements. Recently, Tran et al. (2018) studied the influence of SPM concentration on floc size in laboratory mixing tanks. They found a linear relationship between floc size and SPM concentration, which again results in the linear relationship between settling velocity and SPM concentration as given in Eq. (2.14).

2.2.3.2 First order

At first order, our scaling procedure shows that local inertia (cf. $\partial_t N$ term), settling, and vertical diffusion become significant [see Eq. (2.55)]. Advection and horizontal diffusion are still negligible at this order. The solution then reads as

$$w_s^1 = \underbrace{\beta c^1}_{\text{break-up/aggregation}} - \underbrace{2\tau \frac{\partial_z c^0}{c^0} \left[1 + \frac{K_\nu^0}{w_s^0} \frac{\partial_z c^0}{c^0} \right]}_{\text{inertia, settling, and vertical diffusion}}, \tag{2.16}$$

where τ is defined in Table 2.1. Apart from a contribution to w_s^1 that again scales linearly in c (βc^1 term), we obtain additional terms when compared to the leading-order result.

Because of inertial effects, settling, and vertical diffusion, we obtain an additional contribution that is constant in time and one that varies on the M4 time scale, no additional M2 contribution is generated [see Eqs. (2.86) and (2.87)]. As we show below, we are only interested in the M2 contribution w_s^{12} because this is the only first-order contribution that is important for net sediment transport. The only M2 signal in the first-order settling velocity is related to the first-order balance between aggregation and break-up and reads as

$$w_s^{12} = \beta c^{12}. \tag{2.17}$$

2.2.4 Impact of flocculation on net sediment transport

In the previous section, we discussed the impact of suspended sediment concentration c on settling velocity w_s, which is a direct consequence of flocculation. In the following, we present the influence of settling velocity w_s on suspended sediment concentration c. As flocculation alters the leading and first-order suspended sediment concentration c^0 and c^1, the corresponding net sediment transport $\mathcal{T}$ from Eq. (2.5) is also impacted. We rewrite Eq. (2.5) as

$$\mathcal{T}_{\text{floc}} = \left\langle B \int_{-H}^{R} \underbrace{u^{10}c^{00}_{\text{floc}} + u^{14}c^{04}_{\text{floc}}}_{u^1c^0} + \underbrace{u^{02}c^{12}_{\text{floc}}}_{u^0c^1} - K_h(\partial_x c)dz + u^0c^0\xi^0 \Big|_{z=R} \right\rangle, \tag{2.18}$$

and examine the relation of c^{00}_{floc}, c^{04}_{floc}, and c^{12}_{floc} with the settling velocity w_s.

A careful analysis shows that at leading order, both the settling velocity and suspended sediment concentration consist of a subtidal and M4 tidal signal. This can be inferred from the following argument: if at leading order, the (truncated) suspended sediment concentration c^0 consists of only a subtidal and M4 tidal signal as found for a time-independent w_s [see Eq. (2.2)], the settling velocity also gets an M4 tidal component [see Eq. (2.14)]. This M4 signal impacts the leading-order suspended sediment concentration c^0 through the nonlinear interaction term $w_s^0c^0$ in the leading-order differential equation for c^0 [see Eq. (2.44)]. Interestingly, the nonlinear interaction of c^0 and w_s^0 results in an adjustment of the subtidal and M4 tidal signal in c^0, that is, c^{00} and c^{04}, and generates an infinite number of additional tidal frequencies in c^0 because of its nonlinearity:

$$\underbrace{w_s^0}_{\beta(c^{00}+c^{04}+\kappa)} \times \underbrace{c^0}_{c^{00}+c^{04}} \text{ generates } c^{00}_{\text{floc}} + c^{04}_{\text{floc}}. \tag{2.19}$$

As stated before, frequencies larger than M4 are truncated.

Additionally, the subtidal and M4 tidal signal in w_s^0 impacts the M2 signals in the first-order differential equation for c^1 through the $\sim w_s^0c^1$ forcing term [see Eq. (2.47)], which again results in an adjustment of net sediment transport through c^{12}_{floc}:

$$\underbrace{w_s^0}_{\beta(c^{00}+c^{04}+\kappa)} \times \underbrace{c^1}_{c^{10}+c^{12}+c^{04}} \text{ generates } c^{10}_{\text{floc}} + c^{12}_{\text{floc}} + c^{14}_{\text{floc}}. \tag{2.20}$$

Consequently, at leading order both the subtidal and M4 tidal signal in w_s^0 have an impact on net sediment transport through its impact on c_{floc}^{00} and c_{floc}^{04} and c_{floc}^{12}.

At first order, only the M2 tidal signal in w_s^1, i.e., w_s^{12}, results in net sediment transport through the forcing term $\sim w_s^1 c^0$ in the first-order differential equation for c^1 [see Eq. (2.47)]:

$$w_s^1 \left\{ \begin{array}{l} w_s^{12} \\ w_s^{10} + w_s^{14} \end{array} \right. \times \underbrace{c^0}_{c^{00}+c^{04}} \text{ generates } \left\{ \begin{array}{l} c_{\text{floc}}^{12} \\ c_{\text{floc}}^{10} + c_{\text{floc}}^{14} \end{array} \right. . \tag{2.21}$$

Consequently, when interested in net sediment transport, the first-order settling velocity simplifies to the linear relationship in Eq. (2.17) and the Winterwerp model upto first order is thus equivalent to the equilibrium floc size result in Eq. (2.15).

2.2.5 Solution method

iFlow contains a numerical sediment module that solves for suspended sediment concentration c numerically in x and z using a grid of 200 cells in the x direction and 50 cells in the z direction. To do so, the module requires a leading-order settling velocity w_s^0 and first-order settling velocity w_s^1 as input. A new module is added to iFlow containing the explicit analytical expression of w_s^0 and w_s^1 [Eqs. (2.14) and (2.17)]. The coupling of w_s to c results in a w_s which is a function of time and space. Because the coupling is nonlinear, we solve the coupling iteratively using the Picard method. We start with an initial condition for w_s^0 and w_s^1 as input to the sediment module to acquire a suspended sediment concentration at leading order c^0 and first order c^1. Next we use c^0 and c^1 to recalculate w_s^0 and w_s^1 using Eqs. (2.14) and (2.17). We use the recalculated w_s^0 and w_s^1 as new input to the sediment module. We repeat this procedure until the solution converges using the following stop criterion:

$$\left|\left| \frac{w_s^0(x,z) - w_{s,\text{old}}^0(x,z)}{w_{s,\text{old}}^0(x,z)} \right|\right| < 10^{-3}, \tag{2.22}$$

in which $w_{s,\text{old}}^0$ is the leading-order settling velocity of the previous iteration. The iterative procedure is schematized in Fig. 2.2.

2.3 The Scheldt: observations and calibration

We apply our coupled flocculation-sediment transport model to a winter case (i.e., Jan.-Mar.) in the Scheldt estuary. To do so, we calibrate the model to a unique, long-term turbidity (cf. SPM) dataset for 2015 until 2017 measured within the environmental monitoring program called Onderzoek Milieu Effecten Sigmaplan (OMES). We divide the turbidity dataset in winter and summer because the turbidity data shows a strong seasonality in the Scheldt estuary (Maris and Meire, 2016). This section presents the Scheldt estuary, the long-term turbidity dataset, and the calibration method.

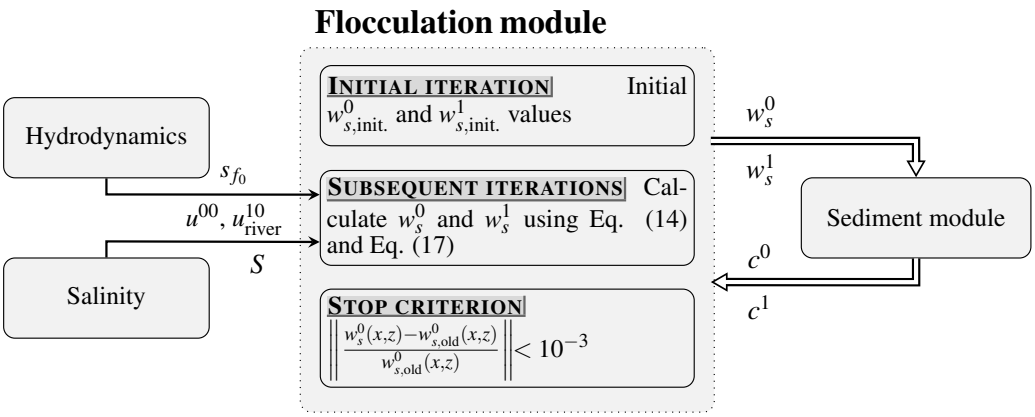

Figure 2.2: Schematic representation of the iterative Picard method used in the flocculation module to compute the suspended sediment distribution. In each iteration, the settling velocity w_s is updated and the corresponding suspended sediment concentration c is recalculated. The iterative procedure is repeated until the updated settling velocity converges (cf. stop criterion). To calculate the impact of shear stress in Eq. (2.8) and salinity in Eq. (2.7) on flocculation, the leading-order velocity u^0, first-order, subtidal, riverine velocity u^{10}_{river}, bed roughness coefficient s_{f_0}, and salinity S are provided by the iFlow packages Hydrodynamics and Salinity.

2.3.1 The Scheldt

The Scheldt estuary (Fig. 2.3) is a funnel-shaped estuary of approximately 160 km long, which flows through Belgium and debouches into the North Sea near Vlissingen (Netherlands). The Scheldt estuary has a relatively low averaged total freshwater discharge (172 $\text{m}^3\ \text{s}^{-1}$ in our winter case) and can be considered a tide-dominated estuary (Meire et al., 2005; Waterinfo.be, 2019). The main tributaries are the Upper Sea Scheldt (upstream boundary; ∼34% of total river discharge), the Rupel (at 95 km from the mouth; ∼54% of total river discharge), and the Dender (at 123 km from the mouth; ∼12% of total river discharge) (Waterinfo.be, 2019). Parameter values used in our winter case study in the Scheldt estuary are summarized in Table 2.2. These parameter values follow from Brouwer et al. (2018) if not mentioned explicitly in the text. The total river discharge Q, erosion parameter M, and floc break-up coefficient k_B follow from calibration to the OMES SPM dataset presented in the following section.

2.3.2 OMES data

We calibrate our coupled flocculation-sediment transport model to a unique dataset representing a typical winter situation of SPM-distribution. In the frame of the ongoing OMES monitoring, vertical turbidity profiles were obtained using conductivity-temperature-depth (CTD) and turbidity casts from aboard a ship at 16 fixed locations

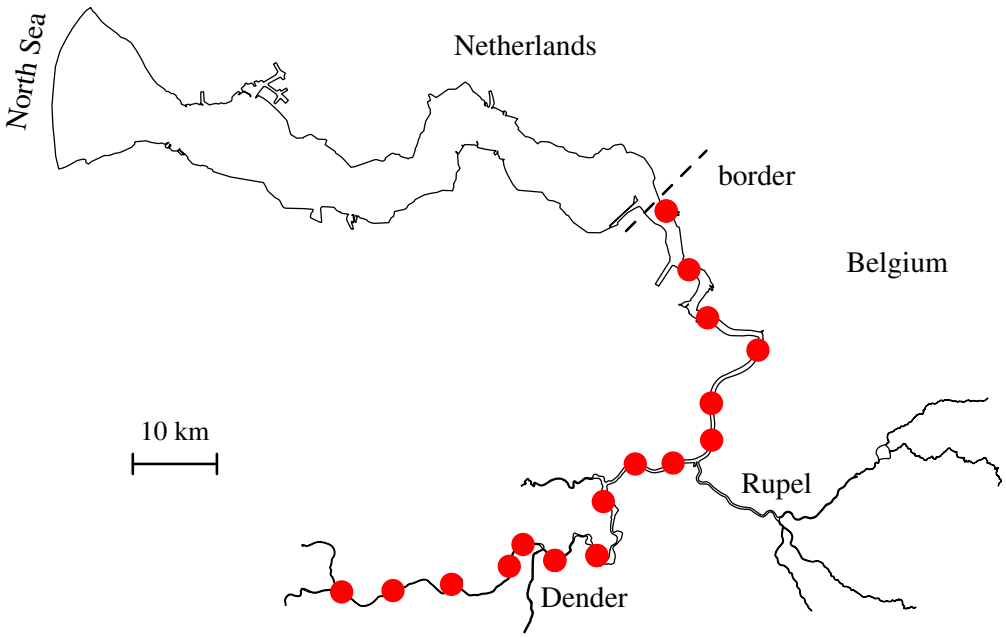

Figure 2.3: The Scheldt estuary and its two main tributaries (Dender and Rupel). The red dots represent locations where monthly and biweekly CTD and turbidity casts were performed in the frame of the environmental monitoring program (OMES).

Table 2.2: Parameter values used in our winter case study in the Scheldt estuary.

Variable	Definition	Value
	Hydrodynamics	
A^0	M_2 water level amplitude at x=0	1.77 m
A^1	M_4 water level amplitude at x=0	0.14 m
ϕ^1	M_4 water level phase relative to M_2 tide at x=0	-1.3 deg
Q	Total river discharge in winter (calibrated)	233 m^3 s^{-1}
	Sediment	
c_{sea}	Depth-averaged subtidal suspended sediment concentration at x=0	0.06 kg m^{-3}
K_h	Horizontal eddy diffusivity coefficient	100 m^2 s^{-1}
K_ν^0	Vertical eddy diffusivity coefficient	3.1×10^{-2} m^2 s^{-1}
M	Erosion parameter in winter (calibrated)	3.36×10^{-3} s m^{-1}
	Turbulence	
σ_ρ	Prandtl-Smidth number ($=A_\nu/K_\nu^0$ with A_ν the vertical eddy viscosity)	1
s_{f_0}	Bed roughness coefficient (calibrated)	4.22 mm s^{-1}
	Flocculation	
$k_A^{\text{min.}}$	Nondimensional minimal aggregation coefficient	0.29
f_s	Shape factor	$\pi/6$
D_p	Diameter primary mud particles	4×10^{-6} m
μ	Dynamic viscosity	0.0010518 Pa s
ρ_s	Density of sediment primary particles	2650 kg m^{-3}
ρ_w	Reference density of water	1000 kg m^{-3}
k_B	Floc break-up coefficient in winter (calibrated)	5600 $s^{1/2}$ m^{-2}
S_1	Flocculation salinity sensitivity calibration parameter	0.078
S_2	Flocculation salinity sensitivity calibration parameter	4.085 ‰
	Salinity	
$ssea$	Salinity boundary condition at the mouth	28.9 ‰
x_c^{sal}	Calibration parameter in postulated tanh salinity distribution in winter	37.8 km
x_L^{sal}	Calibration parameter in postulated tanh salinity distribution in winter	25.3 km

spread over the Belgian part of the Scheldt estuary during monthly or biweekly campaigns (Fig. 2.3). The campaigns were conducted independently of the tidal phase and spring neap tide. To obtain a typical winter distribution, we temporally averaged the Jan.-Mar. data from 2015-2017.

Turbidity was measured at various depths using an optical backscatter point sensor (OBS) of RBR type XR420 CTD+. During each campaign, the sensor was calibrated using a Formazine solution standard (Maris and Meire, 2016). The water body was vertically profiled using a minimal sampling frequency of 10^{-1} s^{-1}.

Simultaneously, two water samples were collected at each location using a Niskin bottle at approximately half the water depth and at the water surface. SPM concentrations were gravimetrically determined after filtration in the laboratory. During each campaign, 16×2 SPM water samples were collected, resulting in 32 SPM estimates. To translate turbidity to SPM, we used these 32 samples to apply a linear data fit. We assumed that the relation between turbidity and SPM is location (and time) independent, that is, equal for every location within one campaign. Calibration of turbidity to SPM resulted in a depth profile of SPM at 16 fixed locations in the Flemish part of the Scheldt estuary.

The winter case covers 11 measuring campaigns. We excluded data at the water surface and river bed because here, we typically have distortions due to, for example, air bubbles and high turbidity, respectively. To do so, we manually excluded depths at which we did not measure 8 of 11 measuring campaigns. We averaged the SPM concentration observations of the 11 measuring campaigns at each depth. We assumed this averaged value approximates the residual SPM concentration following, for example, Dijkstra et al. (2019a) and Cox et al. (2019). This assumption is valid when the number of estimates is sufficiently high, so averaging of the periodic temporal variability of the SPM concentration is negligible compared to the magnitude of the residual SPM concentration. Here, we assumed that the campaigns were randomly distributed within the tidal phase and spring neap tide, which was shown to be valid for OMES SPM sampling between 1995 and 2015 (Vandenbruwaene et al., 2016). Furthermore, we assumed that the SPM distribution within the time frame of our winter case is fixed on an estuarine scale (i.e., the scale of the iFlow model in the longitudinal direction). So, local effects due to, for example, temporal variations in river discharge can be neglected. Given a system-averaged standard deviation relative to the time-averaged SPM concentration of 0.43, we conclude that these assumptions are acceptable and that the number of estimates is sufficiently high.

On average, each turbidity profile consists of 20 individual observations, with an average distance between two consecutive observations of 0.36 m. We vertically interpolated the data to compare the subtidal SPM model output at the vertical model grid cells in our calibration. This results in a total number of 606 (x,z) locations at which we compared data and model output. This number results from the fact that we measured at 16 stations and have 50 vertical model grid cells (a total of 800 grid cells) but excluded data near the water surface and river bed. The average number of data points n for each location (x,z) equals 9.4.

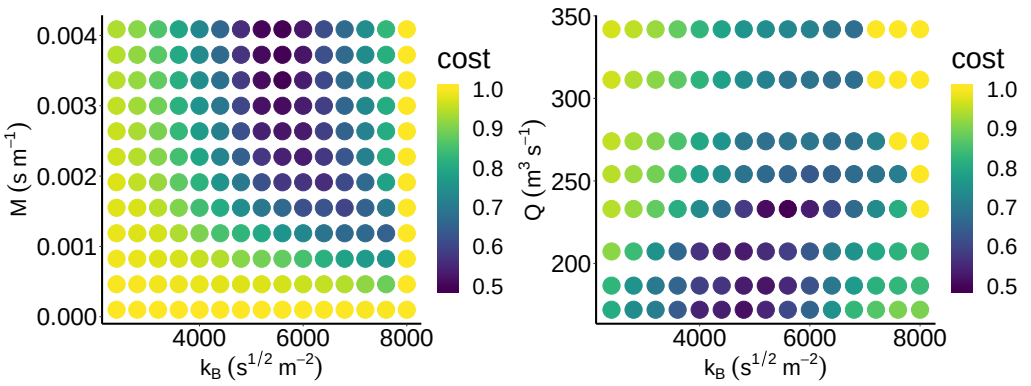

(a) Cost function output

(b) Cost function output

Figure 2.4: Cost function values for (a) various erosion parameter M and floc break-up parameter k_B ($Q = 233$ m^3 s^{-1}) and (b) various total river discharge Q and floc break-up parameter k_B ($M = 0.00336$ s m^{-1}). The optimal calibration parameter set corresponds to $k_B = 5600$ s$^{1/2}$ m^{-2}, $M = 0.00336$ s m^{-1}, and $Q = 233$ m^3 s^{-1}

2.3.3 Calibration

We calibrated the linearized bed roughness coefficient s_{f_0} such that the modeled M2 water levels match observations following Dijkstra et al. (2017). In our coupled flocculation-sediment transport model, we have three additional calibration parameters:

1. floc break-up parameter k_B,
2. erosion parameter M, and
3. river discharge Q.

The iFlow model approximates the freshwater inflow by a subtidal discharge. In reality, the discharge shows a significant temporal variation, and observed average discharge is not always representative of average sediment transport. For example, the standard deviation of the averaged river discharge corresponding to our winter case is equal to 92 m^3 s^{-1} (Waterinfo.be, 2019). To improve the correspondence between model output and observed sediment distribution, we included Q as a calibration parameter.

We run our model for various values of the calibration parameters $k_B \in [2400, ..., 8000]$ s$^{1/2}$ m^{-2}, $M \in [0.1, ..., 4]\times10^{-3}$ s m^{-1}, and $Q \in [172, ..., 340]$ m^3 s^{-1} and compare the model result to the measurements for each setting to find the best parameter values. The choice of the range in k_B and M is based on scaling (see Table 2.C.1) and observations (Zhu et al., 2017), respectively. The range of Q represents from the 60th until 90th percentile of the observations corresponding to our winter case (Waterinfo.be, 2019).

To objectively compare the model output to the measurements, we construct a cost function, which is based on a statistical two-tailed t test. For each SPM data point location (x,z), we compute whether the following test statistic:

$$t_{score} = \frac{< c_{\text{meas.}}(x,z) > - < c_{\text{model}}(x,z) >}{\text{std}/\sqrt{n}}, \tag{2.23}$$

has a t distribution with $n-1$ degrees of freedom. If found to be true, we accept that the model output and data are statistically equal at location (x,z). Here, $< c_{\text{model}}(x,z) >$ and $< c_{\text{meas.}}(x,z) >$ are the model subtidal suspended sediment concentration output and time-averaged measured SPM concentration at location (x,z) respectively, std is the standard deviation of the measured SPM concentration at location (x,z) and n is the total number of data points at location (x,z). We choose a significance level $\alpha = 0.05$. Last, we define a cost function value as

$$\text{cost} = 1 - \frac{N_{\text{equal}}}{N_{\text{loc}}}, \tag{2.24}$$

where N_{equal} is the number of locations at which the suspended sediment concentration model output and data are statistically equal and N_{loc} is the total number of locations for which we have data. Consequently, the cost function output is a value between 1 (*mismatch of model output and data*) and 0 (*perfect match of model output and data*).

Evaluated by our cost function, we obtain an optimal parameter set $k_B = 5600$ s$^{1/2}$ m^{-2}, $M = 0.00336$ s m^{-1}, and $Q = 233$ m^3 s^{-1}. The cost function output for various k_B, M, and Q is presented in Fig. 2.4. We acquire a higher discharge of 233 m^3 s^{-1}in winter when compared with the time-averaged value of 172 m^3 s^{-1}. This larger discharge is expected because of the asymmetry in flushing and buildup of an ETM: the impact of high river discharges on suspended sediment concentration is larger than the impact of low river discharges. Indeed, Brouwer et al. (2018) showed that the time scale of building up an ETM is two orders of magnitude larger ($\sim 10^2$ days) than the flushing of an ETM ($\sim 10^0$days).

2.4 Results

To analyze the relative importance of flocculation on large-scale sediment transport in the Scheldt estuary, we compare the modeled suspended sediment distribution and the different terms contributing to net sediment transport with and without flocculation. Next, we apply a sensitivity analysis of the calibration parameters Q and k_B when including flocculation and compare the results to those without flocculation.

2.4.1 Impact of flocculation on large-scale suspended sediment distribution

Application of the model to the winter case in the Scheldt estuary and model calibration results in the model output presented in Fig. 2.5.

Figure 2.5a shows the result of the subtidal suspended sediment concentration with flocculation. Figure 2.5b shows the long-term, time-averaged suspended sediment concentration dataset for winter in 2015-2017. These observations agree with SPM samples simultaneously taken at the water surface, which are presented in Cox et al. (2019). When we include flocculation (Fig. 2.5a), the model output complies both quantitatively and qualitatively with observations (Fig. 2.5b). The location and intrusion of the ETM are well captured. The model shows typical suspended sediment concentrations of 100-300 mg L^{-1}, which agrees with observations.

Figure 2.5c shows the model output of the leading-order settling velocity corresponding to the case with flocculation. Qualitatively this figure corresponds to the suspended sediment concentration in Fig. 2.5a. We expected this because we showed that the leading-order settling velocity scales linearly to the suspended sediment concentration [see Eq. (2.14)]. The distribution of w_s^0 is only (slightly) altered by the imposed longitudinal variation in shear rate G and aggregation parameter k'_A [see Eqs. (2.7) and (2.8)]. Hence, the dependence of w_s^0 on c^0 is the most important factor affecting w_s^0.

Figure 2.5d shows the subtidal suspended sediment concentration without including flocculation, using a constant w_s and the same river discharge as used in Fig. 2.5a. In the simplest model case in which we excluded flocculation, a constant w_s of 3 mm s^{-1} yields the best comparison to observations (Fig. 2.5b). This value corresponds to the value of the settling velocity found near the ETM (Fig. 2.5c). When we exclude flocculation (Fig. 2.5d), the model output qualitatively agrees with observations; we acquire an ETM at 60-80 km from the mouth and obtain more sediment near the bed than at the water surface. However, quantitatively the suspended sediment concentrations are upto a factor three too low. Furthermore, the intrusion of the ETM is too small. Note that our results are different from Dijkstra et al. (2019a) and Brouwer et al. (2018), since they only considered much lower discharges than what is considered here. Because we are interested in the individual impact of flocculation on the suspended sediment distribution, we did not recalibrate parameters M and Q for the case excluding flocculation. When these parameters are recalibrated, $M = 0.004$ s m^{-1} and $Q = 172$ m^3 s^{-1}, resulting in a cost function value of 0.87. The modeled suspended sediment concentrations are still too low, although slightly higher than the previous case due to a decrease of Q. A further increase of M does not increase the suspended sediment concentrations because we are in a suspended sediment supply-limited condition [see Brouwer et al. (2018)]; that is, all sediment is eroded from the bed during a tidal cycle. This implies that the amount of sediment trapped, and not the erosion from the bed, is the limiting factor for the observed suspended sediment concentrations. Sediment trapping is related to net sediment transport processes, which are clearly less efficient in importing sediment when flocculation is not taken into account (see next section).

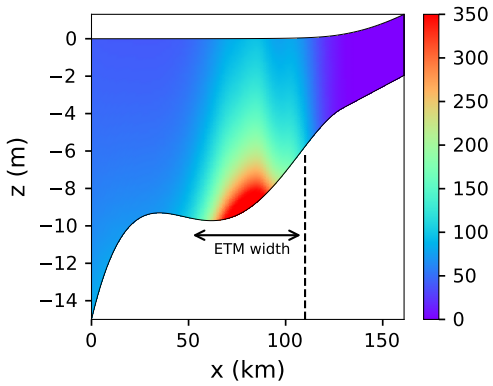

(a) Suspended sediment concentration with flocculation (mg L^{-1})

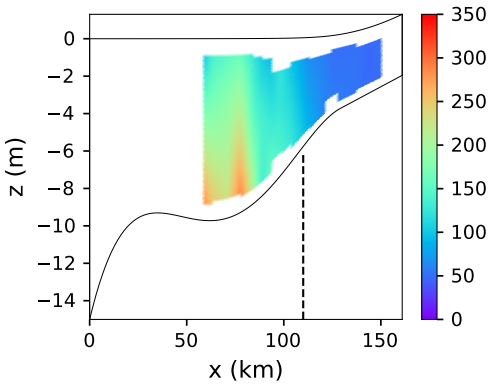

(b) OMES dataset of suspended sediment concentration (mg L^{-1})

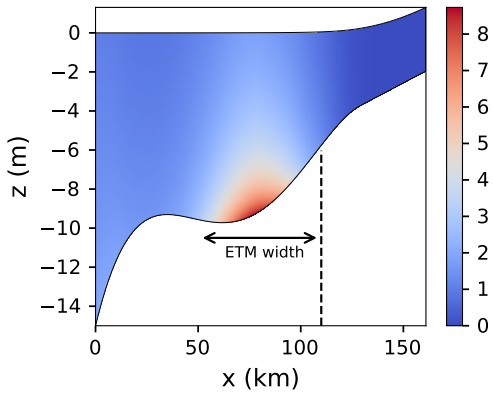

(c) Leading-order, subtidal settling velocity w_s^{00} (mm s^{-1})

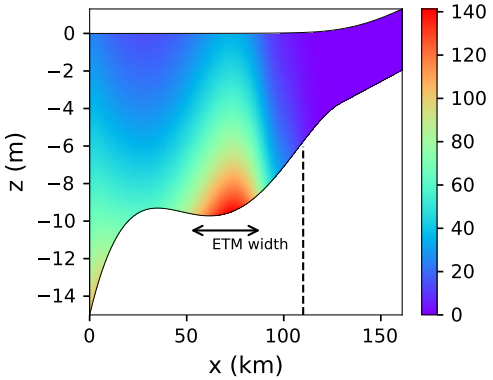

(d) Suspended sediment concentration without flocculation (mg L^{-1})

Figure 2.5: (a) Model output of the subtidal suspended sediment concentration (mg L^{-1}) with flocculation included. The optimal calibration parameters are $k_B = 5600$ $s^{1/2}$ m^{-2}, $M = 0.00336$ s m^{-1}, and $Q = 233$ m^3 s^{-1}. The vertical dashed line depicts the intrusion limit of the observed suspended sediment concentration (i.e., $c \lesssim 50$ mg L^{-1}). (b) The long-term, time-averaged suspended sediment concentration dataset (mg L^{-1}). (c) Leading-order, subtidal settling velocity w_s^{00} with flocculation included (mm s^{-1}). (d) Model output of the subtidal suspended sediment concentration (mg L^{-1}) without including flocculation.

2.4.2 Impact of flocculation on net sediment transport

In this section, we focus on the underlying sediment-transport mechanisms that result in sediment transport and the buildup of an ETM presented in Fig. 2.5. For this, we introduce the advective net transport capacity T, which equals the net redistribution of a (longitudinally) uniform layer of sediment on the bed (Dijkstra et al., 2019b). The net transport capacity only depends on hydrodynamic and sediment features and not on the location of the ETM. Therefore, it is a suitable measure to analyze the impact of various mechanisms on the total net sediment transport (Dijkstra et al., 2019a,b).

Figure 2.6 shows the six most important transport mechanisms contributing to net transport capacity with (Fig. 2.6a) and without (Fig. 2.6b) flocculation together with the total net transport capacity T_{total}. This total net transport capacity T_{total} is the sum of all separate net transport capacities. When $T_{\text{total}} = 0$ and T_{total} changes sign from positive to negative (in land-inward direction), we have a convergence point. Here, we expect sediment to accumulate and thus the formation of an ETM. When comparing Figs. 2.6a and 2.6b, we observe that the convergence point at approximately 80 km in the case with flocculation (Fig. 2.6a) shifted seaward to approximately 70 km when flocculation is not considered (Fig. 2.6b). In both cases, a significant decrease in total net transport capacity is present at 95 km, which is due to the Rupel tributary, resulting in downstream net sediment transport. Figure 2.6a also shows that the additional mechanism related to flocculation, $w_s^1 c^0$ in Eq. (2.21), is always positive and consequently results in land-inward net sediment transport. Furthermore, it is the dominant mechanism at the mouth.

By comparing Figs. 2.6a and 2.6b, it is clear that the contributions of the other transport mechanisms changed when flocculation is included. This is due to the spatial and temporal (M4) variations in the leading-order settling velocity w_s^0, which were absent in the case without flocculation. As mentioned earlier, this alteration of the subtidal and M4 tidal signal in w_s^0 impacts all contributions to the net sediment transport $\mathcal{T}$ [see Eqs. (2.19) and (2.20)].

2.4.3 Sensitivity analysis of floc break-up parameter k_B and total freshwater discharge Q

A sensitivity analysis of the floc break-up parameter k_B and freshwater discharge Q allows us to compute the impact of the magnitude of k_B and Q on the formation of ETM. To stress the importance of spatially varying w_s, we show the sensitivity of ETM formation to k_B with flocculation only varying in space, not in time. We also compare the case with and without flocculation to calculate the impact of space and time dependence in w_s on the emergence of ETM. Finally, we vary the constant settling velocity w_s^0 in the case without flocculation to assess the sensitivity of the ETM characteristics for this parameter.

Figure 2.7 shows the sensitivity of varying k_B ($Q = 233$ m^3 s^{-1} and $M = 0.00336$ s m^{-1}) to depth-averaged subtidal suspended sediment concentration $< \overline{c} >$. In Fig.

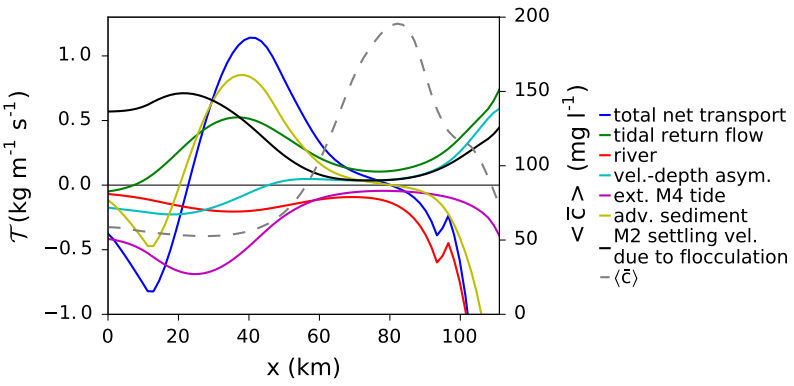

(a) $< \overline{c} >$ and T with flocculation

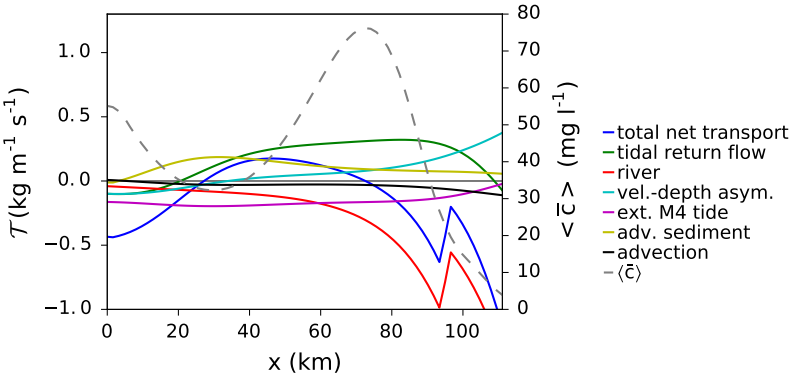

(b) $< \overline{c} >$ and T without flocculation

Figure 2.6: Depth-averaged subtidal suspended sediment concentration $< \overline{c} >$, total advective net transport capacity T_{total}, and the six main hydrodynamical contributions to the total net transport capacity as a function of distance from the mouth (km) of our case study in the Scheldt estuary, showing results (a) with and (b) without flocculation included.

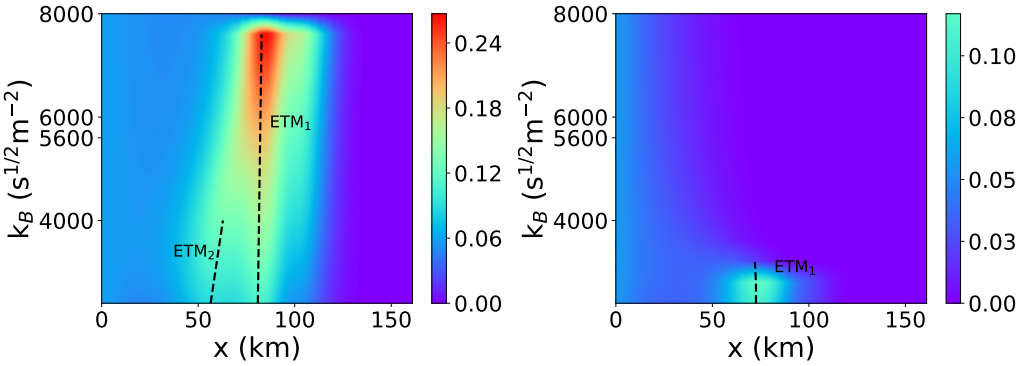

(a) $< \overline{c} >$ with flocculation (g L^{-1})

(b) $< \overline{c} >$ with flocculation without time dependence in w_s (g L^{-1})

Figure 2.7: Depth-averaged subtidal suspended sediment concentration $< \overline{c} >$ (g L^{-1}) for varying floc break-up parameter k_B (Q = 233 m^3 s^{-1} and M = 0.00336 s m^{-1}) in the case with flocculation. The black dashed lines depict the locations of the ETM. (a) Result with time dependence in w_s. (b) Result in which we excluded the time dependence in w_s.

2.7a, the time dependence in w_s is included in the model, whereas in Fig. 2.7b we excluded the temporal dependence in w_s (i.e., w_s^{04} and w_s^{12}) and only considered the spatial dependence in w_s (i.e., w_s^{00}). By excluding the temporal dependence in w_s, we remove the $w_s^1 c^0$ transport mechanism depicted in Fig. 2.6a by the solid black line and the impact of the M4 tidal signal in w_s^0 on net sediment transport [see Eqs. (2.19)-(2.21)].

Figure 2.7 shows that the magnitude of k_B not only determines the location and intensity of ETM, but also the number of ETM. In Fig. 2.7a, for k_B values larger than a critical value of 8000 $s^{1/2}$ m^{-2}, no ETM is found. For values between 4000 $s^{1/2}$ m^{-2} and 8000 $s^{1/2}$ m^{-2}, one ETM is found at a fixed location. For values between 2400 $s^{1/2}$ m^{-2} en 4000 $s^{1/2}$ m^{-2}, two ETM are found, with the most downstream ETM moving downstream with decreasing k_B. This behavior is strongly linked to the temporal variability of settling velocities introduced by the flocculation process. Indeed, Fig. 2.7b shows the impact on ETM formation when only spatial variability in w_s is incorporated. In that case, ETM formation only occurs at significantly smaller k_B values ($\approx$ 3000 $s^{1/2}$ m^{-2}), while multiple ETM are not observed in the domain. Moreover, modeled suspended sediment concentrations are much lower when ignoring temporal variations in w_s.

Figure 2.8 shows the impact of varying river discharge Q (M = 0.00336 s m^{-1}) on the depth-averaged subtidal suspended sediment concentration $< \overline{c} >$ with flocculation (Fig. 2.8a; k_B = 5600 $s^{1/2}$ m^{-2}) and without flocculation (Fig. 2.8b; w_s^0 = 3 mm s^{-1}). We keep Q at typical winter values. Similar to the sensitivity in k_B, the magnitude of Q not only determines the location and intensity of ETM, but also the number of ETM. When flocculation is incorporated (Fig. 2.8a), we have one ETM for values between approximately 200 and 340 m^3 s^{-1}, with suspended sediment concentrations that compare

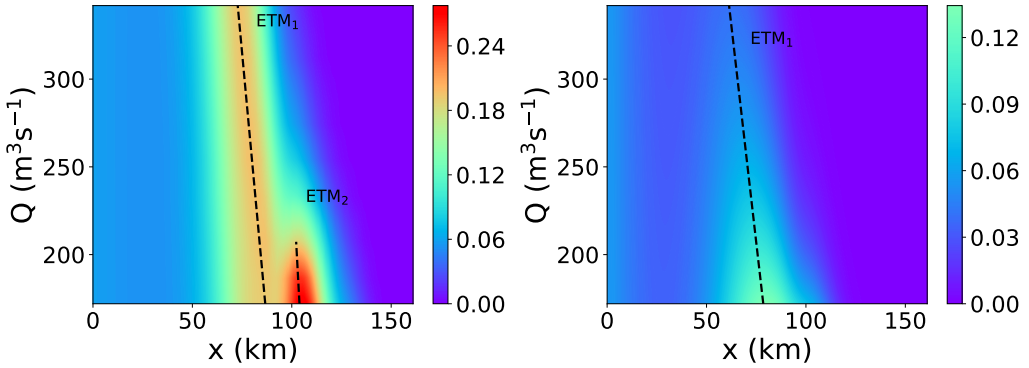

(a) $< \overline{c} >$ with flocculation (g L^{-1}) (b) $< \overline{c} >$ without flocculation (g L^{-1})

Figure 2.8: Depth-averaged subtidal suspended sediment concentration $< \overline{c} >$ (g L^{-1}) for varying freshwater discharge Q ($M = 0.00336$ s m^{-1}). The black dashed lines depict the locations of the ETM. (a) Result with flocculation ($k_B = 5600$ $s^{1/2}$ m^{-2}). (b) Result without flocculation ($w_s^0 = 3$ mm s^{-1}).

well with observations (Fig. 2.5b). For values between approximately 170 and 200 m^3 s^{-1}, we find an additional ETM at approximately 100-120 km. This second ETM has been observed in the Scheldt estuary when discharges are low (Cox et al., 2019). An ETM appearing in the tidal freshwater region during lower discharges was observed in various estuaries (Uncles et al., 2006; Allen et al., 1980). Both ETM move downstream with increasing Q. In the model with fixed settling velocity, only a single ETM is found, which shifts again downstream with increasing Q (Fig. 2.8b). Moreover, the suspended sediment concentrations obtained are low. Consequently, flocculation is important to obtain quantitatively realistic results for relatively large and observed freshwater discharges Q.

Figure 2.9 shows the impact of varying constant settling velocity w_s on $< \overline{c} >$ in case effects of flocculation are not considered ($Q = 233$ m^3 s^{-1} and $M = 0.00336$ s m^{-1}). The magnitude of the settling velocity determines the existence of an ETM. We need a minimal constant settling velocity of approximately 1.8 mm s^{-1} to obtain one ETM. The optimal choice of the constant settling velocity is approximately 3 mm s $^{-1}$, resulting in the best comparison to observations. A settling velocity $w_s^0 = 3$ mm s^{-1} corresponds to a typical value near the ETM (Fig. 2.5c). Moreover, the depth-averaged subtidal suspended sediment concentrations are relatively low compared to the data, for all w_s^0. At $w_s^0 = 3$ mm s^{-1}, although the locations of the ETM are equal, the suspended sediment concentrations are still approximately one-third of those found with time-independent flocculation (Fig. 2.7b), stressing the importance of spatially varying w_s. We cannot resolve the modeled low concentrations (cf. Fig. 2.8b) by altering w_s^0. Consequently, flocculation is required to acquire quantitatively realistic concentrations for large freshwater discharges in winter.

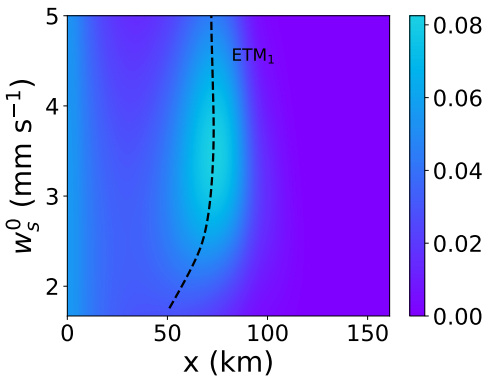

Figure 2.9: Depth-averaged subtidal suspended sediment concentration $< \overline{c} >$ (g L^{-1}) for varying constant settling velocity w_s^0 ($Q = 233$ m^3 s^{-1} and $M = 0.00336$ s m^{-1}) in the case without flocculation. The black dashed line depicts the locations of the ETM.

2.5 Discussion

Our results show that flocculation promotes land-inward net sediment transport in the Scheldt estuary. Relative to the iFlow model without flocculation, the model with flocculation is less sensitive to freshwater discharge. As a result, we still obtain an ETM for high freshwater discharges, which complies with observations (Cox et al., 2019). In addition, the iFlow model without flocculation results in depth-averaged suspended sediment concentrations that are typically too low for large freshwater discharge, stressing the importance of a temporal and spatial dependency of the settling velocity w_s caused by flocculation.

2.5.1 Indications of spatial and temporal variations of the settling velocity in the Scheldt estuary

Observations in the Scheldt estuary confirm both this temporal dependence in w_s, which generates net sediment transport and the modeled magnitude of w_s. Although direct settling velocity measurements are scarce, Manning et al. (2007) measured an averaged settling velocity of macroflocs of 3.9 mm s^{-1} in the ETM of the Scheldt at the entrance of Deurganckdok, approximately 62 km from Vlissingen. When we compare these measured settling velocities to the model output, we find that they more or less comply (Fig. 2.5c). Besides direct settling velocity measurements in the Scheldt estuary, Fettweis and Baeye (2015) observed a strong M2 and M4 tidal signal in floc size and settling velocity in the Southern North Sea, which complies with our model results [Eqs. (2.14) and (2.17)]. Furthermore, Schwarz et al. (2017) measured in situ settling velocities over one tidal cycle in the main channel of the Sieperda March (near the Dutch-Belgian border in Fig. 2.3) using both the Stokes formulation and the Reynolds-flux method. They also found

a distinct M4 tidal signal in settling velocity and floc size, which again agrees with our model results.

2.5.2 Flocculation resulting in land-inward net sediment transport

We showed that flocculation alters the sediment transport mechanisms and generates an additional and important sediment transport mechanism (Figs. 2.6a and 2.6b). Our method enabled a systematic analysis showing that flocculation, and more specifically, the M2 tidal signal in the settling velocity, results in land-inward net sediment transport (solid black line in Fig. 2.6a). Our results comply with Winterwerp (2011) who showed that including flocculation results in land-inward net sediment transport in the Ems River using a 1D vertical model. Xu et al. (2010) also concluded that flocculation results in land-inward sediment transport and promotes accumulation of suspended sediment by performing an idealized 2D model study in the Upper Chesapeake Bay. In general, the direction of net sediment transport depends on the tidal phase difference between flow velocity, suspended sediment concentration, and settling velocity, which might differ for various estuaries and is affected by both the spatial and temporal variations of the settling velocity caused by flocculation.

To estimate a condition for which flocculation results in land-inward net sediment transport, we only consider the M2 tidal signal in the settling velocity w_s^{12}, which we showed can have a significant impact on net sediment transport. When the longitudinal water velocity u (in land-inward direction) is in phase with the suspended sediment concentration c_{floc}^{12} generated by w_s^{12}, we have the condition for maximum land-inward sediment transport related to the flocculation contribution (see Fig. 2.10).

To meet this condition, it is found that w_s^{12} has to be shifted by a $-\pi/2$ phase relative to u, meaning that the M2 tidal signal in the settling velocity peaks at slack tide from flood to ebb (see Fig. 2.10). This condition holds assuming that the water column is fairly well mixed and c_{floc}^{12} and c^{04} are relatively small in comparison with c^{12} and c^{00}. This condition is modified in other cases. Our reasoning is generalized in Appendix 2.E for c^{04} not relatively small when compared with c^{00} and general (i.e., not restricted to maximal) land-inward sediment transport.

2.5.3 The potential impact of flocculation on sediment transport in the Scheldt estuary

Our model results show that the floc break-up parameter k_B determines the position, intensity, and existence of ETM (Fig. 2.7), which complies with Xu et al. (2010) who found that particle stickiness (cf. k_B) can have a significant influence on sediment trapping, especially when the stickiness is small (cf. k_B large). As mentioned earlier, various factors such as salinity (Edzwald et al., 1974) and biotic sticky substances (Fettweis

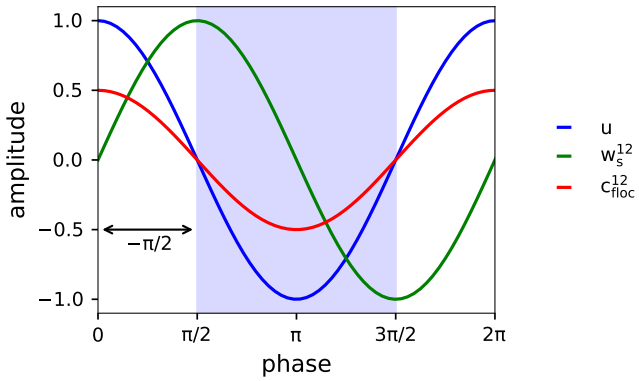

Figure 2.10: Illustration of the optimal condition for land-inward sediment transport with regard to the phase differences between the longitudinal water velocity u, the M2 tidal signal in the settling velocity w_s^{12}, and the suspended sediment concentration due to flocculation c_{floc}^{12} (generated by w_s^{12}). The phase difference between u and w_s^{12} has to be $-\pi/2$, meaning w_s^{12} has to peak at slack tide from flood (white zone) to ebb (blue zone). Because of inertia effects and vertical suspended sediment stratification, this phase condition results in u and c_{floc}^{12} being in phase, resulting in maximal land-inward sediment transport due to flocculation.

et al., 2014) alter k_B. In our case study, the direct impact of salinity on flocculation and resulting sediment transport is relatively small. This complies with Einstein and Krone (1962), who concluded that variations of salinity in most of an estuary have only a small effect on the bond strength. Moreover, the experiments of Edzwald et al. (1974) show a relatively low impact in comparison with the minimal aggregation coefficient (cf. k_B) and saturation at relatively low salinity. Salinity might also have an indirect impact on flocculation through, for example, the production of biotic sticky substances (Alldredge et al., 1993; Bar-Zeev et al., 2015), which is only implicitly included through calibration of k_B.

Over the last two decades, the water quality has significantly improved in the Scheldt estuary because of the implementation of wastewater treatment in Brussels in 2006 (Brion et al., 2015; Cox et al., 2019). Cox et al. (2019) suggested that changes in water quality might result in a large-scale impact on suspended sediment distribution through its influence on flocculation. Our flocculation model can be used to quantify the impact of water quality improvement and verify the hypothesis of Cox et al. (2019), and supplies a tool to systematically assess the mechanisms that explain the changes to the sediment transport. The main unknown for this is the relation between water quality and k_B, and more research is needed to establish practical relations for this.

2.5.4 Parameter variations in the Lagrangian flocculation model

To determine the individual impact of flocculation on the large-scale suspended sediment distribution, we compared a sediment transport model using a constant settling velocity and using the complex Lagrangian flocculation model of Winterwerp (2002). As a first step, we kept most parameters fixed in the Lagrangian flocculation model following Winterwerp (2002).

Over the last decade, various authors extended this flocculation model. For example, Maggi (2009) extended the model by separating the floc volume in a mineral and biomass fraction. More recently, Xu and Dong (2017) were able to model floc size dynamics more accurately when assuming that the fractal dimension n_f follows a normal distribution. As a final example, Kuprenas et al. (2018) implemented a dependence of floc size D_f and shear rate G in the calibration parameter q to correct for an overestimation of floc size at large shear rates (order of 50 s^{-1}).

In further research, the same scaling and perturbation procedure presented in this paper can be applied to extended versions of the Lagrangian model of Winterwerp. For example, by assuming constant parameter values (e.g., $n_f = 2$ and $q = 0.5$), we found a linear relationship between the settling velocity and suspended sediment concentration. Different parameter values might result in a nonlinear relationship. An example of such a relation is given by van Leussen (1994), who proposed an at equilibrium relation between settling velocity, suspended sediment concentration, and shear rate: $w_s = K_{\mathrm{vL}} c^{m_{\mathrm{vL}}}[(1 + a_{\mathrm{vL}}G)/(1 + b_{\mathrm{vL}}G^2)]$, in which a_{vL}, b_{vL}, K_{vL}, and m_{vL} are empirically determined parameters. Such a formulation is similar to ours in that it depends on c and G but with a somewhat different relation, which may lead to a modification of the results. But, further discussion of this is out of the scope of the present paper.

2.6 Conclusions

In this paper, we coupled a flocculation model and a sediment transport model to acquire insight into the impact of flocculation on large-scale sediment transport in a tide-dominated estuary. The combination of this flocculation model and the iFlow model allowed us to identify the relative importance of individual processes for water flow and sediment transport (e.g., river, tide, density forcing, advection). We employed a perturbation approach to gain insight into the highly complex coupled equations that describe flocculation. The result reveals a simple linear relationship between w_s and c, both at leading and first order.

We applied our framework to a winter case in the Scheldt estuary. We showed that the spatial and temporal variations of w_s due to flocculation are essential to reproduce observed suspended sediment concentrations. We were able to identify the impact of flocculation on individual transport mechanisms. We showed that flocculation alters most of the dominant transport mechanisms (e.g., river and tidal return flow) by introducing

both a spatial and temporal dependence in w_s.

To further investigate the impact of flocculation on large-scale sediment transport, we carried out a sensitivity analysis in which we showed that the magnitude of the floc break-up parameter k_B and total freshwater discharge Q determine the existence, intensity, and number of ETM.

Although we found examples in the literature of several other estuaries where flocculation is thought to promote sediment import, we were able to show that flocculation can also theoretically promote sediment export, depending on the phase difference between the tidal flow and suspended sediment concentration. Therefore, the effect of flocculation on the large-scale sediment transport in other estuaries needs to be assessed carefully based on local conditions.

List of symbols

Latin

A^0	Water level amplitude at $x = 0$ corresponding to the M2 tide
A^1	Water level amplitude at $x = 0$ corresponding to the M4 tide
a_{vL}	Parameter in the empirical formulation of van Leussen (1994) for the relation between w_s and c
B	Width of the estuary
b_{vL}	Parameter in the empirical formulation of van Leussen (1994) for the relation between w_s and c
c	Suspended sediment concentration
c^0	Leading-order suspended sediment concentration
c^{00}	Subtidal component of the leading-order c
c^{00}_{floc}	Flocculation-induced c^{00}
$\hat{c}^{00}$	Complex amplitude of c^{00}
c^{02}	Component of the leading-order c corresponding to the M2 tide
$\hat{c}^{02}$	Complex amplitude of c^{02}
c^{04}	Component of the leading-order c corresponding to the M4 tide
c^{04}_{floc}	Flocculation-induced c^{04}
$\hat{c}^{04}$	Complex amplitude of c^{04}
c^1	First-order suspended sediment concentration
c^{10}	Subtidal component of the first-order c
c^{10}_{floc}	Flocculation-induced c^{10}
$\hat{c}^{10}$	Complex amplitude of c^{10}
c^{12}	Component of the first-order c corresponding to the M2 tide
c^{12}_{floc}	Flocculation-induced c^{12}
$\hat{c}^{12}$	Complex amplitude of c^{12}
c^{14}	Component of the first-order c corresponding to the M4 tide
c^{14}_{floc}	Flocculation-induced c^{14}

$\hat{c}^{14}$	Complex amplitude of c^{14}
$< c_{\text{meas.}} >$	Time-averaged measured SPM concentration
$< c_{\text{model}} >$	Modeled subtidal suspended sediment concentration
$< \overline{c} >$	Depth-averaged subtidal suspended sediment concentration
c_{sea}	Depth-averaged subtidal suspended sediment concentration at $x = 0$
D_e	Equilibrium floc size
D_f	Floc size
D_p	Primary particle size
f_s	Shape factor
G	Shear rate
g	Gravitational acceleration
H	Magnitude of the z-coordinate of the river bed
K_h	Horizontal diffusivity coefficient
K_{vL}	Parameter in the empirical formulation of van Leussen (1994) for the relation between w_s and c
K_ν	Vertical eddy diffusivity coefficient
K_ν^0	Leading order vertical eddy diffusivity coefficient
k'_A	Aggregation parameter
$k_A^{\text{min.}}$	Nondimensional minimal aggregation coefficient
k_B	Break-up parameter
M	Erosion parameter
m_{vL}	Parameter in the empirical formulation of van Leussen (1994) for the relation between w_s and c
N	Number of flocs per unit volume
N_{equal}	Number of locations at which the suspended sediment concentration model output and observations are statistically equal
N_{loc}	Total number of locations at which we have SPM observations
n	Number of measured SPM concentrations
n_f	Fractal dimension
$\mathcal{O}$	Order of
p	Calibration parameter in the flocculation model
q	Calibration parameter in the flocculation model
Q	Total freshwater discharge
R	Reference level of the water surface elevation
Re_f	Floc Reynolds number (i.e., $w_s D_f/\nu$)
S	Salinity
S_1	Flocculation salinity sensitivity calibration parameter
S_2	Flocculation salinity sensitivity calibration parameter
s_{f_0}	Bed roughness coefficient
$ssea$	Salinity boundary condition at the mouth
std	Standard deviation of the measured SPM concentration
$\mathcal{T}$	Net sediment transport
$\mathcal{T}_{\text{floc}}$	Flocculation-induced net sediment transport
T_{total}	Total net transport capacity
t	Time
t_{score}	Student's t statistic
u	Water flow velocity in the longitudinal dimension

u_*	Shear velocity
u^0	Leading-order water flow velocity in the longitudinal dimension
u^{00}	Subtidal component of the leading-order u
$\hat{u}^{00}$	Complex amplitude of u^{00}
u^{02}	Component of the leading-order u corresponding to the M2 tide
$\hat{u}^{02}$	Complex amplitude of u^{02}
u^{04}	Component of the leading-order u corresponding to the M4 tide
$\hat{u}^{04}$	Complex amplitude of u^{04}
u^1	First-order velocity in the longitudinal dimension
u^{10}	Subtidal component of the first-order u
$\hat{u}^{10}$	Complex amplitude of the subtidal component of the first-order u
$u^{10}_{\text{riv.}}$	River-induced u^{10}
u^{12}	Component of the first-order u corresponding to the M2 tide
$\hat{u}^{12}$	Complex amplitude of u^{12}
u^{14}	Component of the first-order u corresponding to the M4 tide
$\hat{u}^{14}$	Complex amplitude of u^{14}
w	Water flow velocity in the vertical dimension
w^0	Leading-order water flow velocity in the vertical dimension
w^1	First-order water flow velocity in the vertical dimension
w_s	Settling velocity of suspended sediment
w_s^0	Leading-order settling velocity of suspended sediment
w_s^{00}	Subtidal component of the leading-order w_s
w_s^{02}	Component of the leading-order w_s corresponding to the M2 tide
w_s^{04}	Component of the leading-order w_s corresponding to the M4 tide
$w^0_{s,\text{init.}}$	Initial leading-order w_s in the iteration procedure
$w^0_{s,\text{old}}$	Previous value of the leading-order w_s in the iteration procedure
w_s^1	First-order settling velocity of suspended sediment
w_s^{10}	Subtidal component of the first-order w_s
w_s^{12}	Component of the first-order w_s corresponding to the M2 tide
w_s^{14}	Component of the first-order w_s corresponding to the M4 tide
$w^1_{s,\text{init.}}$	Initial first-order w_s in the iteration procedure
$w_{s,\text{min.}}$	Minimum settling velocity of suspended sediment
x	Spatial coordinate in the longitudinal dimension
x_c^{sal}	Calibration parameter in postulated tanh salinity distribution in winter
x_L^{sal}	Calibration parameter in postulated tanh salinity distribution in winter
z	Spatial coordinate in the vertical dimension
z_1	Distance in the logarithmic layer above the river bed
$\tilde{z}_1$	z_1/H

Greek

β	Parameter defined in Table 2.1
γ	Parameter defined in Table 2.1
∂_t	Partial derivative to t
∂_x	Partial derivative to x
∂_z	Partial derivative to z
ϵ	Small perturbation number (i.e., $\xi/H \ll 1$)

κ	Parameter defined in Table 2.1
κ'	Von Karman constant
μ	Dynamic viscosity of water
ν	Kinematic viscosity of water
ξ	z-coordinate of the water surface
ξ^0	z-coordinate of the water surface at leading order
ρ_s	Density of sediment primary particles
ρ_w	Reference density of water
σ_ρ	Prandtl-Smidth number
τ	Parameter defined in Table 2.1
τ_b	Shear stress at the river bed
ϕ	Volumetric concentration
ϕ^1	Water level phase at $x = 0$ corresponding to the M4 tide
ω_{M2}	Angular frequency corresponding to the semidiurnal lunar M2 tide

Appendix 2.A: salinity dependence

Following Warner et al. (2005), we fit the observed salinity data to the following postulated salinity distribution of our winter case in the Scheldt estuary:

$$\frac{\mathrm{ssea}}{2}\left(1 - \tanh\frac{x - x_c^{\mathrm{Sal.}}}{x_L^{\mathrm{Sal.}}}\right), \tag{2.25}$$

with ssea being the salinity boundary condition at the mouth and $x_c^{\mathrm{Sal.}}$ and $x_L^{\mathrm{Sal.}}$ being further undefined calibration parameters. Figure 2.A.1a shows the data fit. Edzwald

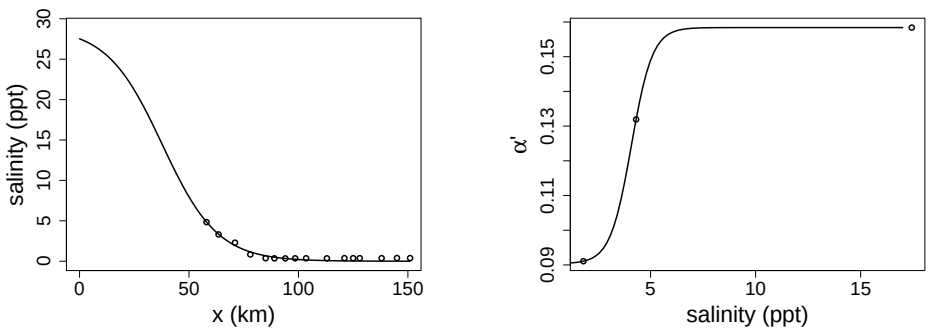

(a) Salinity (ppt)

(b) Stability value α'

Figure 2.A.1: (a) Measured salinity corresponding to our case study in the Scheldt estuary and corresponding data fit using Eq. (2.25). (b) Stability value α' as a function of salinity based on Edzwald et al. (1974).

et al. (1974) calculated the salinity dependence for stability value α' which is defined as

$$\partial_t N^{\text{aggregation}} = \frac{-4\alpha'\phi G N}{\pi}, \tag{2.26}$$

where ϕ is the volumetric concentration, G is the shear rate, and N is the number concentration of flocs. Winterwerp and van Kesteren (2004) showed that

$$\phi = f_s N D_f^3, \tag{2.27}$$

with f_s being the floc shape factor and D_f being the floc size. Consequently, in identification with Eq. (2.6) and assuming the floc shape is spherical ($f_s = \pi/6$), we have

$$k'_A = \frac{2\alpha'}{3}. \tag{2.28}$$

The latter relation allows us to use the salinity dependence of α' for k'_A. We postulate the following salinity S dependence:

$$\alpha' = \left\{ \alpha^{\text{min.}} + S_3[1 + \tanh\left(S(x) - S_2\right)] \right\}, \tag{2.29}$$

and we fit the latter function to the averaged data presented in Edzwald et al. (1974), which is shown in Fig. 2.A.1b. We acquire $\alpha^{\text{min.}} = 0.0904$, $S_2 = 4.085‰$, and $S_3 = 0.03401$. We showed that net sediment transport only depends on the ratio of k'_A and k_B and not on the individual parameters. We can thus decide to make k'_A solely a function of salinity S and keep k_B fixed without restricting the generality of our results:

$$k'_A(x) = k_A^{\text{min.}} \left\{ 1 + S_1 \left[1 + \tanh(S(x) - S_2)\right] \right\}, \tag{2.30}$$

with $k_A^{\text{min.}}$ being the minimal aggregation parameter. Combination of Eqs. (2.28) and (2.30) yields

$$S_1 = \frac{2}{3} \frac{S_3}{k_A^{\text{min.}}}. \tag{2.31}$$

Appendix 2.B: sediment equations with ordering

The width-averaged sediment mass balance equation following Chernetsky et al. (2010) and Dijkstra et al. (2017) reads as

$$\partial_t c + u\partial_x c + w\partial_z c - \partial_z(w_s c + K_\nu \partial_z c) - \partial_x(K_h \partial_x c) = 0, \tag{2.32}$$

where c is the suspended sediment concentration, u and w are the water velocity in the x and z direction, w_s is the settling velocity, K_ν is the constant vertical eddy diffusivity

coefficient, and K_h is the constant horizontal diffusivity coefficient. At the water surface, we require that no sediment particles enter or leave the domain:

$$w_s c + \partial_z (K_\nu c) = 0 \qquad \text{at} \qquad z = R + \xi, \tag{2.33}$$

with R being the reference level and ξ being the water surface elevation. At the bed, we require

$$w_s c + K_\nu \partial_z c = D - E \quad \text{at} \quad z = -H, \tag{2.34}$$

where D and E are the deposition and erosion of sediment defined as

$$D = w_s c \qquad \text{and} \tag{2.35}$$

$$E = M|\tau_b| f(a), \tag{2.36}$$

where M is the erosion parameter, τ_b is the shear stress at the bed, and $f(a)$ is the erodibility.

To apply ordering and perturbation theory, we first have to compute the order of each term in the differential equation and boundary conditions. For this, we use typical scales for each variables following Chernetsky et al. (2010):

$$\begin{aligned} &\partial_{\tilde{t}} \tilde{c} + \underbrace{\frac{U}{\sigma L_{Ems}}}_{\mathcal{O}(1)} \tilde{u} \partial_{\tilde{x}} \tilde{c} + \underbrace{\frac{U}{\sigma L_{Ems}}}_{\mathcal{O}(1)} \tilde{w} \partial_{\tilde{z}} \tilde{c} \\ &- \partial_{\tilde{z}} \left(\underbrace{\frac{W_s}{\sigma H_{0,Ems}}}_{\mathcal{O}(0)} \tilde{w}_s c + \underbrace{\frac{\mathcal{K}_\nu}{\sigma H_{0,Ems}^2}}_{\mathcal{O}(0)} \tilde{K}_\nu \partial_{\tilde{z}} \tilde{c} \right) - \partial_{\tilde{x}} \left(\underbrace{\frac{K_h}{\sigma L_{Ems}^2}}_{\mathcal{O}(4)} \partial_{\tilde{x}} \tilde{c} \right) = 0, \end{aligned} \tag{2.37}$$

where the tilde denotes dimensionless variables, $\mathcal{O}$ is the order of magnitude, σ is the $M2$ tidal angular frequency, U is the typical scale of the horizontal velocity of the M2 tide, A_{M2} is the M2 tidal amplitude at seaward side, $H_{0,Ems}$ is the water depth at the mouth, W_s is the typical settling velocity scale, $\mathcal{K}_\nu$ is the typical vertical eddy diffusivity coefficient scale, and L_{Ems} is the length of the Ems estuary. The typical scales following Chernetsky et al. (2010) are summarized in Table 2.B.1. The boundary conditions in dimensionless form read as

$$\underbrace{\frac{W_s}{\sigma H_0}}_{\mathcal{O}(0)} \tilde{w}_s \tilde{c} + \underbrace{\frac{\mathcal{K}_\nu}{\sigma H_0^2}}_{\mathcal{O}(0)} \tilde{K}_\nu \partial_{\tilde{z}} \tilde{c} = 0 \quad \text{at} \quad \tilde{z} = \frac{R}{H_0} + \underbrace{\frac{A_{M2}}{H_0}}_{\mathcal{O}(1)} \tilde{\xi} \qquad \text{and} \tag{2.38}$$

$$\underbrace{\frac{\mathcal{K}_\nu}{\sigma H_0^2}}_{\mathcal{O}(0)} \tilde{K}_\nu \partial_{\tilde{z}} \tilde{c} = - \underbrace{\frac{\mathcal{E}/C}{\sigma H_0}}_{\mathcal{O}(0)} \tilde{E} \quad \text{at} \quad \tilde{z} = -\tilde{H}, \tag{2.39}$$

where R is the water surface reference level, $\tilde{\xi}$ is the dimensionless water surface elevation, $\mathcal{E}$ is the erosion scale, and C is the suspended sediment concentration scale.

Table 2.B.1: Typical scales of the variables used in the ordering and perturbation analysis by Chernetsky et al. (2010). The variables are deducted from both theoretical equations and measurements in the Ems estuary.

Variable	Definition	Scale	Source
$H_{0,Ems}\tilde{z} = z$	Averaged depth at seaward side	12.2 m	Chernetsky et al. (2010)
A_{M2}	M2 tidal amplitude at seaward side	1.35 m	Chernetsky et al. (2010)
L_{Ems}	Length Ems estuary	63.7×10^3 m	Chernetsky et al. (2010)
σ	Semidiurnal angular tidal frequency scale	1.4×10^{-4} s^{-1}	Chernetsky et al. (2010)
W_s	Settling velocity scale	2×10^{-3} m s^{-1}	Chernetsky et al. (2010)
$\mathcal{K}_\nu \tilde{K}_\nu = K_\nu$	Vertical eddy diffusivity coefficient scale	1.7×10^{-2} m^2 s^{-1}	Chernetsky et al. (2010)
K_h	Horizontal diffusivity coefficient scale	100 m^2 s^{-1}	Chernetsky et al. (2010)
$U = \frac{\sigma A_{M2} L}{H_{0,Ems}}$	Typical horizontal velocity of the M2 tide	1 m s^{-1}	Balance of depth-averaged continuity equation
$W = \frac{H_{0,Ems}}{L} U$	Typical vertical velocity of the M2 tide	1.9×10^{-4} m s^{-1}	Balance of continuity equation
$\mathcal{E}/C = \frac{K_\nu}{H_0}$	Ratio of typical erosion and suspended suspended sediment concentration scale	1.4×10^{-3} m s^{-1}	Balance of Eq. (2.34)

To apply perturbation theory, we write the solutions for u, w, ξ, and c as a power series of a small parameter ϵ with $\mathcal{O}(1)$:

$$u = u^0 + u^1 + u^2 + \mathcal{O}(\epsilon^3), \tag{2.40}$$
$$w = w^0 + w^1 + w^2 + \mathcal{O}(\epsilon^3), \tag{2.41}$$
$$\xi = \xi^0 + \xi^1 + \xi^2 + \mathcal{O}(\epsilon^3), \quad \text{and} \tag{2.42}$$
$$c = c^0 + c^1 + c^2 + \mathcal{O}(\epsilon^3), \tag{2.43}$$

where u^0, w^0, ξ^0, and c^0 are assumed to be of leading order; u^1, w^1, ξ^1, and c^1 are of order ϵ, and so on. Using the scaling, we acquire at leading order

$$\partial_t c^0 - \partial_z(w_s^0 c^0 + K_\nu^0 \partial_z c^0) = 0, \tag{2.44}$$
$$w_s^0 c^0 + K_\nu^0 \partial_z c^0 = 0 \qquad \text{at} \qquad z = R, \qquad \text{and} \tag{2.45}$$
$$K_\nu^0 \partial_z c^0 = -E^0 \qquad \text{at} \qquad z = -H \tag{2.46}$$

and at first order

$$\partial_t c^1 - \partial_z(w_s^0 c^1 + K_\nu^0 \partial_z c^1) = -u^0 \partial_x c^0 - w^0 \partial_z c^0 + \partial_z(w_s^1 c^0) + \partial_z(K_\nu^1 \partial_z c^0), \tag{2.47}$$
$$w_s^0 c^1 + K_\nu^0 \partial_z c^1 = -w_s^1 c^0 - K_\nu^1 \partial_z c^0 - \underbrace{\partial_z(w_s^0 c^0 + K_\nu^0 \partial_z c^0)}_{\partial_t c^0} \xi^0 \qquad \text{at} \qquad z = R, \qquad \text{and} \tag{2.48}$$
$$K_\nu^0 \partial_z c^1 = -E^1 - K_\nu^1 \partial_z c^0 \qquad \text{at} \qquad z = -H, \tag{2.49}$$

in which we linearized around the reference level R (i.e., we applied a Taylor expansion). Chernetsky et al. (2010) and Dijkstra et al. (2017) showed that c^0 has a subtidal and M4 tidal signal and c^1 has an M2 tidal signal given the assumptions listed above.

Appendix 2.C: scaling analysis and perturbation theory

Similarly, we scale the Winterwerp flocculation model shown in Eq. (2.12):

$$
\begin{aligned}
&\underbrace{\frac{1}{\gamma G k_B G^{1/2}(\gamma D_p^{-2})}}_{\tau}\frac{W_s}{C}\frac{\tilde{w}_s}{\tilde{c}}\sigma C W_s^{-2}\Bigg\{\partial_{\tilde{t}}\tilde{c}\tilde{w}_s^{-2}+\frac{U}{\sigma L}\partial_{\tilde{x}}[\tilde{u}\tilde{c}\tilde{w}_s^{-2}]\\
&+\partial_{\tilde{z}}[(\frac{U}{\sigma L}\tilde{w}-\frac{W_s}{\sigma H_0}\tilde{w}_s)\tilde{c}\tilde{w}_s^{-2}]-\frac{1}{L^2\sigma}\partial_{\tilde{x}}[K_h\partial_{\tilde{x}}\tilde{c}\tilde{w}_s^{-2}]\\
&\qquad-\frac{\mathcal{K}_\nu}{\sigma H_0^2}\tilde{K}_v\partial_{\tilde{z}z}\tilde{c}\tilde{w}_s^{-2}\Bigg\}\\
&=\underbrace{\frac{-k_A' D_p^{-2} f_s^{-1}\rho_s^{-1}}{k_B G^{1/2}(\gamma D_p^{-2})}}_{\beta}C\tilde{c}+W_s\tilde{w}_s-\frac{1}{\gamma D_p^{-2}},\\
&\xrightarrow{\times 1/W_s}\underbrace{\tau W_s^{-2}\sigma}_{\mathcal{O}(1)}\frac{\tilde{w}_s}{\tilde{c}}\Bigg\{\partial_{\tilde{t}}\tilde{c}\tilde{w}_s^{-2}+\underbrace{\frac{U}{\sigma L}}_{\mathcal{O}(1)}\partial_{\tilde{x}}[\tilde{u}\tilde{c}\tilde{w}_s^{-2}]\\
&+\partial_{\tilde{z}}[(\underbrace{\frac{U}{\sigma L}}_{\mathcal{O}(1)}\tilde{w}-\underbrace{\frac{W_s}{\sigma H_0}}_{\mathcal{O}(0)}\tilde{w}_s)\tilde{c}\tilde{w}_s^{-2}]-\underbrace{\frac{1}{L^2\sigma}}_{\mathcal{O}(7)}\partial_{\tilde{x}}[K_h\partial_{\tilde{x}}\tilde{c}\tilde{w}_s^{-2}]\\
&\qquad-\underbrace{\frac{\mathcal{K}_\nu}{\sigma H_0^2}}_{\mathcal{O}(0)}\tilde{K}_v\partial_{\tilde{z}z}\tilde{c}\tilde{w}_s^{-2}\Bigg\}\\
&=\underbrace{\beta\frac{C}{W_s}}_{\mathcal{O}(0)}\tilde{c}+\tilde{w}_s-\underbrace{\frac{1}{\gamma D_p^{-2}W_s}}_{\mathcal{O}(2)},
\end{aligned}
\tag{2.50}
$$

in which we used typical scales for the Scheldt and Ems estuary presented in Table 2.C.1 and β, γ, and τ are defined in Table 2.1. To apply perturbation theory, we write the solution of w_s as a power series of a small parameter ϵ with $\mathcal{O}(1)$ following Chernetsky et al. (2010):

$$
w_s = w_s^0 + w_s^1 + w_s^2 + \mathcal{O}(\epsilon^3), \tag{2.51}
$$

$$
\tag{2.52}
$$

where w_s^0 is assumed to be of leading order, w_s^1 is of order ϵ, and so on. Using the scaling from Eq. (2.50), we acquire at leading order in dimensional form the balance between

Table 2.C.1: Typical scales of the variables used in the ordering and perturbation analysis. The variables are deducted from both theoretical equations and measurements in the Scheldt and Ems estuary.

Variable	Definition	Scale	Source
$H_0\tilde{z} = z$	Averaged depth at seaward side	1×10^1 m	Fig. 2.5b; Scheldt estuary
A_{M2}	M2 tidal amplitude scale at seaward side	1×10^0 m	Brouwer et al. (2018); Scheldt estuary
D_p	Primary particle size scale	1×10^{-5} m	Winterwerp (2002); Ems estuary
k'_A	Dimensionless floc aggregation parameter scale	1×10^{-1}	Winterwerp (2002); Ems estuary
L	Length Scheldt estuary	160×10^3 m	Brouwer et al. (2018); Scheldt estuary
$\sigma^{-1}\tilde{t} = t$	Semidiurnal angular tidal frequency scale	1.4×10^{-4} s^{-1}	Chernetsky et al. (2010)
$W_s\tilde{w}_s = w_s$	Settling velocity scale	2×10^{-3} m s^{-1}	Brouwer et al. (2018) and Manning et al. (2007); Scheldt estuary
$\mathcal{K}_\nu\tilde{K}_\nu = K_\nu$	Vertical eddy diffusivity coefficient scale	1.7×10^{-2} m^2 s^{-1}	Chernetsky et al. (2010); Ems estuary
ρ_s	Density of primary particles	2.6×10^3 kg m^{-3}	Chernetsky et al. (2010); Ems estuary
$C\tilde{c} = c$	Suspended sediment concentration scale	2×10^{-1} kg m^{-3}	Fig. 2.5b; Scheldt estuary
G	Shear rate scale	2×10^0 s^{-1}	Eq. (2.8)
k_B	Dimensional floc break-up parameter scale	5×10^3 s$^{1/2}$ m^{-2}	Balance floc aggregation and break-up term
$U = \frac{\sigma A_{M2} L}{H_0}$	Typical horizontal velocity of the M2 tide	2.3 m s^{-1}	Balance depth-averaged continuity equation

floc aggregation and floc break-up:

$$
\begin{aligned}
0 &= \underbrace{-k'_A c^0 D_p^{-2} f_s^{-1} \rho_s^{-1}}_{\text{aggregation}} + \underbrace{k_B G^{1/2} (\gamma D_p^{-2} w_s^0 - 1)}_{\text{break-up}}, \\
\implies w_s^0 &= \underbrace{\frac{k'_A}{k_B \sqrt{G}} f_s^{-1} \rho_s^{-1} \gamma^{-1}}_{\beta} c^0 + \underbrace{\gamma^{-1} D_p^2}_{\beta\kappa}, \\
\implies w_s^0 &= \beta(c^0 + \kappa),
\end{aligned}
\tag{2.53}
$$

with κ defined in Table 2.1. We added the second-order term $-k_B G^{1/2}$ from the break-up term to ensure that, in the limit for $c^0 \to 0$, the floc size is equal to the primary particle size: $D_f \to D_p$, which corresponds to a settling velocity of massive ($n_f = 3$) primary particles:

$$
w_{s,\text{min.}} = \frac{(\rho_s - \rho_w) g D_p^2}{18\mu} = \beta\kappa. \tag{2.54}
$$

We can add this (small) term to our leading-order result and leave out the $\beta\kappa$ term in our higher-order calculations without restricting the generality of our results. The first-order

equation yields

$$\frac{1}{\gamma \underbrace{(w_s^0)^{-1}c^0}_{1/\beta} G}\left\{\partial_t c^0 (w_s^0)^{-2} - \partial_z[c^0(w_s^0)^{-1}] - \partial_z[K_v^0 \partial_z c^0 (w_s^0)^{-2}]\right\}$$

$$= \underbrace{-k_A' D_p^{-2} f_s^{-1} \rho_s^{-1} c^1}_{\text{aggregation}} + \underbrace{k_B G^{1/2}(\gamma D_p^{-2} w_s^1)}_{\text{break-up}}, \tag{2.55}$$

$$\implies w_s^1 - \beta c^1 = \frac{1}{\underbrace{\gamma G k_B G^{1/2}(\gamma D_p^{-2})}_{\tau}} \beta \times$$

$$\left\{\partial_t \underbrace{c^0 (w_s^0)^{-2}}_{1/(\beta^2 c^0)} - \partial_z[\underbrace{c^0(w_s^0)^{-1}}_{1/\beta}] - \partial_z[K_v^0 \partial_z \underbrace{c^0 (w_s^0)^{-2}}_{1/(\beta^2 c^0)}]\right\},$$

$$\xrightarrow{\partial_z(1/\beta)=0} w_s^1 - \beta c^1 = \frac{\tau}{\beta}\left\{ - \frac{1}{(c^0)^2}\partial_t c^0 \right.$$

$$\left. + K_\nu^0 \left[\frac{-2}{(c^0)^3}(\partial_z c^0)^2 + \frac{1}{(c^0)^2}\partial_{zz} c^0\right]\right\},$$

$$\implies w_s^1 - \beta c^1 = \frac{\tau}{\beta}\left\{ \frac{1}{(c^0)^2}\left[\underbrace{-\partial_t c^0 + K_\nu^0 \partial_{zz} c^0}_{-\partial_z(w_s^0 c^0)}\right] - 2K_\nu^0 \frac{(\partial_z c^0)^2}{(c^0)^3}\right\},$$

$$\implies w_s^1 = \beta c^1 - 2\tau \frac{\partial_z c^0}{c^0}\left[1 + \frac{K_\nu^0}{w_s^0}\frac{\partial_z c^0}{c^0}\right]. \tag{2.56}$$

Appendix 2.D: calculation of tidal components of $\mathbf{w}_s$

In iFlow, we work with tidal components instead of time series. Therefore, we project the solutions of w_s^0 and w_s^1 on the subtidal, M_2, and M_4 tidal components. The amplitudes of the terms that are linear in c^0 and c^1 are trivial, for example:

$$\hat{w}_s^{00} = \beta \hat{c}^{00} \qquad \text{and} \tag{2.57}$$

$$\hat{w}_s^{04} = \beta \hat{c}^{04}, \tag{2.58}$$

with $\hat{c}^{00}$ and $\hat{c}^{04}$ being (sub)tidal amplitudes. The projection of the second term in Eq. (2.56) is nontrivial. In general, an amplitudes A^n of a periodic function func(t) can be obtained by

$$A^n = \frac{1}{T}\int_{-\frac{T}{2}}^{+\frac{T}{2}} \text{func}(t) \frac{e^{+i\frac{2\pi n}{T}t} + e^{-i\frac{2\pi n}{T}t}}{2} dt, \tag{2.59}$$

with T being the period of function func(t) and in which n denotes the (sub-)tidal constituent (i.e., subtidal, M2, and M4). Substitution of $\tilde{t} = \mathrm{M2}t = (2\pi/T)t$ yields

$$A^n = \frac{1}{2\pi} \int_{-\pi}^{+\pi} \tilde{\mathrm{func}}(\tilde{t}) \frac{e^{+in\tilde{t}} + e^{-in\tilde{t}}}{2} d\tilde{t}. \tag{2.60}$$

Application to the second term of the right-hand side in Eq. (2.56), without the -2τ factor, and substitution of $\zeta = e^{i\tilde{t}}$ yields

$$\begin{aligned} A^n = \frac{1}{2\pi i} \oint_{|1|} \Bigg\{ \frac{1}{\zeta} \Bigg[& \frac{\partial_z \hat{c}^{00} + \partial_z \hat{c}^{00*} + (\partial_z \hat{c}^{04})\zeta^2 + (\partial_z \hat{c}^{04*})\zeta^{-2}}{\hat{c}^{00} + \hat{c}^{00*} + \hat{c}^{04}\zeta^2 + \hat{c}^{04*}\zeta^{-2}} \\ & \cdot \left(1 + 2\frac{K^0_\nu}{\beta} \frac{\partial_z \hat{c}^{00} + \partial_z \hat{c}^{00*} + (\partial_z \hat{c}^{04})\zeta^2 + (\partial_z \hat{c}^{04*})\zeta^{-2}}{(\hat{c}^{00} + \hat{c}^{00*} + \hat{c}^{04}\zeta^2 + \hat{c}^{04*}\zeta^{-2})^2} \right) \Bigg] \\ & \cdot \frac{\zeta^{-n} + \zeta^{+n}}{2} \Bigg\} d\zeta. \end{aligned} \tag{2.61}$$

We use the residue theorem:

$$\begin{aligned} \oint \mathrm{func}(\zeta) d\zeta = & \\ & 2\pi i \sum_k \underbrace{\frac{1}{(m-1)!} \lim_{\zeta \to \zeta_k} \frac{d^{m-1}}{d\zeta^{m-1}} \Big[(\zeta - \zeta_k)^m \mathrm{func}(\zeta) \Big]}_{\text{Residue}}, \end{aligned} \tag{2.62}$$

in which ζ_k is a pole of integrand func and m is the order of pole ζ_k. The integrand in Eq. (2.61) has five poles:

$$\pm\zeta_{k_1} = \pm \sqrt{\frac{-(\hat{c}^{00} + \hat{c}^{00*}) + \sqrt{(\hat{c}^{00} + \hat{c}^{00*})^2 - 4\hat{c}^{04}\hat{c}^{04*}}}{2\hat{c}^{04}}}, \tag{2.63}$$

$$\pm\zeta_{k_2} = \pm \sqrt{\frac{-(\hat{c}^{00} + \hat{c}^{00*}) - \sqrt{(\hat{c}^{00} + \hat{c}^{00*})^2 - 4\hat{c}^{04}\hat{c}^{04*}}}{2\hat{c}^{04}}}, \tag{2.64}$$

$$\zeta = 0. \tag{2.65}$$

Assuming $|\hat{c}^{00}| > |\hat{c}^{04}|$, only the three poles $\zeta = \pm\zeta_{k_1}$ and $\zeta = 0$ lay inside the curvature of the integral and thus results in a nonzero contribution (this assumption is not necessary to prove that the M2 constituent is equal to 0). Consequently, we have to calculate the residue for three poles in order to compute the integral in Eq. (2.61). In the following, we show that the M2 tidal component is equal to 0 by computing the residue for pole $\zeta = 0$ and using the symmetry of the residue for the other two poles:

$$\mathrm{Res}_{\zeta_{k_1}} = -\mathrm{Res}_{-\zeta_{k_1}} \qquad \text{for n is odd} \qquad \text{and} \tag{2.66}$$

$$\mathrm{Res}_{\zeta_{k_1}} = \mathrm{Res}_{-\zeta_{k_1}} \qquad \text{for n is even.} \tag{2.67}$$

2.D.1 Pole $\zeta = 0$

Calculating the residual for pole $\zeta = 0$ yields

$$\text{for M0,} \qquad \frac{\partial_z \hat{c}^{04*}}{\hat{c}^{04*}}, \tag{2.68}$$

$$\text{for M2,} \qquad 0, \qquad \text{and} \tag{2.69}$$

$$\text{for M4,} \qquad \Bigg\{ 2K_\nu (\partial_z \hat{c}^{04*})^2 + \beta \Bigg[(\hat{c}^{04*})^2 \partial_z (\hat{c}^{00} + \hat{c}^{00*}) - (\hat{c}^{00} + \hat{c}^{00*}) \hat{c}^{04*} \partial_z \hat{c}^{04*} \Bigg] \Bigg\} \frac{1}{2\beta (\hat{c}^{04*})^3}. \tag{2.70}$$

Consequently, the residue corresponding to the M2 constituent for pole $\zeta = 0$ is equal to 0.

2.D.2 Poles $\zeta = \pm\zeta_{k_1}$

We compute the residue for pole $\zeta = +\zeta_{k1}$:

$$\frac{1}{(m-1)!} \lim_{\zeta \to \zeta_{k_1}} \frac{d^{m-1}}{d\zeta^{m-1}} \left\{ \frac{1}{\zeta} \left[\frac{Z_1}{Z_3} \cdot \left(1 + 2\zeta^2 \frac{K_\nu}{\beta} \frac{Z_1}{Z_3^2} \right) \right] \right\}, \tag{2.71}$$

with

$$Z_1 = \partial_z \hat{c}^{04} (\zeta^2 - \zeta_{\partial_z k_1}^2)(\zeta^2 - \zeta_{\partial_z k_2}^2) \qquad \text{symmetric and} \tag{2.72}$$

$$Z_3 = \hat{c}^{04} (\zeta^2 - \zeta_{k_1}^2)(\zeta^2 - \zeta_{k_2}^2), \tag{2.73}$$

and $\zeta_{\partial_z k_{1/2}}$ being the roots of the numerator:

$$\zeta_{\partial_z k_{1/2}} = \Bigg\{ \Bigg[- (\partial_z \hat{c}^{00} + \partial_z \hat{c}^{00*}) \pm \sqrt{(\partial_z \hat{c}^{00} + \partial_z \hat{c}^{00*})^2 - 4(\partial_z \hat{c}^{04})(\partial_z \hat{c}^{04*})} \Bigg] \frac{1}{2\partial_z \hat{c}^{04}} \Bigg\}^{1/2}. \tag{2.74}$$

The order m of the pole $\zeta = \zeta_{k_1}$ in the first term in Eq. (2.71) is equal to 1. In the second term, the order equals 3. Consequently, the residues yield

$$\underbrace{\lim_{\zeta\to\zeta_{k_1}} \frac{\zeta^{-n-1}+\zeta^{+n-1}}{2} F_1}_{\text{first term}}$$
$$+ \frac{K^0_\nu}{2\beta} \lim_{\zeta\to\zeta_{k_1}} \Big\{ (n+1)(n)\zeta^{n-1}F_2 + 2(n+1)\zeta^n \partial_\zeta F_2 + \zeta^{n+1}\partial_{\zeta\zeta}F_2$$
$$\underbrace{+ (-n+1)(-n)\zeta^{-n-1}F_2 + 2(-n+1)\zeta^{-n}\partial_\zeta F_2 + \zeta^{-n+1}\partial_{\zeta\zeta}F_2 \Big\}}_{\text{second term}}, \tag{2.75}$$

with

$$Z_1 = (\partial_z \hat{c}^{04})(\zeta^2 - \zeta^2_{\partial_z k_1})(\zeta^2 - \zeta^2_{\partial_z k_2}) \qquad \text{symmetric,} \tag{2.76}$$
$$Z_2 = \hat{c}^{04}(\zeta + \zeta_{k1})(\zeta^2 - \zeta^2_{k_2}) \qquad \text{asymmetric,} \tag{2.77}$$
$$\partial_\zeta Z_1 = 2\zeta(\zeta^2 - \zeta^2_{\partial_z k_2})\partial_z \hat{c}^{04} + 2\zeta(\zeta^2 - \zeta^2_{\partial_z k_1})\partial_z \hat{c}^{04} \qquad \text{asymmetric,} \tag{2.78}$$
$$\partial_\zeta Z_2 = (\zeta^2 - \zeta^2_{k_2})\hat{c}^{04} + 2\zeta(\zeta + \zeta_{k_1})\hat{c}^{04} \qquad \text{symmetric,} \tag{2.79}$$
$$\partial_{\zeta\zeta} Z_1 = 2(\zeta^2 - \zeta^2_{\partial_z k_1})\partial_z \hat{c}^{04} + 2(\zeta^2 - \zeta^2_{\partial_z k_2})\partial_z \hat{c}^{04} + 8\zeta^2 \partial_z \hat{c}^{04} \qquad \text{symmetric,} \tag{2.80}$$
$$\partial_{\zeta\zeta} Z_2 = 4\zeta \hat{c}^{04} + 2(\zeta + \zeta_{k_1})\hat{c}^{04} \qquad \text{asymmetric,} \tag{2.81}$$
$$F_1 = \frac{Z_1}{Z_2} \qquad \text{asymmetric,} \tag{2.82}$$
$$F_2 = \frac{(Z_1)^2}{(Z_2)^3} \qquad \text{asymmetric,} \tag{2.83}$$
$$\partial_\zeta F_2 = 2\frac{Z_1 \partial_\zeta Z_1}{(Z_2)^3} - 3\frac{(Z_1)^2 \partial_\zeta Z_2}{(Z_2)^4} \qquad \text{symmetric,} \qquad \text{and} \tag{2.84}$$
$$\partial_{\zeta\zeta} F_2 = 2\frac{(\partial_\zeta Z_1)^2}{(Z_2)^3} + 2\frac{Z_1 \partial_{\zeta\zeta} Z_1}{(Z_2)^3} - 6\frac{Z_1(\partial_\zeta Z_1)(\partial_\zeta Z_2)}{(Z_2)^4} - 3\Big\{ 2\frac{Z_1(\partial_\zeta Z_1)\partial_\zeta Z_2}{(Z_2)^4} + \frac{(Z_1)^2 \partial_{\zeta\zeta} Z_2}{(Z_2)^4} - 4\frac{(Z_1)^2(\partial_\zeta Z_2)^2}{(Z_2)^5} \Big\} \qquad \text{asymmetric,} \tag{2.85}$$

in which we used that for pole $\zeta = -\zeta_{k_1}$ the factor $(\zeta + \zeta_{k1})$ is replaced by $(\zeta - \zeta_{k1})$ to determine the symmetry of Z_2. For n is odd (cf. M2, M6, M10, etc.), the solution in Eq. (2.75) is asymmetric and consequently the sum of residuals is equal to 0. For n is even (cf. M0, M4, etc.) the solution is symmetric. Consequently, adding the solution for the

pole $\zeta = 0$, the final solution yields

$$A^1 = 0 \qquad \text{and} \tag{2.86}$$

$$\begin{aligned} A^{0/2} = & \lim_{\zeta \to \zeta_{k_1}} \left(\zeta^{-n-1} + \zeta^{+n-1}\right) F_1 \\ & + \frac{K_\nu^0}{\beta} \lim_{\zeta \to \zeta_{k_1}} \Big\{ (n+1)(n)\zeta^{n-1} F_2 + 2(n+1)\zeta^n \partial_\zeta F_2 \\ & + \zeta^{n+1} \partial_{\zeta\zeta} F_2 + (-n+1)(-n)\zeta^{-n-1} F_2 \\ & + 2(-n+1)\zeta^{-n} \partial_\zeta F_2 + \zeta^{-n+1} \partial_{\zeta\zeta} F_2 \Big\} \\ & + \begin{cases} \frac{\partial_z \hat{c}^{04*}}{\hat{c}^{04*}}, \text{for M0 } (n=0), \\ \frac{2K_\nu (\partial_z \hat{c}^{04*})^2 + \beta \left[(\hat{c}^{04*})^2 \partial_z (\hat{c}^{00} + \hat{c}^{00*}) - (\hat{c}^{00} + \hat{c}^{00*}) \hat{c}^{04*} \partial_z \hat{c}^{04*} \right]}{2\beta (\hat{c}^{04*})^3}, \\ \qquad \text{for M4 } (n=2), \end{cases} \end{aligned} \tag{2.87}$$

which combined with the other trivial terms results in

$$\hat{w}_s^{10} = \beta \hat{c}^{10} - 2\tau A^0, \tag{2.88}$$

$$\hat{w}_s^{12} = \beta \hat{c}^{12}, \qquad \text{and} \tag{2.89}$$

$$\hat{w}_s^{14} = \beta \hat{c}^{14} - 2\tau A^2. \tag{2.90}$$

Appendix 2.E: phase requirements for land-inward sediment transport due to flocculation

In this section, we demonstrate the phase conditions for which the M2 contribution of flocculation (solid black line in Fig. 2.6a) results in land-inward net sediment transport:

$$\mathcal{T}_{\text{floc}}^{12} = \left\langle B \int_{-H}^{R} u^{02} c_{\text{floc}}^{12} dz \right\rangle > 0, \tag{2.91}$$

in which c_{floc}^{12} follows from Eq. (2.47):

$$\partial_t c_{\text{floc}}^1 - \partial_z (w_s^0 c_{\text{floc}}^1 + \partial_z K_\nu^0 c_{\text{floc}}^1) = \beta \partial_z (c^1 c^0). \tag{2.92}$$

We assume that the water column is fairly well mixed, such that the vertical phase differences between u^{02} and c^{12} and c^{04} are negligible. We define the phases in polar coordinates as

$$\hat{u}^{02} = |\hat{u}^{02}|, \tag{2.93}$$

$$\hat{c}^{12} = |\hat{c}^{12}| e^{i\psi}, \tag{2.94}$$

$$\hat{c}^{04} = |\hat{c}^{04}| e^{i\phi}, \qquad \text{and} \tag{2.95}$$

$$\hat{c}_{\text{floc}}^{12} = |\hat{c}_{\text{floc}}^{12}| e^{i\zeta}. \tag{2.96}$$

Using these definitions and Eqs. (2.1) and (2.4), we rewrite Eq. (2.91) as

$$\begin{aligned}\mathcal{T}^{12}_{\text{floc}} &= B \int_{-H}^{R} \frac{1}{4}\left(\hat{u}^{02}\hat{c}^{12*}_{\text{floc}} + \hat{u}^{02*}\hat{c}^{12}_{\text{floc}}\right) dz \\ &= \frac{B}{2}\int_{-H}^{R} |\hat{u}^{02}||\hat{c}^{12}_{\text{floc}}|\text{Re}\left[e^{i\zeta}\right] dz. \end{aligned} \tag{2.97}$$

So, $\mathcal{T}^{12}_{\text{floc}} > 0$ if $\text{Re}\left[e^{i\zeta}\right] > 0$, that is, if $-\pi/2 < \zeta < \pi/2$. In the following, we link ζ to ϕ and ψ by integrating Eq. (2.92):

$$\int_{-H}^{R} \partial_t c^{12}_{\text{floc}} dz = \beta\Delta(c^1 c^0), \tag{2.98}$$

in which we used the fact that only the right-hand side of Eq. (2.92) generates an M2 tidal signal and

$$\Delta(c^1 c^0) = (c^1 c^0)\Big|_{z=R} - (c^1 c^0)\Big|_{z=-H}, \tag{2.99}$$

which results in

$$\begin{aligned} i\omega_{M2}\int_{-H}^{R} \hat{c}^{12}_{\text{floc}} dz &= \beta\Delta\left(\hat{c}^{12}c^{00} + \frac{1}{2}\hat{c}^{12*}\hat{c}^{04}\right), \\ \implies \omega_{M2}\int_{-H}^{R} |\hat{c}^{12}_{\text{floc}}|e^{i\zeta} dz &= \beta\Delta\Big(|\hat{c}^{12}|c^{00}e^{i(\psi-\pi/2)} \\ &\quad + \frac{1}{2}|\hat{c}^{12}||\hat{c}^{04}|e^{i(\phi-\psi-\pi/2)}\Big), \end{aligned} \tag{2.100}$$

where we used Eqs. (2.2) and (2.4) and identified the M2 tidal phases in the right-hand side. We split the problem as

$$\begin{aligned} \omega_{M2}\int_{-H}^{R} |\hat{c}^{12}_{\text{floc},1}|e^{i\zeta_1} dz &= \beta\big|\underbrace{\Delta\left(|\hat{c}^{12}|c^{00}\right)}_{<0}\big|e^{i(\psi-\pi/2+\pi)}, \\ \implies \zeta_1 &= \psi + \pi/2 \qquad \text{and} \end{aligned} \tag{2.101}$$

$$\begin{aligned} \omega_{M2}\int_{-H}^{R} |\hat{c}^{12}_{\text{floc},2}|e^{i\zeta_2} dz &= \frac{\beta}{2}\big|\underbrace{\Delta\left(|\hat{c}^{12}||\hat{c}^{04}|\right)}_{<0}\big|e^{i(\phi-\psi-\pi/2+\pi)}, \\ \implies \zeta_2 &= \phi - \psi + \pi/2, \end{aligned} \tag{2.102}$$

in which we used the fact that a -1 factor results in a π phase. Therefore, as a strong requirement for land-inwards sediment transport due to the M2 contribution of flocculation, we require that

$$\begin{aligned} -\pi < \psi < 0 \qquad & \text{and} \\ -\pi < \phi - \psi < 0. \qquad & \end{aligned} \tag{2.103}$$

Likely, $|\hat{c}^{12}_{\text{floc},1}| \gg |\hat{c}^{12}_{\text{floc},2}|$, so the first requirement may be leading.

Bibliography

Alldredge, A. L., Granata, T. C., Gotschalk, C. C., and Dickey, T. D. (1990). The physical strength of marine snow and its implications for particle disaggregation in the ocean. *LIMNOLOGY AND OCEANOGRAPHY*, 35(7):1415–1428.

Alldredge, A. L., Passow, U., and Logan, B. E. (1993). The abundance and significance of a class of large, transparent organic particles in the ocean. *Deep Sea Research Part I: Oceanographic Research Papers*, 40(6):1131–1140.

Allen, G. P., Salomon, J. C., Bassoullet, P., Du Penhoat, Y., and de Grandpré, C. (1980). Effects of tides on mixing and suspended sediment transport in macrotidal estuaries. *Sedimentary Geology*, 26(1-3):69–90.

Bar-Zeev, E., Passow, U., Romero-Vargas Castrillón, S., and Elimelech, M. (2015). Transparent Exopolymer Particles: From Aquatic Environments and Engineered Systems to Membrane Biofouling. *Environmental Science & Technology*, 49(2):691–707.

Brion, N., Verbanck, M. A., Bauwens, W., Elskens, M., Chen, M., and Servais, P. (2015). Assessing the impacts of wastewater treatment implementation on the water quality of a small urban river over the past 40 years. *Environmental Science and Pollution Research*, 22(16):12720–12736.

Brouwer, R. L., Schramkowski, G. P., Dijkstra, Y. M., and Schuttelaars, H. M. (2018). Time Evolution of Estuarine Turbidity Maxima in Well-Mixed, Tidally Dominated Estuaries: The Role of Availability- and Erosion-Limited Conditions. *Journal of Physical Oceanography*, 48(8):1629–1650.

Burchard, H., Schuttelaars, H. M., and Ralston, D. K. (2018). Sediment Trapping in Estuaries. *Annual Review of Marine Science*, 10(1):371–395.

Chernetsky, A. S., Schuttelaars, H. M., and Talke, S. A. (2010). The effect of tidal asymmetry and temporal settling lag on sediment trapping in tidal estuaries. *Ocean Dynamics*, 60(5):1219–1241.

Cox, T. J. S., Maris, T., Van Engeland, T., Soetaert, K., and Meire, P. (2019). Critical transitions in suspended sediment dynamics in a temperate meso-tidal estuary. *Scientific Reports*, 9(1):12745.

Dijkstra, Y. M., Brouwer, R. L., Schuttelaars, H. M., and Schramkowski, G. P. (2017). The iFlow modelling framework v2.4: a modular idealized process-based model for flow and transport in estuaries. *Geoscientific Model Development*, 10(7):2691–2713.

Dijkstra, Y. M., Schuttelaars, H. M., and Schramkowski, G. P. (2019a). Can the Scheldt River Estuary become hyperturbid? A model analysis of suspended sediment concentrations and transport in response to channel deepening. *Ocean Dynamics*, 69(7):809–827.

Dijkstra, Y. M., Schuttelaars, H. M., Schramkowski, G. P., and Brouwer, R. L. (2019b). Modeling the Transition to High Sediment Concentrations as a Response to Channel Deepening in the Ems River Estuary. *Journal of Geophysical Research-Oceans*.

Ditschke, D. and Markofsky, M. (2008). A time-dependent flocculation model. *Sediment and Ecohydraulics*, 9:241–253.

Dyer, K. R. (1989). Sediment processes in estuaries: Future research requirements. *Journal of Geophysical Research*, 94(C10):14327–14339.

Edzwald, J. K., Upchurch, J. B., and O'Melia, C. R. (1974). Coagulation in estuaries. *Environmental Science & Technology*, 8(1):58–63.

Einstein, H. A. and Krone, R. B. (1962). Experiments to determine modes of cohesive sediment transport in salt water. *Journal of Geophysical Research*, 67(4):1451–1461.

Eisma, D., Kalf, J., and Veenhuis, M. (1980). The formation of small particles and aggregates in the rhine estuary. *Netherlands Journal of Sea Research*, 14(2):172–191.

Fettweis, M. and Baeye, M. (2015). Seasonal variation in concentration, size, and settling velocity of muddy marine flocs in the benthic boundary layer. *Journal of Geophysical Research-Oceans*, 120(8):5648–5667.

Fettweis, M., Baeye, M., Van der Zande, D., Van den Eynde, D., and Lee, B. J. (2014). Seasonality of floc strength in the southern North Sea. *Journal of Geophysical Research-Oceans*, 119(3):1911–1926.

Gourgue, O., Baeyens, W., Chen, M. S., de Brauwere, A., de Brye, B., Deleersnijder, E., Elskens, M., and Legat, V. (2013). A depth-averaged two-dimensional sediment transport model for environmental studies in the Scheldt Estuary and tidal river network. *Journal of Marine Systems*, 128:27–39.

Guo, C., He, Q., Guo, L., and Winterwerp, J. C. (2017). A study of in-situ sediment flocculation in the turbidity maxima of the Yangtze Estuary. *Estuarine, Coastal and Shelf Science*, 191:1–9.

Kranenburg, C. (1994). The Fractal Structure of Cohesive Sediment Aggregates. *Estuarine, Coastal and Shelf Science*, 39(5):451–460.

Kuprenas, R., Tran, D., and Strom, K. (2018). A Shear-Limited Flocculation Model for Dynamically Predicting Average Floc Size. *Journal of Geophysical Research: Oceans*, 123(9):6736–6752.

Lai, H., Fang, H., Huang, L., He, G., and Reible, D. (2018). A review on sediment bioflocculation: Dynamics, influencing factors and modeling. *Science of The Total Environment*, 642:1184–1200.

Maggi, F. (2009). Biological flocculation of suspended particles in nutrient-rich aqueous ecosystems. *Journal of Hydrology*, 376(1-2):116–125.

Manning, A. J., Martens, C., de Mulder, T., Vanlede, J., Winterwerp, J. C., Ganderton, P., and Graham, G. W. (2007). Mud floc observations in the turbidity maximum zone of the scheldt estuary during neap tides. *Journal of Coastal Research*, Special Issue 50 : THE INTERNATIONAL COASTAL SYMPOSIUM (ICS 2007):832–836.

Maris, T. and Meire, P. (2016). Omes rapport 2015. Onderzoek naar de gevolgen van het Sigmaplan, baggeractiviteiten en havenuitbreiding in de Zeeschelde op het milieu. Technical report, University of Antwerp, Antwerp, Belgium.

Meire, P., Ysebaert, T., Van Damme, S., Van den Bergh, E., Maris, T., and Struyf, E. (2005). The Scheldt estuary: a description of a changing ecosystem. *Hydrobiologia*, 540(1-3):1–11.

Mietta, F., Chassagne, C., Manning, A. J., and Winterwerp, J. C. (2009). Influence of shear rate, organic matter content, pH and salinity on mud flocculation. *Ocean Dynamics*, 59(5):751–763.

Pejrup, M. and Mikkelsen, O. A. (2010). Factors controlling the field settling velocity of cohesive sediment in estuaries. *Estuarine, Coastal and Shelf Science*, 87(2):177–185.

Peters, J. J. (1972). Transports de sédiments dans l'estuaire de l'Escaut. Technical report, Flanders Hydraulics Research.

Schwarz, C., Cox, T., Van Engeland, T., Van Oevelen, D., Van Belzen, J., van de Koppel, J., Soetaert, K., Bouma, T. J., Meire, P., and Temmerman, S. (2017). Field estimates of floc dynamics and settling velocities in a tidal creek with significant along-channel gradients in velocity and SPM. *Estuarine, Coastal and Shelf Science*, 197:221–235.

Shen, X., Lee, B. J., Fettweis, M., and Toorman, E. A. (2018). A tri-modal flocculation model coupled with TELEMAC for estuarine muds both in the laboratory and in the field. *Water Research*, 145:473–486.

Sherwood, C. R., Aretxabaleta, A. L., Harris, C. K., Rinehimer, J. P., Verney, R., and Ferré, B. (2018). Cohesive and mixed sediment in the Regional Ocean Modeling System (ROMS v3.6) implemented in the Coupled Ocean-Atmosphere-Wave-Sediment Transport Modeling System (COAWST r1234). *Geoscientific Model Development*, 11(5):1849–1871.

Smoluchowski, M. R. (1918). Versuch einer mathematischen Theorie der Koagulationskinetik kolloider Lösungen. *Zeitschrift für Physikalische Chemie*, 92U(1):129–168.

Tran, D., Kuprenas, R., and Strom, K. (2018). How do changes in suspended sediment concentration alone influence the size of mud flocs under steady turbulent shearing? *Continental Shelf Research*, 158:1–14.

Uncles, R. J., Stephens, J. A., and Harris, C. (2006). Runoff and tidal influences on the estuarine turbidity maximum of a highly turbid system: The upper Humber and Ouse Estuary, UK. *Marine Geology*, 235(1-4 SPEC. ISS.):213–228.

van Leussen, W. (1994). *Estuarine macroflocs and their role in fine-grained sediment transport.* PhD thesis, Utrecht University, Utrecht.

Vandenbruwaene, W., Vanlede, J., Plancke, Y., Verwaest, T., and Mostaert, F. (2016). Slibbalans Zeeschelde: deelrapport 4. Historische evolutie SPM. versie 6.0. WL Reports 00_029_8, Waterbouwkundig Laboratorium/Antea Group, Antwerpen.

Verney, R., Lafite, R., and Brun-Cottan, J. C. (2009). Flocculation potential of estuarine particles: The importance of environmental factors and of the spatial and seasonal variability of suspended particulate matter. *Estuaries and Coasts*, 32(4):678–693.

Verney, R., Lafite, R., Brun-Cottan, J. C., and Le Hir, P. (2011). Behaviour of a floc population during a tidal cycle: Laboratory experiments and numerical modelling. *Continental Shelf Research*, 31(10):S64–S83.

Warner, J. C., Geyer, W. R., and Lerczak, J. A. (2005). Numerical modeling of an estuary: A comprehensive skill assessment. *Journal of Geophysical Research: Oceans*, 110(C5):1–13.

Waterinfo.be (cited 2019). Measurements and predictions of Waterinfo.be [data]. [Available online at `https://www.waterinfo.be/`].

Winterwerp, J. C. (2002). On the flocculation and settling velocity of estuarine mud. *Continental Shelf Research*, 22(9):1339–1360.

Winterwerp, J. C. (2011). Fine sediment transport by tidal asymmetry in the high-concentrated Ems River: indications for a regime shift in response to channel deepening. *Ocean Dynamics*, 61(2-3):203–215.

Winterwerp, J. C. and van Kesteren, W. G. M. (2004). *Introduction to the physics of cohesive sediment in the marine environment*, volume 56. Elsevier Science, Amsterdam, The Netherlands, 1st edition.

Xu, C. and Dong, P. (2017). A Dynamic Model for Coastal Mud Flocs with Distributed Fractal Dimension. *Journal of Coastal Research*, 33(1):218–225.

Xu, F., Wang, D.-P., and Riemer, N. (2010). An idealized model study of flocculation on sediment trapping in an estuarine turbidity maximum. *Continental Shelf Research*, 30(12):1314–1323.

Zhu, Q., Wang, Z., Yang, S. L., and van Prooijen, B. (2017). *Sediment dynamics on intertidal mudflats: A study based on in situ measurements and numerical modelling.* PhD thesis, Delft University of Technology, Delft.

Chapter 3

The impact of temporal variability in phytoplankton on SPM dynamics

Horemans, D. M. L., Dijkstra, Y. M., Schuttelaars, H. M., Sabbe, K., Vyverman, W., Meire, P., & Cox, T. J. S. (2020). Seasonal variations in flocculation and erosion affecting the large-scale suspended sediment distribution in the Scheldt estuary: the importance of biotic effects. *Journal of Geophysical Research: Oceans*, 126, e2020JC016805. https://doi.org/10.1029/2020JC016805.

Abstract

Many estuaries exhibit seasonality in the estuary-scale distribution of suspended particulate matter (SPM). This SPM distribution depends on various factors, including freshwater discharge, salinity intrusion, erodibility, and the ability of cohesive SPM to flocculate into larger aggregates. Various authors indicate that biotic factors, such as the presence of algae and their excretion of sticky transparent exopolymer particles (TEP), affect the flocculation and erosion processes. Consequently, seasonality in these biotic factors may play a role in the observed seasonality in SPM. Whereas the impact of abiotic factors on seasonality in SPM is well studied, the relative contribution of biotically induced seasonality is largely unknown. In this study, we employ two approaches to assess the aggregated importance of biotically induced seasonality in flocculation and erosion on seasonality in SPM in the Scheldt estuary. In the first approach, we focus on seasonality of in situ observations in the Scheldt estuary of turbidity, floc size, Chlorophyll-a, and TEP, showing that the abiotic parameters show seasonality, while seasonality in TEP is ambiguous. The second approach concerns a reverse engineering method to calibrate biotically affected parameters of a coupled sediment transport-flocculation model to turbidity observations, allowing us to compare the modeled SPM concentrations to the observations. Driven by seasonality in freshwater discharge, the model captures both the observed seasonality in SPM without requiring biotically induced seasonality in flocculation and erosion, which is supported by the absence of seasonality in TEP.

3.1 Introduction

The suspended particulate matter (SPM) concentrations in estuaries often show regions in which SPM accumulates, resulting in zones with locally elevated SPM concentrations. These regions are called estuarine turbidity maxima (ETM), of which both the magnitude and location can show a significant seasonality. Such seasonality was observed in, for example, the Scheldt estuary (Cox et al., 2019), the Chesapeake Bay (Stanford et al., 2001), the Weser (Kappenberg and Grabemann, 2001) and the Hudson River estuary (Ralston et al., 2012). This seasonality in ETM is driven by seasonality in factors affecting transport of SPM, such as freshwater discharge (Allen et al., 1980; Uncles et al., 2006), salinity (MacCready and Geyer, 2010), erosion properties of the sediment bed (Stal, 2010), and settling velocity (Kranenburg, 1994; Winterwerp and van Kesteren, 2004; Verney et al., 2009; Fettweis et al., 2014). The latter two are related to both abiotic seasonal variations, such as variations in turbulence, salinity, and SPM (Dyer, 1989; van Leussen, 1994; Lai et al., 2018) and biotic variations (Frostick and McCave, 1979; Alldredge et al., 1993; Passow et al., 2001).

Biotic seasonality may impact the erosion properties of the sediment bed in multiple ways. On the one hand, various authors found that algal activity, which typically peaks in spring and summer, often stabilizes the sediment bed (Frostick and McCave, 1979) and induces the formation of bedforms (Malarkey et al., 2015) by, for example, the excretion of

extracellular polymeric substances (EPS), of which sticky transparent exopolymer particles (TEP) are a particulate form (Passow, 2002), and which bind the sediment together (Stal, 2010). On the other hand, the subsequent grazing of the algae by bioturbatory macroheterotrophs may generate an increase in erodibility (Paterson and Black, 1999).

Besides erosion properties of the sediment bed, biotic factors may also impact flocculation, which is defined as the aggregation and break-up of cohesive SPM, resulting in seasonal variations of the settling velocity of SPM flocs. Biotic characteristics, such as organic content, directly influence the differential density and structure of flocs (Kranenburg, 1994; van Leussen, 1994; Fall et al., 2021). Furthermore, organic content impacts, for example, the floc strength and collision efficiency (Winterwerp and van Kesteren, 2004), averaged floc size (Mietta et al., 2009), and floc break-up (Alldredge et al., 1990). Finally, in situ observations show a correlation between Chlorophyll-a (Chl-a) and flocculation efficiency (Verney et al., 2009), and TEP and floc strength (Fettweis et al., 2014).

These biotic seasonal variations in the settling velocity and erosion properties of the sediment bed are hypothesized to affect seasonality in ETM characteristics in estuaries. However, this hypothesis has not been systematically investigated. Therefore, in this contribution, we focus on quantifying the importance of such biotic seasonal variations to the seasonality in ETM, applied to the Scheldt estuary (Belgium and the Netherlands).

The Scheldt estuary is a particularly good candidate to study the influence of biotic seasonal variations on the seasonality in ETM for two reasons. Firstly, the settling velocity and erosion properties have been found to be important to the ETM formation (Brouwer et al., 2018; Horemans et al., 2020) and the corresponding floc size dynamics have been related to biotic activity (Wartel and Francken, 1998; Chen et al., 2005, 2018). Secondly, a recent study by Cox et al. (2019) reported a change in the seasonal ETM patterns and suggested that a change in biotically induced flocculation dynamics may be responsible for this change.

Assessing the relative importance of the abiotic and biotic factors that impact seasonality in SPM is challenging because of their strong interdependence. In addition, while reasonably accurate models exist to parameterize the effect of abiotic flocculation and erosion, explicit parameterizations of biotic effects relating, for example, Chl-a and TEP to flocculation and erodibility, rely on many assumptions (see Lai et al. (2018) for a recent review). This makes it difficult to dynamically solve the impact of biota on the large-scale ETM dynamics through flocculation and erosion, using explicitly defined bio-physical-chemical interactions.

In view of this, we employ a reverse engineering approach, combined with a detailed analysis of observations to assess the influence of biotically induced seasonality in flocculation and erosion on the large-scale SPM dynamics. Concerning the observations, we quantitatively study the seasonality in observed turbidity (cf. SPM), floc size, Chl-a, and TEP. This provides information on the seasonality of SPM dynamics, flocculation, and biota. Taking a reverse engineering model approach, following Chen et al. (2018), the model does not rely on explicit model parameterizations for biotic flocculation and erosion. Instead, the accumulated biotic impact is accounted for parametrically, using two

empirical parameters; one in the flocculation model of Horemans et al. (2020) and one in the erosion model (Partheniades, 1965; Kandiah, 1974; Dijkstra et al., 2019). Abiotic seasonal variations, including variations of the river discharge, salinity, and abiotic effects on flocculation and erosion are explicitely taken into account. The two biotically affected parameters are calibrated to long-term SPM observations of both summer and winter conditions in the Scheldt estuary. We hypothesize that, if a seasonality in biological factors were to have a significant impact on the large-scale SPM distribution, we would obtain a significantly different value of these biotically affected parameters to represent summer and winter conditions in the Scheldt estuary.

3.2 Material and methods

In this section, we first discuss some of the characteristics of the Scheldt estuary. Next, the measurement methods used to obtain the in situ observations are introduced and the model approach is presented.

3.2.1 Study area

The Scheldt estuary is an approximately 160 km long, funnel-shaped estuary (Fig. 3.1). It flows through Belgium into the North Sea near Vlissingen (Netherlands). Because of its relatively small freshwater discharge, the Scheldt estuary can be considered a tide-dominated and well-mixed estuary (Meire et al., 2005). The total time-averaged freshwater discharge Q over the years 2015-2018 equals 40 $m^3\ s^{-1}$ and 174 $m^3\ s^{-1}$ in summer (Jun.-Aug.) and winter (Jan.-Mar.), respectively (Waterinfo.be, 2019). The main tributaries of the Scheldt estuary are the Rupel and the Dender. The Upper Sea Scheldt boundary (i.e., the upstream boundary of the Scheldt estuary), the Rupel, and the Dender are responsible for 16.4, 77.2, and 6.4 % of the total river discharge in summer and 35.4, 53.1, and 11.5 % in winter, respectively.

The maintenance of the navigation channel to the port of Antwerp (first four red dots from the Dutch-Belgian border in Fig. 3.1) requires intensive dredging activities. To minimize the risk of flooding, the dredged material is dumped back into the Scheldt estuary, which comes with significantly higher SPM loads (10^6 ton $year^{-1}$) than the fluvial input (Dijkstra et al., 2019). At the main dumping locations at km 73 and 78 from the mouth, the time-averaged dumped material between 2001-2015 corresponds to a high SPM input of approximately 60 and 100 kg s^{-1}, respectively. Consequently, these dumping activities impact the SPM concentration locally, which was confirmed by a multivariate regression analysis of SPM observations between 1996-2016. This analysis showed that the SPM concentrations at the dumping sites are dominantly correlated to dumping activities (IMDC, 2016). The yearly fluvial input of SPM at the upstream boundary and tributaries is of the order of 10^4-10^5 ton $year^{-1}$ and is assumed to scale linearly with the freshwater discharge (Plancke et al., 2017; Dijkstra et al., 2019).

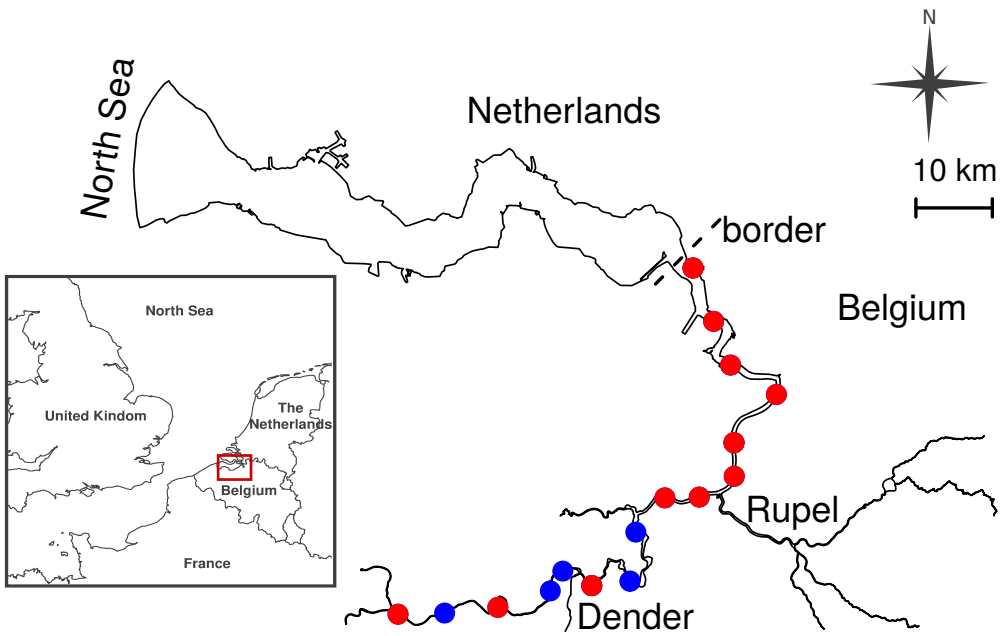

Figure 3.1: The Scheldt estuary and its two main tributaries (Rupel and Dender). The dots represent the locations where monthly and biweekly turbidity and floc size profiles were measured in the frame of the OMES (Dutch: "Onderzoek Milieu Effecten Sigmaplan") environmental monitoring program. The transparent exopolymer particles (TEP) concentration was only measured at 11 instead of the 16 stations, depicted in red.

3.2.2 In situ observations

The Belgian part of the Scheldt estuary has been monitored by the long-term OMES (Dutch: "Onderzoek Milieu Effecten Sigmaplan") monitoring campaign (Maris and Meire, 2017). Within this campaign, various variables, including turbidity, SPM, salinity, primary particle size, floc size, Chl-a, and TEP concentration, have been measured biweekly or monthly and independently of the tidal phase and spring-neap tide at 16 fixed stations (see Fig. 3.1). In the following, we discuss the measurement methods to obtain the observations of the four variables we focus on: turbidity (Maris et al., 2021b), floc size (Maris et al., 2021a), Chl-a (Maris and Meire, 2021), and TEP (Vyverman et al., 2021).

Turbidity depth profiles were measured over the years 2015-2018 using an optical backscatter point sensor (OBS) of RBR type XR420 CTD+. To translate turbidity to SPM concentration, we simultaneously collected two SPM samples at approximately the water surface and half the water depth and applied a linear data fit (Horemans et al., 2020). The observations cover 18 and 14 campaigns in summer (Jun.-Aug.) and winter (Jan.-Mar.), respectively, resulting in 18 and 14 SPM profiles at each of the 16 locations.

From Sep. 2017 until Jan. 2019, floc size profiles were measured mainly in the upper half of the water column, simultaneously with the turbidity profiles. Floc size was measured using an optical laser diffraction instrument, a Sequoia laser in situ scattering and transmissometry (LISST) 200x instrument. The LISST 200x instrument measures the floc size volume distribution for 36, nonequidistant size classes with a floc size ranging between 1-500 μm. This particle size distribution was used to determine the geometric averaged floc size following the averaging method of Sequoia Scientific (2019) to correct for the nonequidistant size classes. Because the estimated floc size is highly sensitive to the averaging method, we also use two additional averaging methods in Appendix 3.A.

Simultaneously with measuring the turbidity and floc size profiles, bucket samples at the water surface were taken to estimate the Chl-a and TEP concentration. The TEP measurements only started in 2018. We estimated the Chl-a concentration, following the spectrophotometric method described in Rice et al. (2017) that corrects for turbidity, Chlorophyll-b, Chlorophyll-c, and Pheophytin pigments. We used 50 ml water samples, a 1 cm pathway cuvette, and a Shimadzu UV-1700 spectrophotometer. The detection threshold of the method is approximately 10 μg L^{-1}. When Chl-a values are below this threshold value, they are put to 10 μg L^{-1}. The total number of observed Chl-a concentrations per station equals 24 in summer and ranges from 11 upto 13 in winter, depending on the station. TEP concentrations were estimated according to the colorimetric method described in Claquin et al. (2008), adapted from the original method described in Passow and Alldredge (1995). TEP concentrations were only measured once a month at 11 stations (see Fig. 3.1, red dots), resulting in 66 estimates in both summer and winter.

3.2.3 Model and model experiments

iFlow model The model used is the process-based, width-averaged, idealized model called 'iFlow' that solves for water motion and SPM trapping in tide-dominated estuaries using the width-averaged shallow water and SPM mass balance equations in equilibrium condition (Dijkstra et al., 2017), including the effects of flocculation (Winterwerp, 2002; Horemans et al., 2020). The width and bathymetry of the estuary are approximated by smooth profiles, focusing on the estuary-scale hydro- and SPM dynamics only. The model resolves the tidal and subtidal water motion and SPM concentration using a scaling and perturbation approach. This approach drastically reduces computation time, allowing us to carry out an extensive sensitivity analysis. Moreover, it simplifies the interpretation of the results as it allows us to study physical processes separately.

The water motion is forced at the mouth by a tidal signal and at the Upper Sea Scheldt boundary and two main tributaries by a constant water inflow that depends on the season. SPM dynamics are forced by a constant concentration of SPM at the mouth and an inflow of SPM at the Upper Sea Scheldt boundary, which is obtained from observations and equals the product of the subtidal SPM concentration and freshwater discharge. Although clearly detectable in the SPM observations at the dumping locations, we do not include dumping of dredged material because it acts locally on a much smaller time scale ($\sim$ hours) and does not show seasonality. Therefore, it is out of the scope of this study, which focuses on large-scale SPM dynamics on the seasonal scale. Moreover, we are interested in biotically affected, and not anthropogenically induced, erosion and flocculation. The longitudinal salinity profile is prescribed as a depth- and tide-independent sigmoid profile (Warner et al., 2005) that depends on the season (see Appendix 3.B). This assumption is reasonable as the Scheldt is a well-mixed estuary in all seasons. Erosion of SPM is assumed to scale with the magnitude of the bed shear stress. The biotic impact on erosion is implicitly included in the corresponding scaling factor called the erosion parameter M. This parameter is an intrinsic property of the sediment bed, including biotic effects, and determines the erosion flux E for a fixed bed shear stress τ_b and erodibility f:

$$E = M|\tau_b|f(a) \tag{3.1}$$

where a is the availability of easily erodible fine sediment and M is the erosion parameter.

The flocculation model describes the spatial and temporal evolution of the settling velocity of a single class of flocs. The effects of abiotic conditions (e.g., salinity, SPM concentration, and turbulence) are contained explicitly, whereas biotic effects (such as that of TEP) are implicitly included in the flocculation model. The parameter controlling the importance of biotic effects is denoted by λ, and is defined as the ratio of the minimal floc aggregation $k_A^{\min}$ and floc break-up parameter k_B. These two parameters characterize the flocculation properties given a fixed SPM concentration, salinity S, and shear rate G. For the model implementation of the shear rate G in summer and winter, we refer the reader to Appendix 3.C. A careful scaling and perturbation analysis shows that λ impacts

the settling velocity w_s (upto fist order) (Horemans et al., 2020) as

$$w_s = \frac{1}{18\mu f_s} \frac{\rho_s - \rho_w}{\rho_s} \frac{g}{\sqrt{G}} \underbrace{\frac{k_A^{\min}}{k_B}}_{\lambda} f^{\text{sal}}(S) \cdot c + w_{s,\min}, \tag{3.2}$$

in which we assumed a fractal dimension $n_f = 2$ (see Appendix 3.D for $n_f \neq 2$), spherical flocs, and that the floc Reynolds Number $\text{Re}_f = w_s D_f / \nu \ll 1$, where ν is the kinematic viscosity of water, and in which $w_{s,\min}$ is the settling velocity of the primary particles, μ is the dynamic viscosity of water, f_s is the shape factor of the flocs, ρ_s is the density of the primary particles, ρ_w is the density of water, g is the gravitational acceleration, c is the SPM concentration, and $f^{\text{sal}}(S)$ describes salinity driven flocculation by increasing the colloid stability for increasing salinity (Edzwald et al., 1974; Horemans et al., 2020). The impact of salinity driven flocculation is relatively low, which agrees with Einstein and Krone (1962), who showed that system-wide variations in salinity have only a minor influence on the bond strength. Salinity may also impact flocculation indirectly through, for example, its impact on TEP production (Alldredge et al., 1993; Bar-Zeev et al., 2015). This biotic impact is parametrically included in λ.

Reverse engineering model approach To detect a biotically induced seasonality that impacts the seasonality in estuary-scale SPM dynamics, we follow Chen et al. (2018) by applying a reverse engineering model approach. This means that the biotically induced parameters λ and M are calibrated to observed SPM concentrations in summer and winter and that we statistically evaluate if the calibrated λ and M are the same in both seasons. We vary λ and M within a realistic range of values. The range in λ is 36-121 10^{-6} $\text{s}^{-1/2}$ m^2 and in M is 0.1-6 10^{-3} s m^{-1}, which is based on scaling (Horemans et al., 2020) and observations (Zhu et al., 2017), respectively.

As a first step in the reverse engineering approach, we average the observed SPM concentrations of the various measuring campaigns at each depth. We assume that this averaged value approximates the residual SPM concentration similar to Dijkstra et al. (2019), Cox et al. (2019), and Horemans et al. (2020). This assumption is reasonable when the number of estimates is sufficiently large ($\gtrsim 10$), so by averaging the periodic temporal variability of the SPM concentration vanishes (Horemans et al., 2020). Here, we assume that the campaigns are homogeneously distributed within the spring-neap cycle and tidal phase, which was shown to be valid for the SPM sampling within the OMES framework between 1995 and 2015 (after 2015, the setup of the campaigns has not changed) (Vandenbruwaene et al., 2016). Moreover, we assume that each year between 2015-2018 corresponds to a similar SPM distribution on the estuary scale. To comply with the latter requirement, we leave out the year 2016 because of its exceptionally high amount of rainfall. Next, to compare the modeled residual SPM concentration to the time-averaged observed SPM concentration, we interpolate the time-averaged SPM observations to a grid with 16 cells in the along-channel direction (corresponding to the observation stations) and 50 cells in the vertical direction (independent of the water depth). The average SPM concentration in each cell is thus based on the average of 18 and 14 observations in summer and winter, respectively. In the remainder of this study, we do not consider the SPM concentration in the vertical cells closest to the sediment bed

and water surface, as there are insufficient measurements there (due to distortions caused by air bubbles and high turbidity at the water surface and sediment bed, respectively). As a second step, we quantify the accuracy of the modeled SPM concentration compared to the observations using a cost function that is based on a statistical two-tailed t test. The cost function varies between 0 (*perfect match between modeled SPM concentration and observations*) and 1 (*complete mismatch between modeled SPM concentration and observations*). We refer the reader to Horemans et al. (2020) for a detailed description of the cost function. We exclude the SPM observations at the dumping locations (total of two stations) because here we expect high variability in SPM due to anthropogenic dumping of sediment, which is out of the scope of this study and not included in the model (see Section 3.2.3).

Finally, uncertainty in the SPM observations results in uncertainty in the optimal (cf. lowest cost function value) (λ,M) pairs. To quantify this uncertainty, we assume that the average SPM concentration in summer and winter is normally distributed with mean value equal to the mean of the OMES observations and standard deviation equal to the standard deviation in the OMES observations divided by the square root of the number of observations (i.e., 18 and 14 in summer and winter, respectively). To equate this to a probability distribution for the optimal (λ, M) pair, we randomly sample 500 averaged SPM concentrations from this normal distribution. Because the SPM concentrations in the vertical direction are not independent, we require that the relative deviation from the mean is equal at every depth at a given station, thus keeping the shape of the vertical time-averaged SPM profile fixed. Next, we calibrate λ and M for each sample. The resulting calibration is used to compute the standard deviation $\sigma_{\lambda,M}$ of the 500 (λ,M) pairs for summer and winter. Note that we do not assume that λ and M are necessarily normally distributed. Finally, to quantitatively compare the optimal (λ,M) pairs in summer and winter conditions, we use this standard deviation $\sigma_{\lambda,M}$ to compute the difference of the optimal λ and M values in summer and winter conditions, relative to the corresponding standard deviation:

$$\Delta_\lambda = \frac{|\lambda^{\text{summer}} - \lambda^{\text{winter}}|}{\sqrt{(\sigma_\lambda^{\text{summer}})^2 + (\sigma_\lambda^{\text{winter}})^2}} \quad \text{and} \quad \Delta_M = \frac{|M^{\text{summer}} - M^{\text{winter}}|}{\sqrt{(\sigma_M^{\text{summer}})^2 + (\sigma_M^{\text{winter}})^2}}. \tag{3.3}$$

If $\Delta_{\lambda,M} < 1$, the average difference between summer and winter is less than one standard deviation and we will conclude that the difference of λ or M in winter and summer conditions is within the uncertainty of the SPM observations. The model parameter values for both the summer and winter conditions in the Scheldt estuary are given in Table 3.1. These values are either based on observations or calibration. Previous work indicated that the average summer discharge is representative, while the representative winter discharge is slightly above the average of 174 $\text{m}^3\ \text{s}^{-1}$ to correct for the large variability in discharges during winter (Horemans et al., 2020). The parameters corresponding to the depth- and tide-independent salinity profile (i.e., x_c and x_L) were fitted to salinity observations (see Appendix 3.B). The system-averaged primary particle size D_p was estimated using observations (see Appendix 3.E). If not mentioned explicitly, other used parameter values are presented in Horemans et al. (2020). For completeness, we repeated these parameter values in Table 3.F.1.

To test the robustness of the model, we apply a sensitivity analysis of two crucial

parameters which are assumed to be fixed in the model: the primary particle size D_p and fractal dimension n_f. To apply a sensitivity analysis to the latter parameter, we have generalized the results presented in Horemans et al. (2020) for $n_f \neq 2$ (see Apppendix 3.D). Based on the experiments presented in Appendix 3.E and the literature (Winterwerp and van Kesteren, 2004), we vary D_p and n_f between 4-25 μm and 1.7-3, respectively.

3.3 Results

This section first introduces the seasonality of the in situ observations of SPM, floc size, Chl-a, and TEP concentrations in the Scheldt estuary. Next, we show the results of our model experiments, focusing on the seasonality in biotically affected calibration parameters λ and M and modeled SPM concentration. Finally, we present the sensitivity analysis of the modeled SPM concentration to D_p and n_f.

3.3.1 Seasonality in the in situ observations

3.3.1.1 Seasonality in SPM

Figure 3.2 shows the observed time-averaged SPM concentration in summer and winter. Both in summer and winter, the concentrations range upto approximately 300 mg L^{-1} and typically increase with depth. In summer (Fig. 3.2a), two ETM are observed, located near km 80 (depicted by (I)) and 120 (depicted by (II)). The ETM have a length of approximately 10 and 30 km, respectively. The ETM near km 80 is potentially due to anthropogenic dumping activities in this region (depicted by the vertical dashed lines), as mentioned above. In winter (Fig. 3.2b), the ETM at km 80 is also present, while the ETM near km 120 moves downstream, and shows significantly lower SPM concentrations (depicted by (II)). Moreover, we detect an additional ETM near km 60 (depicted by (III)). We thus conclude that the SPM distribution in the Scheldt estuary shows strong seasonality, which complies with the results of Cox et al. (2019) and has been observed in many other estuaries (see Burchard et al. (2018) for a recent review).

3.3.1.2 Seasonality in floc size

Figure 3.3 shows the observed depth- and time-averaged floc size measured in summer and winter 2018. The error bars depict the standard error of the depth-averages corresponding to the various campaigns. In summer, we have an approximately constant depth-averaged floc size in the longitudinal direction. The floc sizes are in the order of 100 μm. In winter, the floc sizes decrease in the Upper Sea Scheldt beyond km 120 and are statistically smaller compared to the floc sizes in summer (one-tailed t test, p-value $< 10^{-4}$). The averaged floc sizes in the Upper Sea Scheldt beyond km 120 are 115 and 77 μm in summer

Table 3.1: Parameter values used in our model study in the Scheldt estuary in summer and winter conditions.

Variable	Definition	Value
	Hydrodynamics	
Q^{summer}	Total river discharge in summer (calibrated)	40 m^3 s^{-1}
Q^{winter}	Total river discharge in winter (calibrated)	233 m^3 s^{-1}
	Sediment	
$c_{\text{upper Sea Scheldt}}$	Subtidal SPM concentration at the Upper Sea Scheldt boundary (source)	0.035 kg m^{-3}
M^{summer}	Erosion parameter in summer (calibrated)	2.7×10^{-3} s m^{-1}
M^{winter}	Erosion parameter in winter (calibrated)	3.0×10^{-3} s m^{-1}
	Turbulence	
σ_ρ	Prandtl Schmidt number	0.5
s_{f_0}	Bed roughness coefficient (calibrated)	4.22 mm s^{-1}
	Flocculation	
$k_A^{\text{min.}}$	Nondimensional minimal aggregation coefficient	0.29
f_s	Shape factor	$\pi/6$
n_f	Fractal dimension of flocs	2
D_p	Diameter primary mud particles (source)	14×10^{-6} m
ρ_s	Density of SPM primary particles	2650 kg m^{-3}
ρ_w	Reference density of water	1000 kg m^{-3}
λ^{summer}	Ratio of minimal aggregation and floc break-up parameter in summer (calibrated)	72.5×10^{-6} $s^{-1/2}$ m^2
λ^{winter}	Ratio of minimal aggregation and floc break-up parameter in winter (calibrated)	65.9×10^{-6} $s^{-1/2}$ m^2
	Salinity	
s_{sea}	Salinity boundary condition at the mouth	28.9 psu
$x_c^{\text{sal, summer}}$	Calibration parameter in sigmoid salinity distribution in summer	51.9 km
$x_L^{\text{sal, summer}}$	Calibration parameter in sigmoid salinity distribution in summer	31.2 km
$x_c^{\text{sal, winter}}$	Calibration parameter in sigmoid salinity distribution in winter	38.3 km
$x_L^{\text{sal, winter}}$	Calibration parameter in sigmoid salinity distribution in winter	24.8 km

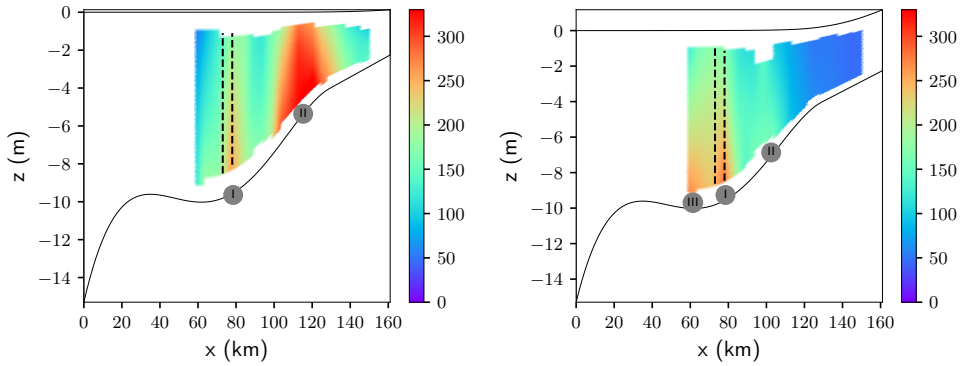

(a) Observations of the SPM concentration (mg L^{-1}) in summer

(b) Observations of the SPM concentration (mg L^{-1}) in winter

Figure 3.2: Measured long-term time-averaged suspended particulate matter (SPM) concentration (mg L^{-1}) over the years 2015-2018 in (a) summer, showing two ETM at locations (I) and (II), and (b) winter showing three ETM at locations (I), (II), and (III). The vertical dashed lines depict the dumping locations.

and winter, respectively. We thus conclude that, on the estuary scale (we observe a local anomaly near km 60 and km 80), the floc sizes only show seasonality in the upstream part of the Scheldt estuary (> 120 km). This is also valid using other averaging methods (see Appendix 3.A).

3.3.1.3 Seasonality in Chl-a and TEP

The measured time averages of the observations of Chl-a and TEP concentrations in summer and winter are shown in Fig. 3.4. The error bars represent the standard error of the mean corresponding to the concentrations of the various campaigns. The Chl-a observations (Fig. 3.4a) show a strong seasonality in the Upper Sea Scheldt (> 100 km), where the Chl-a concentration in summer is an order of magnitude larger than in winter. In contrast, although the TEP observations (Fig. 3.4b) show local seasonality at km 58, 121, and 138, they do not show a significant system-wide seasonality in the Upper Sea Scheldt (one-tailed t test, p-value > 0.38). The error bars corresponding to the TEP measurements are relatively large, especially in the Lower Sea Scheldt (< 100 km). This is due to the relatively small number of estimates and the large temporal variability in TEP, a variability also observed in other estuarine and marine systems, such as the Neuse River Estuary (Wetz et al., 2009), the Pearl River estuary (Sun et al., 2012), and the Chesapeake bay (Malpezzi et al., 2013). What is most important within the scope of this study is that the Chl-a observations show seasonality, whereas the TEP observations do not.

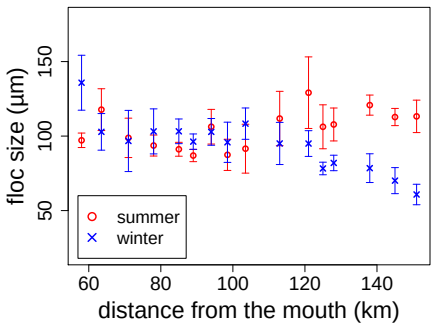

Figure 3.3: Measured time- and depth-averaged floc size in summer (red) and winter (blue). The error bars depict the standard error of the estimates corresponding to the various campaigns.

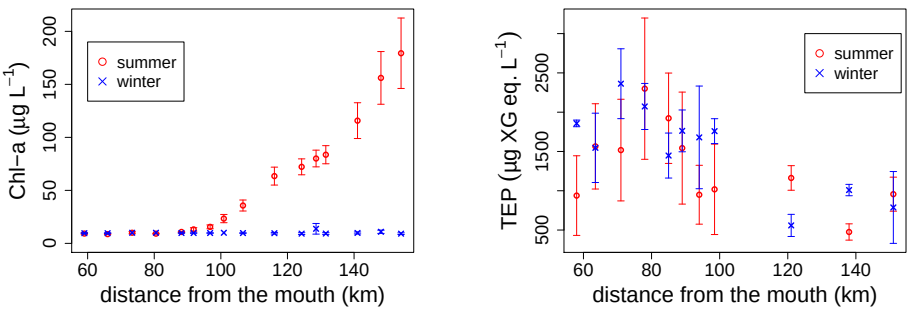

(a) Chl-a concentration

(b) TEP concentration

Figure 3.4: (a) Measured time-averaged Chlorophyll-a (Chl-a) concentration in summer and winter over the years 2015-2018 and (b) corresponding measured transparent exopolymer particles (TEP) concentration of 2018. The error bars depict the standard error of the estimates corresponding to the various campaigns.

We conclude that we observe a clear seasonality in SPM and floc size dynamics beyond km 120, whereas some biotic properties show seasonality, and others do not; the contrast between the strong seasonality in Chl-a and the absence of seasonality in TEP on the estuary scale, both biotic factors reported to (indirectly) influence SPM dynamics, makes it difficult to use these observations as indicators for biotically induced seasonality in SPM. Therefore, the observations are complemented with model experiments which are shown in the following section.

3.3.2 Seasonality in the model experiments

3.3.2.1 Model parameters λ and M

Minimizing the cost function separately for summer and winter results in an optimal parameter set $\lambda = 72.5 \times 10^{-6}$ s$^{-1/2}$ m^2, $M = 2.7 \times 10^{-3}$ s m^{-1} in summer (cost value equals 0.22) and $\lambda = 65.9 \times 10^{-6}$ s$^{-1/2}$ m^2, $M = 3.0 \times 10^{-3}$ s m^{-1} in winter (cost value equals 0.17). These optimal (λ,M) pairs thus show a weak ($\sim 10\%$) seasonality in both λ and M.

To explore the sensitivity of the model results to variations of the calibration parameters λ and M, Fig. 3.5 shows the cost function as a function of λ (horizontal axis) and M (vertical axis), with the value of the cost function indicated by color. Optimal values are indicated by ①. The dark blue colors indicate the range of (λ,M) pairs with a good performance: the white dashed contours depict the cost function values which are 25 % larger than the optimal cost function value. In summer (Fig. 3.5a), this contour covers a range with λ close to 70×10^{-6} s$^{-1/2}$ m^2 and $2 \times 10^{-3} < M < 5 \times 10^{-3}$ s m^{-1}. So, the optimal λ value is found in a relatively narrow parameter range and is quite insensitive to the value of M. In winter (Fig. 3.5b), the range of optimal values is around $\lambda \approx 60 \times 10^{-6}$ s$^{-1/2}$ m^2 and $M > 2 \times 10^{-3}$ s m^{-1}. Note our winter result slightly differs from the winter result presented in Horemans et al. (2020) because we added fluvial inflow of SPM at the Upper Sea Scheldt boundary (see Table 3.1), used a Prandtl Schmidt number of 0.5 instead of 1, and excluded the observations at the dumping locations in our calibration. We also included turbidity observations of 2018 in our calibration.

The red dots in Fig. 3.5 depict the probability density of (λ,M) given the uncertainty in the residual SPM data set to which the model is calibrated. Bigger dots signify a higher probability density, while smaller dots signify a lower probability density. We use these distributions of (λ,M) in summer and winter to quantitatively compare the optimal (λ,M) pairs using Eq. (3.3) and detect a potential seasonality given the uncertainty in the residual SPM observations. The standard deviation of the λ and M distributions in the summer and winter conditions are $\sigma_\lambda^{\text{summer}} = 12.9 \times 10^{-6}$ s$^{-1/2}$ m^2, $\sigma_\lambda^{\text{winter}} = 10.5 \times 10^{-6}$ s$^{-1/2}$ m^2, $\sigma_M^{\text{summer}} = 0.9 \times 10^{-3}$ s m^{-1}, and $\sigma_M^{\text{winter}} = 1.4 \times 10^{-3}$ s m^{-1}. Consequently, the relative difference of the optimum values in summer and winter Δ [see Eq. (3.3)] for λ and M are $\Delta_\lambda = 0.4$ and $\Delta_M = 0.18$, respectively. We thus conclude that we do not detect seasonality in λ and M given the uncertainty of the residual SPM observations.

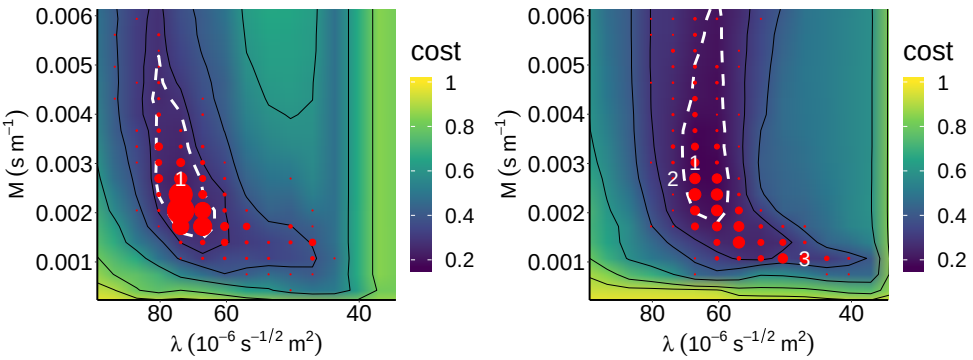

(a) Cost function output in summer

(b) Cost function output in winter

Figure 3.5: Cost function values for various λ and M calibrated to the observed residual SPM data set in (a) summer and (b) winter. The optimal calibration parameter set corresponds to ① $\lambda = 72.5 \times 10^{-6}$ s$^{-1/2}$ m^2, $M = 2.7 \times 10^{-3}$ s m^{-1} in summer and ① $\lambda = 65.9 \times 10^{-6}$ s$^{-1/2}$ m^2, $M = 3 \times 10^{-3}$ s m^{-1} in winter. The white dashed contours depict the cost function values which are 25 % larger than the optimal cost function value. The red dots depict the probability density of the 500 (λ,M) pairs given the uncertainty in the residual SPM data set to which the model is calibrated. Bigger dots signify a higher probability density, while smaller dots signify a lower probability density. We choose two additional (λ,M) pairs, depicted by ② and ③, to study the impact of the choice in (λ,M) located in the zone of high probability density on the corresponding model output. The corresponding λ and M values are $\lambda = 72.5 \times 10^{-6}$ s$^{-1/2}$ m^2, $M = 2.7 \times 10^{-3}$ s m^{-1} (i.e., optimal summer conditions) and $\lambda = 45.3 \times 10^{-6}$ s$^{-1/2}$ m^2, $M = 1.1 \times 10^{-3}$ s m^{-1}, respectively.

3.3.2.2 Seasonality in modeled SPM concentration

To further investigate the optimal calibration values of λ and M, we analyze the corresponding modeled SPM distribution for the optimal (λ,M) pair (see ① in Fig. 3.5) for both summer and winter conditions. Given the estuary-scale of the model and measurement uncertainty (cf. dark blue regions and distribution of (λ,M) pairs in Fig. 3.5), we also show the SPM distribution corresponding to two additional (λ,M) pairs (see ② and ③ in Fig. 3.5b). We require that these two pairs result in an acceptable model performance and are within the zone of high probability density in winter (red dots in Fig. 3.5b). We choose the first pair to be equal to the optimal (λ,M) pair in summer and the second pair to be located in the second zone of (λ,M) pairs in winter where we detect a high probability density (depicted by the red dots in Fig. 3.5b). The corresponding λ and M values are $\lambda = 72.5 \times 10^{-6}$ s$^{-1/2}$ m^2, $M = 2.7 \times 10^{-3}$ s m^{-1} and $\lambda = 45.3 \times 10^{-6}$ s$^{-1/2}$ m^2, $M = 1.1 \times 10^{-3}$ s m^{-1}, respectively. The corresponding cost function values equal 0.26 and 0.30, respectively.

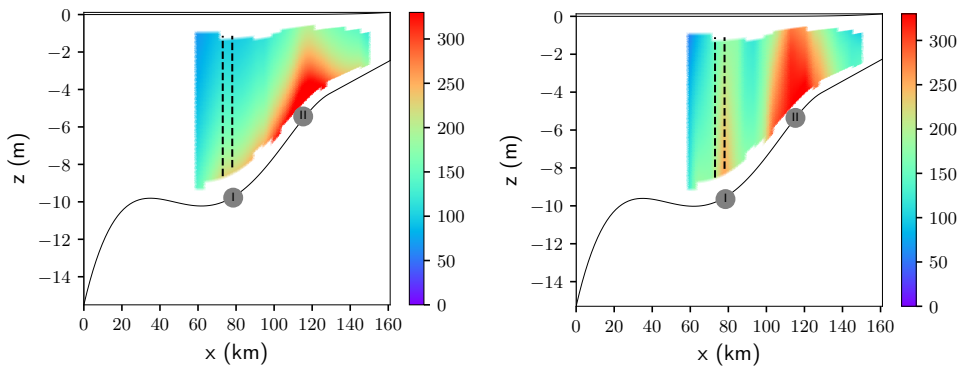

(a) Model output of the SPM concentration (mg L^{-1}) in summer ①

(b) Observations of the SPM concentration (mg L^{-1}) in summer

Figure 3.6: (a) Model output of the suspended particulate matter (SPM) concentration in summer. The optimal calibration parameters are ① $\lambda = 72.5 \times 10^{-6}$ s$^{-1/2}$ m^2 and $M = 3 \times 10^{-3}$ s m^{-1}. The vertical dashed lines depict the dumping locations and the symbols (I), (II) the locations of the observed ETM. (b) The long-term, time-averaged SPM concentration observations (mg L^{-1}) in summer.

Figures 3.6-3.7 show the modeled SPM concentration in summer and winter using these values of λ and M and the corresponding observations. We present the model result and observations in summer in Fig. 3.6a and Fig. 3.6b, respectively. Figure 3.6a shows two modeled ETM at the correct locations, that is, a weak ETM at the dumping location near km 80 and an ETM at km 120 (depicted by (I) and (II), respectively). The length of the ETM is approximately 10 and 30 km, respectively. Both model results and observations show concentrations upto approximately 300 mg L^{-1}. The model seems to overestimate the vertical gradient in SPM.

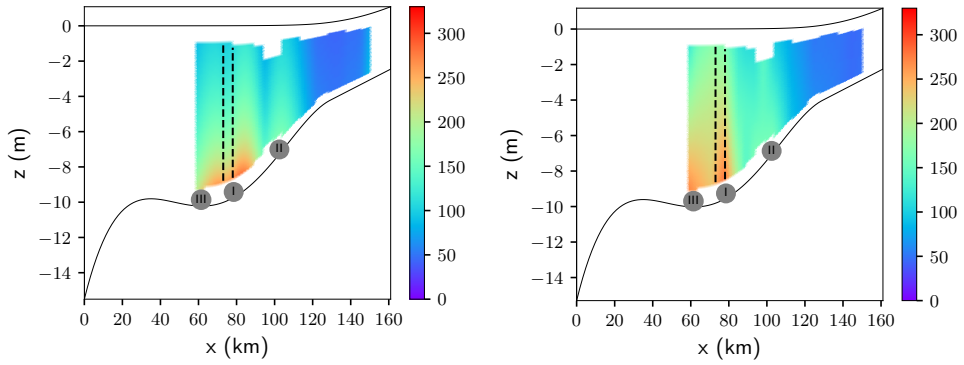

(a) Model output of the SPM concentration (mg L^{-1}) in winter ①

(b) Observations of the SPM concentration (mg L^{-1}) in winter

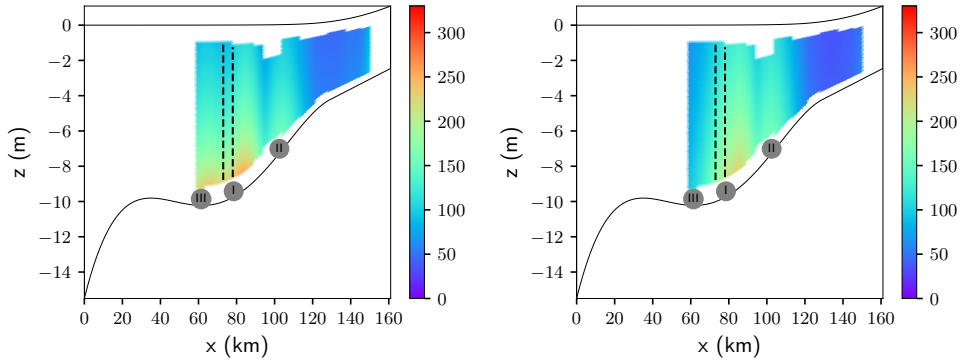

(c) Model output of the SPM concentration (mg L^{-1}) in winter ②

(d) Model output of the SPM concentration (mg L^{-1}) in winter ③

Figure 3.7: (a) Model output of the suspended particulate matter (SPM) concentration in winter. The optimal calibration parameters are ① $\lambda = 65.9 \times 10^{-6}$ $s^{-1/2}$ m^2 and $M = 3.0 \times 10^{-3}$ s m^{-1}. The vertical dashed lines depict the dumping locations and the symbols (I), (II), and (III) the locations of the observed ETM. (b) The long-term, time-averaged SPM concentration observations (mg L^{-1}) in winter. (c)-(d) Model output of the SPM concentration in winter with ② $\lambda = 72.5 \times 10^{-6}$ $s^{-1/2}$ m^2, $M = 2.7 \times 10^{-3}$ s m^{-1} and ③ $\lambda = 45.3 \times 10^{-6}$ $s^{-1/2}$ m^2, $M = 1.1 \times 10^{-3}$ s m^{-1}, respectively.

In winter, the model also captures the locations of the ETM for the optimal (λ,M) pair ①. The model result (Fig. 3.7a) and observations (Fig. 3.7b) both show an ETM near km 80, approximately 10 km long (depicted by (I)). The ETM in the model result potentially merged into the ETM caused by dumping activities, which are not considered in the model setup. The model also correctly captures the accumulation of SPM at km 100 (depicted by (II)) and km 60 (depicted by (III)). The concentrations are in the order of 100-300 mg L^{-1}. What is most important within the scope of this study is that the

ETM near km 120 in summer shifts downstream to km 100 and an additional ETM near km 60 arises in winter. In other words, the model captures this seasonality in the ETM.

Figures 3.7c and 3.7d show the modeled SPM concentration corresponding to the two alternative (λ,M) pairs (see ② and ③ in Fig. 3.5b). Compared to our previous result (Fig. 3.7a), no major change in case of parameter values associated with ② is observed (Fig. 3.7c). We observe a slight decrease in the SPM concentration, especially near the sediment bed, but the locations of the ETM are unchanged. The modeled SPM concentration corresponding to pair ③ (Fig. 3.7d) is different when compared to the optimal SPM concentration (Fig. 3.7a): the ETM near km 60 (depicted by (III)) vanished, the ETM near km 80 and 100 are still present (depicted by (I) and (II), respectively). Although the cost function showed that ③ is a reasonable calibration, visual inspection favors ① and ②. Accepting ② as a good fit further supports our conclusions that we can explain the observed seasonality in the estuary-scale SPM distribution without requiring seasonality in biotically induced flocculation and erosion parameters. The seasonality in SPM can be captured by only accounting for seasonality in freshwater discharge and turbulence.

3.3.3 Sensitivity analysis of the modeled SPM concentration to D_p and n_f

Figure 3.8 shows the sensitivity of the depth-averaged SPM concentration to D_p and n_f. The results of the SPM concentration in summer and winter are neither quantitatively nor qualitatively changed significantly when varying D_p (Figs. 3.8a-b) and n_f (Figs. 3.8c-d). To conclude, our sensitivity analysis of the modeled SPM concentration to D_p and n_f shows that our results and conclusions do not change when choosing different parameter values.

3.4 Discussion

3.4.1 Model performance and reverse engineering approach

In this contribution, we aim to answer the question whether biotically induced seasonality has a dominant impact on the observed seasonality in SPM on the estuary scale in the Scheldt estuary. We take estuary scale to mean the location and approximate SPM concentration of the ETM, which are captured in our model. On this scale, seasonal differences in parameters representing biotic effects are not necessary. To be specific, any seasonal differences in optimal calibration of (λ,M) is within the uncertainty in the observations. Furthermore, choosing between optimally calibrated (λ,M) for summer and winter or equal (λ,M) in summer and winter only has an $\mathcal{O}(10^{-2})$ effect on the cost function representing goodness-of-fit. Moreover, by lumping all biotic effects of different scale and nature in only two parameters, our conclusions are only valid for the aggregated

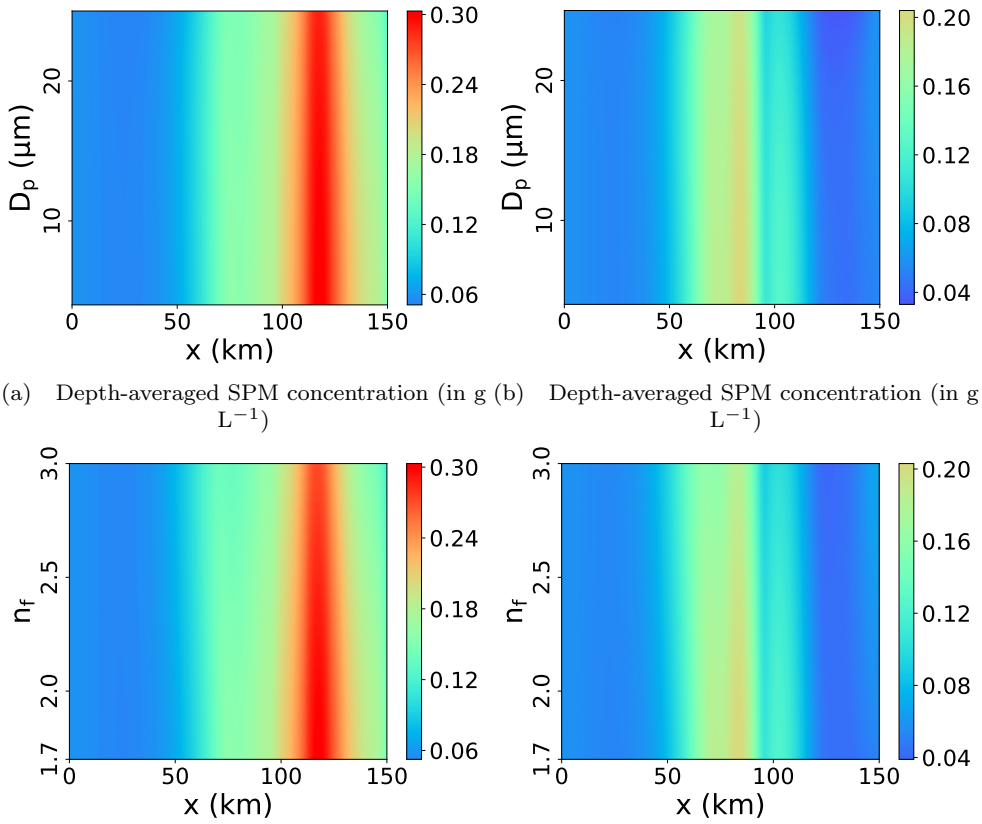

(a) Depth-averaged SPM concentration (in g L^{-1})

(b) Depth-averaged SPM concentration (in g L^{-1})

(c) Depth-averaged SPM concentration (in g L^{-1})

(d) Depth-averaged SPM concentration (in g L^{-1})

Figure 3.8: Sensitivity of the depth-averaged suspended particulate matter (SPM) concentration to the primary particle size D_p in (a) summer and (b) winter, and to the fractal dimension n_f in (c) summer and (d) winter.

biotic impact on a large scale. This may still imply that the effect of individual biotic processes approximately cancel out against each other or are of significant importance locally, for example, in shallow areas.

3.4.2 Biotic seasonality in floc size in the Scheldt estuary

Various studies on the seasonality in floc size dynamics in the Scheldt estuary have been reported in the literature. These studies have linked these dynamics to the presence of biota but read different conclusions. We explain the seasonality in floc size by seasonality in freshwater discharge and corresponding SPM concentrations: a larger discharge results in flushing of the SPM concentrations and a larger shear rate locally at the upstream boundary [see Eq. (3.5) and Fig. 3.C.1]. A decrease in SPM concentration and an increase in shear rate result in a decrease in floc size. Hence, it is worth discussing this.

Wartel and Francken (1998) measured in situ floc size between km 40 and 100 using a Benthos plankton camera, which measures in situ flocs ranging in size from 30- to 1625 μm (the LISST 200x instrument we used measures floc sizes ranging from 1 to 500 μm). They found slightly lower averaged floc sizes of approximately 70 μm, but did not measure a longitudinal trend in floc size between km 60-100. Their averaged floc size of approximately 90 μm at km 110 in winter and the absence of a significant seasonality (autumn versus spring) of the floc size at km 100 compare well to our observations. They attributed this slightly larger floc size at km 110 to an increase in organic content and the presence of micro-organisms, which excrete EPS (of which TEP is a subgroup).

In contrast, Chen et al. (2005) measured floc size locally at both a freshwater and brackish tidal flat in the Scheldt estuary. They used the so called 'pipette-method' to determine floc sizes. Eisma et al. (1991) showed that observations using this method did not correlate to observations carried out using the in situ Benthos plankton camera. At the freshwater tidal flat (at approximately km 100), the mean floc size increased from approximately 40 μm in winter upto 80 μm in spring. In the brackish tidal flat (at approximately km 20), it increased from approximately 30 μm in winter upto 90 μm in summer. Interestingly, the measured floc sizes in Chen et al. (2005) are significantly smaller in winter compared to our observations and the ones of Wartel and Francken (1998). Chen et al. (2005) also found a significant seasonality in floc size, which they linked to the presence of biota (i.e., organic content).

More recently, Chen et al. (2018) measured in situ floc sizes, again not in the estuary as a whole, but locally in the coastal region at the mouth (i.e., southern North Sea). By using a reverse engineering model approach, they found a significant seasonality in floc strength, which was inversely related to floc break-up. More specifically, they showed that by decreasing the floc strength in winter (Feb. and Mar.) from 3 10^{-11} N to 1 10^{-11} N, their model simulations of floc size significantly improved when compared to the in situ observations. They attributed this seasonality in floc strength to biological effects (i.e., seasonality in TEP), which we did not observe in the Scheldt estuary as a whole (Fig. 3.4b).

To conclude, floc size observations in the Scheldt estuary show different trends in the literature. These differences may be attributed to the usage of different methodologies (e.g., pipette method, in situ Benthos plankton camera) and the high dependency on the system of interest (e.g., main channel, tidal flat, coastal region). Our observations comply with the main trends found by Wartel and Francken (1998), who also used an in situ method to measure floc size in the main channel.

3.5 Conclusions

In this contribution, we studied the importance of biotically induced seasonality in flocculation and erosion to seasonality in ETM formation applied to the Scheldt estuary. We presented in situ observations of SPM, floc size, Chl-a, and TEP. The SPM and floc size observations show seasonality. Chl-a and TEP observations show no correlation: Chl-a observations show a significant seasonality, whereas we do not detect seasonality in TEP on the estuary scale. These unrelated results make it difficult to use observations of Chl-a and TEP alone as indicators for a potential seasonal impact of biota on the seasonality in ETM formation. Therefore, we combined the observations with a reverse engineering model approach to assess the aggregated impact of biotically induced seasonality in flocculation and erosion on the seasonality in large-scale ETM formation. In the model, this aggregated biotic impact through flocculation and erosion is implicitly parameterized by the ratio of the minimal floc aggregation and floc break-up parameter λ and the erosion parameter M.

Our model results suggest a weak ($\sim 10\%$) seasonality in both λ and M, which is within the uncertainty of the SPM observations. Hence, to explain the observed seasonality in large-scale ETM formation, our results suggest that seasonality in λ and M is not required on the estuary scale. We capture the seasonality in SPM mainly by seasonality in freshwater discharge and resulting seasonality in SPM concentration and shear rate.

List of symbols

Ⓘ	Denotes the region where the first ETM is located
Ⓘⓘ	Denotes the region where the second ETM is located
Ⓘⓘⓘ	Denotes the region where the third ETM is located
①	Denotes the optimal (λ,M) pair in winter
②	Denotes the first alternative (λ,M) pair in winter
③	Denotes the second alternative (λ,M) pair in winter

Latin

a	Availability of easily erodible fine sediment at the sediment bed

c	Suspended sediment concentration
$c_{\text{upper Sea Scheldt}}$	Subtidal SPM concentration at the Upper Sea Scheldt boundary
D_f	Floc size
D_p	Primary particle size
E	Erosion flux of suspended sediment from the sediment bed
$f(a)$	Erodibility
f_s	Shape factor
f^{sal}	Function that describes salinity driven flocculation
G	Shear rate
g	Gravitational acceleration
$k_A^{\text{min.}}$	Nondimensional minimal aggregation coefficient
k_B	Break-up parameter
M	Erosion parameter
M^{summer}	Erosion parameter in summer
M^{winter}	Erosion parameter in winter
n_f	Fractal dimension
$\mathcal{O}$	Order of
Q	Total freshwater discharge
Q^{summer}	Total freshwater discharge in summer
Q^{winter}	Total freshwater discharge in winter
Re_f	Floc Reynolds number (i.e., $w_s D_f/\nu$)
S	Salinity
s_{f_0}	Bed roughness coefficient
s_{sea}	Salinity boundary condition at the mouth
w_s	Settling velocity of suspended sediment
$w_{s,\text{min.}}$	Minimum settling velocity of suspended sediment
x_c	Calibration parameter in postulated tanh salinity distribution
$x_c^{\text{sal, summer}}$	Calibration parameter in postulated tanh salinity distribution in summer
x_L	Calibration parameter in postulated tanh salinity distribution
$x_L^{\text{sal, summer}}$	Calibration parameter in postulated tanh salinity distribution in summer
$x_c^{\text{sal, winter}}$	Calibration parameter in postulated tanh salinity distribution in winter
$x_L^{\text{sal, winter}}$	Calibration parameter in postulated tanh salinity distribution in winter

Greek

Δ_λ	Difference of the optimal λ-values in summer and winter, relative to the corresponding standard deviation (see Eq. 3.3)
Δ_M	Difference of the optimal M-values in summer and winter, relative to the corresponding standard deviation (see Eq. 3.3)
λ	Ratio of the minimal aggregation and floc break-up parameter
λ^{summer}	Ratio of the minimal aggregation and floc break-up parameter in summer
λ^{winter}	Ratio of the minimal aggregation and floc break-up parameter in winter
μ	Dynamic viscosity of water
ν	Kinematic viscosity of water
ρ_s	Density of sediment primary particles
ρ_w	Reference density of water

σ_λ	Standard deviation of the 500 calibrated λ-values
$\sigma_\lambda^{\text{summer}}$	Standard deviation of the 500 calibrated λ-values in summer
$\sigma_\lambda^{\text{winter}}$	Standard deviation of the 500 calibrated λ-values in winter
σ_M	Standard deviation of the 500 calibrated M-values
σ_M^{summer}	Standard deviation of the 500 calibrated M-values in summer
σ_M^{winter}	Standard deviation of the 500 calibrated M-values in winter
σ_ρ	Prandtl-Smidth number
τ_b	Shear stress at the river bed

Appendix 3.A: floc size using various averaging methods

To show that the estimated floc size is highly sensitive to the averaging method, we use two additional averaging methods: 1. the same averaging method as proposed by Sequoia Scientific (2019) but weighting the midpoint instead of the class number and 2. the median floc size by mass instead of volume. The difference between weighting by mass instead of volume depends on the structure of the flocs. Using our reference floc model assumption (fractal dimension is 2), averaging by mass is equivalent to averaging by area (Bowers et al., 2017). So, we divided the volume concentration of each size class by the corresponding midpoint.

Figure 3.A.1 shows the observed depth- and time-averaged floc size measured in summer and winter 2018 using the averaging method proposed by Sequoia Scientific (2019) (circles), weighting the midpoint instead of the size class number (triangles), and the time- and depth-averaged median floc size by mass (rectangles). The error bars depict the standard error of the depth-averages corresponding to the various campaigns. Using other averaging methods may increase (weighting the midpoint by volume) or decrease (weighting by mass) the overall floc size. However, using all three averaging methods, we observe seasonality in the upstream region of the Scheldt estuary. We thus conclude that, on the estuary scale (we have a local anomaly near km 60 and km 80, depending on the averaging method), the floc sizes only show seasonality in the upstream part of the Scheldt estuary ($>$ 120 km).

Appendix 3.B: salinity profile

Following Warner et al. (2005), we fit the salinity data measured in summer and winter in the Scheldt estuary to the following postulated salinity distribution:

$$\frac{s_{\text{sea}}}{2}\left(1-\tanh\frac{x-x_c^{\text{Sal.}}}{x_L^{\text{Sal.}}}\right), \tag{3.4}$$

where s_{sea} is the salinity boundary condition at the mouth and $x_c^{\text{Sal.}}$ and $x_L^{\text{Sal.}}$ are further undefined calibration parameters. Figure 3.B.1 shows the salinity data and corresponding

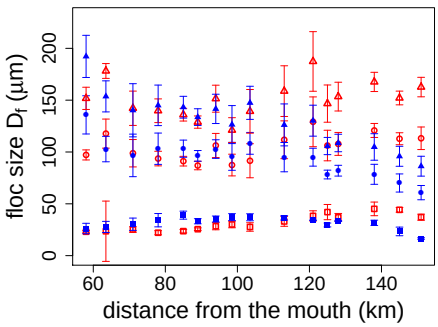

Figure 3.A.1: Measured time- and depth-averaged floc size in summer (red) and winter (blue) using the averaging method proposed by Sequoia Scientific (2019) (circles), weighting the midpoint instead of the size class number (triangles), and the time- and depth-averaged median floc size by mass (rectangles). The error bars depict the standard error of the estimates corresponding to the various campaigns.

data fit in summer and winter. Table 3.1 lists the corresponding parameter values.

Appendix 3.C: shear rate in the flocculation model

Following Pejrup and Mikkelsen (2010), the shear rate G reads

$$G(x, \tilde{z}_1) = \sqrt{\frac{\langle u_* \rangle^3 (1 - \tilde{z}_1)}{\nu H \kappa' \tilde{z}_1}}, \tag{3.5}$$

in which x is the coordinate in the longitudinal direction, κ' is the Von Karman constant, ν is the kinematic viscosity of water, H is the water depth, $\tilde{z}_1 = z_1/H$ is the relative water depth, and $\langle u_* \rangle$ is the subtidal friction velocity. To ensure that the model captures the impact of seasonality in river discharge on G, we define the subtidal friction velocity following Horemans et al. (2020) as

$$\langle u_* \rangle(x) = \frac{\kappa'}{\ln \frac{z_1(x)}{s_{f_0}}} \langle |u^0(x, z_1) + u_{\text{riv.}}(x, z_1)| \rangle, \tag{3.6}$$

where z_1 is the distance in the logarithmic layer above the bed, s_{f_0} the bed roughness coefficient, u^0 the leading-order, longitudinal flow velocity, which consist of an M2 tidal signal (Chernetsky et al., 2010; Dijkstra et al., 2017), and $u_{\text{riv.}}$ the (subtidal) longitudinal, river-induced flow velocity. Consequently, an increase in freshwater discharge (cf. $u_{\text{riv.}}$) results in an increase in shear rate G. Following Horemans et al. (2020), we approximate G by its value at $z_1 = H/2$ and use this value $G(x, \tilde{z}_1 = 1/2)$ as a proxy for the whole water column, which is acceptable because vertical variations in G are relatively small

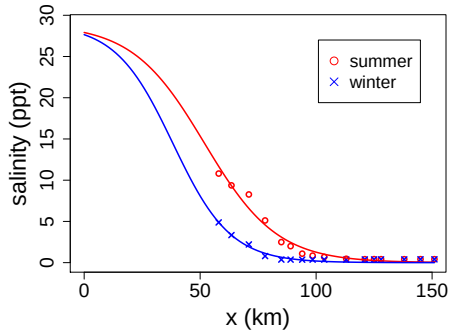

Figure 3.B.1: Measured salinity corresponding to our case study in the Scheldt estuary and corresponding data fit using Eq. (3.4) in summer and winter.

in the logarithmic layer (typically $< 10\%$ in our case study). Moreover, we neglect tidal variation in G which is, within the scope of this study, acceptable because the seasonality in tidal variability in our case study is small; the main difference in longitudinal water velocity between summer and winter is the riverine influence, locally at the upstream boundary, which is thus captured by the model. Figure 3.C.1 shows the shear rate in both summer and winter conditions.

The increase of freshwater discharge in winter increases the shear rate locally at the upstream boundary. Further downstream, between km 100-140, it decreases the shear rate slightly because of a decrease of the tidal energy in this region.

Appendix 3.D: perturbation approach for $n_f \neq 2$

We extend the flocculation model for general n_f. This requires a reanalysis of the results presented in Horemans et al. (2020). However, the same semianalytical perturbation approach can be applied. At leading order $\mathcal{O}(1)$, a careful analysis shows that only the second term in the result of the leading order settling velocity w_s^0 presented in Horemans et al. (2020) changes:

$$w_s^0 = \beta c^0 + \frac{D_p}{\tilde{D}_f}(w_s^0)^{\frac{n_f-2}{n_f-1}}, \tag{3.7}$$

with

$$\tilde{D}_f = 18^{\frac{1}{n_f-1}} \left(\frac{\mu D_p^{n_f-3}}{g(\rho_s - \rho_w)} \right)^{\frac{1}{n_f-1}}, \tag{3.8}$$

and where $\beta = (\rho_s - \rho_w) g k_A' / (18 \mu f_s \rho_s \sqrt{G} k_B)$, with k_A' being the aggregation parameter, and c^0 is the leading order SPM concentration. For $n_f = 2$, the second term in Eq. (3.7)

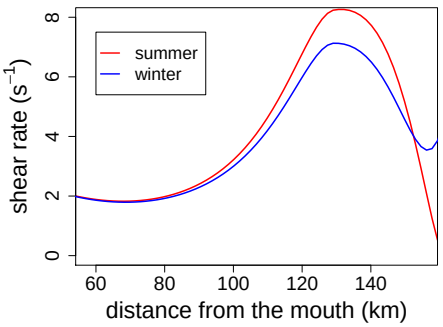

Figure 3.C.1: Modeled shear rate in summer and winter. The increase of freshwater discharge in winter increases the shear rate locally at the upstream boundary. Further downstream between km 100-140, it decreases the shear rate slightly due to a decrease of tidal energy in this region.

is a constant value, being the settling velocity of the primary particles (Horemans et al., 2020). For $n_f \neq 2$, this second term is a function of both time and space. Consequently, at first order $\mathcal{O}(\epsilon)$ (with ϵ being the small perturbation parameter), the result becomes more complex but can still be easily solved to the first order settling velocity w_s^1:

$$
\begin{aligned}
w_s^1 = & \frac{1}{-A\frac{(c^0)^2(3-2n_f)(w_s^0)^{-1+\frac{3-2n_f}{n_f-1}}}{n_f-1} + B\frac{c^0(2-n_f)(w_s^0)^{-1+\frac{2-n_f}{-1+n_f}}}{-1+n_f}} \times \\
& \left\{ \frac{n_f}{n_f-1} K_v \left[2(w_s^0)^{\frac{1-2n_f}{n_f-1}} (\partial_z c^0)(\partial_z w_s^0) + c^0 \frac{1-2n_f}{n_f-1} (w_s^0)^{\frac{2-3n_f}{n_f-1}} (\partial_z w_s^0)^2 \right] \right. \\
& + (w_s^0)^{\frac{-n_f}{n_f-1}} (w_s^0 \partial_z c^0 + c^0 \partial_z w_s^0) - \frac{n_f}{n_f-1} c^0 (w_s^0)^{\frac{1-2n_f}{n_f-1}} \left[\partial_t w_s^0 - K_v \partial_{zz} w_s^0 \right] \\
& \left. - (w_s^0)^{\frac{-1}{n_f-1}} \partial_z c^0 + \frac{1}{n_f-1} c^0 (w_s^0)^{\frac{-n_f}{n_f-1}} \partial_z w_s^0 + c_1 \left[2Ac^0 (w_s^0)^{\frac{3-2n_f}{n_f-1}} - B(w_s^0)^{\frac{2-n_f}{n_f-1}} \right] \right\},
\end{aligned}
\tag{3.9}
$$

with

$$
A = \frac{Gk'_A 18^{\frac{3}{n_f-1}} \left(\frac{1}{D_p}\right)^{6-2n_f} \left(18^{\frac{1}{n_f-1}} \left(\frac{\mu D_p^{n_f-3}}{g(\rho_s-\rho_w)} \right)^{\frac{1}{n_f-1}} \right)^{-2n_f} \left(\frac{\mu D_p^{n_f-3}}{g(\rho_s-\rho_w)} \right)^{\frac{3}{n_f-1}}}{(fs\rho_s)^2} \quad \text{and} \tag{3.10}
$$

$$
B = \frac{G^{1.5} k_B 18^{\frac{2}{n_f-1}} \left(\frac{1}{D_p}\right)^{3-n_f} \left(18^{\frac{1}{n_f-1}} \left(\frac{\mu D_p^{n_f-3}}{g(\rho_s-\rho_w)} \right)^{\frac{1}{n_f-1}} \right)^{-n_f} \left(\frac{\mu D_p^{n_f-3}}{g(\rho_s-\rho_w)} \right)^{\frac{2}{n_f-1}}}{f_s \rho_s}. \tag{3.11}
$$

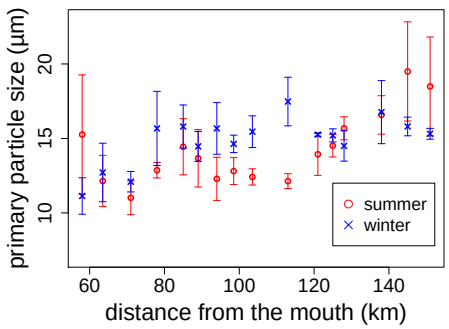

Figure 3.E.1: Primary particle size measured in summer and winter within the OMES (Dutch: "Onderzoek Milieu Effecten Sigmaplan") monitoring campaign.

Appendix 3.E: primary particle size and density

Within the OMES campaign, we took 1 L samples from a bucket sample conducted at the water surface to estimate primary particle size (Maris et al., 2021c). Samples were collected once a month at each station, which resulted in three samples per station for both summer and winter. At km 58, we exceptionally have only two samples per season.

Primary particle size distribution was measured using a Mastersizer2000. The detection range of the Mastersizer2000 is 0.02 to 2000 μm. After shaking the 1 L samples intensively, the samples were decanted in the dispersion unit of the Mastersizer2000 until the obscuration reached a value of approximately 10 %. We used the default absorption and refractive index (i.e., 0.1 and 1.52, respectively) and standard Lorenz-Mie method for spherical particles. The samples were stirred and pumped with a frequency of 750 and 2000 rpm, respectively, using tap water as a dispersant. Using this primary particle size distribution, we calculate the primary particle size corresponding to summer and winter using two averaging procedures. Figure 3.E.1 shows the primary particle size using a standard geometric average method often referred to as $D[1,0]$. The corresponding system averaged value is 14.2 and 14.9 μm in summer and winter, respectively. The error bars represent the (Gaussian) standard error. Based on these estimates, we chose a primary particle size of 14 μm in our model.

The organic fractions of SPM, which have a density of ~ 1000 kg m^{-3}, can reach upto 30 % in Scheldt estuary (Maris and Meire, 2017), and thus the organic fraction may have a relative impact via primary particle density (i.e., 2650 kg m^{-3}) according to Fall et al. (2021) of

$$\Delta\rho_s = 1 - \frac{0.3 \cdot 1000 + 0.7 \cdot 2650}{2650} \sim 20\% \tag{3.12}$$

This sensitivity was tested, and for such a decrease in ρ_s, we found a slight land-inward shift of the ETM in both summer and winter. We also observed this land-inward shift for

decreasing λ (Fig. 3.7). This is to be expected because a decrease in ρ_s is equivalent to a decrease in λ, which follows from the factor $(\rho_s - \rho_w)/\rho_s$ in Eq. (3.2).

Table 3.F.1: Parameter values used in our model study in the Scheldt estuary in summer and winter conditions.

Variable	Definition	Value
	Hydrodynamics	
A^0	M_2 water level amplitude at x=0	1.77 m
A^1	M_4 water level amplitude at x=0	0.14 m
ϕ^1	M_4 water level phase relative to M_2 tide at x=0	-1.3 deg
Q^{summer}	Total river discharge in summer (calibrated)	40 m^3 s^{-1}
Q^{winter}	Total river discharge in winter (calibrated)	233 m^3 s^{-1}
	Sediment	
c_{sea}	Depth-averaged subtidal SPM concentration at x=0	0.06 kg m^{-3}
$c_{\text{upper Sea Scheldt}}$	Subtidal SPM concentration at the Upper Sea Scheldt boundary (source)	0.035 kg m^{-3}
K_h	Horizontal eddy diffusivity coefficient	100 m^2 s^{-1}
K_ν^0	Vertical eddy diffusivity coefficient	3.1×10^{-2} m^2 s^{-1}
M^{summer}	Erosion parameter in summer (calibrated)	2.7×10^{-3} s m^{-1}
M^{winter}	Erosion parameter in winter (calibrated)	3.0×10^{-3} s m^{-1}
	Turbulence	
σ_ρ	Prandtl Schmidt number	0.5
s_{f_0}	Bed roughness coefficient (calibrated)	4.22 mm s^{-1}
	Flocculation	
$k_A^{\text{min.}}$	Nondimensional minimal aggregation coefficient	0.29
f_s	Shape factor	$\pi/6$
n_f	Fractal dimension of flocs	2
q	Calibration parameter in flocculation model	0.5
p	Calibration parameter in flocculation model	1
D_p	Diameter primary mud particles	14×10^{-6} m
μ	Dynamic viscosity	0.0010518 Pa s
ρ_s	Density of SPM primary particles	2650 kg m^{-3}
ρ_w	Reference density of water	1000 kg m^{-3}
λ^{summer}	Ratio of minimal aggregation and floc break-up parameter in summer (calibrated)	72.5×10^{-6} $s^{-1/2}$ m^2
λ^{winter}	Ratio of minimal aggregation and floc break-up parameter in winter (calibrated)	65.9×10^{-6} $s^{-1/2}$ m^2
	Salinity	
s_{sea}	Salinity boundary condition at the mouth	28.9 psu
$x_c^{\text{sal, summer}}$	Calibration parameter in sigmoid salinity distribution in summer	51.9 km
$x_L^{\text{sal, summer}}$	Calibration parameter in sigmoid salinity distribution in summer	31.2 km
$x_c^{\text{sal, winter}}$	Calibration parameter in sigmoid salinity distribution in winter	38.3 km
$x_L^{\text{sal, winter}}$	Calibration parameter in sigmoid salinity distribution in winter	24.8 km

Bibliography

Alldredge, A. L., Granata, T. C., Gotschalk, C. C., and Dickey, T. D. (1990). The physical strength of marine snow and its implications for particle disaggregation in the ocean. *LIMNOLOGY AND OCEANOGRAPHY*, 35(7):1415–1428.

Alldredge, A. L., Passow, U., and Logan, B. E. (1993). The abundance and significance of a class of large, transparent organic particles in the ocean. *Deep Sea Research Part I: Oceanographic Research Papers*, 40(6):1131–1140.

Allen, G. P., Salomon, J. C., Bassoullet, P., Du Penhoat, Y., and de Grandpré, C. (1980). Effects of tides on mixing and suspended sediment transport in macrotidal estuaries. *Sedimentary Geology*, 26(1-3):69–90.

Bar-Zeev, E., Passow, U., Romero-Vargas Castrillón, S., and Elimelech, M. (2015). Transparent Exopolymer Particles: From Aquatic Environments and Engineered Systems to Membrane Biofouling. *Environmental Science & Technology*, 49(2):691–707.

Bowers, D. G., McKee, D., Jago, C. F., and Nimmo-Smith, W. A. (2017). The area-to-mass ratio and fractal dimension of marine flocs. *Estuarine, Coastal and Shelf Science*, 189:224–234.

Brouwer, R. L., Schramkowski, G. P., Dijkstra, Y. M., and Schuttelaars, H. M. (2018). Time Evolution of Estuarine Turbidity Maxima in Well-Mixed, Tidally Dominated Estuaries: The Role of Availability- and Erosion-Limited Conditions. *Journal of Physical Oceanography*, 48(8):1629–1650.

Burchard, H., Schuttelaars, H. M., and Ralston, D. K. (2018). Sediment Trapping in Estuaries. *Annual Review of Marine Science*, 10(1):371–395.

Chen, M. S., Wartel, S., and Temmerman, S. (2005). Seasonal variation of floc characteristics on tidal flats, the Scheldt estuary. *Hydrobiologia*, 540(1-3):181–195.

Chen, P. H., Yu, J. C. S., and Fettweis, M. (2018). Modeling Storm-Influenced Suspended Particulate Matter Flocculation Using a Tide-Wave-Combined Biomineral Model. *Water Environment Research*, 90(3):244–257.

Chernetsky, A. S., Schuttelaars, H. M., and Talke, S. A. (2010). The effect of tidal asymmetry and temporal settling lag on sediment trapping in tidal estuaries. *Ocean Dynamics*, 60(5):1219–1241.

Claquin, P., Probert, I., Lefebvre, S., and Veron, B. (2008). Effects of temperature on photosynthetic parameters and TEP production in eight species of marine microalgae. *Aquatic Microbial Ecology*, 51(1):1–11.

Cox, T. J. S., Maris, T., Van Engeland, T., Soetaert, K., and Meire, P. (2019). Critical transitions in suspended sediment dynamics in a temperate meso-tidal estuary. *Scientific Reports*, 9(1):12745.

Dijkstra, Y. M., Brouwer, R. L., Schuttelaars, H. M., and Schramkowski, G. P. (2017). The iFlow modelling framework v2.4: a modular idealized process-based model for flow and transport in estuaries. *Geoscientific Model Development*, 10(7):2691–2713.

Dijkstra, Y. M., Schuttelaars, H. M., and Schramkowski, G. P. (2019). Can the Scheldt River Estuary become hyperturbid? A model analysis of suspended sediment concentrations and transport in response to channel deepening. *Ocean Dynamics*, 69(7):809–827.

Dyer, K. R. (1989). Sediment processes in estuaries: Future research requirements. *Journal of Geophysical Research*, 94(C10):14327–14339.

Edzwald, J. K., Upchurch, J. B., and O'Melia, C. R. (1974). Coagulation in estuaries. *Environmental Science & Technology*, 8(1):58–63.

Einstein, H. A. and Krone, R. B. (1962). Experiments to determine modes of cohesive sediment transport in salt water. *Journal of Geophysical Research*, 67(4):1451–1461.

Eisma, D., Bernard, P., Cadée, G. C., Ittekkot, V., Kalf, J., Laane, R., Martin, J. M., Mook, W. G., Van Put, A., and Schuhmacher, T. (1991). Suspended-matter particle size in some west-European estuaries; part I: Particle-size distribution. *Netherlands Journal of Sea Research*, 28(3):193–214.

Fall, K. A., Friedrichs, C. T., Massey, G. M., Bowers, D. G., and Smith, S. J. (2021). The Importance of Organic Content to Fractal Floc Properties in Estuarine Surface Waters: Insights From Video, LISST, and Pump Sampling. *Journal of Geophysical Research: Oceans*, 126(1):e2020JC016787.

Fettweis, M., Baeye, M., Van der Zande, D., Van den Eynde, D., and Joon Lee, B. (2014). Seasonality of floc strength in the southern North Sea. *Journal of Geophysical Research: Oceans*, 119(3):1911–1926.

Frostick, L. E. and McCave, I. N. (1979). Seasonal shifts of sediment within an estuary mediated by algal growth. *Estuarine and Coastal Marine Science*, 9(5):569–576.

Horemans, D. M. L., Dijkstra, Y. M., Schuttelaars, H. M., Meire, P., and Cox, T. J. S. (2020). Unraveling the essential effects of flocculation on large-scale sediment transport patterns in a tide-dominated estuary. *Journal of Physical Oceanography*, 50(7):1957–1981.

IMDC (2016). Monitoringprogramma Flexibel Storten. Multivariate analyse van metingen van sedimentconcentratie in de Zeeschelde. WL Reports I /RA/11353/15.228/THL, IMDC, Antwerpen.

Kandiah, A. (1974). *Fundamental aspects of surface erosion of cohesive soils*. PhD thesis, University of California, Davis.

Kappenberg, J. and Grabemann, I. (2001). Variability of the mixing zones and estuarine turbidity maxima in the Elbe and Weser estuaries. *Estuaries*, 24(5):699–706.

Kranenburg, C. (1994). The Fractal Structure of Cohesive Sediment Aggregates. *Estuarine, Coastal and Shelf Science*, 39(5):451–460.

Lai, H., Fang, H., Huang, L., He, G., and Reible, D. (2018). A review on sediment bioflocculation: Dynamics, influencing factors and modeling. *Science of The Total Environment*, 642:1184–1200.

MacCready, P. and Geyer, W. R. (2010). Advances in Estuarine Physics. *Annual Review of Marine Science*, 2(1):35–58.

Malarkey, J., Baas, J. H., Hope, J. A., Aspden, R. J., Parsons, D. R., Peakall, J., Paterson, D. M., Schindler, R. J., Ye, L., Lichtman, I. D., Bass, S. J., Davies, A. G., Manning, A. J., and Thorne, P. D. (2015). The pervasive role of biological cohesion in bedform development. *Nature Communications*, 6(1):1–6.

Malpezzi, M., Sanford, L., and Crump, B. (2013). Abundance and distribution of transparent exopolymer particles in the estuarine turbidity maximum of Chesapeake Bay. *Marine Ecology Progress Series*, 486:23–35.

Maris, T., Claus, J., and Meire, P. (2021a). Floc size distribution measured monthly or bi-weekly in the zeeschelde at 12 stations using a lisst 200x instrument. Data set. Ecosystem Management Research Group - Uantwerpen; International Marine and Dredging Consultants nv.; De Vlaamse Waterweg; Belgium.

Maris, T., Claus, J., and Meire, P. (2021b). Turbidity and suspended sediment concentration profiles measured monthly or bi-weekly in the zeeschelde at 16 stations using an obs instrument. Data set. Ecosystem Management Research Group - Uantwerpen; International Marine and Dredging Consultants nv.; De Vlaamse Waterweg; Belgium.

Maris, T. and Meire, P. (2017). Omes rapport 2016. Onderzoek naar de gevolgen van het Sigmaplan, baggeractiviteiten en havenuitbreiding in de Zeeschelde op het milieu. Technical Report Report Ecosystem Management Research Group ECOBE, 017-R206, University of Antwerp, Antwerp, Belgium.

Maris, T. and Meire, P. (2021). Chlorophyll a measured monthly or bi-weekly in the zeeschelde at 16 stations. Data set. Ecosystem Management Research Group - Uantwerpen; De Vlaamse Waterweg; Belgium.

Maris, T., Van Der Spiet, T., and Meire, P. (2021c). Primary particle size distribution measured monthly in the zeeschelde at 16 stations using a mastersizer2000 instrument. Data set. Ecosystem Management Research Group - Uantwerpen; De Vlaamse Waterweg; Belgium.

Meire, P., Ysebaert, T., Van Damme, S., Van den Bergh, E., Maris, T., and Struyf, E. (2005). The Scheldt estuary: a description of a changing ecosystem. *Hydrobiologia*, 540(1-3):1–11.

Mietta, F., Chassagne, C., Manning, A. J., and Winterwerp, J. C. (2009). Influence of shear rate, organic matter content, pH and salinity on mud flocculation. *Ocean Dynamics*, 59(5):751–763.

Partheniades, E. (1965). Erosion and Deposition of Cohesive Soils. *Journal of the Hydraulics Division*, 91(1):105–139.

Passow, U. (2002). Transparent exopolymer particles (TEP) in aquatic environments. *Progress in Oceanography*, 55(3-4):287–333.

Passow, U. and Alldredge, A. L. (1995). A dye-binding assay for the spectrophotometric measurement of transparent exopolymer particles (TEP). *Limnology and Oceanography*, 40(7):1326–1335.

Passow, U., Shipe, R. F., Murray, A., Pak, D. K., Brzezinski, M. A., and Alldredge, A. L. (2001). The origin of transparent exopolymer particles (TEP) and their role in the sedimentation of particulate matter. *Continental Shelf Research*, 21(4):327–346.

Paterson, D. and Black, K. (1999). Water flow, sediment dynamics and benthic ecology. *Advances in Ecological Research*, 29:155–193. This volume: 'Estuaries'. ISBN for this volume: 978-0-12-013929-3.

Pejrup, M. and Mikkelsen, O. A. (2010). Factors controlling the field settling velocity of cohesive sediment in estuaries. *Estuarine, Coastal and Shelf Science*, 87(2):177–185.

Plancke, Y., Van De Moortel, I., Hertogs, R., Vereecken, H., Vos, G., Verdoodt, N., Meire, D., Deschamps, M., and Mostaert, F. (2017). Monitoring Effecten Ontwikkelingsschets (MONEOS) - Jaarboek monitoring 2016: Deelrapport 6 - Factual data rapportage van monitoring waterbeweging en fysische parameters in de Zeeschelde in 2016. WL Reports 12_070_6, Flanders Hydraulics Research, Antwerpen.

Ralston, D. K., Geyer, W. R., and Warner, J. C. (2012). Bathymetric controls on sediment transport in the Hudson River estuary: Lateral asymmetry and frontal trapping. *Journal of Geophysical Research: Oceans*, 117(C10013).

Rice, E. W., Baird, R. B., Eaton, A. D., and editors (2017). *Standard Methods for the Examination of Water and Wastewater*. American Public Health Association, American Water Works Association, and Water Environment Federation, 23rd edition.

Sequoia Scientific (cited 2019). How to compute the mean particle diameter from a LISST volume distribution. [Available online at `http://www.sequoiasci.com/article/how-to-compute-the-mean-particle-diameter-from-a-lisst-volume-distribution-2/`].

Stal, L. J. (2010). Microphytobenthos as a biogeomorphological force in intertidal sediment stabilization. *Ecological Engineering*, 36(2):236–245.

Stanford, L. P., Suttles, S. E., and Halka, J. P. (2001). Reconsidering the physics of the Chesapeake Bay estuarine turbidity maximum. *Estuaries*, 24(5):655–669.

Sun, C. C., Wang, Y. S., Li, Q. P., Yue, W. Z., Wang, Y. T., Sun, F. L., and Peng, Y. L. (2012). Distribution characteristics of transparent exopolymer particles in the Pearl River estuary, China. *Journal of Geophysical Research G: Biogeosciences*, 117(4).

Uncles, R. J., Stephens, J. A., and Harris, C. (2006). Runoff and tidal influences on the estuarine turbidity maximum of a highly turbid system: The upper Humber and Ouse Estuary, UK. *Marine Geology*, 235(1-4 SPEC. ISS.):213–228.

van Leussen, W. (1994). *Estuarine macroflocs and their role in fine-grained sediment transport.* PhD thesis, Utrecht University, Utrecht.

Vandenbruwaene, W., Vanlede, J., Plancke, Y., Verwaest, T., and Mostaert, F. (2016). Slibbalans Zeeschelde: deelrapport 4. Historische evolutie SPM. versie 6.0. WL Reports 00_029_8, Waterbouwkundig Laboratorium/Antea Group, Antwerpen.

Verney, R., Lafite, R., and Brun-Cottan, J. C. (2009). Flocculation potential of estuarine particles: The importance of environmental factors and of the spatial and seasonal variability of suspended particulate matter. *Estuaries and Coasts*, 32(4):678–693.

Vyverman, W., Maris, T., Daveloose, I., Sabbe, K., and Meire, P. (2021). Transparent exopolymer particles measured monthly in the zeeschelde at 11 stations. Data set. Protistology & Aquatic Ecology - Ugent; Ecosystem Management Research Group - Uantwerpen; De Vlaamse Waterweg, Belgium.

Warner, J. C., Geyer, W. R., and Lerczak, J. A. (2005). Numerical modeling of an estuary: A comprehensive skill assessment. *Journal of Geophysical Research: Oceans*, 110(C5):1–13.

Wartel, S. and Francken, F. (1998). Sedimenttransport en sedimentatieprocessen in de Schelde tussen Zandvliet en Gent: suspensiemateriaal in de Schelde. Technical Report AMIS DS6.1-7-vol. III, Royal Belgian Institute of Natural Sciences, Brussels, Belgium.

Waterinfo.be (cited 2019). Measurements and predictions of Waterinfo.be [data]. [Available online at `https://www.waterinfo.be/`].

Wetz, M. S., Robbins, M. C., and Paerl, H. W. (2009). Transparent Exopolymer Particles (TEP) in a River-Dominated Estuary: Spatial–Temporal Distributions and an Assessment of Controls upon TEP Formation. *Estuaries and Coasts*, 32(3):447–455.

Winterwerp, J. C. (2002). On the flocculation and settling velocity of estuarine mud. *Continental Shelf Research*, 22(9):1339–1360.

Winterwerp, J. C. and van Kesteren, W. G. M. (2004). *Introduction to the physics of cohesive sediment in the marine environment*, volume 56. Elsevier Science, Amsterdam, The Netherlands, 1st edition.

Zhu, Q., Wang, Z., Yang, S. L., and van Prooijen, B. (2017). *Sediment dynamics on intertidal mudflats: A study based on in situ measurements and numerical modelling.* PhD thesis, Delft University of Technology, Delft.

Chapter 4

The impact of temporal variability in SPM on phytoplankton

Horemans, D. M. L., Meire, P., & Cox, T. J. S. (2020). The impact of temporal variability in light-climate on time-averaged primary production and a phytoplankton bloom in a well-mixed estuary. *Ecological Modelling*, 436, 109287. https://doi.org/10.1016/j.ecolmodel.2020.109287

Abstract

Phytoplankton primary production (PP) in turbid estuaries is often limited by light availability. Two important factors altering light climate are solar irradiance at the water surface and exponential light extinction coefficient within the water column. Additionally, the depth of the water body changes the light climate and corresponding PP by altering the ratio of the euphotic and mixing depth in a well-mixed estuary. These three parameters are highly variable yet are often assumed to be constant by both experimental scientists and modelers because of a lack of data or to reduce complexity. Because assuming constant parameters introduces an error, we utilize an idealized model of depth-integrated PP to analyze the (individual) impact of temporal variability in these three parameters. We only consider the main tidal and solar constituents in temporal variability of the forcings and apply a second-order moment approximation to analyze the bias introduced to time-averaged PP estimates by neglecting temporal fluctuations. We demonstrate that the sign and magnitude of this bias are system-specific and depend on two nondimensional parameters that characterize the system. The first is equivalent to the ratio of mixing and photic depth. The second accounts for typical incident irradiance and the photosynthetic parameters of the phytoplankton population present. To demonstrate the applicability of our approach, we apply the model to two cases in the Scheldt estuary (Belgium) in the brackish and freshwater part. In the first application, we study the impact of fluctuations on phytoplankton in dynamic equilibrium, where biomass is assumed to be constant. We show that variability in solar irradiance has the largest impact on time-averaged PP in dynamic equilibrium, resulting in a 30 % decrease compared to time-invariant forcing. By comparing with a numerical integrator, we show that a second-order moment approximation correctly predicts the order of magnitude of the impact of temporal variability of the individual parameters. In the second application, we study the impact of fluctuations on unbounded exponential phytoplankton growth. Also here, fluctuations in solar irradiance have the largest impact and lead to a significant decrease in exponential growth. In this case study, we show that temporal fluctuations delay the onset of the biomass by two weeks and decrease the biomass by a factor of 14 after two weeks compared to time-invariant forcing. Additionally, we show that the temporal fluctuations induce low-frequency variability in phytoplankton biomass with similar periodicity as the spring-neap cycle, making it challenging to observe these phenomena in real-world time series.

4.1 Introduction

Primary production (PP) in estuaries and the corresponding phytoplankton biomass dynamics result from a complex interaction of physical and biological processes (Alpine and Cloern, 1992; Dijkstra et al., 2019). Examples of factors that directly impact PP and phytoplankton biomass dynamics are physical-chemical aspects such as river flushing (Filardo and Dunstan, 1985; Liu and de Swart, 2015), temperature (Eppley, 1972), salinity (Lucas et al., 1998), nutrients (Tilman et al., 1982; Cira et al., 2016), and light

availability (Sverdrup, 1953; Desmit et al., 2005), or biological factors such as grazing (Lionard et al., 2005). Due to these complex interactions, we expect both strong high-frequency ($\sim$hours^{-1}-days^{-1}) and low-frequency ($\sim$ weeks^{-1}-months^{-1}) dynamics generated by water flow and seasonality in, for example, water temperature, light availability, and freshwater discharge.

To acquire insight into the complex interacting processes affecting PP and phytoplankton biomass dynamics, both intensive monitoring campaigns (Maris and Meire, 2016) and a broad range of models have been set up, ranging from numerically-costly three-dimensional models (Chen and Mynett, 2006; Chao et al., 2010), idealized two-dimensional models (McSweeney et al., 2017), one-dimensional models (Brinkman, 1993; Soetaert and Herman, 1995; Vanderborght et al., 2002; Volta et al., 2016; Liu et al., 2018) to zero-dimensional models (Desmit et al., 2005; Cox et al., 2009).

Due to the high complexity of PP and phytoplankton biomass dynamics, idealized models are particularly well suited because they simplify the interpretation of the model results and reduce computational costs, allowing for long-term simulations and extensive sensitivity analyses. More specifically, often model parameters are considered constant to remove nonlinearities and allow for analytical solution procedures (Dijkstra et al., 2017) instead of computationally costly iterative solution methods that tidally resolve the phytoplankton dynamics (Arndt et al., 2011). By using constant model parameters, the impact of temporal variability, which is clearly present in factors affecting PP, is neglected. Only a few studies focus on the individual effect of this, sometimes neglected, high-frequency temporal variability in the factors affecting PP and phytoplankton biomass dynamics. The few studies that do exist are limited to specific examples (Desmit et al., 2005).

Therefore, this study aims to construct a generic, idealized model that allows us to study the impact of temporal fluctuations of individual tidal and solar variables of PP and the corresponding phytoplankton dynamics on an hourly-daily time scale.

We focus on well-mixed, turbid- and nutrient-rich estuarine systems, allowing to analytically compute depth-averaged PP and only consider light limitation, thereby excluding nutrient depletion and temperature dependence. The biological impact of grazing is implicitly included in a constant mortality rate and calibrated to Chlorophyll-a (Chl-a) observations. Moreover, we assume tide-dominated systems and only include periodic temporal variability due to the tides and solar cycle. We focus on the three important factors altering the light climate on the hourly-daily time scale: solar irradiance at the water surface, exponential light extinction coefficient within the water column, and depth of the water body, which changes the ratio of euphotic and mixing depth in a well-mixed estuary.

To model the impact of a changing light climate on phytoplankton biomass growth, we use the Platt light limitation function (Platt et al., 1980). By assuming a well-mixed estuary, we focus on depth-averaged Platt light limitation (DAP), allowing for an analytical solution approach. Moreover, to explicitly compute the impact of temporal variability of the individual parameters and correct for the usage of averaged parameter values, we

use the analytical, second-order up-scaling method often referred to as the moment approximation. This method is based on a second-order Taylor expansion. In the past, the moment approximation has been successfully applied to terrestrial PP (Bolker and Pacala, 1997; Wirtz, 2000). However, terrestrial PP significantly differs from estuarine PP because the light climate in estuarine systems also depends on the tidal variability in depth, suspended sediment concentration, and its corresponding complex temporal variability.

To show the applicability of our approach, we work out two applications in the Scheldt estuary (Belgium). Firstly, we apply our framework to a time-averaged production assuming dynamic equilibrium (application 1). This reflects the situation where phytoplankton biomass is top-down controlled by grazing organisms (e.g., zooplankton), which is often the case in real ecosystems, and remains relatively constant during a large part of the season when primary productivity rates are positive. Such dynamic equilibrium is commonly observed after an initial spring bloom. Secondly, we utilize our idealized model to study phytoplankton dynamics at the onset of a phytoplankton bloom with unbounded biomass growth (application 2).

In this paper, we first introduce the phytoplankton model and DAP function, the corresponding moment approximation, and the two applications in the Scheldt estuary in Section 4.2. In Section 4.3, we present the generic results of the moment approximation and apply these results to our two applications in the Scheldt estuary. Finally, we discuss our results in Section 4.4 and summarize our conclusions in Section 4.5.

4.2 Material and methods

This section presents the depth-integrated model for phytoplankton biomass dynamics and corresponding DAP function Λ that includes our three main parameters of interest: the solar irradiance at the water surface E_0, exponential light extinction coefficient k_d, and water depth d. Next, we apply a second-order moment approximation to the DAP function Λ, which forms the basis of our subsequent analysis. Finally, we work out applications 1 and 2 in the Scheldt estuary using our framework and present the corresponding observations. To acquire an analytical solution in application 2, we only include sinusoidal (cf. periodic) temporal variability in E_0, k_d, and d (see Section 4.2.4). A conceptual diagram of our approach is illustrated in Fig. 4.1.

4.2.1 Phytoplankton model

To describe PP in a tidal, well-mixed system, we start from the following one-dimensional, differential equation for depth-averaged phytoplankton biomass concentration growth rate

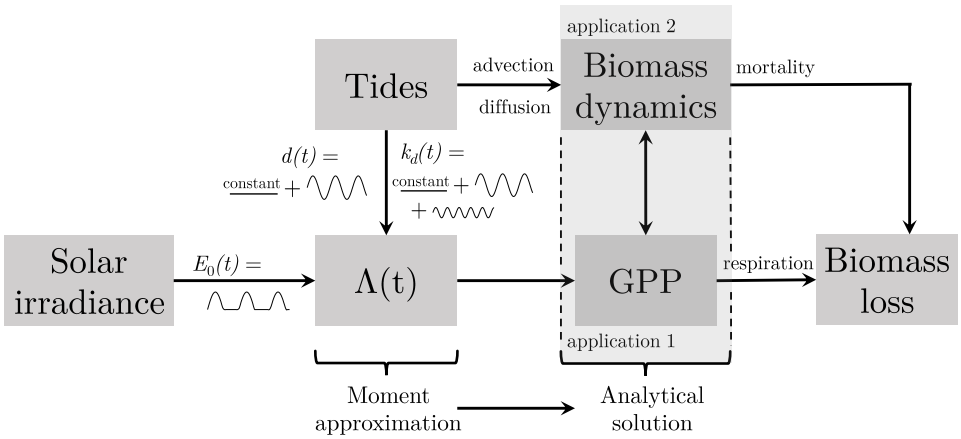

Figure 4.1: Conceptual diagram of our idealized model. In a well-mixed, light-limited tidal system, gross primary production (GPP) is limited by the DAP function $\Lambda(t)$, which is influenced by solar irradiance and tides. The tides also directly alter biomass dynamics through advection and diffusion in the longitudinal direction. We apply the moment approximation to $\Lambda(t)$ and idealize temporal variability in E_0, k_d, and d. This simplification results in an analytical expression that relates temporal variability of GPP and corresponding phytoplankton biomass dynamics to variability in E_0, k_d, and d. We apply the idealized model to time-averaged GPP in dynamic equilibrium (application 1) and a phytoplankton bloom (application 2) in the Scheldt estuary (Belgium).

(units kg m^{-3} s^{-1}) (Langdon, 1993; Desmit et al., 2005):

$$\underbrace{\frac{\partial \tilde{B}(x,t)}{\partial t}}_{\text{phytoplankton biomass growth rate}} + \underbrace{\frac{1}{d}\int_0^d \left[\frac{\partial}{\partial x}(\tilde{\tilde{u}}\tilde{B}) + \frac{\partial}{\partial x}\left(K_h \frac{\partial}{\partial x}\tilde{B}\right)\right] dz}_{\text{change in } \tilde{B}(t) \text{ due to advection/diffusion}}$$

$$= \underbrace{\tilde{B} \cdot \left[P_{\max} \cdot \left(\frac{1}{d}\int_0^d \tilde{\Lambda} dz\right)}_{\text{gross primary production (GPP)}} \cdot \underbrace{(1-\rho_B)}_{\text{respiration}} \underbrace{-m}_{\text{mortality}}\right], \tag{4.1}$$

where $\tilde{B}$ is the depth-averaged phytoplankton biomass concentration, x is the distance from the mouth, z is the distance from the water surface in the downward direction, t is the time, ρ_B is the respiration and excretion coefficient, m is the mortality coefficient, $P_{\max}$ is the maximum photosynthetic rate, $\tilde{\Lambda}$ is a GPP light limitation function, $\tilde{\tilde{u}}$ is the (vertically homogeneous) water velocities in the longitudinal direction, and K_h is the longitudinal eddy diffusivity coefficient.

In Eq. (4.1), we assume vertically, well-mixed systems resulting in a depth-independent phytoplankton biomass concentration $\tilde{B}(x,t)$. Furthermore, we exclude nutrient limitation since we consider PP in nutrient replete, light-limited systems. Moreover, we also exclude temperature dependence and implicitly included grazing of phytoplankton in the mortality coefficient m. Crucially, we assume balanced-growth conditions: growth and photosynthesis are considered never to be decoupled on the time scale of our application (i.e., hours-days). All photosynthesis is used for biomass production (Berman-Frank and Dubinsky, 1999). Such decoupling is typical in nutrient limitation situations, which we assume not to occur in the turbid, nutrient replete estuaries under study. Furthermore, we assume that phytoplankton species surviving in turbid conditions are adapted to harvest every photon possible and are thus able to store excess photosynthesized material rather than excrete photosynthetically-derived dissolved organic carbon compounds (PDOC). Consequently, also during the short periods that cells reside in the upper part of the water column where light availability is maximal, growth is balanced. To model light limitation, we use the Platt light limitation function $\tilde{\Lambda}$ (Platt et al., 1980):

$$\tilde{\Lambda} = \left\{1 - \exp\left[-\frac{\alpha}{P_{\max}} I\right]\right\}, \tag{4.2}$$

in which α is the photosynthetic efficiency and I is the light intensity. Using the Lambert-Beer expression for exponential light attenuation in a water body, Eq. (4.2) yields

$$\tilde{\Lambda}(z,t) = \left\{1 - \exp\left[-\tilde{\beta}\exp\left(-\tilde{z}\right)\right]\right\}, \tag{4.3}$$

in which $\tilde{\beta}$ and $\tilde{z}$ are dimensionless numbers defined as

$$\tilde{\beta} = \frac{\alpha E_0}{P_{\max}} \qquad \text{and} \qquad \tilde{z} = k_d \cdot z. \tag{4.4}$$

Because the system is assumed to be well-mixed, the total biomass production GPP(t) integrated over the water depth at a fixed location x reads as

$$\mathrm{GPP}(t) = B(t) \cdot P_{\max} \cdot \Lambda(t), \tag{4.5}$$

with Λ being the depth-averaged Platt expression:

$$\Lambda(t) = \frac{1}{d}\int_0^d \tilde{\Lambda}(z,t)dz. \tag{4.6}$$

For an analytical solution of the DAP, the reader is referred to Appendix 4.A. In the following section, we apply the moment approximation to $\Lambda(t)$ to study the impact of temporal variability in the individual factors E_0, k_d, and d and their interactions on PP.

4.2.2 Moment approximation

Temporal variability in E_0, k_d, and d impacts phytoplankton dynamics through the time integral of the DAP. This is our starting point to assess the impact of tidal and solar

fluctuations on GPP using the moment approximation. As a first step, we add a (further unspecified) time dependence to the variables in the DAP:

$$E_0(t) = \langle E_0 \rangle + E_0'(t), \tag{4.7}$$
$$k_d(t) = \langle k_d \rangle + k_d'(t), \quad \text{and} \tag{4.8}$$
$$d(t) = \langle d \rangle + d'(t), \tag{4.9}$$

in which the angle brackets denote 'time-averaged value of'. This construction allows us to perform a Taylor expansion of the DAP. Consequently, we can estimate the impact of temporal variability of the individual parameters on phytoplankton dynamics and their interactions. Also, it is easy to revert to the time-independent result by making $E_0'(t)$, $k_d'(t)$, and $d'(t)$ equal to zero. As a second step, we apply a Taylor expansion to the analytic expression of the DAP around the time-averaged values in Eqs. (4.8) and (4.9). For a detailed analysis, we refer the reader to Appendix 4.B. Upto second order, this Taylor expansion reads as

$$\begin{aligned}\Lambda(t) \approx \mathrm{mfun}_0(\beta,\lambda) \times \Big\{ 1 + \\ &+ \mathrm{mfun}_\kappa(\beta,\lambda) \cdot [\kappa(t) + \delta(t)] \\ &+ \mathrm{mfun}_\epsilon(\beta,\lambda) \cdot \epsilon(t) \\ &+ \mathrm{mfun}_{\kappa^2}(\beta,\lambda) \cdot \left[\kappa^2(t) + \delta^2(t)\right] \\ &+ \mathrm{mfun}_{\epsilon^2}(\beta,\lambda) \cdot \epsilon^2(t) \\ &+ \mathrm{mfun}_{\epsilon\kappa}(\beta,\lambda) \cdot [\epsilon(t) \cdot \kappa(t) + \epsilon(t) \cdot \delta(t)] \\ &+ \mathrm{mfun}_{\kappa\delta}(\beta,\lambda) \cdot [\delta(t) \cdot \kappa(t)] \Big\},\end{aligned} \tag{4.10}$$

in which κ, ϵ, and δ are dimensionless relative fluctuations defined as

$$\epsilon(t) = \frac{E_0'(t)}{\langle E_0 \rangle}, \quad \kappa(t) = \frac{k_d'(t)}{\langle k_d \rangle}, \quad \text{and}$$
$$\delta(t) = \frac{d'(t)}{\langle d \rangle} \tag{4.11}$$

and β and λ are defined as

$$\beta = \frac{\alpha \langle E_0 \rangle}{P_{\max}} \qquad \text{and} \qquad \lambda = \langle k_d \rangle \cdot \langle d \rangle. \tag{4.12}$$

The mfun functions determine the impact of temporal variability in E_0, k_d, and d on the DAP upto second order and are defined in Appendix 4.B. By definition, the function mfun_0 is the DAP without temporal parameter fluctuations. The other terms in Eq. (4.10) quantify the impact of temporal variability of the individual forcings (terms $\sim$ $\mathrm{mfun}_\kappa, \mathrm{mfun}_\epsilon, \mathrm{mfun}_{\kappa^2}$, and $\mathrm{mfun}_{\epsilon^2}$) and their interactions (terms $\sim \mathrm{mfun}_{\epsilon\kappa}$ and $\mathrm{mfun}_{\kappa\delta}$). By construction of Λ, κ and δ come with identical mfun functions:

$$\mathrm{mfun}_{\delta} = \mathrm{mfun}_{\kappa}, \tag{4.13}$$
$$\mathrm{mfun}_{\delta^2} = \mathrm{mfun}_{\kappa^2}, \tag{4.14}$$
$$\mathrm{mfun}_{\delta\epsilon} = \mathrm{mfun}_{\kappa\epsilon}. \tag{4.15}$$

The mfun functions are determined by two dimensionless numbers λ and β, which characterize the system under study and have a clear physical interpretation. λ is a measure for the photic properties of the water column. Turbid and deep systems have a large λ, while transparent and shallow systems correspond with a small λ. For fully mixed systems, λ is proportional to the ratio of the mixing depth and euphotic depth, that is, the depth at which the light intensity is 1 % of the incident light (Sverdrup, 1953; Kromkamp and Peene, 1995; Desmit et al., 2005). This ratio determines the time phytoplankton spends in the dark and thus affects net PP. Often a critical depth is defined: net positive PP can only occur when the depth of the mixed layer is less than the critical value (Sverdrup, 1953). Our results confirm that this ratio is an important characteristic of the system, not only controlling the potential for net PP but also controlling the response of PP to temporal variability in light climate. The second dimensionless number β increases with increasing solar irradiance and photosynthetic efficiency. Consequently, for a fixed $P_{\max}/\alpha$ ratio, an equatorial system (cf. more solar irradiance) typically corresponds to a larger value of β than a system in the northern hemisphere. In the following, we apply our approach to two case studies in the Scheldt estuary using real observations.

4.2.3 Application 1: time-averaged GPP

In the first application, we use our idealized model to analyze the impact of temporal fluctuations on time-averaged GPP in case phytoplankton biomass is top-down controlled by grazing organisms (e.g., zooplankton) and can be considered constant, although GPP > 0. Consequently, time-averaged GPP becomes proportional to time-averaged DAP:

$$\big\langle \mathrm{GPP}(t) \big\rangle = B \cdot P_{\max} \cdot \big\langle \Lambda(t) \big\rangle. \tag{4.16}$$

We compute $\langle \Lambda(t) \rangle$ using Eq. (4.10):

$$\begin{aligned}\langle \Lambda(t) \rangle \approx \mathrm{mfun}_0(\beta,\lambda)\Big\{ 1+ \\ + \mathrm{mfun}_{\kappa^2}(\beta,\lambda)\Big[\tilde{\mathrm{Var}}[k_d(t)] + \tilde{\mathrm{Var}}[d(t)]\Big] \\ + \mathrm{mfun}_{\epsilon^2}(\beta,\lambda)\cdot \tilde{\mathrm{Var}}[E_0(t)] \\ + \mathrm{mfun}_{\epsilon\kappa}(\beta,\lambda)\Big[\tilde{\mathrm{Cov}}[E_0(t),k_d(t)] \\ + \tilde{\mathrm{Cov}}[E_0(t),d(t)]\Big] \\ + \mathrm{mfun}_{\kappa\delta}(\beta,\lambda)\cdot \tilde{\mathrm{Cov}}[k_d(t),d(t)]\Big\},\end{aligned} \tag{4.17}$$

in which $\tilde{\mathrm{Var}}$ and $\tilde{\mathrm{Cov}}$ are the relative statistical identities variance and covariance. For example, we have

$$\tilde{\mathrm{Var}}[k_d(t)] = \langle \kappa^2(t) \rangle \quad \text{and} \tag{4.18}$$

$$\tilde{\mathrm{Cov}}[E_0(t),k_d(t)] = \langle \epsilon(t)\cdot\kappa(t) \rangle. \tag{4.19}$$

As a result of the definitions in Eqs. (4.8) and (4.9), the time averages of the $\sim \mathrm{mfun}_\kappa$- and mfun_ϵ-terms in Eq. (4.10) disappear in Eq. (4.17).

Eq. (4.17) reveals an important interpretation of the second-order mfun functions; variability in k_d, d, and E_0 results in a systematic upward or downward shift in its time-average $\langle \Lambda(t) \rangle$. The second-order mfun functions represent the factors by which the variances and covariances have to be multiplied to calculate the magnitude of this shift. Moreover, the mfun functions define the sign of the shift in $\langle \Lambda(t) \rangle$ and corresponding $\langle \mathrm{GPP} \rangle$. The magnitude is both determined by the average system characteristics (λ, β) and the temporal variability in E_0, k_d, and d, which define the magnitude of the variance and covariance factors in Eq. (4.17), and is thus different when considering typical summer or winter conditions.

Therefore, we apply our idealized model to both a summer (10-06-2013 until 02-07-2013) and winter (20-02-2013 until 13-03-2013) case in the Scheldt estuary. Figures 4.2 and 4.3 show the high-frequency observations of E_0, turbidity, and d we use in our first application. The observations were measured in the Scheldt estuary in the brackish region at Kruibeke (∼85 km from the mouth). We choose Kruibeke because here our assumptions (e.g., well-mixed, light-limited) are valid and a long-term record of continuous time series of turbidity exists (Cox et al., 2015).

The turbidity time series were obtained using a YSI 6600 multiparameter probe, equipped with an optical turbidity sensor (YSI6136). Turbidity is expressed in NTU (Nephelometric Turbidity Units). Light from the emitter enters the sample and scatters off particles in the water. The light, scattered at 90 degrees, enters a detector fiber and

Table 4.1: Summarized values corresponding to the time series from Figs. 4.2 and 4.3. N is the number of measurements of E_0, k_d, and d. $\tilde{\text{Var}}$ and $\tilde{\text{Cov}}$ are the relative variance and covariance as defined in Eqs. (4.18) and (4.19).

Summer case							
N	3000	$\langle E_0 \rangle$	171 J m^{-2} s^{-1}	$\tilde{\text{Var}}[E_0]$	1.633	$\tilde{\text{Cov}}[E_0, k_d]$	0.043
λ	92.6	$\langle k_d \rangle$	10.8 m^{-1}	$\tilde{\text{Var}}[k_d]$	0.099	$\tilde{\text{Cov}}[k_d, d]$	0.036
β	3	$\langle d \rangle$	8.60 m	$\tilde{\text{Var}}[d]$	0.049	$\tilde{\text{Cov}}[E_0, d]$	0.002
Winter case							
N	3000	$\langle E_0 \rangle$	70.0 J m^{-2} s^{-1}	$\tilde{\text{Var}}[E_0]$	2.704	$\tilde{\text{Cov}}[E_0, k_d]$	-0.021
λ	95.2	$\langle k_d \rangle$	11.1 m^{-1}	$\tilde{\text{Var}}[k_d]$	0.143	$\tilde{\text{Cov}}[k_d, d]$	0.037
β	1.05	$\langle d \rangle$	8.60 m	$\tilde{\text{Var}}[d]$	0.045	$\tilde{\text{Cov}}[E_0, d]$	-0.013

Table 4.2: Overview of parameter values used in this paper. The values are based on the literature (Kromkamp and Peene, 1995, 2005; Cox et al., 2010; Maris and Meire, 2016).

$P_{\max}$	5	mg C (mg Chl-a)$^{-1}$ h^{-1}	C:Chl-a	25	mg C (mg Chl-a)$^{-1}$
α	0.21	mg C (mg Chl-a)$^{-1}$h^{-1} $\cdot$ (J m^{-2} s^{-1})$^{-1}$	B_0	775	μg L^{-1}

is measured by a photodiode (YSI, 2017a). The turbidity probe was calibrated in the laboratory using calibration liquid YSI6074 and demineralized water as a zero reference. To compute k_d [m^{-1}] from turbidity [NTU], we used the following expression (Cox et al., 2017):

$$k_d = 0.39(2.1\text{NTU}^{-1} \cdot \text{turb.} - 1.82)^{0.64}\ \text{m}^{-1}. \tag{4.20}$$

Data sets of turbidity and depth at Kruibeke were obtained from waterinfo.be (Waterinfo.be, 2019). We used depth recordings from the tidal gauge at Hemiksem, located approximately 4 km upstream from Kruibeke. Incident irradiance data E_0(t) was obtained from the Royal Meteorological Institute (RMI) of Belgium (RMI, 2013) in Stabroek ($\sim$ 25 km from Kruibeke and 50 km from Schellebelle, the other case study site, see below). The sampling interval of E_0, turbidity, and depth was 10, 15, and 15 min, respectively. A summary of the parameter values corresponding to the data sets is presented in Table 4.1. Other parameter values used in our calculations are summarized in Table 4.2. These parameters were based on the literature (Kromkamp and Peene, 1995, 2005; Cox et al., 2010; Maris and Meire, 2016). To assess the accuracy of the moment approximation upto second-order terms, we compare the results to the output of a numerical integrator of DAP, making use of the same time series.

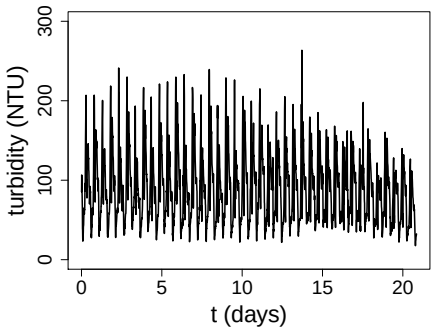

(a) Turbidity in summer

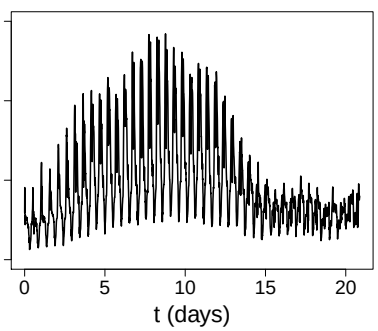

(b) Turbidity in winter

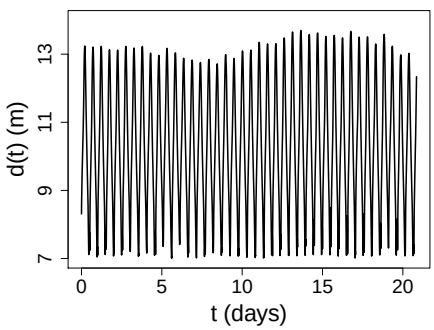

(c) Water depth in summer

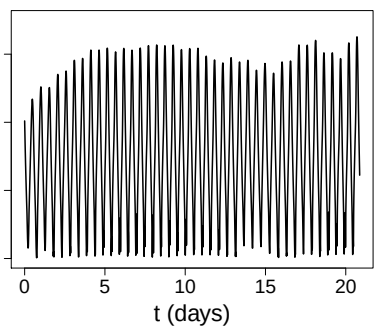

(d) Water depth in winter

Figure 4.2: (a)-(b) Turbidity and (c)-(d) water depth measured in the Scheldt estuary at Kruibeke station (Belgium) in summer and winter.

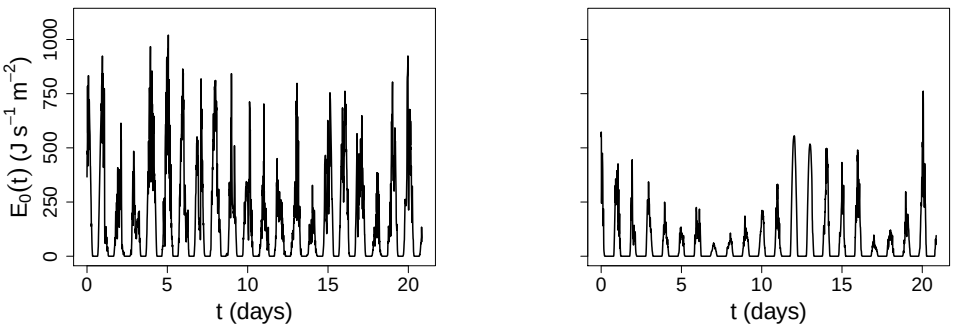

(a) Solar irradiance in summer

(b) Solar irradiance in winter

Figure 4.3: Solar irradiance E_0 measured at Stabroek (Belgium) in (a) summer and (b) winter. Stabroek is located approximately 25 km from the monitoring station at Kruibeke.

4.2.4 Application 2: phytoplankton bloom

During typically observed phytoplankton spring blooms, we cannot assume dynamic equilibrium of $\tilde{B}(t,x)$ in Eq. (4.1). In the following, we study the full solution of Eq. (4.1). This spatio-temporal differential equation cannot be solved analytically without further assumptions. Therefore, we again focus on a specific location $x = x^*$ and assume that $\tilde{B}(t,x)$ evolves linearly along the estuarine axis near $x = x^*$. Moreover, we suppose that its shape in the longitudinal direction is time-independent on the time scale of our application (∼days):

$$\tilde{B}(x,t) = B(t)f(x), \tag{4.21}$$

in which $f(x)$ is a linear function of x. Furthermore, we assume a phase of $-\pi/2$ between the longitudinal velocity $u(t)$ and the water elevation (cf. d) following van Rijn (2010). For a detailed derivation, the reader is referred to Appendix 4.C. The solution of $B(t)$ yields

$$\begin{aligned} B(t) =& \tilde{A} e^{-m^* \cdot t + (1-\rho_B)\cdot \mathrm{P}_m \int \Lambda(t) dt} \\ & \times e^{\left[\frac{\gamma}{\omega_{M2}} \cdot \cos(\omega_{M2} \cdot t + \Phi_{M2} + \theta)\right]}, \end{aligned} \tag{4.22}$$

with

$$\tilde{A} = B_0 e^{-(1-\rho_B)\cdot \mathrm{P}_m \int \Lambda(t) dt|_{t=0} - \frac{\gamma}{\omega_{M2}} \cdot \cos(\Phi_{M2} + \theta)} \quad \text{and} \tag{4.23}$$

where ω_{M_2} is the angular frequency corresponding to the semidiurnal lunar M2 tide and Φ_{M_2} and θ are the phases corresponding to the idealized time dependence of the water depth d [see below, Eq. (4.28)]. The coefficients m^* and γ are defined in Appendix 4.C. The integrated loss rate m^* incorporates losses due to grazing, mortality, and residual

water currents. γ is a measure of the amplitude of the sinusoidal behavior due to advective transport of phytoplankton biomass [see Eq. (4.41)]. Again, we apply the moment approximation to the solution of $B(t)$ in Eq. (4.22), which yields

$$\begin{aligned}\int \Lambda(t)dt \approx \mathrm{mfun}_0 \cdot t \times \Big\{ 1 + \\ + \frac{\mathrm{mfun}_\kappa(\beta,\lambda)}{t} \cdot \int \left[\kappa(t) + \delta(t)\right] dt \\ + \frac{\mathrm{mfun}_\epsilon(\beta,\lambda)}{t} \cdot \int \epsilon(t) \cdot dt \\ + \frac{\mathrm{mfun}_{\kappa^2}(\beta,\lambda)}{t} \cdot \int \left[\kappa^2(t) + \delta^2(t)\right] dt \\ + \frac{\mathrm{mfun}_{\epsilon^2}(\beta,\lambda)}{t} \cdot \int \epsilon^2(t) dt \\ + \frac{\mathrm{mfun}_{\epsilon\kappa}(\beta,\lambda)}{t} \cdot \int \left[\epsilon(t) \cdot \kappa(t) \right. \\ + \qquad\qquad \left. \epsilon(t) \cdot \delta(t)\right] dt \\ + \frac{\mathrm{mfun}_{\kappa\delta}(\beta,\lambda)}{t} \cdot \int \left[\delta(t) \cdot \kappa(t)\right] dt \Big\}. \end{aligned} \tag{4.24}$$

To calculate the integrals in Eq. (4.24), we use approximate expressions for $\epsilon(t)$, $\kappa(t)$, and $\delta(t)$. We assume that solar irradiance E_0 is given by a truncated sinusoid following Cox et al. (2015):

$$E_0(t) = \max(0, a + b\cos(\omega_{S1} t)), \tag{4.25}$$

in which a and b are further unspecified parameters and ω_{S1} is the diurnal angular frequency. Consequently, we neglect aperiodic temporal variability in E_0 over more rapid time scales (seconds to minutes, due to, for example, cloud shading) and only include the dominant day-night pattern. We simplify Eq. (4.25) by only including the first three temporal terms of the Fourier series:

$$E_0(t) = \left\langle E_0 \right\rangle + \underbrace{\sum_{n=1}^{3} \hat{E}_n \cos(n\omega_{S1} t)}_{E_0'(t)}. \tag{4.26}$$

Similarly, we only consider the dominant and periodic ω_{M2} and $\omega_{M4} = 2\omega_{M2}$ temporal fluctuations in k_d and d and truncate frequencies larger than M4 (i.e., M6, M8, etc. are neglected) following Chernetsky et al. (2010), Dijkstra et al. (2017), and Horemans et al. (2020):

$$k_d'(\mathrm{t}) = \hat{K}_2 \cos(\omega_{M2} t + \Phi_{\mathrm{M}_2}) + \hat{K}_4 \cos(\omega_{M4} t + \Phi_{\mathrm{M}_4}), \tag{4.27}$$

$$d'(\mathrm{t}) = \hat{D}_2 \cos(\omega_{M2} t + \Phi_{\mathrm{M}_2} + \theta), \tag{4.28}$$

in which $\hat{K}_2$, $\hat{K}_4$, and $\hat{D}_2$ and Φ_{M_2}, Φ_{M_4}, and θ are (calibrated) amplitudes and phases, respectively. To estimate these amplitudes and phases, we fitted Eqs. (4.26)-(4.28) to

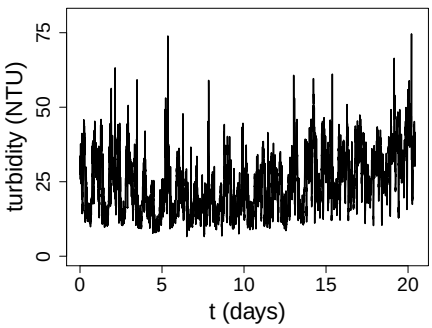

(a) Turbidity in spring

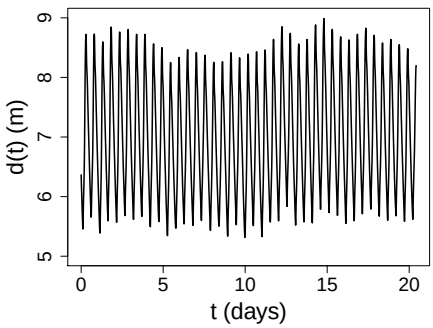

(b) Water depth in spring

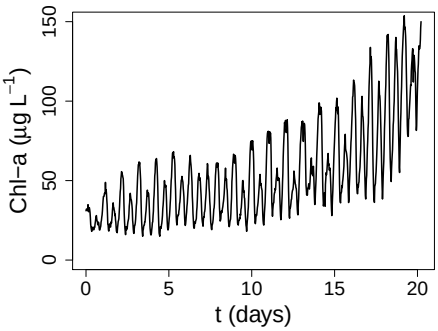

(c) Chl-a concentration in spring

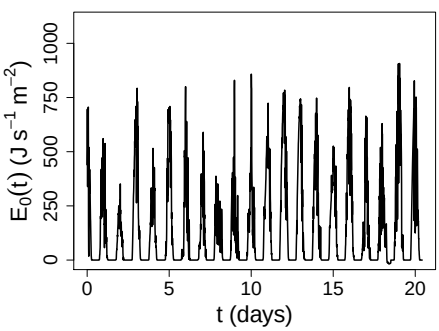

(d) Solar irradiance in spring

Figure 4.4: (a) Turbidity, (b) water depth, and (c) Chlorophyll-a (Chl-a) concentration measured in the Scheldt estuary at Schellebelle (Belgium) in spring during a phytoplankton bloom. (d) The solar irradiance E_0 is measured at Stabroek (Belgium), located approximately 50 km from Schellebelle.

observed time series (see Appendix 4.D). We use time series measured in the Scheldt estuary in the freshwater zone at Schellebelle (∼140 km from the mouth) during a spring bloom (29-03-2017 until 19-04-2017, Fig. 4.4). The same methodology and sensors as in application 1 were used. Chl-a concentration was measured using a fluorescence sensor [YSI6025, wavelength 435-470 nm (YSI, 2017b)] with a sampling interval of 5 minutes. Parameters m^*, γ, and ρ_B are obtained by fitting Eq. (4.22) to the observed Chl-a time series. We used a fixed ratio of 25 mg C (mg Chl-a)$^{-1}$ to transform Chl-a concentration to phytoplankton biomass concentration (Maris and Meire, 2016), assuming balanced-growth conditions. Table 4.3 summarizes the resulting estimated parameters. The order of magnitude of γ and m^* corresponds to the estimated order in Appendix 4.C, that is, $\mathcal{O}(10^{-1})$ h^{-1} and $\mathcal{O}(10^{-2})$ h^{-1}, respectively. The order of the fitted value for ρ_B agrees with values found by Desmit et al. (2005).

Table 4.3: Parameter values estimated by fitting the presumed idealized time dependencies for E_0(t), k_d(t), and $d(t)$ [Eqs. (4.26)-(4.28)] and analytical solution of $B(t)$ to the corresponding data sets of k_d(t), E_0(t), $d(t)$, and $B(t)$ measured in the Scheldt estuary at Schellebelle (Figs. 4.4a-c).

	J m^{-2} s^{-1}		m^{-1}				h^{-1}				
$\hat{E}_1$	142	$\langle k_d \rangle$	4.56	$\langle d \rangle$	4.5 m	ω_{S1}	$\frac{2\pi}{24}$	Φ_{M2}	-3.59	$\langle E_0 \rangle$	168 J m^{-2} s^{-1}
$\hat{E}_2$	75.3	$\hat{K}_2$	0.82	$\hat{D}_2$	1.36 m	ω_{M2}	$\frac{2\pi}{12.42}$	Φ_{M4}	-0.253	m^*	0.0834 h^{-1}
$\hat{E}_3$	3.44	$\hat{K}_4$	0.43	ρ_B	0.837	ω_{M4}	$2{\cdot}\omega_{M2}$	θ	-0.30	γ	0.156 h^{-1}

To summarize, the combination of the moment approximation in Eq. (4.24) and idealized time dependence in E_0, k_d, and d [Eqs. (4.26)-(4.28)] allows us to analytically solve the time integral of $\Lambda(t)$ and corresponding analytical solution of $B(t)$ presented in Eq. (4.22). The main advantage of this approach is that it enables us to directly analyze the propagation of the dominant harmonics in forcings E_0, k_d, d, and advective water flow into the dynamics of $B(t)$. The analytical solution of $\int \Lambda(t)dt$ is listed in Appendix 4.E.

4.3 Results

We first show the generic results of the moment approximation by presenting the mfun functions [see Eq. (4.10)], which translate temporal variability in k_d, E_0, and d to temporal variability in Λ, GPP, and phytoplankton biomass dynamics. Next, using these mfun functions, we present the results of our two applications in the Scheldt estuary, i.e., time-averaged GPP in dynamic equilibrium (application 1) and a phytoplankton bloom in dynamic non-equilibrium (application 2).

4.3.1 Moment approximation: the mfun functions

4.3.1.1 mfun functions of the zeroth- and first-order terms

The zeroth-order mfun$_0$ function is, by definition, equal to the time-averaged DAP factor $\langle \Lambda \rangle$ in the absence of temporal variability in E_0, k_d, and d. Figure 4.5 shows mfun$_0$ for various β and λ. mfun$_0$ ranges from 0 (*maximal light limitation; no GPP*) to 1 (*no light limitation; maximal GPP*) and has a simple structure; it increases with increasing β (cf. increasing solar irradiance/ PP efficiency) and decreases with increasing λ (cf. increasing turbidity/depth). The mfun$_\kappa$ and mfun$_\epsilon$ functions are plotted in Figs. 4.6a and 4.6b, respectively. These first-order functions represent the system-dependent multiplication factors that are required to compute the amplitude of different harmonics in light climate (cf. Λ), GPP, and corresponding biomass dynamics from the respective amplitudes in E_0, k_d, and d. mfun$_\kappa$ is negative for every value of λ and β (Fig. 4.6a), simply reflecting

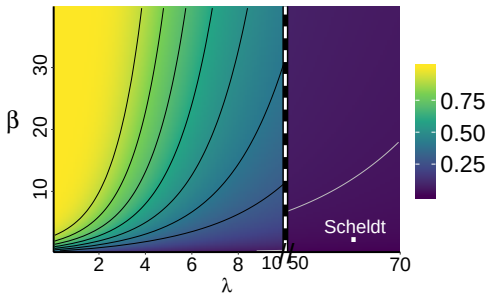

Figure 4.5: The mfun_0 function for various β and λ. mfun_0 corresponds to the DAP function Λ in the absence of fluctuations. The averaged parameter set corresponding to the Scheldt estuary cases described in this paper is also illustrated (i.e., $\lambda \approx 60, \beta \approx 3$).

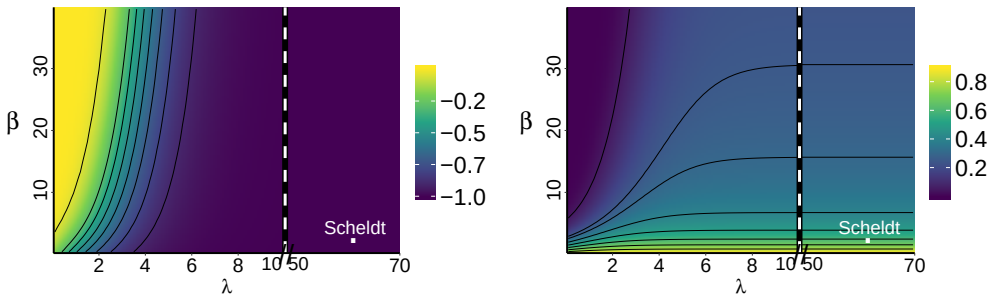

(a) mfun_κ (b) mfun_ϵ

Figure 4.6: The first-order mfun functions (a) mfun_κ and (b) mfun_ϵ for various β and λ. The averaged parameter set corresponding to the Scheldt estuary cases described in this paper is also illustrated (i.e., $\lambda \approx 60, \beta \approx 3$).

the fact that an increase in k_d (or d) leads to a decrease in $B(t)$. In contrast, mfun_ϵ is positive, reflecting the fact that increasing incident irradiance leads to increasing $B(t)$ (Fig. 4.6b).

4.3.1.2 mfun functions of the second-order terms

The second-order mfun functions represent the factors by which the variances and covariances have to be multiplied to calculate the magnitude of a systematic upward or downward shift in its time-average $\langle \Lambda(t) \rangle$ [Eq. (4.17)]. They have a more interesting structure (Fig. 4.7). Figure 4.7b shows that mfun_{ϵ^2} is always negative. In contrast, the

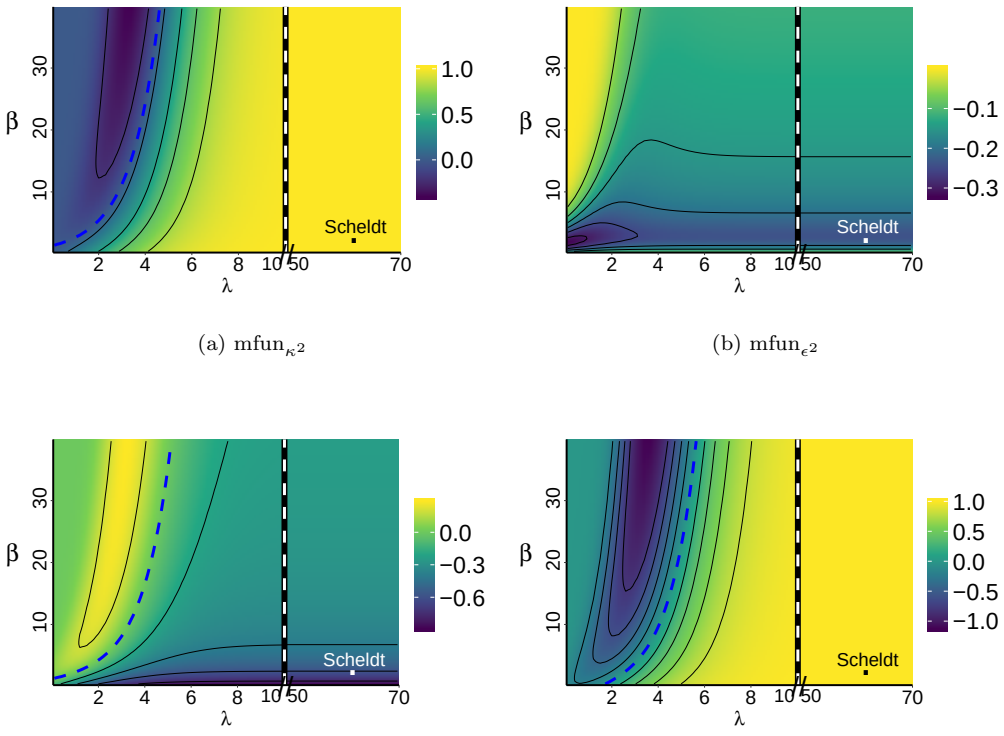

(a) mfun_{κ^2}

(b) mfun_{ϵ^2}

(c) $\text{mfun}_{\kappa\epsilon}$

(d) $\text{mfun}_{\kappa\delta}$

Figure 4.7: The second-order mfun functions (a) mfun_{κ^2}, (b) mfun_{ϵ^2}, (c) $\text{mfun}_{\kappa\epsilon}$, and (d) $\text{mfun}_{\kappa\delta}$ for various β and λ. The averaged parameter set corresponding to the Scheldt estuary cases described in this paper is also illustrated (i.e., $\lambda \approx 60, \beta \approx 3$). The contour where the mfun function equals zero and changes sign is depicted by a dashed curved line.

sign of the other second-order mfun functions depends on the specific values of λ and β (Figs. 4.7a, 4.7c, and 4.7d). This has a simple interpretation for the time-averaged $\langle \mathrm{GPP} \rangle$ [Eqs. (4.16) and (4.17)]. Indeed, temporal variability in E_0 always results in a decrease in $\langle \mathrm{GPP} \rangle$, while variability in light attenuation and depth can lead to both a decrease or an increase in $\langle \mathrm{GPP} \rangle$, depending on the characteristics of the system under study. Here, we assumed that the covariance terms due to E_0 ($\sim \mathrm{mfun}_{\epsilon\kappa}$) are negligible compared to the variance term ($\sim \mathrm{mfun}_{\epsilon^2}$) in Eq. (4.17). Similarly, for phytoplankton in the exponential growth phase (cf. bloom), second-order temporal variability in E_0 always result in a decrease of the exponential growth, while variability in light attenuation and depth can lead to both a decrease or an increase of the exponential growth. It must be noted that tidal systems for which mfun_{κ^2} is negative ($\lambda \lesssim 5$, Figs. 4.7a, 4.7c, and 4.7d), correspond to shallow and clear systems which can be found in, for example, the Dutch Wadden Sea or the Oosterschelde (Rijkswaterstaat, 2020). These systems often experience nutrient limitation, and thus the results presented here are valid only during periods without nutrient limitation.

To summarize, the results of the mfun functions show that the propagation of temporal variability in the parameters affecting light climate (i.e., E_0, k_d, and d) to temporal variability in GPP and phytoplankton biomass dynamics may show opposing trends for the different parameters. Moreover, this propagation depends on the time-independent characteristics of the system (i.e., λ and β) and may thus differ for different systems and seasons. In the following sections, we use these results to study our two applications in the Scheldt estuary, covering different seasons.

4.3.2 Application 1: time-averaged GPP

In this section, we use the mfun function results from the moment approximation presented in the previous section to study the impact of temporal variability in light climate (cf. E_0, k_d, and d) on time-averaged $\langle \mathrm{GPP} \rangle$ in dynamic equilibrium in the brackish part of the Scheldt estuary. Because we expect different results for different seasons, we analyze both a summer and winter case.

At our relatively deep and turbid case study location, mfun_{κ^2} is always positive (Fig. 4.7a) and thus temporal variability in k_d and d lead to an increase in $\langle \mathrm{GPP} \rangle$. In contrast, temporal variability in E_0 decreases $\langle \mathrm{GPP} \rangle$ (Fig. 4.7b). Figure 4.8 shows the results of $\langle \mathrm{GPP} \rangle$ when including temporal variability in all parameters (all var), normalized with $\langle \mathrm{GPP} \rangle$ with time-averaged parameters (i.e., $\langle E_0 \rangle$, $\langle k_d \rangle$, and $\langle d \rangle$) for various integration times T (8.5 h-21 days) using the moment approximation (left) and a numerical integrator (right), applied to a summer (top) and winter (bottom) case. When the presented value is ≈ 1, the impact of temporal variability is negligible. To compute the separate impact of temporal variability in E_0, k_d, and d on $\langle \mathrm{GPP} \rangle$, we also show the results exclusively including temporal variability in the individual parameters E_0 ($\mathrm{E_0}$ var), k_d (k_d var), and d (d var).

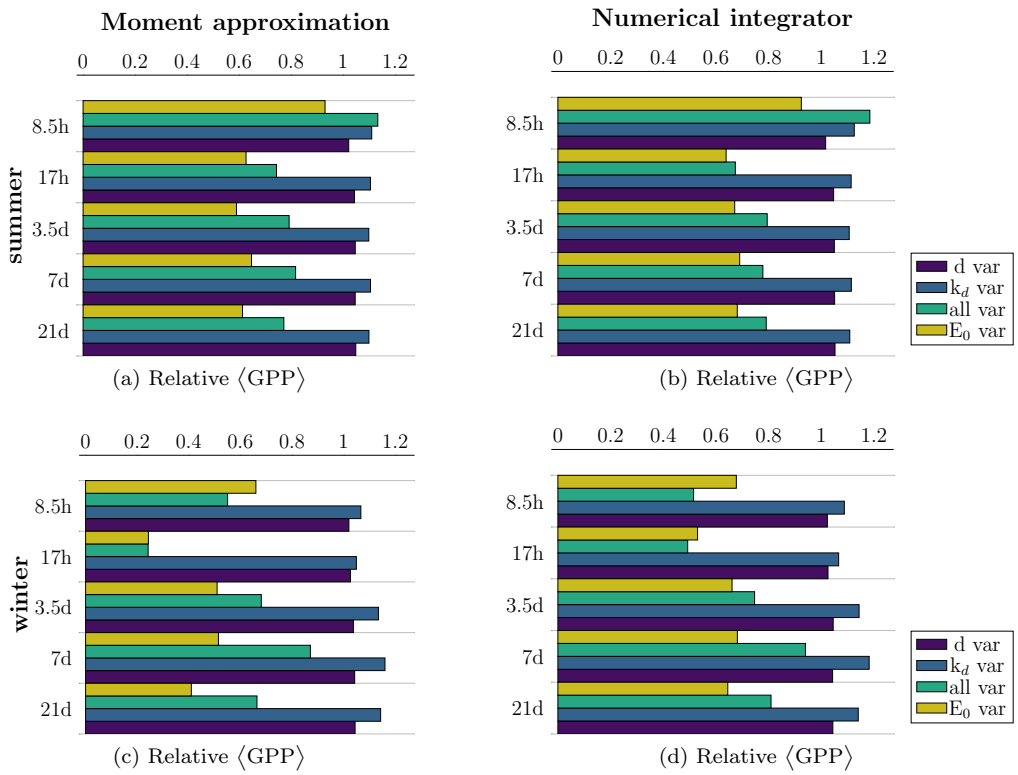

Figure 4.8: Time-averaged gross primary production $\langle \mathrm{GPP} \rangle$ in dynamic equilibrium, relative to $\langle \mathrm{GPP} \rangle$ using time-averaged parameters $\langle E_0 \rangle$, $\langle k_d \rangle$, and $\langle d \rangle$ for various integration times (8.5 h-21 days) using the moment approximation (left) and a numerical integrator (right) in (a)-(b) summer and (c)-(d) winter. Our framework allows us to compute the impact of temporal variability in an individual parameter on $\langle \mathrm{GPP} \rangle$ (cf. d var, k_d var, and E_0 var) or when temporal variability in all parameters is included (cf. all var). When the presented value is ≈ 1, the impact of temporal variability is negligible.

4.3.2.1 Summer case

In summer, the relative impact of temporal variability on $\langle \mathrm{GPP} \rangle$ is < 10 % for k_d and d and 10-30 % for E_0. Overall, Fig. 4.8 shows good correspondence between the moment approximation and the numerical integrator, even for integration times $T < 24$ h, that is, the period corresponding to the angular frequency of temporal variability in E_0. In this specific summer case study, excluding temporal fluctuations in E_0, k_d, and d results in an error of approximately 20 %. Temporal variability in E_0 (E_0 var) has the largest impact on $\langle \mathrm{GPP} \rangle$.

4.3.2.2 Winter case

Also in the winter case, the moment approximation is in good correspondence with the numerically integrated impact of temporal variability in E_0, k_d, and d on $\langle \mathrm{GPP} \rangle$, respectively approximately 20-50, 5-20, and < 10 %. However, we have a slight decrease in accuracy, which is due to the relatively large temporal fluctuations in solar irradiance compared to the averaged solar irradiance in winter. This results in a less accurate approximation by sinusoids of the solar temporal fluctuations [Eq. (4.26)]. The main difference with the summer case is an increase in the relative importance of fluctuations in k_d. This difference follows from the relative magnitude of temporal variability in k_d (cf. $\tilde{\mathrm{V}}\mathrm{ar}[k_d(t)]$), which is in winter an order of magnitude larger compared to summer (see Table 4.1).

To summarize, our summer and winter cases illustrate that the impact of fluctuations in light climate on $\langle \mathrm{GPP} \rangle$ in dynamic equilibrium may be important, season-dependent, and that a careful analysis based on the observed time series of E_0, k_d, and d is required.

4.3.3 Application 2: phytoplankton bloom

In this section, we apply our idealized model to study $B(t)$ in the exponential growth phase. Using our analytical solution of $B(t)$ and corresponding second-order approximation and results of the mfun functions, our approach allows for an extensive analysis by separating the individual impact of temporal variability in E_0, k_d, and d and their interactions on (exponential) phytoplankton biomass growth. We analyze the time series of the onset of a phytoplankton bloom in spring in the freshwater region of the Scheldt estuary.

Figure 4.9 shows both the observed $B(t)$ (cf. Chl-a) and model result using our idealized model [Eq. (4.22)] with fitted and idealized expressions of temporal fluctuations in E_0, k_d, and d [Eqs. (4.26)-(4.28)]. Our model captures the exponential growth of $B(t)$: both the observed (data) and modeled (all var) $B(t)$ doubles after approximately two weeks (from $\sim$750 μg L^{-1} to $\sim$1500 μg L^{-1}). To study the impact of individual temporal variability on $B(t)$, Fig. 4.9 shows the modeled $B(t)$ in which we only include

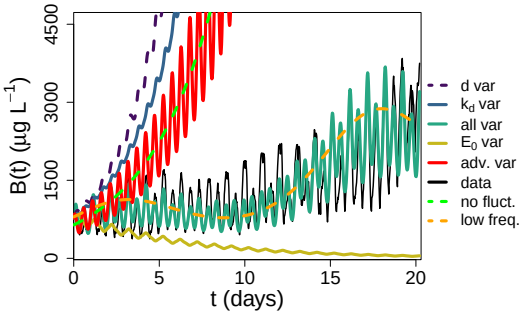

Figure 4.9: Observed phytoplankton biomass $B(t)$ (data) and model result by including all temporal fluctuations (all var) using our second-order approximation. Our approach allows us to easily identify and exclude individual forcings. The dashed green line (no fluct.) shows the model output for $B(t)$ which is only forced by time-invariant $\langle E_0 \rangle$, $\langle k_d \rangle$, and $\langle d \rangle$. We also show $B(t)$ when we exclusively include temporal fluctuations in d (d var), k_d (k_d var), E_0 (E_0 var), and temporal fluctuations due to advective transport of $B(t)$ (adv. var). The orange dashed graph (low freq.) shows $B(t)$ when, on top of the exponential growth, low-frequency fluctuations due to interactions between temporal variability in E_0 and k_d and d are included, which results in exponential coefficients $\sim \sin[(\omega_{M2} - 2\omega_{S1})t]$.

specific temporal variability. When $B(t)$ is forced by time-invariant $\langle E_0 \rangle$, $\langle k_d \rangle$, and $\langle d \rangle$ (Fig. 4.9, no fluct.), it grows much faster than observed. After two weeks, $B(t)$ when no temporal fluctuations are included is approximately a factor of 14 larger than observed. This illustrates the importance of the $\sim t$ terms generated by temporal variability in E_0, k_d, and d (see Appendix 4.E for definitions of these terms). In particular, this overestimation is due to the absence of temporal variability in E_0, which again decreases phytoplankton growth. If we solely include temporal variability in E_0, the modeled $B(t)$ is lower than observed (Fig. 4.9, E_0 var). Including temporal fluctuations in E_0, but excluding fluctuations in k_d and d, leads to underestimating $B(t)$ with a factor of 15 after two weeks. In contrast, exclusively including temporal fluctuations in d (Fig. 4.9, d var) and k_d (Fig. 4.9, k_d var) results in an overestimation of $B(t)$ with, respectively, a factor of 75 and 34 after two weeks. These results are consistent with application 1, but show that the accumulated impact is much larger than expected from the calculations assuming dynamic equilibrium. Finally, temporal fluctuations due to advective transport of $B(t)$ do not results in additional exponential growth (Fig. 4.9, adv. var) when compared to $B(t)$ forced by time-invariant parameters $\langle E_0 \rangle$, $\langle k_d \rangle$, and $\langle d \rangle$ (Fig. 4.9, no fluct.).

Temporal variability significantly reduces the exponential increase in our case study, which has important consequences, particularly at the onset of phytoplankton blooms. Indeed, during the onset of a phytoplankton bloom, a slight change in phytoplankton growth rate can change the balance with loss terms (e.g., respiration, grazing, and flushing), and result in net growth. Thus, other characteristics being equal, a system with fluctuating parameters has an earlier/later onset of the spring phytoplankton bloom than

a system without fluctuations. In our case study, temporal variability in E_0, k_d, and d delay the onset of the bloom by approximately two weeks (see Appendix 4.F for a detailed derivation). Therefore, knowing the magnitude of fluctuations in the forcings E_0, k_d, and d is at least as important as having a good and realistic estimate of respiration, grazing, and flushing, which in our analysis are included in m^*.

Temporal fluctuations in E_0, k_d, and d do not only result in additional $\sim t$ terms in the exponential in Eq. (4.22), but also result in sinusoidal terms. Of particular interest are the nontrivial interaction terms leading to additional low-frequency variability in $B(t)$ (Fig. 4.9, low freq.). These low-frequency fluctuations have a frequency similar to a spring-neap cycle of the horizontal tide (see Appendix 4.E for a definition of these low-frequency fluctuations $\sim \sin[(\omega_{M2} - 2\omega_{S1})t]$). This makes it difficult to separate the effects of spring-neap cycles of the horizontal tide from the interaction terms. The model seems to overestimate the impact of interaction terms on $B(t)$. A potential explanation is that the idealized expressions for temporal variability in k_d and d do not include the spring-neap cycle. These results highlight the need for caution when interpreting low-frequency patterns in observed Chl-a time series. As shown, these may both result from the spring-neap cycle and interaction terms in the light limitation factor.

To summarize, our analysis of the phytoplankton bloom in spring illustrates that the impact of temporal variability in light climate and advective water flow on $B(t)$ in the exponential growth phase may have crucial consequences: it may result in a 14 times lower $B(t)$ after two weeks, delay the onset of the bloom by two weeks, and result in low-frequency temporal variability with similar periodicity as the spring-neap cycle. As in application 1, temporal variability in k_d and d increases, whereas temporal variability in E_0 decreases phytoplankton growth.

4.4 Discussion

In this section, we first compare our case study results of the impact of temporal variability on time-averaged GPP in dynamic equilibrium (application 1) and unbound $B(t)$ (application 2) to the literature. Next, we discuss the implications of our results for both modelers and experimental scientists. Finally, we discuss the limitations of our approach, focusing on non-local processes and temporal variability in phytoplankton characteristics affecting $B(t)$ dynamics.

4.4.1 The impact of temporal variability on phytoplankton growth

We constructed an idealized model to study the impact of temporal variability in light climate and advective water flow on time-averaged GPP and $B(t)$ dynamics. Our approach allows for an extensive analysis by separating the individual impact of temporal variability in E_0, k_d, and d and their interactions on time-averaged GPP and (exponential) growth of $B(t)$.

In our first application, we found that temporal fluctuations in light climate impact time-averaged GPP: temporal variability in k_d and d increase, whereas temporal variability in E_0 decrease time-averaged GPP and has a dominant impact (a decrease upto 50 %, depending on the season). The dominant impact of temporal variability in E_0 complies with the results of Cox et al. (2015). They developed a novel technique to estimate GPP using oxygen time series. A core assumption in this method states that GPP follows a truncated sinusoidal pattern over time with a 24 h period. Consequently, the method assumes that the main contribution of temporal variability in the forcings is due to temporal variability in E_0 (cf. the 24 h period).

In our second application, we studied the impact of temporal variability in light climate and advective water flow on $B(t)$ dynamics in the exponential growth phase (i.e., phytoplankton bloom). Our results comply with the results of Desmit et al. (2005) who studied the impact of temporal variability in E_0, k_d, and d within a 40-day time frame for a specific case in the Scheldt estuary. Firstly, the exponential increase in $B(t)$ is very sensitive to temporal variability in E_0, k_d, and d (Fig. 4.9). Secondly, temporal variability in k_d and d increases the exponential growth, whereas temporal variability in E_0 decreases the exponential growth (Fig. 4.9). Moreover, the magnitude of the exponential increase is determined by the ratio of time-averaged depth $\langle d \rangle$ and corresponding temporal fluctuations $\langle d'(t) \rangle$, which agrees with our definition of $\delta(t)$ in Eq. (4.11). Last, a clear link exists between our implementation of advective transport of $B(t)$ and the one presented in Desmit et al. (2005). To include advective transport of $B(t)$, Desmit et al. (2005) postulated an additional term in Eq. (4.1) that is proportional to the derivative of $d(t)$, which agrees with our result in Eq. (4.50) [from Eq. (4.28) follows that $\partial_t d(t) \sim \sin(t)$]. However, our approach generalizes the work of Desmit et al. (2005) who only studied a specific case in the Scheldt estuary. In contrast to Desmit et al. (2005), our approach is more generic and can be applied to other estuarine well-mixed, light-limited systems. Moreover, our framework allows us to easily compute the impact of temporal fluctuations in the individual parameters and their interactions on phytoplankton growth because we derived an explicit analytical solution for phytoplankton growth and applied a second-order moment approximation.

We thus conclude that our results of the impact of temporal variability on time-averaged GPP and exponential phytoplankton growth comply with results found in the literature and that they allow for a more generic analysis of well-mixed, light-limited estuaries.

4.4.2 Implications of our findings for modelers and experimental scientists

Our generic approach may be used to study present-day challenges by both modelers and experimental scientists. Modelers may use our approach to easily assess the error by neglecting temporal fluctuations in parameters affecting $B(t)$ dynamics. As mentioned in the introduction, various models have been used to model $B(t)$ dynamics. Although complex tide-explicit models exist (Arndt et al., 2011), various models often keep certain

parameters constant to reduce complexity and allow for fast analytical solution procedures (Dijkstra et al., 2017). Examples are tidally averaged and daily-averaged numerical models to compute estuarine PP (Brinkman, 1993; Soetaert et al., 1994). The light extinction coefficient k_d, which is an important parameter in light-limited estuarine systems, is one of the main parameters which contributes to the complexity of PP dynamics because it is affected by suspended particulate matter (SPM) dynamics. Modeling SPM dynamics, even the corresponding large-scale estuarine turbidity maxima, is difficult because they result from a complex concurrence of ETM formation mechanisms [see Burchard et al. (2018) for a recent review]. However, our analysis framework provides a tool to assess the error made by neglecting such complex temporal variability in parameters affecting PP dynamics. As such, it may help to assess whether a given model with given accuracy and performance is sufficient to realistically simulate and study phytoplankton dynamics. This is particularly important when strong spatial and seasonal gradients in temporal variability in E_0, k_d (cf. SPM), and d exist. After all, this temporal variability can falsely be attributed (cf. calibrated) to spatial and seasonal variations in intrinsic features of phytoplankton dynamics such as $P_{\max}$, α, and m. Finally, to use our framework for a model assessment, only basic knowledge on time-average parameter values and corresponding S1, M2, and M4 amplitudes is required.

Our results are also particularly useful for experimental scientists interested in data-based estimation of GPP. They may partly answer the long-standing question of why bottle incubations underestimate in situ GPP. Often, bottle incubations are used to estimate GPP in estuaries and coasts. This means that the parameters of the Platt equation α and $P_{\max}$ in Eq. (4.2) are determined by incubating a sample at different light intensities (Vegter and De Visscher, 1984; Kromkamp and Peene, 1995). Consequently, the Platt equation needs to be numerically integrated over depth and time. This requires time series of E_0, k_d, and d. Whereas time series of incident irradiance are often available, k_d is often estimated as an average on a short time interval during sampling, and linearly interpolated between consecutive sampling (Kromkamp and Peene, 2005). Our results show that in systems with large temporal variability in k_d, this approach leads to a systematic underestimation of time-averaged PP. Indeed, temporal variability in k_d has a positive impact on GPP (Fig. 4.8). It has often been found that bottle incubations underestimate PP when compared to in situ methods. The reason why this occurs is still poorly understood (Westberry et al., 2012). In addition to so-called 'bottle effects' (Swaney et al., 1999) and physiological adaptation effects (Halsey et al., 2010), our results show that large variability in light attenuation can additionally result in an underestimation when this variability is not taken into account.

4.4.3 Non-local processes and temporal variability in phytoplankton characteristics affecting the phytoplankton dynamics

Although our approach is generically applicable to well-mixed, light-limited estuaries, an extrapolation of our findings to other estuarine cases should be taken with care.

As a first step, we approximated the non-local processes caused by advective and

diffusive transport of $B(t)$ by a term that is proportional to the derivative of the water depth. As mentioned above, this complies with the postulation presented in Desmit et al. (2005). By applying this idealization, we partly neglected the impact of temporal variability caused by complex interactions between $B(t)$ and the water flow. We assumed that $B(t)$ growth is mainly caused by local processes, which complies with the model study carried out by Dijkstra et al. (2019), who focused on the phytoplankton dynamics in the Delaware River Estuary. However, we are aware that this may not be valid in the Scheldt estuary. To correct for complex, non-local interactions between the water flow and $B(t)$, our model can still be used by coupling the model to a hydrodynamical model. By doing so, the impact of individual temporal variability in light climate on $B(t)$ growth can be investigated, including these complex non-local $B(t)$ and water flow interactions, as done by Dijkstra et al. (2019).

Additionally, we focused on temporal variability in parameters affecting the light climate E_0, k_d, and d on an hourly-daily time scale and kept most other parameters fixed. For example, we assumed balanced growth conditions and the absence of significant temporal variations in the phytoplankton characteristics (e.g., $P_{\max}$, α) on this hourly-daily time scale. In further research, the same approach as presented in this study can be applied assuming temporal variability in the latter parameters. This may cause additional (correlation) terms in the second-order approximation of Λ [Eq. (4.10)] and thus alter time-averaged GPP and $B(t)$ dynamics.

4.5 Conclusions

We constructed an idealized model to analyze the impact of temporal variability in solar irradiance at the water surface E_0, exponential light extinction coefficient k_d, and water depth d on phytoplankton biomass $B(t)$ and corresponding time-averaged gross primary production $\langle \mathrm{GPP} \rangle$ in light-limited, vertically well-mixed systems. Apart from providing a full theoretical analysis, our approach allows us to quantify the impact of the temporal variability without a numerical model, to separate the impact of different sources of the temporal variability and their covariance, and it does so for a general light-limited, well-mixed tidal system.

To present the applicability of our idealized model, we applied the model to two cases in the Scheldt estuary. Our results showed that temporal variability in E_0, k_d, and d can have an important impact on $\langle \mathrm{GPP} \rangle$ in dynamic equilibrium and corresponding $B(t)$ dynamics. In the first application, we showed that $\langle \mathrm{GPP} \rangle$ in dynamic equilibrium is mainly impacted by temporal variability in E_0 and results in a 30 % decrease. In contrast, temporal variability in k_d and d increased $\langle \mathrm{GPP} \rangle$. Furthermore, the results showed a seasonality; in winter, temporal variability in k_d had a larger impact on $\langle \mathrm{GPP} \rangle$ than in summer, due to the larger tidal amplitude in k_d in winter. Finally, our idealized model correctly predicted the order of magnitude of the impact of temporal variability of the individual parameters.

In the second application, we showed that during a phytoplankton bloom, temporal variability significantly contributes to the exponential $B(t)$ growth and generates additional low-frequency fluctuations similar to the spring-neap cycle. Moreover, we showed that temporal variability may delay the onset of the phytoplankton bloom by two weeks and may decrease $B(t)$ by a factor of 14 after two weeks. Again, our approach allowed us to apply an extensive analysis in which we showed that these low-frequency fluctuations in $B(t)$ are due to covariance of temporal variability in E_0 and k_d, and d.

List of symbols

Latin

a	Parameter defining the truncated sinusoidal behavior of E_0
$\tilde{B}$	Depth-averaged phytoplankton biomass concentration
B	Local depth-averaged phytoplankton biomass concentration
B_0	Initial depth-averaged phytoplankton biomass concentration (at $t = 0$)
b	Parameter defining the truncated sinusoidal behavior of E_0
C:Chl-a	Carbon to Chlorophyll-a ratio in a phytoplankton cell
$\tilde{\text{Cov}}$	Statistical covariance operator in which the parameter of interest is divided by its time average
$\hat{D}_2$	Amplitude corresponding to the M2 tidal component of d'
d	Water depth
d'	Temporal variability of d relative to its time average
$\langle d \rangle$	Time average of d
E_0	Solar irradiance at the water surface
E_0'	Temporal variability of E_0 relative to its time average
$\langle E_0 \rangle$	Time average of E_0
$\hat{E}_1$	Amplitude corresponding to the ω_{S1} component of E_0'
$\hat{E}_2$	Amplitude corresponding to the $2\omega_{S1}$ component of E_0'
$\hat{E}_3$	Amplitude corresponding to the $3\omega_{S1}$ component of E_0'
$\hat{E}_n$	Amplitude corresponding to the $n\omega_{S1}$ component of E_0'
$f(x)$	Linear function that captures the spatial dependence of $\tilde{B}$
$\langle \text{GPP} \rangle$	Time-averaged gross primary production
I	Light intensity in the water column
$\hat{K}_2$	Amplitude corresponding to the M2 tidal component of k_d'
$\hat{K}_4$	Amplitude corresponding to the M4 tidal component of k_d'
K_h	Horizontal diffusivity coefficient
k_d	Exponential light extinction coefficient
k_d'	Temporal variability of k_d relative to its time average
$\langle k_d \rangle$	Time average of k_d
m	Mortality rate of phytoplankton
m^*	Integrated mortality rate, including the effects of advective transport of phytoplankton
mfun_0	Λ without temporal variability in its parameters

mfun_{δ}	First-order mfun function corresponding to δ
mfun_{δ^2}	Second-order mfun function corresponding to δ
$\text{mfun}_{\delta\epsilon}$	Second-order mfun function corresponding to the correlation of δ and ϵ
mfun_{ϵ}	First-order mfun function corresponding to ϵ
mfun_{ϵ^2}	Second-order mfun function corresponding to ϵ
$\text{mfun}_{\epsilon\kappa}$	Second-order mfun function corresponding to the correlation of ϵ and κ
mfun_{κ}	First-order mfun function corresponding to κ
mfun_{κ^2}	Second-order mfun function corresponding to κ
$\text{mfun}_{\kappa\delta}$	Second-order mfun function corresponding to the correlation of κ and δ
N	Total number of field observations
n	Natural number
$\mathcal{O}$	Order of
$P_{\max}$	Maximum photosynthetic rate
t	Time
u	Local depth-averaged water flow velocity in the longitudinal dimension
$\tilde{\tilde{u}}$	Water flow velocity in the longitudinal dimension
$\tilde{\text{Var}}$	Statistical variance operator in which the parameter of interest is divided by its time average
x	Spatial coordinate in the longitudinal dimension
x^*	Location of interest in the longitudinal dimension
z	Spatial coordinate in the vertical dimension
$\tilde{z}$	Nondimensional parameter (i.e., $k_d z$) defining $\tilde{\Lambda}$

Greek

α	Photosynthetic growth efficiency
β	Time-averaged $\tilde{\beta}$
γ	Amplitude corresponding to the advective transport of phytoplankton
$\tilde{\beta}$	Nondimensional parameter (i.e., $\alpha E_0 / P_{\max}$) defining $\tilde{\Lambda}$
δ	Temporal variability of d divided by its time average (i.e., $d' / \langle\ \text{d}\ \rangle$)
∂_t	Partial derivative to t
ϵ	Temporal variability of E_0 divided by its time average (i.e., $E_0' / \langle\ \text{d}\ \rangle$)
θ	Phase corresponding to the M2 tidal component of d'
κ	Temporal variability of k_d divided by its time average (i.e., $k_d' / \langle\ \text{d}\ \rangle$)
Λ	Depth-averaged Platt light limitation function
$\tilde{\Lambda}$	Platt light limitation function
λ	$\tilde{z}$ using time-averaged parameters (i.e., $\langle k_d \rangle \langle d \rangle$)
ρ_B	Respiration and excretion coefficient of phytoplankton
Φ_{M_2}	Phase corresponding to the M2 tidal component of k_d'
Φ_{M_4}	Phase corresponding to the M4 tidal component of k_d'
ω_{M2}	Angular frequency corresponding to the semidiurnal lunar M2 tide
ω_{M4}	Angular frequency corresponding to the M4 tide
ω_{S1}	Diurnal angular frequency

Appendix 4.A: analytical solution of DAP

Substitution of $q = \tilde{\beta} \cdot \exp(-k_d z)$ in Eq. (4.6) allows us to analytically solve the DAP. The result reads as

$$\frac{1}{d}\int_0^d \tilde{\Lambda}(\mathrm{z})dz = 1 + \frac{1}{\tilde{d}}\left[E_1(\tilde{\beta}) - E_1(\tilde{\beta}\exp(-\tilde{d}))\right], \tag{4.29}$$

in which we used the definition of the exponential integral $E_1(x)$ (Bender and Orszag, 2013):

$$E_1(x) = \int_x^\infty \frac{\exp(-q)}{q} dq \tag{4.30}$$

where

$$\tilde{d} = k_d \cdot d. \tag{4.31}$$

Consequently, the DAP is defined by two dimensionless numbers $\tilde{d}$ and $\tilde{\beta}$.

Appendix 4.B: application of a Taylor expansion to Λ: definition of the mfun functions

Consider a function f that depend on a set of variables $\mathbf{a} = \{k_d, E_0, d\}$. Furthermore, assume that the variables are constructed as a mean value $\langle k_d \rangle, \langle E_0 \rangle, \langle d \rangle$ plus a (small) variation k_d', E_0', and d', respectively. Consequently, the Taylor expansion at the mean values $\langle k_d \rangle, \langle E_0 \rangle, \langle d \rangle$ upto second-order terms yields

$$\begin{aligned}
&f\left(\langle k_d \rangle + k_d'(t), \langle E_0 \rangle + E_0'(t), \langle d \rangle + d'(t)\right) \approx f\left(\langle \mathbf{a} \rangle\right) \\
&+ \frac{\partial f}{\partial k_d}\bigg|_{\mathbf{a}=<\mathbf{a}>} k_d'(t) + \frac{\partial f}{\partial E_0}\bigg|_{\mathbf{a}=<\mathbf{a}>} E_0'(t) + \frac{\partial f}{\partial d}\bigg|_{\mathbf{a}=<\mathbf{a}>} d'(t) \\
&+ \frac{1}{2}\frac{\partial^2 f}{\partial k_d^2}\bigg|_{\mathbf{a}=<\mathbf{a}>} [k_d'(t)]^2 + \frac{1}{2}\frac{\partial^2 f}{\partial E_0^2}\bigg|_{\mathbf{a}=<\mathbf{a}>} [E_0'(t)]^2 \\
&+ \frac{1}{2}\frac{\partial^2 f}{\partial d^2}\bigg|_{\mathbf{a}=<\mathbf{a}>} [d'(t)]^2 + \frac{\partial^2 f}{\partial k_d \partial E_0}\bigg|_{\mathbf{a}=<\mathbf{a}>} k_d'(t)E_0'(t) \\
&+ \frac{\partial^2 f}{\partial k_d \partial d}\bigg|_{\mathbf{a}=<\mathbf{a}>} k_d'(t)d'(t) + \frac{\partial^2 f}{\partial d \partial E_0}\bigg|_{\mathbf{a}=<\mathbf{a}>} d'(t)E_0'(t).
\end{aligned} \tag{4.32}$$

Applying this Taylor expansion to the DAP using the following property of the exponential integral E_1 (Bender and Orszag, 2013):

$$\frac{dE_1(x)}{dx} = -\frac{\exp[-x]}{x}, \tag{4.33}$$

yields the definitions of the mfun functions:

$$\mathrm{mfun}_0 = \frac{\left(E_1(\beta) - E_1\left(e^{-\lambda}\beta\right)\right)}{\lambda} + 1, \tag{4.34}$$

$$\mathrm{mfun}_{\kappa/\delta} = \frac{1}{\mathrm{mfun}_0} \cdot \left[-e^{\beta\left(-e^{-\lambda}\right)} - \mathrm{mfun}_0 + 1\right], \tag{4.35}$$

$$\mathrm{mfun}_{\epsilon} = \frac{1}{\mathrm{mfun}_0} \cdot \left[\frac{e^{\beta\left(-e^{-\lambda}\right)} - e^{-\beta}}{\lambda}\right], \tag{4.36}$$

$$\mathrm{mfun}_{\kappa^2/\delta^2} = \frac{1}{\mathrm{mfun}_0} \cdot \left[\frac{\beta\lambda}{2}\left(-e^{\beta\left(-e^{-\lambda}\right)-\lambda}\right) + e^{\beta\left(-e^{-\lambda}\right)} + \mathrm{mfun}_0 - 1\right], \tag{4.37}$$

$$\mathrm{mfun}_{\epsilon^2} = \frac{1}{\mathrm{mfun}_0} \cdot \frac{1}{2}\frac{-\beta e^{\beta\left(-e^{-\lambda}\right)-\lambda} - e^{\beta\left(-e^{-\lambda}\right)} + e^{-\beta}\beta + e^{-\beta}}{\lambda}, \tag{4.38}$$

$$\mathrm{mfun}_{\epsilon\kappa/\epsilon\delta} = \frac{1}{\mathrm{mfun}_0} \cdot \left[\beta e^{\beta\left(-e^{-\lambda}\right)-\lambda} - \frac{e^{\beta\left(-e^{-\lambda}\right)} - e^{-\beta}}{\lambda}\right], \quad \text{and} \tag{4.39}$$

$$\mathrm{mfun}_{\kappa\delta} = \frac{1}{\mathrm{mfun}_0} \cdot \left[\beta\lambda\left(-e^{\beta\left(-e^{-\lambda}\right)-\lambda}\right) + e^{\beta\left(-e^{-\lambda}\right)} + \mathrm{mfun}_0 - 1\right]. \tag{4.40}$$

In the R programming language, the package *expint* can be used to implement these mfun functions.

Appendix 4.C: solution of phytoplankton biomass concentration

We rewrite Eq. (4.1) for depth-averaged phytoplankton biomass concentration $\tilde{B}(t)$:

$$\frac{\partial \tilde{\mathrm{B}}(t,x)}{\partial t} + \underbrace{\frac{1}{d}\int_0^d \left[\frac{\partial}{\partial x}(\tilde{\tilde{u}}\tilde{\mathrm{B}}) + \frac{\partial}{\partial x}\left(K_h \frac{\partial}{\partial x}\tilde{\mathrm{B}}\right)\right]}_{\text{change in } B(t) \text{ due to transport}} = \tilde{\mathrm{B}}(x,t) \cdot [P_{\max} \cdot \Lambda \cdot (1-\rho_B) - m]. \tag{4.41}$$

Scaling of the longitudinal terms in Eq. (4.41) shows that the longitudinal diffusion term is $\sim 10^3$ times smaller than the longitudinal advection term. To obtain the latter result, we assumed that typical scales for $\tilde{\tilde{u}}$, x, and K_h are 1 m s^{-1}, 10^5 m, and 10^2 m^2 s^{-1}, respectively (de Swart et al., 2009). Consequently,

$$\text{the change in } \tilde{B}(t) \text{ due to transport} \approx \frac{\partial}{\partial x}\left[\tilde{u}(x,t)\tilde{\mathrm{B}}(x,t)\right], \tag{4.42}$$

where $\tilde{u}$ is the depth-averaged velocity in the longitudinal direction. This results in

$$\begin{aligned}\frac{\partial \tilde{B}(t,x)}{\partial t} =& \tilde{B}(x,t)\cdot[P_{\max}\cdot\Lambda\cdot(1-\rho_B)-m] \\ &- \frac{\partial}{\partial x}\left[\tilde{u}(x,t)\tilde{B}(x,t)\right].\end{aligned} \tag{4.43}$$

We need further simplification to solve this differential equation analytically. The change in phytoplankton biomass concentration due to advection is given by

$$\begin{aligned}\left.\frac{dB}{dt}\right|_{\text{advection}} &= -\frac{\partial(\tilde{u}\cdot\tilde{B})}{\partial x} \\ &= -\left[\tilde{u}\frac{\partial\tilde{B}}{\partial x}+\tilde{B}\frac{\partial\tilde{u}}{\partial x}\right].\end{aligned} \tag{4.44}$$

We assume that

$$\tilde{B}(x,t) = B(t)\cdot f(x). \tag{4.45}$$

Alternatively put, the phytoplankton biomass concentration $\tilde{B}(x,t)$ only scales to the magnitude of the biomass $B(t)$ in time. Here, $B(t)$ is the local carbon biomass concentration at the location $x = x^*$ where the Chl-a sensor is deployed. The assumption states that the spatial distribution $f(x)$ of $\tilde{B}(x,t)$ is time-independent. For example, if $f(x)$ is linear, we assume it stays linear over time. Because, in this study, we are interested in high-frequency dynamics ($\sim$days^{-1}), we argue that this assumption is acceptable. Furthermore, we state that $f(x)$ can be approximated by a linear function (first-order Taylor expansion); we argue that the impact due to advection is a local phenomenon near the location of the Chl-a sensor x*:

$$\frac{\partial\tilde{B}(x,t)}{\partial x} \approx B(t)\cdot\left.\frac{df(x)}{dx}\right|_{x=x^*}. \tag{4.46}$$

Similarly, we assume that

$$\frac{\partial\tilde{u}(x,t)}{\partial x} \approx u(t)\cdot\left.\frac{dg(x)}{dx}\right|_{x=x^*}, \tag{4.47}$$

where $u(t)$ is the water velocity in the x direction towards the mouth. Furthermore, we assume that the water velocity $u(t)$ mainly consists of a subtidal and an M2 tidal constituent:

$$u(t) = v_0 + A_v\cdot\sin(\omega_{M2}\cdot t+\Phi_{M2}+\theta), \tag{4.48}$$

in which $v_0 > 0$ is the residual velocity and A_v is the amplitude of the M2 tidal constituent. To obtain Eq. (4.48), we assumed a phase shift between the horizontal tide (current velocity) and vertical tide (water level d) of approximately $-\pi/2$ (van Rijn, 2010). If this is not valid, the results can be generalized using an additional phase shift. This is out of the scope of this study. In Eq. (4.48), A_v has the same sign as $\hat{D}_2$. If we define A_v as being positive, we have

$$u(t) = v_0 + |A_v|\ \text{sign}(\hat{D}_2)\cdot\sin(\omega_{M2}\cdot t+\Phi_{M2}+\theta), \tag{4.49}$$

where sign() denotes the sign function. Combining Eqs. (4.44), (4.46), (4.47), and (4.49), the change in phytoplankton biomass concentration due to advection yields

$$\left.\frac{dB}{dt}\right|_{\text{advection}} = - \left[\tilde{v_0^*} + \tilde{\gamma} \cdot \sin(\omega_{M2} \cdot t + \Phi_{M2} + \theta)\right] \cdot B(t), \tag{4.50}$$

in which

$$\tilde{\gamma} = |A_v| \text{sign}(\hat{D}_2) \cdot \left[g(x) \left.\frac{df(x)}{dx}\right|_{x=x^*} + f(x) \left.\frac{dg(x)}{dx}\right|_{x=x^*}\right] \quad \text{and} \tag{4.51}$$

$$\tilde{v}_0^* = v_0 \cdot \left[g(x) \left.\frac{df(x)}{dx}\right|_{x=x^*} + f(x) \left.\frac{dg(x)}{dx}\right|_{x=x^*}\right]. \tag{4.52}$$

By filling in the latter results into the differential equation for $B(x,t)$ in Eq. (4.43) at $x = x^*$, we have

$$\frac{\partial \text{B}(t)}{\partial t} = \text{B}(t) \cdot [P_{\max} \cdot \Lambda \cdot (1 - \rho_B) - m] + \text{B}(t) \cdot \Big[- v_0^* - \gamma \cdot \sin(\omega_{M2} \cdot t + \Phi_{M2} + \theta)\Big], \tag{4.53}$$

with

$$\gamma = |A_v| \text{sign}(\hat{D}_2) \cdot \left[\left.\frac{df(x)}{dx}\right|_{x=x^*} + \left.\frac{dg(x)}{dx}\right|_{x=x^*}\right] \quad \text{and} \tag{4.54}$$

$$v_0^* = v_0 \cdot \left[\left.\frac{df(x)}{dx}\right|_{x=x^*} + \left.\frac{dg(x)}{dx}\right|_{x=x^*}\right], \tag{4.55}$$

in which we used $f(x)\big|_{x=x^*} = 1$ and $g(x)\big|_{x=x^*} = 1$. The term due to advection in Eq. (4.53) is linear to $B(t)$. Consequently, this differential equation can be solved analytically. Because the v_0^*-term results in an $\exp(v_0^* \cdot t)$ factor, we define the mortality m^* as

$$m^* = m + v_0^*. \tag{4.56}$$

In the following, we estimate the order of magnitude of γ, v_0^*, and m^* at our case study site. In the Scheldt estuary, the water is pushed several kilometers $\sim \mathcal{O}(1)$ up and down over the longitudinal direction every approximately 12.4 h. So,

$$\int_0^{6.2h} A_v \sin(M2 \cdot t) dt \sim \mathcal{O}(1), \quad \Rightarrow A_v \sim \mathcal{O}(1) \text{ km h}^{-1}. \tag{4.57}$$

Furthermore, near our case study site, the phytoplankton biomass concentration increases with a factor of 1-10 $\sim \mathcal{O}(1)$ over a longitudinal distance of approximately 10 km (Maris and Meire, 2016). Consequently,

$$\frac{df(x)}{dx} \sim \frac{\mathcal{O}(1)}{10 \text{ km}} \sim \mathcal{O}(10^{-1}) \text{ km}^{-1}. \tag{4.58}$$

Therefore, assuming that the longitudinal gradient in velocity u is negligible ($df/dx \gg dg/dx$), we have

$$\gamma \approx A_v \cdot \frac{df(x)}{dx} \sim \mathcal{O}(10^{-1})\ \mathrm{h}^{-1}. \tag{4.59}$$

Similarly, if we assume $v_0 \sim \mathcal{O}(10^{-1})$ km h^{-1}, we have

$$v_0^* \sim \mathcal{O}(10^{-2})\ \mathrm{h}^{-1}. \tag{4.60}$$

Consequently, if we assume m$\sim \mathcal{O}(10^{-3})$ h^{-1} (Desmit et al., 2005), we have

$$m^* \sim \mathcal{O}(10^{-2})\ \mathrm{h}^{-1}. \tag{4.61}$$

Appendix 4.D: application 2: calibration of the amplitudes and phases

We calibrate the amplitudes and phases using the postulated expressions:

$$E_0'(t) = \sum_{n=1}^{3} \hat{E}_n \cos(n\omega_{S1}t), \tag{4.62}$$

$$k_d'(t) = \hat{K}_2 \cos(\omega_{M2}t + \Phi_{\mathrm{M}_2}) + \hat{K}_4 \cos(\omega_{M4}t + \Phi_{\mathrm{M}_4}), \quad \text{and} \tag{4.63}$$

$$d'(t) = \hat{D}_2 \cos(\omega_{M2}t + \Phi_{\mathrm{M}_2} + \theta), \tag{4.64}$$

and the data sets of E_0, k_d, and d at Schellebelle. This calibration results in Figs. 4.D.1a-c, respectively. We utilized the *nls()* function of the R programming language to obtain these data fits. We used subsets to diminish the impact of (low-frequency) temporal variability we did not include in the idealized time dependence in Eqs. (4.62)-(4.64). For example, we excluded long-term periodic temporal fluctuations (e.g., spring-neap) and aperiodic temporal fluctuations (e.g., the impact of clouds).

Appendix 4.E: time integration of $\Lambda(t)$

$$\int \kappa(t)dt = \frac{1}{\langle k_d \rangle}\left[\frac{\hat{K}_2\ \sin\left(\omega_{M2}\, t + \Phi_{M2}\right)}{\omega_{M2}} + \frac{\hat{K}_4\ \sin\left(\omega_{M4}\, t + \Phi_{M4}\right)}{\omega_{M4}}\right] \tag{4.65}$$

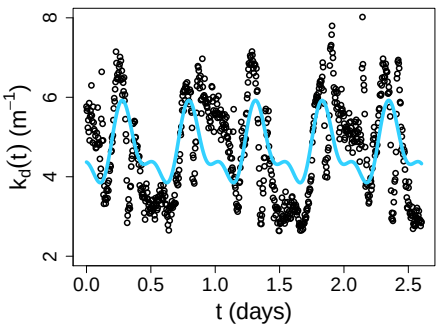

(a) k_d(t) data fit

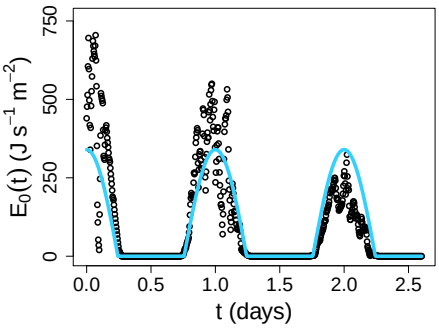

(b) E_0(t) data fit

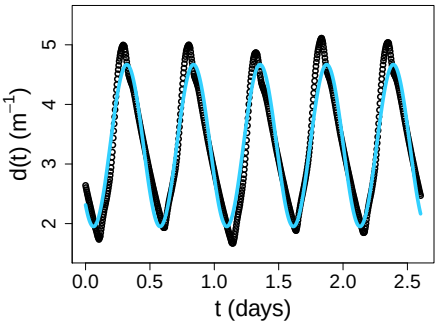

(c) d(t) data fit

Figure 4.D.1: The calibration of the postulated time dependencies (solid line) to a subset of the observation (dots) in the Scheldt estuary at Schellebelle (Belgium) of (a) the light extinction coefficient $k_d(t)$, (b) solar irradiance at the water surface $E_0(t)$, and (c) water depth $d(t)$.

$$\int \epsilon(t)dt = \frac{1}{\langle E_0 \rangle}\left[\frac{\hat{E}_1 \sin(\omega_{S1}\, t)}{\omega_{S1}} + 1/2\,\frac{\hat{E}_2 \sin(2\,\omega_{S1}\, t)}{\omega_{S1}} + 1/3\,\frac{\hat{E}_3 \sin(3\,\omega_{S1}\, t)}{\omega_{S1}}\right] \tag{4.66}$$

$$\int \delta(t)dt = \frac{1}{\langle d \rangle}\left[\frac{\hat{D}_2 \sin(\omega_{M2}\, t + \Phi_{M2} + \theta)}{\omega_{M2}}\right] \tag{4.67}$$

$$\int \epsilon^2(t)dt = \frac{1}{\left\langle E_0 \right\rangle^2}\Bigg[1/2\,\hat{E}_1^2 t + 1/2\,\hat{E}_2^2 t + 1/2\,\hat{E}_3^2 t + \frac{\left(\hat{E}_2\,\hat{E}_1 + \hat{E}_3\,\hat{E}_2\right)\sin\left(\omega_{S1}\,t\right)}{\omega_{S1}} + 1/2\,\frac{\left(1/2\,\hat{E}_1^2 + \hat{E}_3\,\hat{E}_1\right)\sin\left(2\,\omega_{S1}\,t\right)}{\omega_{S1}} + 1/3\,\frac{\hat{E}_2\,\hat{E}_1\,\sin\left(3\,\omega_{S1}\,t\right)}{\omega_{S1}} + 1/5\,\frac{\hat{E}_3\,\hat{E}_2\,\sin\left(5\,\omega_{S1}\,t\right)}{\omega_{S1}} + 1/12\,\frac{\hat{E}_3^2\sin\left(6\,\omega_{S1}\,t\right)}{\omega_{S1}} + 1/4\,\frac{\left(\hat{E}_3\,\hat{E}_1 + 1/2\,\hat{E}_2^2\right)\sin\left(4\,\omega_{S1}\,t\right)}{\omega_{S1}}\Bigg] \tag{4.68}$$

$$\int \kappa^2(t)dt = \frac{1}{\left\langle k_d \right\rangle^2}\Bigg[1/4\,\frac{\hat{K}_2^2\sin\left(2\,\omega_{M2}\,t + 2\,\Phi_{M2}\right)}{\omega_{M2}} + 1/2\,\hat{K}_2^2 t + \frac{\hat{K}_2\,\hat{K}_4\,\sin\left(\left(\omega_{M2} - \omega_{M4}\right)t + \Phi_{M2} - \Phi_{M4}\right)}{\omega_{M2} - \omega_{M4}} + \frac{\hat{K}_2\,\hat{K}_4\,\sin\left(\left(\omega_{M2} + \omega_{M4}\right)t + \Phi_{M2} + \Phi_{M4}\right)}{\omega_{M2} + \omega_{M4}} + 1/4\,\frac{\hat{K}_4^2\sin\left(2\,\omega_{M4}\,t + 2\,\Phi_{M4}\right)}{\omega_{M4}} + 1/2\,\hat{K}_4^2 t\Bigg] \tag{4.69}$$

$$\int \delta^2(t)dt = \frac{1}{\left\langle d \right\rangle^2}\Bigg[\frac{\hat{D}_2^2 1/2\,\cos\left(\omega_{M2}\,t + \Phi_{M2} + \theta\right)}{\omega_{M2}} \times \sin\left(\omega_{M2}\,t + \Phi_{M2} + \theta\right) + \hat{D}_2^2\,\frac{\omega_{M2}\,t + \Phi_{M2} + \theta}{2\omega_{M2}}\Bigg] \tag{4.70}$$

$$\int \delta(t)\epsilon(t)dt = \frac{\hat{D}_2}{\langle E_0\rangle\langle d\rangle}\Bigg[1/2\,\frac{\hat{E}_1\,\sin\left(\left(\omega_{M2}-\omega_{S1}\right)t+\Phi_{M2}+\theta\right)}{\omega_{M2}-\omega_{S1}} + 1/2\,\frac{\hat{E}_1\,\sin\left(\left(\omega_{M2}+\omega_{S1}\right)t+\Phi_{M2}+\theta\right)}{\omega_{M2}+\omega_{S1}} + 1/2\,\frac{\hat{E}_2\,\sin\left(\left(\omega_{M2}-2\,\omega_{S1}\right)t+\Phi_{M2}+\theta\right)}{\omega_{M2}-2\,\omega_{S1}} + 1/2\,\frac{\hat{E}_2\,\sin\left(\left(\omega_{M2}+2\,\omega_{S1}\right)t+\Phi_{M2}+\theta\right)}{\omega_{M2}+2\,\omega_{S1}} + 1/2\,\frac{\hat{E}_3\,\sin\left(\left(\omega_{M2}-3\,\omega_{S1}\right)t+\Phi_{M2}+\theta\right)}{\omega_{M2}-3\,\omega_{S1}} + 1/2\,\frac{\hat{E}_3\,\sin\left(\left(\omega_{M2}+3\,\omega_{S1}\right)t+\Phi_{M2}+\theta\right)}{\omega_{M2}+3\,\omega_{S1}}\Bigg] \tag{4.71}$$

$$\int \kappa(t)\delta(t)dt = \frac{1}{\langle k_d\rangle\langle d\rangle}\Bigg[\hat{D}_2\left(1/2\,\hat{K}_2\,\cos\left(\theta\right)t + 1/4\,\frac{\hat{K}_2\,\sin\left(2\,\omega_{M2}\,t+2\,\Phi_{M2}+\theta\right)}{\omega_{M2}} + 1/2\,\frac{\hat{K}_4\,\sin\left(\left(\omega_{M2}-\omega_{M4}\right)t+\Phi_{M2}-\Phi_{M4}+\theta\right)}{\omega_{M2}-\omega_{M4}} + 1/2\,\frac{\hat{K}_4\,\sin\left(\left(\omega_{M2}+\omega_{M4}\right)t+\Phi_{M2}+\Phi_{M4}+\theta\right)}{\omega_{M2}+\omega_{M4}}\right)\Bigg] \tag{4.72}$$

$$
\begin{aligned}
\int \kappa(t)\epsilon(t)dt = \frac{1}{\langle E_0\rangle\langle k_d\rangle}\Bigg[& \\
& 1/2\,\frac{\hat{K}_2\,\hat{E}_1\,\sin\left((\omega_{M2}-\omega_{S1})\,t+\Phi_{M2}\right)}{\omega_{M2}-\omega_{S1}} \\
& +1/2\,\frac{\hat{K}_2\,\hat{E}_1\,\sin\left((\omega_{M2}+\omega_{S1})\,t+\Phi_{M2}\right)}{\omega_{M2}+\omega_{S1}} \\
& +1/2\,\frac{\hat{K}_2\,\hat{E}_2\,\sin\left((\omega_{M2}-2\,\omega_{S1})\,t+\Phi_{M2}\right)}{\omega_{M2}-2\,\omega_{S1}} \\
& +1/2\,\frac{\hat{K}_2\,\hat{E}_2\,\sin\left((\omega_{M2}+2\,\omega_{S1})\,t+\Phi_{M2}\right)}{\omega_{M2}+2\,\omega_{S1}} \\
& +1/2\,\frac{\hat{K}_2\,\hat{E}_3\,\sin\left((\omega_{M2}-3\,\omega_{S1})\,t+\Phi_{M2}\right)}{\omega_{M2}-3\,\omega_{S1}} \\
& +1/2\,\frac{\hat{K}_2\,\hat{E}_3\,\sin\left((\omega_{M2}+3\,\omega_{S1})\,t+\Phi_{M2}\right)}{\omega_{M2}+3\,\omega_{S1}} \\
& +1/2\,\frac{\hat{K}_4\,\hat{E}_1\,\sin\left((\omega_{M4}-\omega_{S1})\,t+\Phi_{M4}\right)}{\omega_{M4}-\omega_{S1}} \\
& +1/2\,\frac{\hat{K}_4\,\hat{E}_1\,\sin\left((\omega_{M4}+\omega_{S1})\,t+\Phi_{M4}\right)}{\omega_{M4}+\omega_{S1}} \\
& +1/2\,\frac{\hat{K}_4\,\hat{E}_2\,\sin\left((\omega_{M4}-2\,\omega_{S1})\,t+\Phi_{M4}\right)}{\omega_{M4}-2\,\omega_{S1}} \\
& +1/2\,\frac{\hat{K}_4\,\hat{E}_2\,\sin\left((\omega_{M4}+2\,\omega_{S1})\,t+\Phi_{M4}\right)}{\omega_{M4}+2\,\omega_{S1}} \\
& +1/2\,\frac{\hat{K}_4\,\hat{E}_3\,\sin\left((\omega_{M4}-3\,\omega_{S1})\,t+\Phi_{M4}\right)}{\omega_{M4}-3\,\omega_{S1}} \\
& +1/2\,\frac{\hat{K}_4\,\hat{E}_3\,\sin\left((\omega_{M4}+3\,\omega_{S1})\,t+\Phi_{M4}\right)}{\omega_{M4}+3\,\omega_{S1}}\Bigg]
\end{aligned}
\tag{4.73}
$$

Appendix 4.F: the impact of temporal variability in light climate on the onset of a phytoplankton bloom

We estimate the impact of temporal fluctuations in E_0, k_d, and d on the onset of a phytoplankton bloom using our idealized model. After two weeks, the modeled phytoplankton biomass when no fluctuations are present is approximately a factor of 14 larger than observed. Using Eqs. (4.22) and (4.24), we estimate the difference in β which is required to

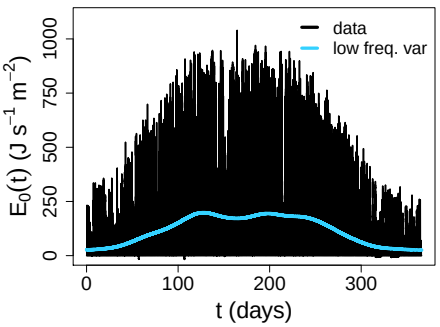

Figure 4.F.1: Observed solar irradiance E_0 in 2016 at Stabroek (data) and corresponding low-frequency temporal variation (low freq. var).

obtain the same difference in phytoplankton biomass after 14 days:

$$\begin{aligned}
&\frac{B_{\text{no fluct.}}(t = 14 \text{ days}, \beta + \Delta\beta)}{B_{\text{no fluct.}}(t = 14 \text{ days}, \beta)} = 14, \\
&\implies \text{mfun}_0(\lambda, \beta + \Delta\beta) - \text{mfun}_0(\lambda, \beta) = \\
&\qquad \frac{1}{(1 - \rho_B) P_{\max}} \frac{\log 14}{14 \text{ days}}, \\
&\implies \Delta\beta \approx 1.3.
\end{aligned} \tag{4.74}$$

Using Eq. (4.12), we compute the corresponding difference in solar irradiance $\Delta < E_0 > \approx$ 31 J s^{-1} m^{-2}. We use time series of E_0 observed in 2016 at Stabroek (Fig. 4.F.1) to compute the number of days required to increase the (daily-averaged) solar irradiance E_0 (low freq. var in Fig. 4.F.1) by 31 J s^{-1} m^{-2} in April, which equals approximately two weeks. Consequently, temporal variability in light climate may delay the onset of a phytoplankton bloom by approximately two weeks.

Bibliography

Alpine, A. E. and Cloern, J. E. (1992). Trophic interactions and direct physical effects control phytoplankton biomass and production in an estuary. *Limnology and Oceanography*, 37(5):946–955.

Arndt, S., Lacroix, G., Gypens, N., Regnier, P., and Lancelot, C. (2011). Nutrient dynamics and phytoplankton development along an estuary-coastal zone continuum: A model study. *Journal of Marine Systems*, 84(3-4):49–66.

Bender, C. M. and Orszag, S. A. (2013). *Advanced mathematical methods for scientists and engineers I: Asymptotic methods and perturbation theory*. Springer Science & Business Media.

Berman-Frank, I. and Dubinsky, Z. (1999). Balanced growth in aquatic plants: Myth or reality? Phytoplankton use the imbalance between carbon assimilation and biomass production to their strategic advantage. *BIOSCIENCE*, 49(1):29–37.

Bolker, B. and Pacala, S. W. (1997). Using Moment Equations to Understand Stochastically Driven Spatial Pattern Formation in Ecological Systems. *Theoretical Population Biology*, 52(3):179–197.

Brinkman, A. G. (1993). Biological processes in the EcoWasp ecosystem model. Technical report, Institute for Forestry and Nature Research, Wageningen.

Burchard, H., Schuttelaars, H. M., and Ralston, D. K. (2018). Sediment Trapping in Estuaries. *Annual Review of Marine Science*, 10(1):371–395.

Chao, X., Jia, Y., Shields, F. D., Wang, S. S. Y., and Cooper, C. M. (2010). Three-dimensional numerical simulation of water quality and sediment-associated processes with application to a Mississippi Delta lake. *Journal of Environmental Management*, 91(7):1456–1466.

Chen, Q. and Mynett, A. E. (2006). Modelling algal blooms in the Dutch coastal waters by integrated numerical and fuzzy cellular automata approaches. *Ecological Modelling*, 199(1):73–81.

Chernetsky, A. S., Schuttelaars, H. M., and Talke, S. A. (2010). The effect of tidal asymmetry and temporal settling lag on sediment trapping in tidal estuaries. *Ocean Dynamics*, 60(5):1219–1241.

Cira, E. K., Paerl, H. W., and Wetz, M. S. (2016). Effects of Nitrogen Availability and Form on Phytoplankton Growth in a Eutrophied Estuary (Neuse River Estuary, NC, USA). *PLOS ONE*, 11(8).

Cox, T., Soetaert, K., Vanderborght, J. P., Kromkamp, J., and Meire, P. (2010). Modelling photosynthesis-irradiance curves: effects of temperature, dissolved silica depletion and changing community assemblage on community photosynthesis. *Limnology and Oceanography - Methods*, 8:424–440.

Cox, T. J. S., Horemans, D. M. L., De Mulder, T., and Meire, P. (2017). Hoogfrequente in-situ metingen van de interactie tussen spm- en zuurstofdunamiek in het scheldeestuarium. Deelrapport 1. Metingen nabij het oppervlak. Report ECOBE 018-R215, University of Antwerp, Ecosystem Management Group and University of Ghent, Hydraulics Laboratory.

Cox, T. J. S., Maris, T., Soetaert, K., Conley, D. J., Van Damme, S., Meire, P., Middelburg, J. J., Vos, M., and Struyf, E. (2009). A macro-tidal freshwater ecosystem recovering from hypereutrophication: the Schelde case study. Technical report.

Cox, T. J. S., Maris, T., Soetaert, K., Kromkamp, J. C., Meire, P., and Meysman, F. (2015). Estimating primary production from oxygen time series: A novel approach in the frequency domain. *Limnology and Oceanography-Methods*, 13(10):529–552.

de Swart, H. E., Schuttelaars, H. M., and Talke, S. A. (2009). Initial growth of phytoplankton in turbid estuaries: {A} simple model. *Continental Shelf Research*, 29(1):136–147.

Desmit, X., Vanderborght, J. P., Regnier, P., and Wollast, R. (2005). Control of phytoplankton production by physical forcing in a strongly tidal, well-mixed estuary. *Biogeosciences*, 2(2):205–218.

Dijkstra, Y. M., Brouwer, R. L., Schuttelaars, H. M., and Schramkowski, G. P. (2017). The iFlow modelling framework v2.4: a modular idealized process-based model for flow and transport in estuaries. *Geoscientific Model Development*, 10(7):2691–2713.

Dijkstra, Y. M., Chant, R. J., and Reinfelder, J. R. (2019). Factors Controlling Seasonal Phytoplankton Dynamics in the Delaware River Estuary: an Idealized Model Study. *Estuaries and Coasts*, 42(7):1839–1857.

Eppley, R. W. (1972). Temperature and phytoplankton growth in the sea. *Fish. bull*, 70(4):1063–1085.

Filardo, M. J. and Dunstan, W. M. (1985). Hydrodynamic control of phytoplankton in low salinity waters of the James River estuary, Virginia, U.S.A. *Estuarine, Coastal and Shelf Science*, 21(5):653–667.

Halsey, K. H., Milligan, A. J., and Behrenfeld, M. J. (2010). Physiological optimization underlies growth rate-independent chlorophyll-specific gross and net primary production. *Photosynthesis Research*, 103(2):125–137.

Horemans, D. M. L., Dijkstra, Y. M., Schuttelaars, H. M., Meire, P., and Cox, T. J. S. (2020). Unraveling the essential effects of flocculation on large-scale sediment transport patterns in a tide-dominated estuary. *Journal of Physical Oceanography*, 50(7):1957–1981.

Kromkamp, J. and Peene, J. (1995). Possibility of net phytoplankton primary production in the turbid Schelde Estuary (SW Netherlands). *Marine Ecology Progress Series*, 121:249–259.

Kromkamp, J. C. and Peene, J. (2005). Changes in phytoplankton biomass and primary production between 1991 and 2001 in the Westerschelde estuary (Belgium/The Netherlands). *Hydrobiologia*, 540(1 - 3):117–126.

Langdon, C. (1993). The significance of respiration in production measurements based on oxygen. *ICES Marine Science Symposia*, 197:69–78.

Lionard, M., Azémar, F., Boulêtreau, S., Muylaert, K., Tackx, M., and Vyverman, W. (2005). Grazing by meso- and microzooplankton on phytoplankton in the upper reaches of the Schelde estuary (Belgium/The Netherlands). *Estuarine, Coastal and Shelf Science*, 64(4):764–774.

Liu, B. and de Swart, H. E. (2015). Impact of river discharge on phytoplankton bloom dynamics in eutrophic estuaries: A model study. *Journal of Marine Systems*, 152:64–74.

Liu, B., de Swart, H. E., and de Jonge, V. N. (2018). Phytoplankton bloom dynamics in turbid, well-mixed estuaries: A model study. *Estuarine, Coastal and Shelf Science*, 211:137–151.

Lucas, L. V., Cloern, J. E., Koseff, J. R., Monismith, S. G., and Thompson, J. K. (1998). Does the Sverdrup critical depth model explain bloom dynamics in estuaries? *Journal of Marine Research*, 56(2):375–415.

Maris, T. and Meire, P. (2016). Omes rapport 2015. Onderzoek naar de gevolgen van het Sigmaplan, baggeractiviteiten en havenuitbreiding in de Zeeschelde op het milieu. Technical report, University of Antwerp, Antwerp, Belgium.

McSweeney, J. M., Chant, R. J., Wilkin, J. L., and Sommerfield, C. K. (2017). Suspended-Sediment Impacts on Light-Limited Productivity in the Delaware Estuary. *Estuaries and Coasts*, 40(4):977–993.

Platt, T., Gallegos, C. L., and Harrison, W. G. (1980). Photoinhibition of Photosynthesis in Natural Assemblages of Marine-Phytoplankton. *Journal of Marine Research*, 38(4):687–701.

Rijkswaterstaat (2020). Rijkswaterstaat official website.

RMI (2013). Global solar radiation in stabroek for the year 2013. `https://www.meteo.be`. Accessed: 2017-06-08.

Soetaert, K., Herman, P., and Kromkamp, J. (1994). Living in the Twilight - Estimating Net Phytoplankton Growth in the Westerschelde Estuary (the Netherlands) by Means of an Ecosystem Model (moses). *Journal of Plankton Research*, 16(10):1277–1301.

Soetaert, K. and Herman, P. M. J. (1995). Carbon flows in the westerschelde estuary (the netherlands) evaluated by means of an ecosystem model (moses). *Hydrobiologia*, 311(1):247–266.

Sverdrup, H. U. (1953). On Conditions for the Vernal Blooming of Phytoplankton. *ICES Journal of Marine Science*, 18(3):287–295.

Swaney, D. P., Howarth, R. W., and Butler, T. J. (1999). A novel approach for estimating ecosystem production and respiration in estuaries: Application to the oligohaline and mesohaline Hudson River. *Limnology and Oceanography*, 44(6):1509–1521.

Tilman, D., Kilham, S. S., and Kilham, P. (1982). Phytoplankton Community Ecology: The Role of Limiting Nutrients. *Annual Review of Ecology and Systematics*, 13(1):349–372.

van Rijn, L. C. (2010). Tidal phenomena in the scheldt estuary. Report 1202016-000, Deltares.

Vanderborght, J. P., Wollast, R., Loijens, M., and Regnier, P. (2002). Application of a transport-reaction model to the estimation of biogas fluxes in the Scheldt estuary. *Biogeochemistry*, 59(1/2):207–237.

Vegter, F. and De Visscher, P. R. M. (1984). Phytoplankton primary production in Brackish Lake Grevelingen (SW Netherlands) during 1976-1981. *Netherlands Journal of Sea Research*, 18(3-4):246–259.

Volta, C., Laruelle, G. G., Arndt, S., and Regnier, P. (2016). Linking biogeochemistry to hydro-geometrical variability in tidal estuaries: a generic modeling approach. *Hydrology and Earth System Sciences*, 20(3):991–1030.

Waterinfo.be (cited 2019). Measurements and predictions of Waterinfo.be [data]. [Available online at `https://www.waterinfo.be/`].

Westberry, T. K., Williams, P. J. L., and Behrenfeld, M. J. (2012). Global net community production and the putative net heterotrophy of the oligotrophic oceans. *Global Biogeochemical Cycles*, 26(4).

Wirtz, K. W. (2000). Second order up-scaling: theory and an exercise with a complex photosynthesis model. *Ecological Modelling*, 126(1):59–71.

YSI (2017a). Chlorophyll a measurement. `https://www.ysi.com/parameters/chlorophyll`. Accessed: 2018-01-23.

YSI (2017b). Turbidity measurement. `https://www.ysi.com/parameters/turbidity`. Accessed: 2018-01-23.

Chapter 5

Applying the sediment transport - phytoplankton model: the disappearance of phytoplankton blooms in spring in the brackish region in the Scheldt estuary

Horemans, D. M. L., Dijkstra, Y. M., Tackx, M., Meire, P., & Cox, T. J. S. (submitted to Estuarine, Coastal and Shelf Science). Evolution of the multi-annual and large-scale phytoplankton patterns in the Scheldt estuary: the disappearance of phytoplankton accumulation in the brackish region.

Abstract

Estuaries often show regions in which Chlorophyll-a (Chl-a) accumulates. The location and magnitude corresponding to such accumulation result from a complex interplay between processes such as river flushing, salinity, nutrients, grazing on phytoplankton, and the light climate in the water column. An example is the multi-annual evolution of the estuary-scale Chl-a distribution in the Scheldt estuary (Belgium/Netherlands) in spring. From 2004-2007, we observed a limited spring bloom in the brackish region (km 60-90 from the mouth, salinity $\sim$ 1-10 ppt). This bloom intensified in 2008-2014 and disappeared after 2015. This multi-annual evolution of Chl-a has been linked to simultaneous multi-annual trends in the suspended particulate matter (SPM) distribution and the improvement of the water quality, which affects grazing on phytoplankton by zooplankton. However, this hypothesis has not been systematically investigated. In this contribution, we apply a modeling approach in which observations are the core. We first analyze multi-annual in situ observations covering the full estuary. These observations include the SPM concentration, zooplankton abundance, and other variables affecting the Chl-a concentration. They show a multi-annual estuary-scale evolution not only in the SPM distribution but also in zooplankton abundance, freshwater discharge, and maximum photosynthetic rate. Next, we apply a model approach supported by these observations to constrain the processes and corresponding parameter variability that may have caused the observed change in Chl-a. Our results suggest that a change in SPM alone cannot explain the Chl-a observations. Instead, a multi-annual change in mortality rate, which we can attribute to both grazing by zooplankton and phytoplankton community characteristics (i.e., mortality dependence on salinity), may explain the multi-annual estuary-scale evolution of Chl-a in spring. Different model parameter choices may thus lead to similar model results, which is known as equifinality. Our results highlight that insight into the zooplankton dynamics and phytoplankton community characteristics is essential to understand the phytoplankton (cf. Chl-a) dynamics in the Scheldt estuary and that additional data regarding mortality and grazing rates is required to further constrain the model parameters.

5.1 Introduction

Estuaries regularly exhibit zones with locally elevated Chlorophyll-a (Chl-a) concentrations, which result from a complex interaction between physical, transport-related processes and chemical-biotic factors that determine net local phytoplankton growth. Such processes are governed by water temperature variations (Eppley, 1972), river flushing (Filardo and Dunstan, 1985; Liu and de Swart, 2015), salinity variations (Lucas et al., 1998), grazing on phytoplankton (Alpine and Cloern, 1992; Lionard et al., 2005), nutrient dynamics (Tilman et al., 1982; Cira et al., 2016), and the light climate in the water column (Sverdrup, 1953; Desmit et al., 2005).

Human influences may cause gradual (i.e., multi-annual) changes in multiple of these

interacting processes. Examples are the multi-annual changes in suspended particulate matter (SPM) dynamics caused by channel deepening in the Ems estuary (Winterwerp and Wang, 2013; Dijkstra et al., 2019c) and the multi-annual evolution in nutrients in the Scheldt estuary resulting from an increase in wastewater treatment capacity (Brion et al., 2015). Determining the exact factors that may have caused the observed changes in phytoplankton dynamics is challenging due to the high complexity and because many of the biological interactions are poorly constrained by available data, especially when considering multi-annual time scales.

In view of multi-annual changes in phytoplankton dynamics and the various interacting processes, the Scheldt estuary is an interesting example. Between 2004-2018, the estuary showed the appearance and disappearance of a phytoplankton spring (Apr-May) bloom in the brackish region (km 60-90 from the mouth, salinity $\sim$ 1-10 ppt) (Maris and Meire, 2017). From 2004 until 2007, almost no spring bloom was observed in the brackish region. Such a spring bloom was consistently observed between 2008-2014 but disappeared after 2015. Covering the same period, Cox et al. (2019) reported a multi-annual estuary-scale change in SPM dynamics in the Scheldt estuary. From 2009 onwards, a change in the estuarine turbidity maximum dynamics and an overall increase in SPM concentration were observed. Simultaneously, the water quality in the Scheldt estuary improved drastically, mainly because of a significant increase in wastewater treatment capacity in Brussels around 2006 (Brion et al., 2015). This resulted in increasing oxygen concentrations and changes in the zooplankton community and abundance. The reported changes in SPM and zooplankton dynamics have been hypothesized to link to the multi-annual disappearance of phytoplankton blooms (Maris and Meire, 2017). However, this has not been systematically investigated, which is necessary given the complex interplay between factors affecting phytoplankton growth.

As discussed by Franks (2009), the choice of an appropriate modeling approach to acquire insight into the phytoplankton(-zooplankton) dynamics depends on the research questions and data availability. Arndt et al. (2011), Naithani et al. (2016), and Gypens et al. (2013) explicitly resolved the phytoplankton-zooplankton(-nutrient) dynamics over one year in the Scheldt estuary using a complex model that includes multiple phytoplankton and zooplankton groups. This resulted in valuable insight into the transient behavior of phytoplankton and zooplankton groups covering the full estuary in 1995, 2003, and 2006, respectively. However, using such models to study multi-annual changes is challenging. The main reason is that (long-term) experimental data is often unavailable, which has three important consequences. Firstly, some of the modeled planktonic groups cannot be observationally validated. Secondly, such models require many ($\sim$ dozens) calibration parameters that are often poorly constrained (e.g., maximum grazing rate, mortality rate per species). These parameters are generally calibrated by fitting them to data and assumed to be fixed in time. Although assuming fixed parameters may be acceptable when focusing on one year, this assumption may be invalid when interested in multi-annual trend changes, suggesting that (some of these) parameters must have changed over time. Thirdly, different model input parameter choices may lead to similar model results, which is known as equifinality. Equifinality has been studied using sediment-transport (van Maren and Cronin, 2016) and planktonic ecosystem models (Friedrichs et al., 2006, 2007) applied to estuarine and marine systems. This phenomenon especially occurs when using

more complex models because the number of model parameters increases by as much as the square of the number of state variables (Denman and Pea, 2002).

In this contribution, we aim to answer whether the appearance and disappearance of the phytoplankton bloom in the brackish zone in the Scheldt estuary should be attributed to changes in SPM or changes in the phytoplankton or zooplankton properties. We choose our model such that it is mainly data-driven and most of its parameters directly follow from observations. We aim to minimize the number of variables and calibration parameters that we cannot validate using data, requiring the combining of several biological factors into lumped parameters related to sediment, phytoplankton properties, and zooplankton grazing. Hence, the model is used to constrain which of these combined sets of processes may explain the observed changes. Although it may still occur using our model approach, we thereby limit the effect of equifinality.

This contribution is structured as follows. We first introduce the Scheldt estuary, the methodology to obtain the observations, and the model approach in Section 5.2. In Section 5.3, we show the multi-annual observations of Chl-a and factors impacting phytoplankton growth in the Scheldt estuary in spring. Next, we present the results of our model experiments: we calibrate the model, apply a sensitivity analysis of factors that may explain the disappearance of phytoplankton accumulation in the brackish region, and run different model scenarios. We study whether this multi-annual trend in phytoplankton accumulation may be constrained by an individual multi-annual change in grazing by zooplankton or other processes contributing to the phytoplankton mortality rate. In Section 5.4, we discuss the model results and approach. Finally, we conclude in Section 5.5.

5.2 Material and methods

5.2.1 Study area

The Scheldt estuary is a funnel-shaped estuary that flows through Belgium into the North Sea near Vlissingen (Netherlands) over a distance of approximately 160 km (Fig. 5.1). Given its relatively small freshwater discharge compared to the tidal volumes, the Scheldt estuary is tide-dominated (Baeyens et al., 1997; Meire et al., 2005). The total time-averaged freshwater discharge Q in spring (Apr.-May) equaled 85, 81, and 72 $m^3\ s^{-1}$ in 2004-2007, 2008-2014, and 2015-2018, respectively (Waterinfo.be, 2019, gauge station *zes29f-1066* $\sim$ 1 km downstream from the Rupel tributary). The main tributaries of the Scheldt estuary are the Rupel and the Dender. They are responsible for 64.2, 59.3, 63.3 % and 9.4, 9.2, 9.6 % of the total river discharge in 2004-2007, 2008-2014, and 2015-2018, respectively (Waterinfo.be, 2019, deducted from gauge stations at the upstream boundary *zes57a-1066*, at the Dender tributary *den02a-1066*, and downstream from the Rupel tributary *zes29f-1066* assuming conservation of mass). The Scheldt estuary is a nutrient-rich estuary (Cox et al., 2009; Maris and Meire, 2017). The dissolved nitrogen, phosphorous, and silicon concentrations in spring range from 0.1 mmol L^{-1}, 0.001 mmol

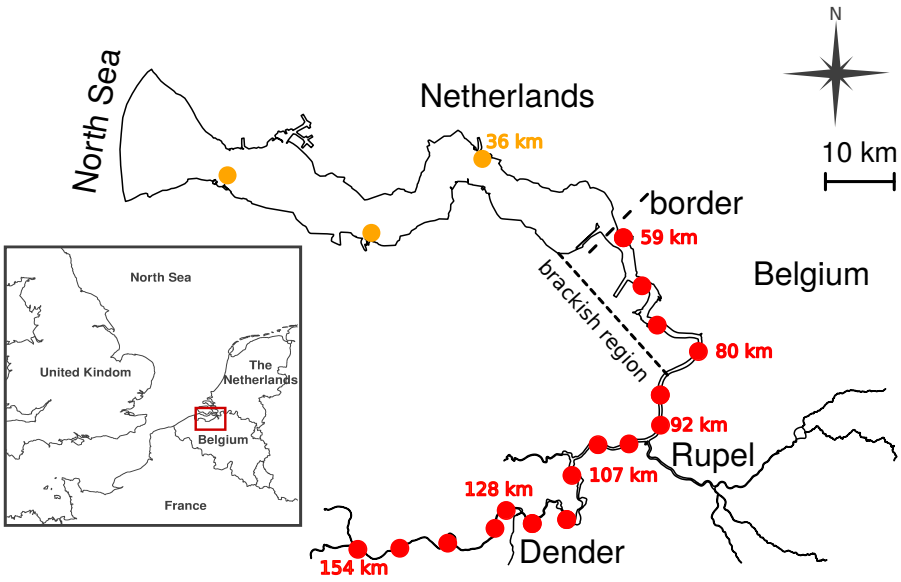

Figure 5.1: The Scheldt estuary and its two main tributaries (Rupel and Dender). The red dots represent the locations where was sampled monthly and biweekly in the frame of the OMES environmental monitoring program. The orange dots depict the locations of the observations conducted by Rijkswaterstaat.

L^{-1}, and 0.005 mmol L^{-1} at the seaside boundary to 0.4 mmol L^{-1}, 0.007 mmol L^{-1}, and 0.13 mmol L^{-1} at the upstream boundary, respectively. These concentrations are at least one order of magnitude larger than the half-saturation constants at which we expect nutrient depletion (Billen and Garnier, 1997; Lancelot et al., 2005; Arndt et al., 2011; Naithani et al., 2016).

5.2.2 In situ observations

Both the Belgian and Dutch part of the Scheldt estuary have been monitored intensively over the last two decades. In the Belgian region, various variables have been measured within the multi-annual OMES (Dutch: "Onderzoek Milieu Effecten Sigmaplan") monitoring program (Maris and Meire, 2017), independently of the tidal phase and spring-neap tide biweekly or monthly at 16 fixed stations (Fig. 5.1). These variables include Chl-a, SPM, salinity, and phytoplankton characteristics, such as the maximum photosynthetic rate $P_{\max}$ and growth efficiency α. In the Dutch region, we only use observations of Chl-a and SPM conducted by Rijkswaterstaat at three stations in the main channel (Fig. 5.1). In the following, we briefly introduce the methodology used to obtain the observations presented in this contribution. For a detailed methodological description, we refer the reader to the OMES reports (Maris and Meire, 2017) and the website of Rijkswaterstaat (Rijkswaterstaat, 2020).

5.2.2.1 Chl-a and zooplankton abundance

Within the OMES monitoring program, sub-surface bucket samples were taken to estimate the Chl-a concentration and the mesozooplankton abundance between 2004-2018. The Chl-a concentration was estimated following the spectrophotometric method described in Rice et al. (2017) that corrects for turbidity, Chlorophyll-b, Chlorophyll-c, and Pheophytin pigments, using 50 ml water samples, a 1-cm pathway cuvette, and a Shimadzu UV-1700 spectrophotometer. The observations conducted by Rijkswaterstaat in the Dutch part of the Scheldt estuary were estimated using High-performance liquid chromatography (HPLC) after filtration and extraction.

To estimate the mesozooplankton abundance, 50-250 L sub-surface water samples were collected and filtered over a 50 μm mesh. Next, the mesozooplankton was fixed using formaldehyde and stained with erythrosine in the laboratory. Finally, the organisms were counted in a counting wheel under a binocular microscope using a subsample. A minimum of 500 individuals per subsample was counted (Le Coz et al., 2017). In the brackish region in spring, which is the main focus of this paper, the mesozooplankton community dominantly consists of calanoids (Appeltans, 2003; Mialet et al., 2011). Therefore, we divide the community into two groups: adult calanoids and adult non-calanoids (i.e., cladocerans, harpacticoids, and cyclopoids).

5.2.2.2 Turbidity and SPM concentration

Within the OMES campaign, turbidity depth profiles were measured in 2015-2018 using an Optical Backscatter point Sensor (OBS) of RBR type XR420 CTD+ at the 16 OMES stations. Simultaneously, two SPM samples were collected at approximately the water surface and half the water depth. These SPM samples were used to translate turbidity to SPM concentration (Horemans et al., 2020a). The number of spring campaigns between 2015-2018 equals 16.

To determine the SPM concentration, 1 L water samples were collected and filtered in the laboratory using a GF/C 50 mm filter. To remove salinity, the filters were rinsed with 3×50 ml demineralized water before gravimetrically determining the SPM concentrations (norm NBN-EN872). Also within the monitoring program of Rijkswaterstaat, SPM concentrations were gravimetrically determined after filtration on a glass microfiber filter.

5.2.2.3 Light extinction coefficients, temperature, and salinity

The light climate was measured by estimating the light extinction coefficient k_d. Two light sensors (LiCOR) measured the light intensity near the water surface E_1 and the light-intensity E_2 at a fixed distance $\Delta z = 40$ cm from the sub-surface sensor. Next, the light extinction coefficient was estimated as $k_d = \log(E_1/E_2)/\Delta z$, assuming exponential

decrease of light as a function of depth. To correct for small-scale temporal variability (cf. seconds) in the light climate, the time-averaged value of k_d was estimated over a time interval of 3-5 minutes, using a sampling frequency of 1 s^{-1} (Maris and Meire, 2017). An estimate at the water surface suffices because, given the high turbidity in the Scheldt estuary, the euphotic depth is relatively small ($\sim$ dm) compared to the total water depth ($\sim$ m). We thus expect phytoplankton growth only near the water surface, where we do not expect strong vertical stratification of SPM.

Temperature and specific conductivity were determined in situ using a WTW LF 318 instrument directly after taking the bucket samples. Specific conductivity was transformed to salinity using the Practical Salinity Scale 1978 (Perkin and Lewis, 1980).

5.2.2.4 Photosynthetic parameters

To estimate the maximum photosynthetic rate $P_{\max}$ and growth efficiency α, the incubation method described in Kromkamp and Peene (1995) was applied using the incubator presented in Vegter and De Visscher (1984) and assuming a photosynthesis-irradiance (P-I) curve introduced in Eilers and Peeters (1988). Briefly explained, the Chl-a concentration was determined and water samples were placed at fixed distances from a constant light source. Each distance thus corresponds to a given solar irradiance I. Next, the water samples were incubated for approximately 2 hours, while gently being rotated to avoid settling. The photosynthesis was determined using a C-14 isotope method for each I, resulting in an estimate of the amount of carbon that is consumed per unit of time per unit of Chl-a. Finally, a P-I curve was constructed to estimate $P_{\max}$ and α.

5.2.3 Model set-up

Before presenting the technical details of our model approach, we introduce its core characteristic (see Fig. 5.2 for a schematic overview of the model approach). To constrain the processes and parameter variations as much as possible, we require that our model is mainly data-driven and most of its parameters directly follow from the observations. The remaining (lumped) parameters are calibration parameters and are subject to extensive sensitivity study. We do not explicitly resolve planktonic groups that we cannot validate using observations and only include processes and planktonic groups that are shown by the observations to have a dominant impact. Therefore, we only dynamically resolve freshwater and marine diatoms as they are dominantly abundant in the Scheldt estuary in spring (Maris and Meire, 2007; Muylaert et al., 2009; Maris and Meire, 2009, 2013, 2017). With the exception of grazing by zooplankton, all processes contributing to phytoplankton mortality are lumped into parameters $m_0^{\text{fresh.}}$ and $m_0^{\text{mar.}}$ for the freshwater and marine diatoms, respectively, as they cannot be validated by data. Zooplankton is not resolved dynamically but observed zooplankton abundances are directly used in the model, hence eliminating the uncertainty of a dynamic zooplankton model. Observations allow us to distinguish between calanoids and non-calanoids, where calanoids are dominant in the brackish region in spring (Appeltans, 2003; Mialet et al., 2011). Grazing by

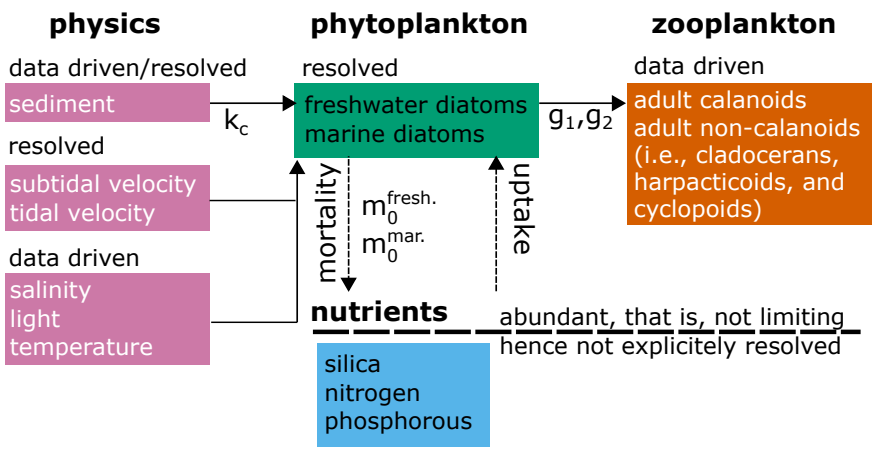

Figure 5.2: To constrain the processes and parameter variations as much as possible, we construct a model such that it is mainly data-driven and most parameters directly follow from the observations. The remaining (lumped) parameters are calibration parameters and are subject to extensive sensitivity analysis. We only dynamically resolve freshwater and marine diatoms as they are dominantly abundant in the Scheldt estuary in spring (Apr.-May). Zooplankton is not resolved dynamically but observed zooplankton abundances are directly used in the model. Observations allow us to distinguish between calanoids and non-calanoids. Grazing by zooplankton is not well constrained and thus included using calibration parameters g_1 and g_2. All processes contributing to phytoplankton mortality are lumped into parameters $m_0^{\text{fresh.}}$ and $m_0^{\text{mar.}}$ for the freshwater and marine diatoms, respectively, as they cannot be validated by data. The hydrodynamics are explicitly resolved in the vertical and longitudinal direction. The sediment dynamics are both resolved and data-driven. We use the resulting SPM distributions in combination with observed light extinction coefficients to estimate the sediment-induced light extinction coefficient k_c. As we are interested in multi-annual changes in sediment characteristics, we also apply a sensitivity study of the Chl-a distribution to k_c. As nutrients are abundant, we do not focus on nutrient dynamics.

zooplankton is not well constrained and therefore included using calibration parameters g_1, g_2. The hydrodynamics are explicitly resolved in the vertical and longitudinal direction. The sediment dynamics are both resolved and data-driven as we do not have the required data to calibrate the model for all years considered. More specifically, following Horemans et al. (2021), they are resolved for 2015-2018, resulting in a 2D SPM distribution. As we lack turbidity data (which is needed to calibrate the model) for the other years considered, this 2D distribution is scaled based on SPM observations at the water surface in 2004-2018. Here, we assumed that the vertical gradient in SPM did not change. We use the resulting SPM distributions with observed light extinction coefficients to estimate the sediment-induced light extinction coefficient k_c [see Eq. (5.7 for its definition)]. As we are interested in multi-annual changes in sediment characteristics, we also apply a sensitivity analysis of the Chl-a distribution to k_c (see Scenario 2, below). We do not focus on nutrient (and detritus) dynamics as nutrients are abundant in the entire estuary,

except possibly for a small part close to the mouth, which is not our area of interest (see Section 5.2.1). The model is thus driven by data-driven time-dependent parameters and four calibration parameters related to phytoplankton ($m_0^{\text{fresh.}}$, $m_0^{\text{mar.}}$), and zooplankton characteristics (g_1, g_2). To study the individual impact of potential multi-annual changes in SPM and phytoplankton and zooplankton characteristics on the multi-annual evolution of Chl-a accumulation, we consider four model scenarios:

1. We calibrate the parameters $m_0^{\text{fresh.}}$, $m_0^{\text{mar.}}$, g_1, and g_2 for the three distinct periods and determine the minimal multi-annual change in these calibration parameters required to capture the accumulation of Chl-a in the brackish region in spring.

2. We test what multi-annual change in sediment characteristics (i.e., k_c) is required to capture the accumulation of Chl-a in 2008-2014 in the brackish region assuming no multi-annual change in $m_0^{\text{mar.}}$, g_1, and g_2 after 2007. Here, we do not focus on $m_0^{\text{fresh.}}$ because we show that marine diatoms dominate the brackish region.

3. We assume a dominant impact of grazing by zooplankton on the mortality rate (i.e., $m_0^{\text{fresh.}} \approx 0$ and $m_0^{\text{mar.}} \approx 0$ s^{-1}) and test what multi-annual change in grazing parameters (i.e., g_1 and g_2) is required to capture the multi-annual evolution of Chl-a accumulation.

4. We neglect the impact of grazing by zooplankton on the mortality rate (i.e., $g_1 \approx 0$ and $g_2 \approx 0$ s^{-1} L) and test what multi-annual change in the mortality rate parameters (i.e., $m_0^{\text{fresh.}}$ and $m_0^{\text{mar.}}$) is required to capture the multi-annual evolution of Chl-a accumulation.

5.2.3.1 iFlow model

We chose to implement this model in the iFlow model, which we briefly introduce in this section. The iFlow model is a process-based, width-averaged, idealized model (Dijkstra et al., 2017). The model solves for water motion and cohesive SPM trapping in tide-dominated estuaries by resolving the width-averaged shallow water and SPM mass balance equations in equilibrium condition. For this, we use an equidistant grid of 100 cells in the longitudinal and 50 in the vertical direction. The flocculation dynamics of cohesive SPM are resolved using a single-class dynamic flocculation model (Winterwerp, 2002; Horemans et al., 2020a). The model focuses on the estuary-scale hydro- and SPM dynamics only by approximating the estuary's bathymetry and width by smooth profiles. The model resolves the tidal and subtidal dynamics of water motion and cohesive SPM concentration and provides approximate solutions of the complex and nonlinear set of equations for hydro- and SPM dynamics using a scaling and perturbation approach.

The hydrodynamics are forced at the upstream boundary and two main tributaries by a fixed water inflow and at the mouth by a tidal signal. Following Warner et al. (2005), the longitudinal salinity profile is implemented as a tide- and depth-independent profile (see the Appendix 5.A). This assumption is consistent with the Scheldt estuary being well-mixed (Baeyens et al., 1997). The SPM dynamics are forced by a constant inflow of

SPM that equals the product of the water discharge and subtidal SPM concentration at the upstream boundary, and by a fixed SPM concentration at the mouth. We assume that erosion of sediment scales to the magnitude of the bed shear stress. For details on the performance of this model for the Scheldt estuary, we refer to Horemans et al. (2020a). For this study, it suffices to mention that the M2 tidal and subtidal surface elevation correspond well to observations and that the magnitude of the SPM concentration and location of the estuarine turbidity maxima are reproduced.

We adapted iFlow's phytoplankton module (Dijkstra et al., 2019a). The width-averaged differential equation for the phytoplankton concentration P^i of phytoplankton group i and corresponding boundary conditions read as (Dijkstra et al., 2019a)

$$\partial_t P^i + \underbrace{u\partial_x P^i + (w - w_P)\partial_z P^i - \frac{1}{B}\partial_x(BK_h\partial_x P^i) - \partial_z(K_\nu \partial_z P^i)}_{\text{advection-diffusion}} = \underbrace{(\mu - m)P^i}_{\text{balance between local growth and mortality}}, \tag{5.1}$$

$$\begin{cases} w_P P^i + K_\nu \partial_z P^i = 0, & \text{at the bed and water surface (no flux),} \\ \left\langle \frac{1}{H+\zeta} \int_{-H}^{\zeta} P^i dz \right\rangle = P_{\text{sea}}, & \text{at the seaside boundary (constant concentration),} \\ B\left\langle \int_{-H}^{\zeta} (uP^i - K_h \partial_x P^i) dz \right\rangle = QP, & \text{at the upstream boundary (constant influx).} \end{cases} \tag{5.2}$$

Here, t represents time, x and z are the coordinates in the longitudinal and vertical direction, u and w are the water velocities in the longitudinal and vertical direction, w_P is the constant settling velocity of phytoplankton cells, B is the width of the estuary, K_h and K_ν are the horizontal and vertical eddy diffusivities, the angle brackets denote averaging over a long time scale (i.e., larger than a tide or day $\sim$ 1-2 weeks), $-H$ and ζ are the z-coordinates of the bed and water surface, P_{sea} is the constant phytoplankton concentration at the seaside boundary, QP is the constant influx of phytoplankton at the upstream boundary, and μ and m are the growth and mortality rate of phytoplankton. We divide the model into two phytoplankton classes: freshwater diatoms $P^{\text{fresh.}}$ and marine diatoms $P^{\text{mar.}}$. Following Naithani et al. (2016), most parameters of the two phytoplankton groups are equal, except the mortality rate m and maximum growth rate $\mu_{\max}$, which is $\sim$ 1.6 times larger for marine diatoms. The mortality rate depends on salinity S and the abundance of phytoplankton grazers Z:

$$m = m_0^i f_S(S) + f_Z(Z), \tag{5.3}$$

in which m_0^i is a (calibrated) constant mortality rate parameter of phytoplankton group i (i.e., the freshwater or marine diatoms) and f_S and f_Z are functions that determine the salinity and zooplankton dependence of the mortality rate m, respectively. Following Naithani et al. (2016), we assume the following (normalized) salinity stress:

$$f_S(S) = \begin{cases} \frac{1.07^S}{1.07^{S^{\text{ssea}}}}, & \text{freshwater diatoms,} \\ \frac{1+5\times0.85^S}{1+5\times0.85^{S^{\text{upstream}}}}, & \text{marine diatoms,} \end{cases} \tag{5.4}$$

in which ssea and S^{upstream} are the salinity at the downstream and upstream boundary (in ppt), respectively. For the zooplankton dynamics, we follow a data-driven approach and parameterize the corresponding grazing by zooplankton. We include the two dominant zooplankton groups $Z^{\text{calanoids}}$ and $Z^{\text{non-calanoids}}$ (units ind. L^{-1}, where 'ind.' denotes 'individuals'), which directly follow from the observations. More specifically, we linearly interpolate the zooplankton abundance observations and extrapolate the zooplankton abundance in the downstream region where we do not have observations using the system-averaged abundance. In the literature, multiple zooplankton dependencies of the phytoplankton mortality rate have been studied (Steele and Henderson, 1992). We consider the following longitudinal variation in m due to zooplankton abundance:

$$f_Z(Z^{\text{calanoids}}, Z^{\text{non-calanoids}}) = g_1 Z^{\text{calanoids}}(x) + g_2 Z^{\text{non-calanoids}}(x) \tag{5.5}$$

in which g_1, and g_2 are grazing parameters that follow from calibration (units s^{-1} L).

Given that the Scheldt estuary is a turbid system, we use the Platt formulation for light limitation of the time-averaged growth rate μ. This formulation is suitable for turbid systems as it does not consider an inverse relationship between μ and the photosynthetically active radiation (PAR) E at large E (cf. cell burning). Without nutrient limitation, μ then reads

$$\mu = \mu_{\max}(T)\left\langle \underbrace{\left[1 - \exp\left(\frac{\alpha}{P_{\max}}E\right)\right]}_{\text{Platt light limitation}} \right\rangle, \tag{5.6}$$

in which T is the water temperature and the angle brackets again denote averaging over a long time scale (i.e., larger than a tide or day). The photosynthetically active radiation E reads as

$$E(z,t;P^i,c) = E_{00}(t) \underbrace{\exp\left(k_{\text{bg}}z - k_c\int_z^0 c(z,t)dz - k_P\int_z^0 P^i(z,t)dz\right)}_{\text{Lambert-Beer light extinction}} \times \underbrace{\begin{cases}\sin\left[\omega_E \mod (t, 24\text{h})\right] & \text{if} \mod (t, 24\text{h}) < \pi/\omega_E \\ 0 & \text{elsewhere}\end{cases}}_{\text{truncated sinusoid representing the day/night cycle}}, \tag{5.7}$$

in which E_{00} represents the maximum PAR during mid-day, k_{bg}, k_c, and k_P are the background, sediment-induced, and self-shading exponential light extinction coefficients, respectively, c is the SPM concentration, ω_E is the angular frequency for day length, and mod denotes the modulus operator. Following Eppley (1972), we postulate the following temperature dependence of the maximum growth rate $\mu_{\max}(T)$:

$$\mu_{\max}(T) = \mu_{00}\mu_{01}^{\left(\frac{T}{1^\circ\text{C}}\right)}, \tag{5.8}$$

in which μ_{00} and μ_{01} are calibration parameters and T is expressed in ° C.

As with the hydro- and SPM dynamics, the model solves the approximated phytoplankton dynamics in equilibrium conditions (Dijkstra et al., 2019a). By doing so, we do

not have to postulate initial conditions, which further simplifies our sensitivity analysis. We argue that this assumption of equilibrium conditions is acceptable because the accumulation of phytoplankton in the brackish region covers approximately two months, which is large compared to the time scale of a bloom ($\sim$ 2-3 weeks). As shown by Regnier et al. (1997), the accuracy of their coupled reaction-transport in equilibrium conditions applied to the Scheldt estuary depends on the biological rates; higher rates (which are typical for the spring/summer months) result in higher model performance. We solve the marine and freshwater diatom dynamics separately and thereby neglect their coupling through shading by marine diatoms on freshwater diatoms and vice versa. This assumption is acceptable as we show later that freshwater and marine diatoms are spatially separated. In the region where we have similar concentrations of freshwater and marine (cf. coupling), self-shading is negligible due to the high SPM concentrations in this region. Last, for the implementation of time-averaged μ, we use the approximated Platt light limitation function presented in Horemans et al. (2020b). By solving approximate solutions for the phytoplankton dynamics, our model approach comes with very low computation times ($\sim$ s) when compared to more realistic models ($\sim$ hours-days), allowing for an extensive sensitivity analysis.

5.2.3.2 Calibration and parameter values

To determine potential environmental changes that may have caused the disappearance of phytoplankton accumulation in the brackish region, we apply a sensitivity study and run four different model scenarios (see Section 5.2.3). Here, most model parameter values directly follow from observations. Using the $P_{\max}$ and temperature observations, we derive the calibration parameters μ_{00} and μ_{01}, which contain the temperature dependence of $\mu_{\max}$ [Eq. (5.8), see the Appendix 5.B]. The influx of phytoplankton at the upstream boundary QP follows from the Chl-a observations at the upstream boundary. To correct for the large temporal variability in discharges (Waterinfo.be, 2019) and correctly resolve the sediment dynamics in spring, we use the procedure of Horemans et al. (2020a) to determine representative values of the freshwater discharge and determine the erosion and flocculation characteristics.This results in a representative modeled SPM distribution in 2004-2007, 2008-2014, and 2015-2018. We refer the reader to the Appendix 5.C for the technical details. To ensure that we correctly model light extinction, we use these modeled SPM distributions in combination with the observations of the light extinction coefficient k_d to estimate the sediment-induced light extinction coefficient k_c (see the Appendix 5.D for the technical details). We estimate the grazing parameters g_1 and g_2 corresponding to the calanoids and non-calanoids, respectively, and mortality rate parameters $m_0^{\text{fresh.}}$, $m_0^{\text{mar.}}$ corresponding to freshwater and marine diatoms, respectively, by calibrating modeled Chl-a concentrations to the Chl-a observations. Here, we again use the calibration method described in Horemans et al. (2020a) in which the phytoplankton model results and observations (cf. Chl-a) are quantitatively compared. The model parameters that are the focus of this paper are summarized in Table 5.1. The full parameter list is provided in Table 5.A.1. The reported values follow from observations, calibration, Dijkstra et al. (2019a), Horemans et al. (2020a), and other published studies.

Table 5.1: Parameter values used in our model experiments based on observations (source), model calibration (calibrated), and the literature. If only one parameter value is presented, we used this value for all three periods.

Variable	Definition	Value 2004-2007	Value 2008-2014	Value 2015-2018	Unit
$\mu_{00}^{\text{fresh.}}$	Maximum growth rate at 0 ° C of freshwater diatoms (source)	0.96×10^{-5}	1.04×10^{-5}	0.86×10^{-5}	s^{-1}
$\mu_{00}^{\text{mar.}}$	Maximum growth rate at 0 ° C of marine diatoms (source)	1.59×10^{-5}	1.72×10^{-5}	1.43×10^{-5}	s^{-1}
μ_{01}	Calibration parameter in temperature dependence for $\mu_{\max}$ (source)	1.10	1.07	1.05	/
g_1	Calanoids grazing parameter (calibrated)	0.8×10^{-7}	0.13×10^{-7}	0.8×10^{-7}	s^{-1} L
g_2	Non-calanoids grazing parameter (calibrated)	0.47×10^{-7}	0.32×10^{-7}	0.47×10^{-7}	s^{-1} L
$m_0^{\text{fresh.}}$	Mortality rate parameter for freshwater diatoms (calibrated)	1.89×10^{-6}	3.30×10^{-6}	8.30×10^{-6}	s^{-1}
$m_0^{\text{mar.}}$	Mortality rate parameter for marine diatoms (calibrated)	3.21×10^{-6}	1.06×10^{-6}	3.35×10^{-6}	s^{-1}
E_{00}	Maximum PAR (source)		1007		μmol photons m^{-2} s^{-1}
ω_E	Angular frequency for day length (source)		0.215		d^{-1}
T	Water temperature (source)	14.3	14.7	14.7	° C
P_{sea}	Phytoplankton boundary concentration at the mouth (source)	15.9	17.1	15.8	μg L^{-1}
QP	Influx of phytoplankton at the upstream boundary (source)	1.5	1.8	2.5	g s^{-1}
w_P	Settling velocity of phytoplankton cells (Sarthou et al., 2005)		1.15×10^{-5}		m s^{-1}
k_{bg}	Background exponential light extinction coefficient (Pennock and Sharp, 1994)		0.095		m^{-1}
k_P	Self-shading exponential light extinction coefficient (Pennock and Sharp, 1994)		18		m^2 $(\text{mol N})^{-1}$
k_c	Sediment-induced exponential light extinction coefficient (source)	81.4	77.9	72.0	m^2 kg^{-1}
α	Growth efficiency (source)	0.0165	0.0168	0.0188	mg C (mg Chl-a)$^{-1}h^{-1}$ [μmol photons m^{-2} s^{-1}]$^{-1}$

5.3 Results

5.3.1 Evolution of Chl-a and corresponding environmental conditions of the in situ observations

5.3.1.1 Evolution of Chl-a and zooplankton

Figure 5.3a presents the evolution of the sub-surface Chl-a concentration in 2004-2018, showing a clear seasonality and corresponding phytoplankton blooms; at the upstream boundary ($\sim$ km 160), the Chl-a concentration can reach values above 400 μg L^{-1} in summer and, although local maxima are observed, decays in the downstream direction. We divide the time series into three distinct periods and focus on the time-averaged Chl-a concentration in spring (Apr.-May) (Fig. 5.3b). In 2004-2007, we detect time-averaged Chl-a concentrations above 50 μg L^{-1} in the upstream region, $>$ km 80. In 2008-2014 and 2015-2018, this region is limited to $>$ 100 km and $>$ 110 km, respectively. In 2008-2014, we also observe concentrations $>$ 50 μg L^{-1} more downstream in the brackish region between km 60-90. The Chl-a concentrations are significantly larger in 2008-2014 in the brackish region compared to the concentrations in 2004-2007 (Welch t-test, p-value $< 10^{-3}$) and 2015-2018 (Welch t-test, p-value $< 10^{-12}$).

Figure 5.4 displays the time-averaged calanoids and non-calanoids abundance in spring for the three distinct periods considered. The shaded area depicts the standard error of the zooplankton abundance. The calanoids abundance (Fig. 5.4a) also shows distinct trends in the three periods considered. In 2004-2007, we observe a relatively low mean calanoids abundance between km 110-150, ranging upto approximately 5 ind. L^{-1}. Downstream from km 110, we observe an increase in calanoids, resulting in a local maximum of the mean values of calanoids of approximately 10 ind. L^{-1}, centered near km 90. In 2008-2014, the local maximum of the mean values in calanoids abundance shifts in the upstream direction and increases. The overall calanoid abundance increases, with a maximum of the mean values of approximately 17.5 ind. L^{-1} at km 110. In 2015-2018, the local maximum of the mean values in calanoids abundance shifts further landwards to approximately km 140, with again a maximum of approximately 17.5 ind. L^{-1}. We thus observe a land-inward shift and estuary-scale increase of the local calanoids abundance over time. The calanoids concentrations are significantly larger between km 110-150 in 2015-2018 compared to 2004-2007 (Welch t-test, p-value $< 10^{-4}$). However, the system-averaged, volume-weighted calanoids abundances are 4.9 ind. L^{-1}, 6.43 ind. L^{-1}, and 4.3 ind. L^{-1} in 2004-2007, 2008-2014, and 2015-2018, respectively. With 'volume-weighted', we mean that we weigh the abundance with the water volume corresponding to the location at which the abundance is estimated. So, we take into account the fact that the funnel-shaped estuary is narrow and shallow in the upstream region and we thus attribute more weight to observations in the downstream direction. At the upstream boundary, non-calanoids are dominantly present (Fig. 5.4b). On average, we observe an increase of the non-calanoids abundance in the landward direction on the estuary scale in all three periods. As illustrated by the large standard error, the differences of the non-calanoids

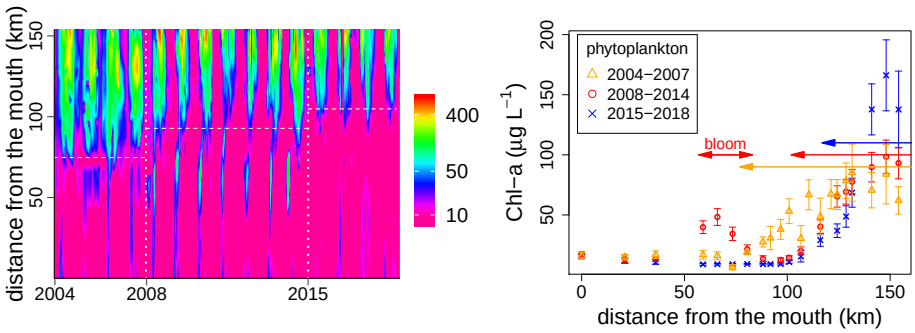

(a) Chl-a concentration (μg L^{-1})

(b) Time-averaged Chl-a concentration in spring

Figure 5.3: (a) Observed Chl-a concentration (μg L^{-1}) in 2004-2018 and (b) time-averaged Chl-a concentration in spring. We observe a phytoplankton bloom in the brackish region (km 60-90) in spring in 2008-2014, which is absent in the other years considered. The Chl-a concentration also decreases faster in the downstream direction in more recent years (illustrated by the horizontal arrows).

abundance are not statistically significant between the three distinct periods (Welch t-test, p-value = 0.10 and 0.22 when comparing the abundances between km 110-150 in 2015-2018 to 2004-2007 and 2008-2014, respectively).

5.3.1.2 Evolution of SPM and light extinction

Figure 5.5a shows the sub-surface time-averaged SPM concentration in the three periods considered in spring. In all three periods, the SPM concentrations range upto approximately 150 mg L^{-1}. However, we observe significantly lower concentrations between approximately km 50-100 in 2004-2007 (Welch t-test, p-value $< 10^{-5}$ and $< 10^{-6}$ when compared to 2008-2014 and 2015-2018, respectively). The lower SPM concentrations are especially visible between km 70-80, where we have concentrations below 50 mg L^{-1} in 2004-2007 and upto 150 mg L^{-1} after 2007. Moreover, in 2015-2018, we observe the largest SPM concentrations between km 80-120 (Welch t-test, p-value $< 10^{-3}$ and $< 10^{-4}$ when compared to 2008-2014 and 2004-2007, respectively).

The time-averaged light extinction coefficient in spring shows a similar evolution to the SPM concentration (Fig. 5.5b), with significantly lower values of approximately 4 m^{-1} between km 50-100 in 2004-2007 compared to the values of approximately 7 m^{-1} after 2007 (Welch t-test, p-value $< 10^{-8}$ and $< 10^{-10}$ when compared to 2008-2014 and 2015-2018, respectively). We have the largest time-averaged values between km 80-120 in 2015-2018, which is consistent with the SPM observations (Welch t-test, p-value $= 3.4 \times 10^{-2}$ and $< 10^{-5}$ when compared to 2008-2014 and 2004-2007, respectively).

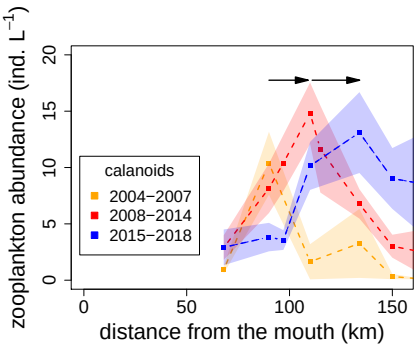

(a) Calanoid abundance in spring

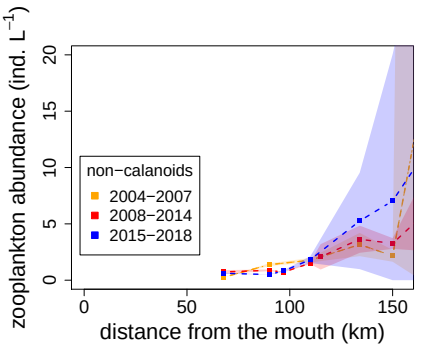

(b) Non-calanoid abundance in spring

Figure 5.4: Multi-annual time averages of (a) calanoids and (b) non-calanoids abundance in spring (Apr.-May). The shaded area depicts the standard error. We observe a dominant abundance of calanoids in the brackish region and a land-inward shift of calanoids in time. The non-calanoids are mainly situated at the upstream boundary.

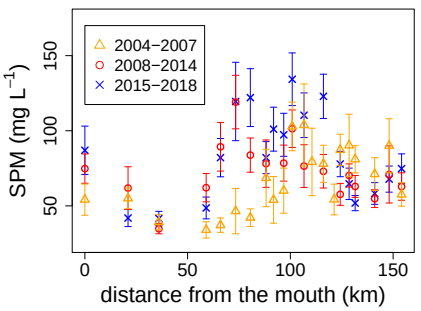

(a) Time-averaged SPM concentration in spring

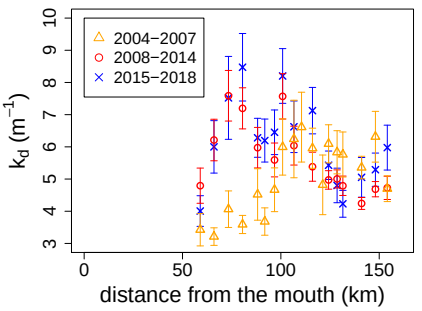

(b) Time-averaged light-extinction coefficient in spring

Figure 5.5: Multi-annual time-averaged observations in spring (Apr.-May) in 2004-2018 of (a) the water surface SPM concentration and (b) the light extinction coefficient k_d. The error bars depict the standard error of the observations.

5.3.1.3 Evolution of discharge, salinity intrusion, and photosynthetic parameters

In spring (Apr.-May), the average discharge is 85, 81, and 72 m^{-3} s^{-1} in 2004-2007, 2008-2014, and 2015-2018, respectively. We thus observe a slight decrease in total freshwater discharge over time. We define the salinity intrusion as the distance from the mouth

at which the salinity equals 2 ppt. The corresponding time-averaged values in spring are 81 km, 79 km, and 83 km in 2004-2007, 2008-2014, and 2015-2018, respectively. In spring, the salinity intrusion does not show major changes during the study period 2004-2018. The time-and system-averaged maximum photosynthetic rate $P_{\max}$ in spring is approximately equal in 2004-2007 and 2008-2014, but significantly lower in 2015-2018. The corresponding time-averaged values are 6.59, 6.44, and 4.31 mg C (mg Chl-a)$^{-1}$ h^{-1}, respectively. The corresponding time-and system-averaged growth efficiency α are 0.0165, 0.0168, and 0.0188 mg C (mg Chl-a)$^{-1}$ h^{-1} [μmol photons m^{-2} s^{-1}]$^{-1}$, respectively. For the monthly averaged data of the discharge, salinity intrusion, $P_{\max}$, and α covering the full year, we refer the reader to the Appendix 5.E.

Multi-annual observations in the Scheldt estuary thus show an estuary-scale increasing or decreasing development in zooplankton abundance, SPM (cf. light extinction), $P_{\max}$, and, to a minor extent, in the freshwater discharge in the Scheldt estuary in 2004-2018 in spring. Based on the observations alone, it is difficult to determine the change in parameters that is responsible for the evolution of Chl-a concentration. Therefore, we apply a complementary model approach in the following section.

5.3.2 Evolution of Chl-a studied using model experiments

To quantify the impact of the observed trends presented in the previous section and alterations of other factors affecting phytoplankton growth on the Chl-a concentration, we consider the four model scenarios presented in Section 5.2.3.

5.3.2.1 Scenario 1: minimum multi-annual change in calibration parameters required to capture the accumulation of Chl-a in the brackish region in spring

We calibrate the mortality rate parameters $m_0^{\text{fresh.}}$ and $m_0^{\text{mar.}}$ and grazing parameters g_1 and g_2 to the observed multi-annual time-averaged Chl-a concentrations for the three periods considered. The corresponding values are listed in Table 5.1. In 2004-2007 and 2015-2018, we capture the estuary-scale patterns of Chl-a by keeping the parameters $m_0^{\text{mar.}}$, g_1, and g_2 more or less fixed and only changing $m_0^{\text{fresh.}}$ (Figs. 5.6a and 5.6c). We require a significantly larger mortality rate parameter of the freshwater diatoms in 2015-2018 than in 2004-2007 ($m_0^{\text{fresh.}} = 8.30 \times 10^{-6}$ versus $m_0^{\text{fresh.}} = 1.89 \times 10^{-6}$ s^{-1}, respectively) to capture the faster decrease of the Chl-a concentrations in the downstream direction over the years 2004-2018 (depicted by the horizontal arrows in Fig. 5.3b). Here, it is important to note that the observed Chl-a values between km 50 and 100 are below the detection limit of 10 μg L^{-1} and all modeled Chl-a concentrations lower than this limit are considered as equally good in the calibration. In 2008-2014, we only obtain the accumulation of Chl-a in the brackish region if we also assume a multi-annual evolution in parameters $m_0^{\text{mar.}}$, g_1, and g_2 (see Table 5.1). The calibrated $m_0^{\text{mar.}}$ and g_1 values are ~ 3 and ~ 7 times lower, respectively. If we were to assume no multi-annual evolution of parameters $m_0^{\text{mar.}}$, g_1, and g_2 after 2007, we would not capture the accumulation of Chl-a

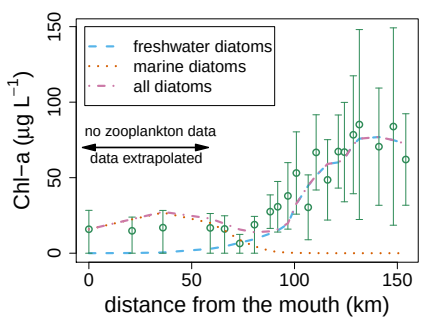

(a) Model and observed Chl-a concentration in spring 2004-2007

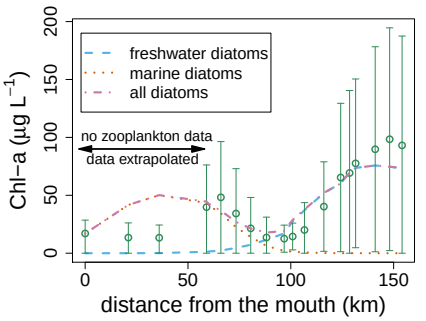

(b) Model and observed Chl-a concentration in spring 2008-2014

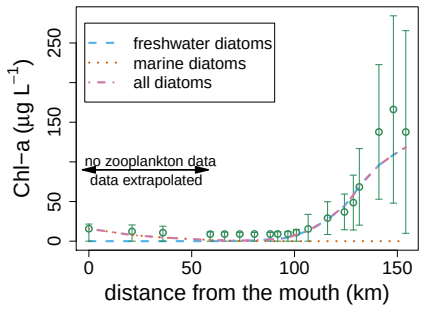

(c) Model and observed Chl-a concentration in spring 2015-2018

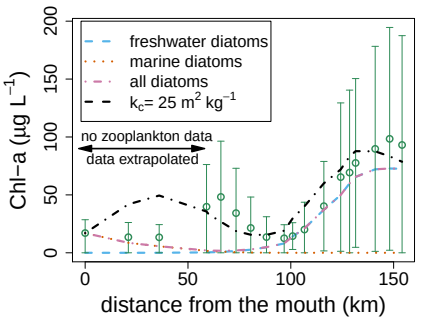

(d) Model and observed Chl-a concentration in spring 2008-2014 using the $m_0^{\text{mar.}}$, g_1, and g_2 values from 2004-2007

Figure 5.6: Multi-annual time-averaged Chl-a observations (dots) and depth-averaged model result (dashed line) in spring (Apr.-May) in (a) 2004-2007, (b) 2008-2014, and (c) 2015-2018 (Scenario 1). (d) When we do not consider a multi-annual evolution of parameters $m_0^{\text{mar.}}$, g_1, and g_2 (Scenario 2), we do not capture the estuary-scale Chl-a distribution in 2008-2014 beyond km 60 (for which we have zooplankton data). A sensitivity analysis shows that by decreasing k_c by a factor ~ 3 ($k_c = 25$ versus $k_c = 78$ m^2 kg^{-1}), we also obtain accumulation of Chl-a in the brackish region. However, this difference is significantly larger than the variability of k_c that follows from the observations.

in the brackish region (Fig. 5.6d). To summarize, to capture accumulation of Chl-a in the brackish region in 2008-2014, we require a (significant) multi-annual change in parameters $m_0^{\text{fresh.}}$, $m_0^{\text{mar.}}$, g_1, and g_2.

5.3.2.2 Scenario 2: multi-annual change in sediment characteristics required to capture the accumulation of Chl-a in the brackish region in spring

Keeping all parameters fixed to their values presented in Table 5.1 and assuming no multi-annual change after 2007 in parameters $m_0^{\text{mar.}}$, g_1, and g_2, a careful sensitivity analysis shows that variability in μ_{00}, Q, P_{sea}, and QP does not result in accumulation of Chl-a in the brackish region in 2008-2014 (for the details, see the Appendix 5.F). Only by decreasing k_c by a factor ~ 3 ($k_c = 25$ versus $k_c = 78$ m^2 kg^{-1}), we obtain accumulation of Chl-a in the brackish region (Fig. 5.6d). This difference is significantly larger than the variability that follows from the observations, which is between ~ 65 and 80 m^2 kg^{-1} (for the details, see the Appendix 5.D). Therefore, a multi-annual change in sediment characteristics alone cannot explain the multi-annual evolution in the Chl-a distribution.

5.3.2.3 Scenario 3: the individual effect of grazing by zooplankton

In this section, we assume a dominant impact of grazing by zooplankton on the mortality rate (i.e., $m_0^{\text{fresh.}} \approx 0$ and $m_0^{\text{mar.}} \approx 0$ s^{-1}). Calibration of the grazing parameters g_1 and g_2 to the Chl-a observations in 2004-2007 and 2015-2018, and the Chl-a observations in the brackish region only in 2008-2014 results in the modeled Chl-a concentration presented in Figs. 5.7a, 5.7c, and 5.7b, respectively. Our calibration results in larger grazing parameters because we neglected other processes contributing to the mortality rate (e.g., salinity stress). The grazing parameters are $g_1 = 2.5$ and $g_2 = 0.93 \times 10^{-7}$ s^{-1} L, $g_1 = 0.51$ and $g_2 = 0.71 \times 10^{-7}$ s^{-1} L, and $g_1 = 2.5$ and $g_2 = 0.93 \times 10^{-7}$ s^{-1} L in 2004-2007, 2008-2014, and 2015-2018, respectively. In 2004-2007 and 2015-2018, although we detect some local anomalies (for example, the underestimation near km 90 in 2004-2007), the model captures the Chl-a distribution on the estuary-scale using the same g_1 and g_2 values. In contrast, if we were to choose these calibrated grazing parameter values in 2008-2014, we would obtain a Chl-a distribution very similar to the case presented in Fig. 5.6d (all diatoms) and we would thus not capture the accumulation of Chl-a in the brackish region (not shown). Considering different values for g_1 and g_2 in 2008-2014, we can again model the estuary-scale Chl-a patterns. Here, the local minimum near km 100 is due to a local increase in mortality rate resulting from the high calanoid abundance in this region. If we were to consider only the calanoids (so a reduction of one calibration parameter), we would not obtain the clear local minimum in Chl-a near km 100 (not shown). Finally, choosing the g_1 and g_2 values corresponding to 2008-2014 in 2015-2018 results in a system-scale overestimation of Chl-a (not shown). To summarize, when only including the effect of grazing by zooplankton, we again require a (significant) multi-annual evolution of g_1 and g_2 to capture the accumulation of Chl-a in the brackish region in spring in 2008-2014.

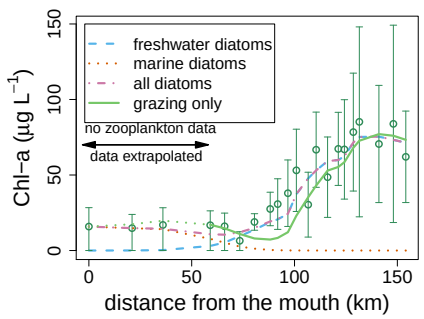

(a) Model and observed Chl-a concentration in spring 2004-2007

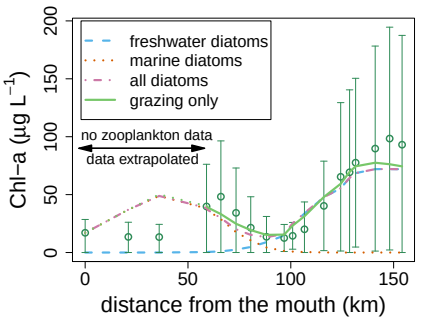

(b) Model and observed Chl-a concentration in spring 2008-2014

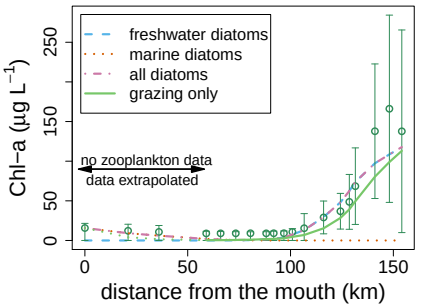

(c) Model and observed Chl-a concentration in spring 2015-2018

Figure 5.7: Multi-annual time-averaged Chl-a observations (dots) and depth-averaged model result (dashed/solid line) in spring (Apr.-May) in (a) 2004-2007, (b) 2008-2014, and (c) 2015-2018 assuming a mortality rate exclusively caused by grazing (Scenario 3, denoted by 'grazing only') and neglecting the effect of grazing by zooplankton (Scenario 4, denoted by 'freshwater diatoms', 'marine diatoms', and 'all diatoms'). Except for the Chl-a concentrations downstream from km 60 in 2008-2014 (for which we do not have zooplankton data), the model captures the estuary-scale Chl-a distribution. We can thus obtain the multi-annual evolution in Chl-a accumulation in the brackish region in spring (Apr.-May) by both a change in phytoplankton community characteristics and grazing by zooplankton. In Scenario 3 (cf. 'grazing only'), we attribute the local minimum near km 100 in 2008-2014 to a local increase in mortality rate resulting from the high calanoid abundance in this region. In Scenario 4 (cf. 'all diatoms'), this local minimum in Chl-a results from the spatial separation between marine and freshwater diatoms that is caused by salinity stress.

5.3.2.4 Scenario 4: neglecting the effect of grazing by zooplankton

In this section, we neglect the impact of grazing by zooplankton to the mortality rate (i.e., $g_1 \approx 0$ and $g_2 \approx 0$ s^{-1} L). We calibrate the mortality rate parameters $m_0^{\text{fresh.}}$ and $m_0^{\text{mar.}}$, while keeping all other parameters fixed to the calibrated values presented in Table 5.1 (Figs. 5.7a-5.7c). The calibration results in larger mortality rate parameters, which is due to the absence of grazing pressure. In 2004-2007, we capture the large-scale pattern of the Chl-a distribution using a ~ 70 % larger mortality rate parameter for the marine diatoms ($m_0^{\text{fresh.}} = 3.8 \times 10^{-6}$ versus $m_0^{\text{mar.}} = 6.4 \times 10^{-6}$ s^{-1}). In 2008-2014, the model captures the Chl-a distribution beyond km 59 and the local minimum near $\sim$ km 100. This local minimum results from a clear spatial separation between marine and freshwater diatoms that is caused by salinity stress. In Scenario 3, we attributed this minimum to a local increase in mortality rate resulting from the high calanoid abundance in this region. The model overestimates the Chl-a concentration in the marine region at $\sim$ km 21 and 36. The accumulation of Chl-a in the brackish region mainly corresponds to marine diatoms. This accumulation requires a ~ 3 times lower mortality rate parameter for the marine diatoms ($m_0^{\text{fresh.}} = 6.6 \times 10^{-6}$ versus $m_0^{\text{mar.}} = 2.1 \times 10^{-6}$ s^{-1}). Upstream from the local minimum at $\sim$ km 100, we mainly have freshwater diatoms. In 2015-2018, we again model the Chl-a distribution accurately on the estuary-scale and have a clear spatial separation between freshwater and marine diatoms. The marine diatoms have a significantly lower mortality rate parameter ($m_0^{\text{fresh.}} = 6.7 \times 10^{-6}$ versus $m_0^{\text{mar.}} = 16..6 \times 10^{-6}$ s^{-1}). In the following, we focus on the multi-annual evolution of the calibration parameters. The mortality rate parameter corresponding to the marine diatoms is equal in 2004-2007 and 2015-2018 ($m_0^{\text{mar.}} = 6.5 \times 10^{-6}$ s^{-1}), but significantly lower in 2008-2014 ($m_0^{\text{mar.}} = 2.1 \times 10^{-6}$ s^{-1}). As found before, the model also shows a multi-annual increase of $m_0^{\text{fresh.}}$. For the freshwater diatoms, we have $m_0^{\text{fresh.}} = 3.8 \times 10^{-6}$ s^{-1}, $m_0^{\text{fresh.}} = 6.6 \times 10^{-6}$ s^{-1}, and $m_0^{\text{fresh.}} = 16.6 \times 10^{-6}$ s^{-1} in 2004-2007, 2008-2014, and 2015-2018, respectively. To summarize, when excluding the effect of grazing on the mortality rate, we again require a (significant) multi-annual evolution of $m_0^{\text{fresh.}}$ and $m_0^{\text{mar.}}$ to capture the accumulation of Chl-a in the brackish region in spring in 2008-2014.

5.4 Discussion

5.4.1 Suggested importance of grazing and phytoplankton community characteristics

We studied the appearance and disappearance of accumulation of Chl-a in the brackish region of the Scheldt estuary in spring in 2008-2014. To this end, we analyzed multi-annual observations of factors affecting phytoplankton growth and ran various model scenarios. The model approach allowed us to detect which combination of multi-annual parameter change may result in the multi-annual evolution of the Chl-a concentrations. Our results suggest that we require a multi-annual shift in phytoplankton mortality rate to capture the appearance and disappearance of Chl-a accumulation in the brackish region and that

other parameters (e.g., SPM) alone cannot explain this observed trend of Chl-a.

The multi-annual evolution in mortality rate may be attributed to either a change in phytoplankton community characteristics or grazing by zooplankton (Fig. 5.7) or a combination (Figs. 5.6a-c). We thus found different model input parameter choices leading to similar model results, which is known as equifinality.

Equifinality is important because in the literature various authors presented opposing explanations regarding the relative contribution of grazing by zooplankton and phytoplankton community characteristics (cf. salinity stress) to the mortality rate. It is not clear whether these opposing explanations are caused by real changes of the estuarine system or whether they may be attributed to equifinality. For example, on the one hand, a model study by Gypens et al. (2013) showed that salinity is a crucial driver for the spatial phytoplankton distribution in the Scheldt estuary in 2006, while grazing pressure has a negligible role. The authors thus stress the importance of salinity stress (cf. phytoplankton community characteristics) instead of grazing by zooplankton. On the other hand, a dominant impact of zooplankton grazing on the mortality rate was found by Calbet and Landry (2004) who studied 136 estuarine systems and showed that zooplankton grazes on average approximately 60 % of the primary production. Moreover, by comparing Chl-a concentrations and biomass concentrations of the *Eurytemora affinis*-dominated zooplankton population in the St Lawrence estuary (Canada), Winkler et al. (2003) showed that *Eurytemora affinis* is likely to be a major cause of the downstream decrease in Chl-a concentration. This agrees with the multi-annual observations in the Scheldt estuary: in 1996, calanoid copepods, in casu *Eurytemora affinis*, dominated in the downstream brackish region and were quasi absent in the freshwater region. From 2009, they gradually developed more upstream to also become dominant there (Appeltans, 2003; Mialet et al., 2010, 2011; Chambord et al., 2016).

Although we may not further constrain the relative importance of grazing by zooplankton and phytoplankton community characteristics to the mortality rate, we can compare our model parameter values to the literature as a first verification of our model results. Our mortality rate (i.e., m) values $\sim 10^{-6}$ s^{-1} comply with the value of $\sim 1.1 \times 10^{-6}$ s^{-1} presented in Desmit et al. (2005) who studied a real-case in the Scheldt estuary near km 115. Additionally, incubation experiments carried out with adult *Eurytemora affinis* around km 80 in the Scheldt estuary during spring 2013 and 2014 show g values between 1.54×10^{-8} and 2.78×10^{-6} s^{-1} L (Chambord et al., in prep.), overlapping with the modeled values in this study, but also showing large variability.

Therefore, to further constrain which multi-annual change in model parameters may have resulted in the multi-annual change in Chl-a accumulation, additional observations are required. Firstly, to determine the relative importance of grazing by zooplankton, observational studies on the mortality rate are needed. Measurements of rates (e.g., grazing rate) are better constraints than state variables (e.g., Chl-a) (Franks, 2009). For example, Friedrichs et al. (2007) showed that different model and parameter choices may fit the data equally well, although the grazing rates may differ by more than an order of magnitude. Secondly, a larger spatial and temporal resolution of the observations is recommended as different model and parameter choices may converge at the specific times

and locations for which data is present, while in between the observations the distinct models may show very distinct results (Friedrichs et al., 2007).

5.4.2 Model limitations

In this section, we present our main model limitations, compare our model approach to state-of-the-art models applied to the Scheldt estuary, and discuss its implication for other studies and future research.

Following Naithani et al. (2016), we assumed stenohaline marine and freshwater diatoms adapted to the extreme high or low salinities. However, in the literature, also euryhaline species were considered (Roubeix et al., 2008; Gypens et al., 2013). As pointed out by Gypens et al. (2013), the presence of euryhaline phytoplankton species may have a significant impact on the magnitude and distribution of both freshwater and marine phytoplankton. Additionally, in the summer of 2003, the phytoplankton community characteristics showed species with different salinity optima and rather restricted salinity tolerances (Muylaert et al., 2009). The existence of such a phytoplankton group adapted to more intermediate salinity may explain the overestimation of Chl-a by our model at $\sim$ km 21 and 36 (Fig. 5.7b).

Compared to models such as presented by Arndt et al. (2011), Gypens et al. (2013), and Naithani et al. (2016), we idealized the biochemical processes. Based on observations, we excluded nutrient limitation, only included two zooplankton groups using a data-driven approach, and only distinguished between freshwater and marine diatoms.

Although we made significant model assumptions, our model approach resulted in valuable insights. Before our work, the observed trend change in Chl-a in spring was poorly described and it was unclear whether this trend change is related to changes in physical characteristics (sediment, discharge, temperature) or changes in biological characteristics. In our contribution, we can constrain this to a change in biological characteristics related to phytoplankton mortality that seems to have some correlation with zooplankton grazing and phytoplankton community characteristics. As discussed by Oreskes et al. (1994), we used our model approach to illuminate which features of the systems mainly require further research and which empirical data is lacking.

To summarize, although a careful assessment of the model assumptions is required, our model is generally applicable to turbid nutrient-rich, tide-dominated estuaries. The approach is particularly useful to constrain parameter ranges, quantify model parameters in more advanced state-of-the-art models, and determine which empirical data is recommended for further research on this topic.

5.5 Conclusions

In this contribution, we studied the multi-annual estuary-scale evolution of the spring phytoplankton (cf. Chl-a) distribution in the Scheldt estuary. We focused on the appearance and disappearance of phytoplankton accumulation in the brackish region in spring in 2004-2018.

We first analyzed multi-annual in situ observations covering the SPM concentration, zooplankton abundance, and other variables affecting net phytoplankton growth, showing a multi-annual estuary-scale evolution of not only the SPM distribution and zooplankton abundance, but also of the freshwater discharge and maximum photosynthetic rate. Next, to detect the multi-annual evolution of these variables that can be linked to the evolution of phytoplankton, we employed a model approach in which the observations were the core. Our model allowed us to significantly constrain which evolution of variables may explain the evolution of phytoplankton; both a multi-annual change in mortality rate and corresponding grazing by zooplankton and phytoplankton community characteristics may have caused the multi-annual estuary-scale evolution of phytoplankton in spring. We were thus able to limit the number of model input parameter choices leading to similar model results, which is known as equifinality.

Although our model approach simplifies reality and shows (local) anomalies when comparing phytoplankton model results and observations, it allowed us to quantitatively determine the importance of various factors affecting phytoplankton growth on the estuary scale. This knowledge is important for moving forward using more complex numerically costly models. Our results highlight the importance of insight into the zooplankton dynamics and phytoplankton community characteristics to understand the phytoplankton dynamics in the Scheldt estuary. Further research and experimental validation are required to determine the mechanisms that may have caused these multi-annual estuary-scale changes in mortality rate, grazing, and phytoplankton community characteristics.

List of symbols

Latin

B	Width of the estuary
c	Suspended sediment concentration
E	Photosynthetically active radiation
E_{00}	Maximum photosynthetically active radiation
E_1	Sub-surface light intensity
E_2	Light intensity measured at a fixed distance Δz from the sub-surface sensor
f_S	Function that determines the salinity stress of phytoplankton
f_Z	Function that determines the grazing pressure of phytoplankton
g	Grazing parameter

g_1	Calanoids grazing parameter
g_2	Non-calanoids grazing parameter
H	Magnitude of the z-coordinate of the river bed
K_h	Horizontal diffusivity coefficient
K_ν	Vertical eddy diffusivity coefficient
k_{bg}	Background exponential light extinction coefficient
k_c	Sediment-induced exponential light extinction coefficient
k_d	Exponential light extinction coefficient
k_P	Self-shading exponential light extinction coefficient
m	Mortality rate of phytoplankton
m_0^i	Mortality rate parameter of phytoplankton class i
$m_0^{\text{fresh.}}$	Mortality rate parameter of the freshwater diatoms
$m_0^{\text{mar.}}$	Mortality rate parameter of the marine diatoms
P	Phytoplankton concentration
P^i	Phytoplankton concentration of class i
$P^{\text{fresh.}}$	Phytoplankton concentration of the freshwater diatoms
$P^{\text{mar.}}$	Phytoplankton concentration of the marine diatoms
$P_{\max}$	Maximum photosynthetic rate
P_{sea}	Phytoplankton boundary concentration at the mouth
QP	Influx of phytoplankton at the upstream boundary
S	Salinity
S^{upstream}	Salinity at the upstream boundary
ssea	Salinity at the downstream boundary
T	Water temperature
t	Time
u	Water flow velocity in the longitudinal dimension
w	Water flow velocity in the vertical dimension
w_P	Settling velocity of phytoplankton cells
x	Spatial coordinate in the longitudinal dimension
Z	Concentrations of phytoplankton grazers
Z	Abundance of phytoplankton grazers
$Z^{\text{calanoids}}$	Calanoids concentration
$Z^{\text{non-calanoids}}$	Non-calanoids concentration
z	Spatial coordinate in the vertical dimension

Greek

α	Photosynthetic growth efficiency
Δz	Distance between the sub-surface surface and second light sensor
∂_t	Partial derivative to t
∂_x	Partial derivative to x
∂_z	Partial derivative to z
ζ	z-coordinate of the water surface
μ	Growth rate of phytoplankton
μ_{00}	Maximum growth rate at 0 ° C
$\mu_{00}^{\text{fresh.}}$	Maximum growth rate at 0 ° C of the freshwater diatoms
$\mu_{00}^{\text{mar.}}$	Maximum growth rate at 0 ° C of the marine diatoms

μ_{01}	Calibration parameter in the temperature dependence for $\mu_{\max}$
$\mu_{\max}$	Maximum growth rate
ω_E	Angular frequency for day length

Appendix 5.A: salinity profile

Following Warner et al. (2005), we fit the salinity data measured in spring in the Scheldt estuary to the following postulated salinity distribution:

$$\frac{s_{\text{sea}}}{2}\left(1-\tanh\frac{x-x_c^{\text{Sal.}}}{x_L^{\text{Sal.}}}\right), \tag{5.9}$$

where s_{sea} is the salinity boundary condition at the mouth and $x_c^{\text{Sal.}}$ and $x_L^{\text{Sal.}}$ are further undefined calibration parameters. Figure 5.A.1 shows the salinity data and corresponding data fit in spring for the three periods considered. The corresponding parameter values are listed in Table 5.A.1.

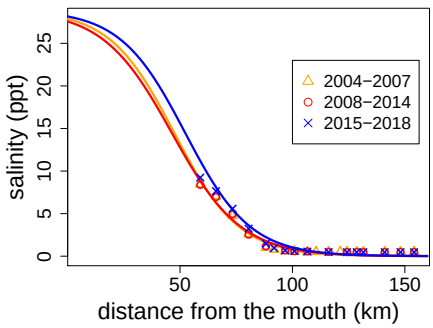

Figure 5.A.1: Measured salinity in the Scheldt estuary in spring and the corresponding data fit using Eq. (5.9).

Appendix 5.B: temperature dependence of $\mu_{\max}$

Following Eppley (1972), we postulate the following temperature dependence of the maximum growth rate $\mu_{\max}(T)$:

$$\mu_{\max}(T) = \mu_{00}\mu_{01}^{T}, \tag{5.10}$$

in which T is the water temperature and μ_{00} and μ_{01} are calibration parameters. Figure 5.B.1a shows the multi-annual averaged temperature dependence in 2004-2018. Figure 5.B.1b shows the $P_{\max}$-T plot for the 2015-2018 reference case and the corresponding

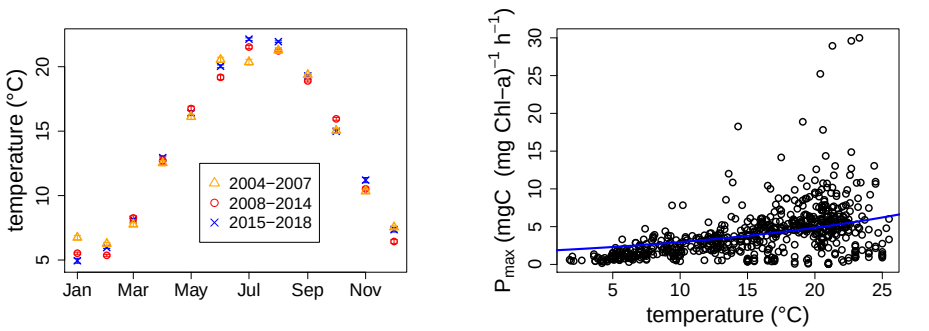

(a) Time-averaged temperature

(b) Temperature dependence of $P_{\max}$

Figure 5.B.1: (a) The multi-annual time-averaged temperature observations between 2004-2018. (b) $P_{\max}$-T plot for the 2015-2018 reference case and the corresponding data fit using Eq. (5.10), resulting in $\mu_{00} = 1.00 \times 10^{-5}$ s^{-1} and $\mu_{01} = 1.05$.

data fit following Eq. (5.10), resulting in $\mu_{00} = 1.00 \times 10^{-5}$ s^{-1} and $\mu_{01} = 1.05$. Note that to translate $P_{\max}$ to $\mu_{\max}$, we have to divide by the C:Chla ratio. Similarly, we have $\mu_{00} = 1.21 \times 10^{-5}$ s^{-1} and $\mu_{01} = 1.07$ and $\mu_{00} = 1.12 \times 10^{-5}$ s^{-1} and $\mu_{01} = 1.10$ in 2008-2014 and 2004-2007, respectively.

We divide the phytoplankton abundance into freshwater and marine diatoms. Assuming that in the Belgian region of the Scheldt estuary (for which we have observations), phytoplankton consists of $\sim$ 75 %-25% freshwater and marine diatoms, respectively, and assuming that μ_{00} of marine diatoms is $\sim$ 1.66 larger (Naithani et al., 2016), we can compute the freshwater $\mu_{00}^{\text{fresh.}}$ and marine $\mu_{00}^{\text{mar.}}$ maximum growth rate at 0 ° C:

$$\mu_{00}^{\text{fresh.}} = \frac{\mu_{00}}{0.75 + 0.25 \times 1.66} \tag{5.11}$$

$$\mu_{00}^{\text{mar.}} = \frac{\mu_{00}}{\frac{0.75}{1.66} + 0.25} \tag{5.12}$$

Appendix 5.C: SPM distribution

Following Horemans et al. (2020a), we calibrate the erosion and flocculation characteristics by calibrating the residual SPM model output to the corresponding multi-annual residual SPM observations in 2015-2018 (Fig. 5.C.1a). The corresponding model parameters are the erosion parameter M and λ, which determine the strength of the flocs. The optimal values are $\lambda = 65.9 \times 10^{-6}$ s$^{-1/2}$ m^2 and $M = 4 \times 10^{-3}$ s m^{-1}.

As reasoned by Brouwer et al. (2018), Dijkstra et al. (2019b), and Horemans et al.

(2020a), between km 70-80 we have an increase in SPM due to dumping and dredging activities. However, this is not included in the model because the dredging and dumping activities act on a much smaller temporal scale ($\sim$ hours) and can thus be considered as a background SPM concentration, whereas our model computes the multi-annual SPM distribution. To guaranty that we capture the magnitude of the observed SPM concentrations at the dredging and dumping location, we add a background SPM concentration originated by dredging and dumping activities to our model results. More specifically, we replace the model concentration with the (smoothed) SPM observations between km 70 and 80 and beyond km 125. The resulting modeled SPM distribution is presented in Fig. 5.C.1b.

To estimate the sensitivity of phytoplankton growth to the SPM concentration, we estimate the SPM distribution between 2004-2007 and 2008-2014, for which we only have water surface SPM observations. To this end, we first divide the water surface SPM concentration observed in 2004-2007 and 2008-2014 by the observations between 2015-2018. The resulting (interpolated) ratios are presented in Figs. 5.C.1a and 5.C.1b, respectively. Next, we use these ratios to scale the profiles of the modeled SPM concentrations in 2015-2018, thus keeping the shape of the vertical profiles the same. This results in the estimated modeled SPM distribution in 2004-2007 and 2008-2014 presented in Figs. 5.C.1c and 5.C.1d, respectively.

Appendix 5.D: sediment-induced light extinction coefficient

Within the OMES campaign, the exponential light extinction coefficient k_d is computed by measuring the solar irradiance at the water surface E_0 and the light intensity at a depth d of approximately 1 m. Neglecting background and self-shading light extinction (which is acceptable given the high turbidity in the Scheldt estuary), we can compute the sediment-induced light extinction k_c as

$$k_d d = k_c \int_0^d c(z', t) dz', \tag{5.13}$$

in which z' is the water depth and c is the modeled SPM concentration (Fig. 5.C.1). Consequently, the time-averaged sediment-induced light extinction coefficient $\overline{k_c}$ can be

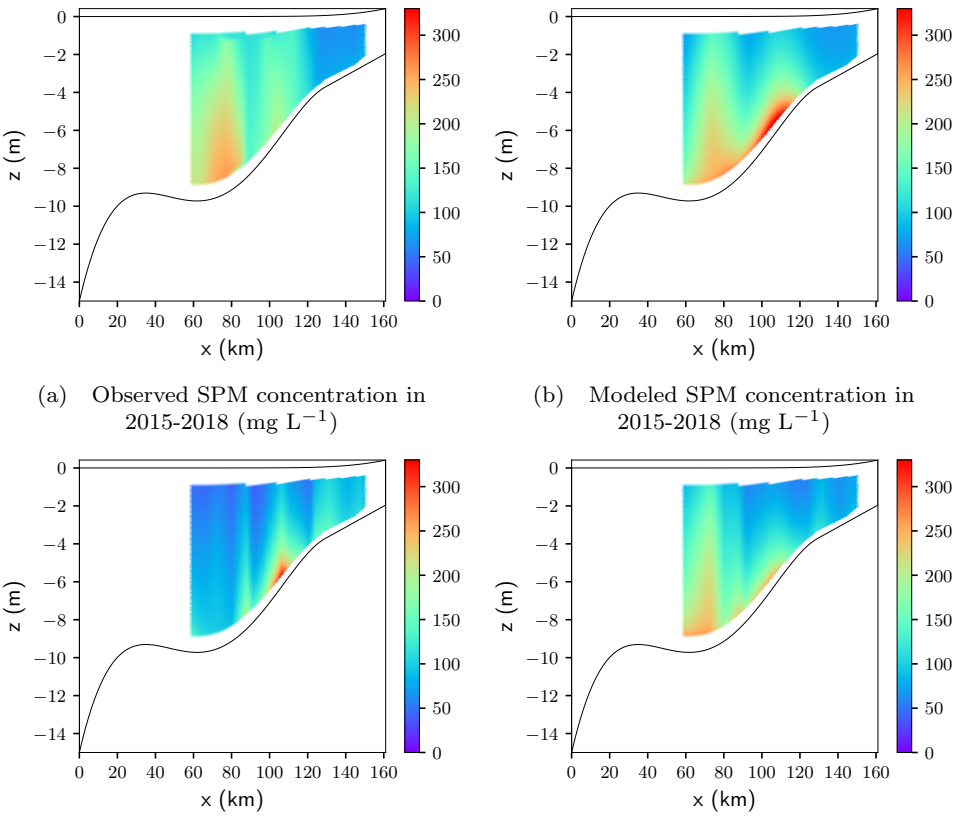

(a) Observed SPM concentration in 2015-2018 (mg L^{-1})

(b) Modeled SPM concentration in 2015-2018 (mg L^{-1})

(c) Modeled SPM concentration in 2004-2007 (mg L^{-1})

(d) Modeled SPM concentration in 2008-2014 (mg L^{-1})

Figure 5.C.1: (a) The multi-annual time-averaged observations and (b) the modeled SPM concentration in spring 2015-2018. (c)-(d) Modeled SPM concentrations, which follow from scaling the vertical profiles presented in (a). The scaling is quantified by computing the ratio of the observed surface SPM concentrations of the various periods.

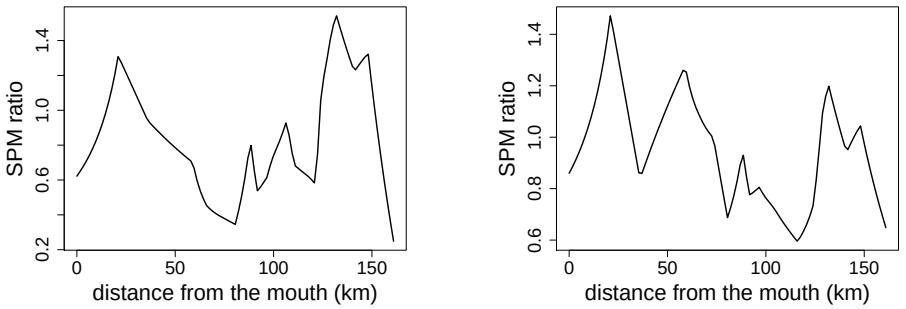

(a) SPM ratio in 2004-2007 (b) SPM ratio in 2008-2014

Figure 5.C.1: The (interpolated) water surface SPM observations divided by the observations in 2015-2018 between (a) 2004-2007 and (b) 2008-2014.

approximated by

$$\overline{k_c} = \frac{\overline{k_d d}}{\int_0^d c(z',t)dz'}, \tag{5.14}$$

$$\approx \frac{\overline{k_d}\,\overline{d}}{\int_0^d c(z',t)dz'}, \tag{5.15}$$

which results in $k_c \approx 72$ m^2 kg^{-1} in 2015-2018 for $d = 1$ m. To quantify the impact of variability in the integration depth d on the estimated value of k_c, Fig. 5.D.1a shows the estimated k_c value as a function of d. If we assume a vertically constant sediment concentration, Eq. (5.13) simplifies to the linear relationship $k_d = k_c c(t)$, which results in a slightly lower k_c value of approximately 68 m^2 kg^{-1}. The corresponding data fit for 2015-2018 is presented in Fig. 5.D.1b. Similarly, k_c approximates 78 m^2 kg^{-1} and 81 m^2 kg^{-1} in 2008-2014 and 2004-2007, respectively.

Appendix 5.E: evolution in discharge, salinity intrusion, and photosynthetic parameters

Figure 5.E.1a shows the multi-annual, monthly-averaged discharge in the three periods considered. In spring (Apr.-May), the average discharge is 85, 81, and 72 m^{-3} s^{-1} in 2004-2007, 2008-2014, and 2015-2018, respectively. We thus observe a slight decrease in total freshwater discharge over time.

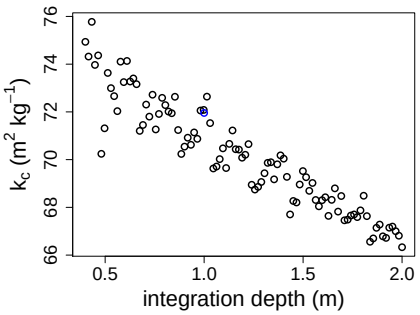

(a) Sediment-induced light extinction coefficient assuming a vertically non-constant SPM profile

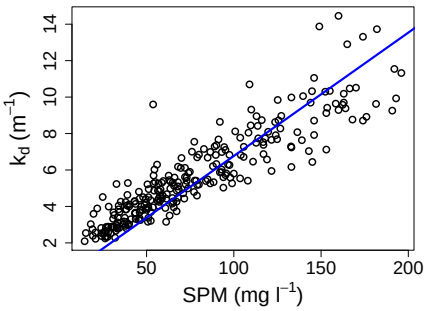

(b) Sediment-induced light extinction coefficient assuming a vertically constant SPM profile

Figure 5.D.1: (a) Sediment-induced light extinction coefficient k_c in 2015-2018 for various integration depths d using Eq. (5.14). Because the light extinction coefficient k_d is measured at approximately 1 m depth, we use the corresponding k_c value of 72 m^2 kg^{-1} in our model (depicted in blue). (b) Estimation of k_c in 2015-2018 assuming a vertically constant suspended sediment profile. By doing so, k_c equals the slope of the linear relationship between k_d and SPM (depicted by the blue line).

Figure 5.E.1b presents the monthly-averaged salinity intrusion, which is defined as the distance from the mouth at which the salinity equals 2 ppt. We typically observe the opposite trend compared to the freshwater discharge: a larger discharge comes with a smaller salt intrusion. However, this is not always valid. For example, in March, we have a similar time-averaged discharge in the three periods considered, while the salinity intrusion is significantly different. What is most important within the scope of this paper is the fact that in spring (Apr.-May) the salinity intrusion does not show major changes during the study period 2004-2018.

Figure 5.E.2a displays the monthly- and system-averaged maximum photosynthetic rate $P_{\max}$ in the three periods considered. In spring (Apr.-May), $P_{\max}$ is approximately equal in 2004-2007 and 2008-2014, but significantly lower in 2015-2018. The corresponding time-averaged values are 6.59, 6.44, and 4.31 mg C (mg Chl-a)$^{-1}$ h^{-1}, respectively.

Figure 5.E.2b shows the monthly- and system-averaged photosynthetic efficiency α in 2004-2018. What is most important within the scope of this paper is that α is not significantly different in all three periods 2004-2007, 2008-2014, and 2015-2018 in spring. The corresponding time-averaged values are 0.0165, 0.0168, and 0.0188 mg C (mg Chl-a)$^{-1}$ h^{-1} [PAR]$^{-1}$, respectively.

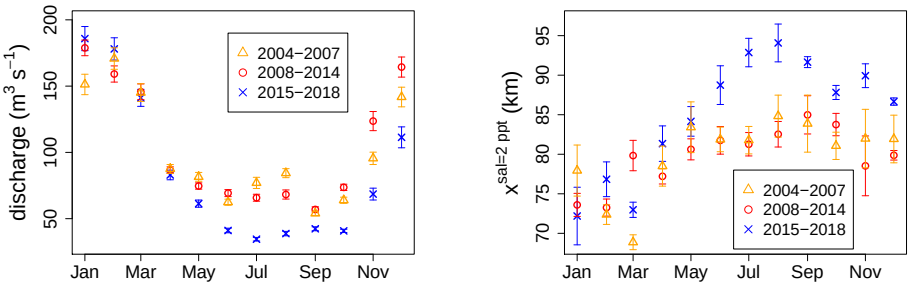

(a) Time-averaged discharge (b) Time-averaged salt intrusion

Figure 5.E.1: Multi-annual monthly-averaged observations in 2004-2018 of (a) the total freshwater discharge (at the upstream boundary and tributaries) and (b) the salinity intrusion defined as the distance at which the salinity equals 2 ppt. The error bars depict the standard error of the observations.

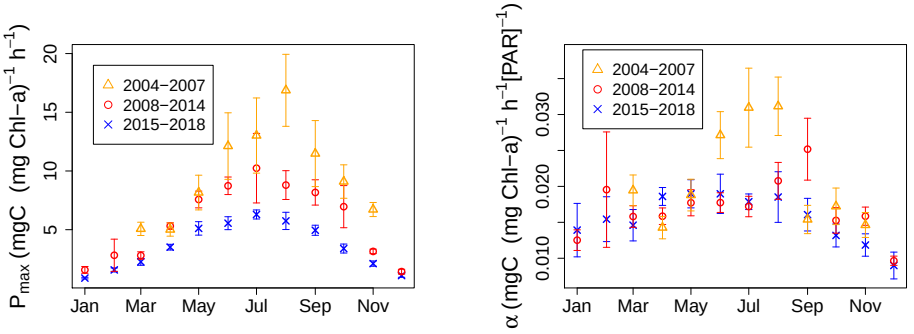

(a) Time-averaged $P_{\max}$ (b) Time-averaged α

Figure 5.E.2: Multi-annual monthly-averaged observations in 2004-2018 of the photosynthetic parameters (a) $P_{\max}$ and (b) α. The error bars depict the standard error of the observations. With '[PAR]', we denote 'the units of PAR', i.e. μmol photons m^{-2} s^{-1}.

Appendix 5.F: sensitivity study of model parameters

Figures 5.F.1a-d show the impact of variations in the sediment-induced light extinction coefficient k_c and the maximum growth rate μ_{00} at 0 °C on the Chl-a model result for both the freshwater and marine diatoms in 2008-2014, keeping other parameters at their default values. The parameters $m_0^{\text{mar.}}$, g_1, and g_2 are assumed to be fixed and set to the values corresponding to 2004-2007 and 2015-2018. We have to decrease k_c by a factor of approximately 3 to obtain accumulation of Chl-a in the brackish region. This difference is significantly larger than the variability that follows from the observations, which is between approximately 65 and 80 $\text{m}^2\ \text{kg}^{-1}$ (see Section 5.D). Similarly, at large μ_{00}, we do not detect accumulation of Chl-a in the brackish region. Changes in the freshwater discharge Q, the influx of Chl-a at the upstream boundary QP, and the Chl-a concentration at the seaside boundary P_{sea} in 2008-2014 only lead to changes in the upstream or downstream Chl-a concentration, but do not result in the accumulation of Chl-a in the brackish region (Figs. 5.F.2a-d). Therefore, changes in these parameters alone cannot explain the disappearance of accumulation of Chl-a in the brackish region.

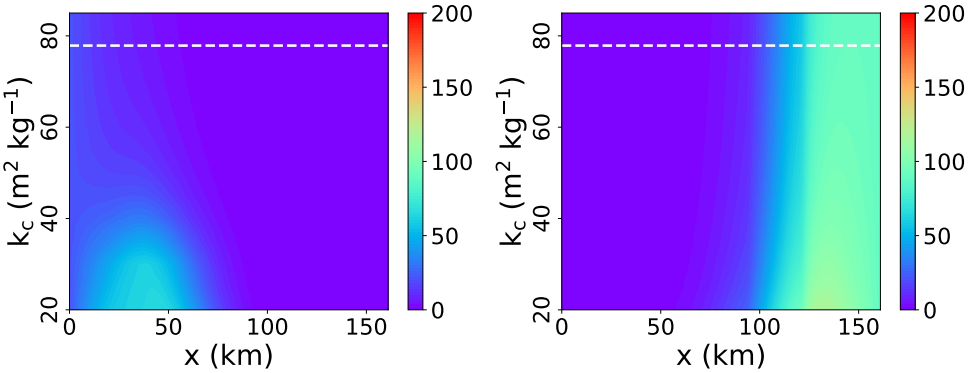

(a) Depth-averaged Chl-a concentration of marine diatoms (μg L^{-1})

(b) Depth-averaged Chl-a concentration of freshwater diatoms (μg L^{-1})

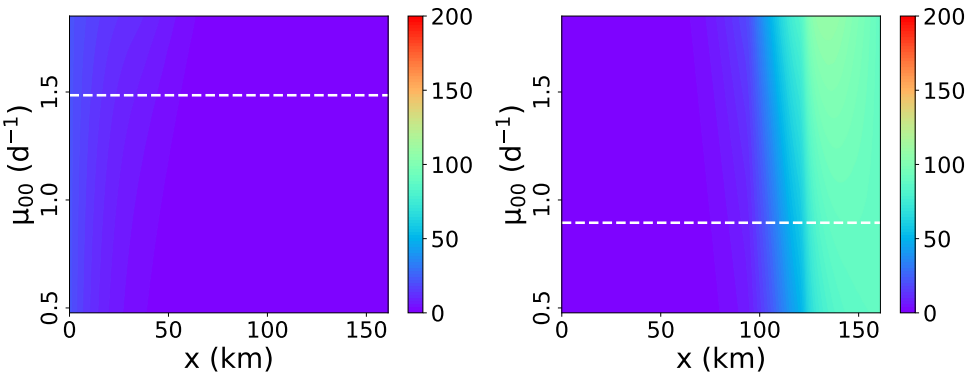

(c) Depth-averaged Chl-a concentration of marine diatoms (μg L^{-1})

(d) Depth-averaged Chl-a concentration of freshwater diatoms (μg L^{-1})

Figure 5.F.1: Sensitivity study of the depth-averaged Chl-a concentration in 2008-2014 to the (a)-(b) sediment-induced light extinction coefficient k_c and (c)-(d) the maximum growth rate μ_{00} at 0 °C for both freshwater and marine diatoms. The default parameter values are depicted by the dashed horizontal lines.

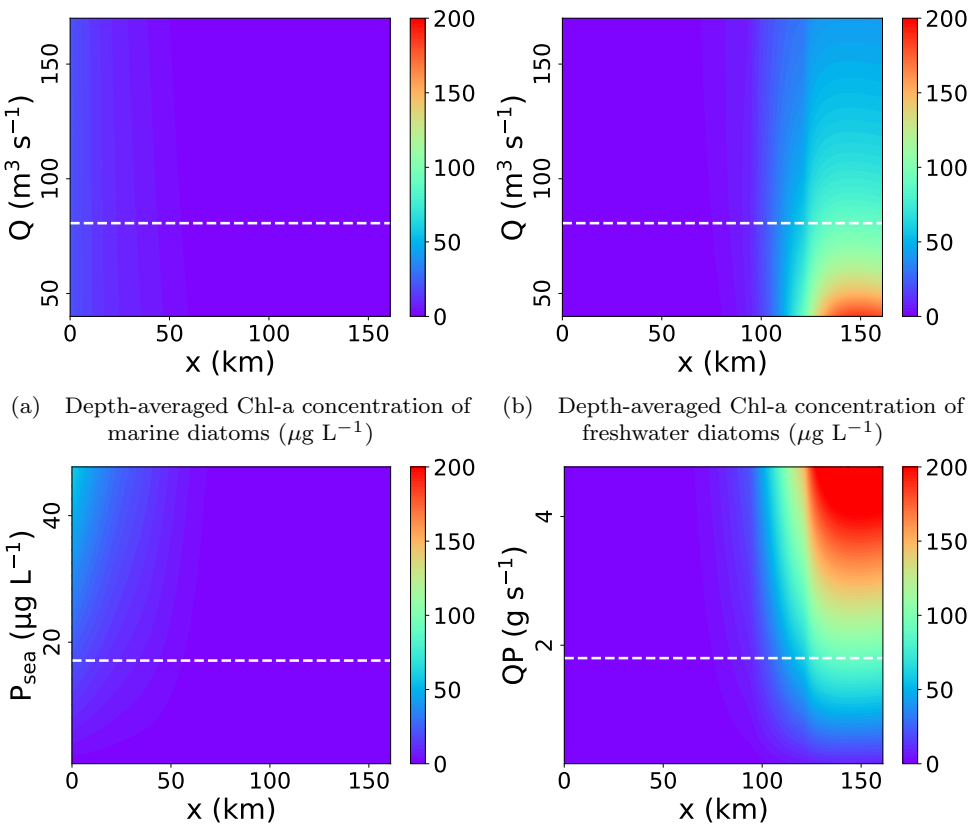

(a) Depth-averaged Chl-a concentration of marine diatoms (μg L^{-1})

(b) Depth-averaged Chl-a concentration of freshwater diatoms (μg L^{-1})

(c) Depth-averaged Chl-a concentration of marine diatoms (μg L^{-1})

(d) Depth-averaged Chl-a concentration of freshwater diatoms (μg L^{-1})

Figure 5.F.2: Sensitivity study of the depth-averaged Chl-a concentration in 2008-2014 to the (a)-(b) the total freshwater discharge Q, (c) the Chl-a concentration at the seaside boundary P_{sea}, and (d) the phytoplankton influx at the upstream boundary QP. The default parameter values are depicted by the dashed horizontal lines.

Table 5.A.1: Parameter values used in our model experiments. If only one parameter value is presented, we used this value for all three periods.

Variable	Definition	Value 2004-2007	Value 2008-2014	Value 2015-2018	Unit
	Hydrodynamics				
A^0	M_2 water level amplitude at x=0		1.77		m
A^1	M_4 water level amplitude at x=0		0.14		m
ϕ^1	M_4 water level phase relative to M_2 tide at x=0		-1.3		deg
Q	Total river discharge to resolve the phytoplankton dynamics	85	81	72	$m^3\ s^{-1}$
Q_{USS}	Relative discharge contribution of the Upper Sea Scheldt boundary	26.4 %	31.5 %	27.1 %	/
Q_{Rupel}	Relative discharge contribution of the Rupel tributary	64.2 %	59.3 %	63.3 %	/
Q_{Dender}	Relative discharge contribution of of the Dender tributary	9.4 %	9.2 %	9.6 %	/
$Q^{\text{sed.}}$	Total river discharge to resolve the sediment dynamics		180		$m^3\ s^{-1}$
	Sediment				
c_{sea}	Depth-averaged subtidal concentration at x=0		0.06		$kg\ m^{-3}$
c_{USS}	Subtidal SPM concentration at the Upper Sea Scheldt boundary		0.01		$kg\ m^{-3}$
K_h	Horizontal eddy diffusivity coefficient		100		$m^2\ s^{-1}$
K_ν^0	Vertical eddy diffusivity coefficient		3.1×10^{-2}		$m^2\ s^{-1}$
M	Erosion parameter		4×10^{-3}		$s\ m^{-1}$
	Turbulence				
σ_ρ	Prandtl-Smidth number		1		/
sf_0	Bed roughness coefficient		4.22		$mm\ s^{-1}$
	Flocculation				
$k_A^{\text{min.}}$	Nondimensional minimal aggregation coefficient		0.29		/
f_s	Shape factor		$\pi/6$		/
D_p	Diameter primary mud particles		25×10^{-6}		m
μ	Dynamic viscosity		0.0010518		Pa s
ρ_s	Density of sediment primary particles		2650		$kg\ m^{-3}$
ρ_w	Reference density of water		1000		$kg\ m^{-3}$
λ^{spring}	Ratio of minimal aggregation and floc break-up parameter in spring		65.9×10^{-6}		$s^{-1/2}\ m^2$
	Salinity				
$ssea$	Salinity boundary condition at the mouth		28.9 ‰		/
$x_c^{\text{sal, spring}}$	Calibration parameter in sigmoid salinity distribution in spring	47.5	46.4	49.0	km
$x_L^{\text{sal, spring}}$	Calibration parameter in sigmoid salinity distribution in spring	28.8	30.7	29.9	km
	Nutrients				
H_N	Half-saturation constant for PP dependence on N availability		0.003		$mol\ N\ m^{-3}$
H_P	Half-saturation constant for PP dependence on P availability		0.0002		$mol\ P\ m^{-3}$
N_{sea}	Nitrogen boundary concentration at the mouth		0.025		$mmol\ N\ L^{-1}$
Phos_{sea}	Phosphorous boundary concentration at the mouth		0.0011		$mmol\ P\ L^{-1}$
N_{USS}	Influx of nitrogen at the upstream boundary		3		$mol\ N\ s^{-1}$
Phos_{USS}	Influx of phosphorous at the upstream boundary		0.2		$mol\ P\ s^{-1}$
$N_{\text{Rup.}}$	Influx of nitrogen at Rupel tributary		5.1		$mol\ N\ s^{-1}$
$\text{Phos}_{\text{Rup.}}$	Influx of phosphorous at Rupel tributary		0.12		$mol\ P\ s^{-1}$
C:N:P	Ratio between carbon, nitrogen, and phosphorous (in mol)		106:16:1		/
	Phytoplankton				
$\mu_{00}^{\text{fresh.}}$	Maximum growth rate at 0 ° C of to freshwater diatoms (source)	0.96×10^{-5}	1.04×10^{-5}	0.86×10^{-5}	s^{-1}
$\mu_{00}^{\text{mar.}}$	Maximum growth rate at 0 ° C of to marine diatoms (source)	1.59×10^{-5}	1.72×10^{-5}	1.43×10^{-5}	s^{-1}
μ_{01}	Calibration parameter in temperature dependence for $\mu_{\max}$	1.10	1.07	1.05	/
g_1	Calanoids grazing parameter (calibrated)	0.8×10^{-7}	0.13×10^{-7}	0.8×10^{-7}	$s^{-1}\ L$
g_2	Non-calanoids grazing parameter (calibrated)	0.47×10^{-7}	0.32×10^{-7}	0.47×10^{-7}	$s^{-1}\ L$
$m_0^{\text{fresh.}}$	Mortality rate parameter for freshwater diatoms (calibrated)	1.89×10^{-6}	3.30×10^{-6}	8.30×10^{-6}	s^{-1}
$m_0^{\text{mar.}}$	Mortality rate parameter for marine diatoms (calibrated)	3.21×10^{-6}	1.06×10^{-6}	3.35×10^{-6}	s^{-1}
C:Chla	Carbon to Chlorophyll-a ratio		50		/
E_{00}	Maximum PAR		1007		$\mu mol\ photons\ m^{-2}\ s^{-1}$
ω_E	Angular frequency for day length		0.215		d^{-1}
T	Water temperature	14.3	14.7	14.7	° C
P_{sea}	Marine phytoplankton boundary concentration at the mouth (source)	15.9	17.1	15.8	$\mu g\ L^{-1}$
QP	Influx of freshwater phytoplankton at the upstream boundary (source)	1.5	1.8	2.5	$g\ s^{-1}$
w_P	Settling velocity of phytoplankton cells (Sarthou et al., 2005)		1.15×10^{-5}		$m\ s^{-1}$
k_{bg}	Background exponential light extinction coefficient (Pennock and Sharp, 1994)		0.095		m^{-1}
k_P	Self-shading exponential light extinction coefficient (Pennock and Sharp, 1994)		18		$m^2\ (mol\ N)^{-1}$
k_c	Sediment-induced exponential light extinction coefficient	81.4	77.9	72.0	$m^2\ kg^{-1}$
α	Growth efficiency (source)	0.0165	0.0168	0.0188	$mg\ C\ (mg\ Chl\text{-}a)^{-1}h^{-1}\ [\mu mol\ photons\ m^{-2}\ s^{-1}]^{-1}$

Bibliography

Alpine, A. E. and Cloern, J. E. (1992). Trophic interactions and direct physical effects control phytoplankton biomass and production in an estuary. *Limnology and Oceanography*, 37(5):946–955.

Appeltans, W. (2003). Zooplankton in the Schelde estuary (Belgium/The Netherlands). The distribution of Eurytemora affinis: effect of oxygen? *Journal of Plankton Research*, 25(11):1441–1445.

Arndt, S., Lacroix, G., Gypens, N., Regnier, P., and Lancelot, C. (2011). Nutrient dynamics and phytoplankton development along an estuary-coastal zone continuum: A model study. *Journal of Marine Systems*, 84(3-4):49–66.

Baeyens, W., Van Eck, B., Lambert, C., Wollast, R., and Goeyens, L. (1997). General description of the Scheldt estuary. *Hydrobiologia*, 366(1-3):1–14.

Billen, G. and Garnier, J. (1997). The Phison River plume: Coastal eutrophication in response to changes in land use and water management in the watershed. *Aquatic Microbial Ecology*, 13(1):3–17.

Brion, N., Verbanck, M. A., Bauwens, W., Elskens, M., Chen, M., and Servais, P. (2015). Assessing the impacts of wastewater treatment implementation on the water quality of a small urban river over the past 40 years. *Environmental Science and Pollution Research*, 22(16):12720–12736.

Brouwer, R. L., Schramkowski, G. P., Dijkstra, Y. M., and Schuttelaars, H. M. (2018). Time Evolution of Estuarine Turbidity Maxima in Well-Mixed, Tidally Dominated Estuaries: The Role of Availability- and Erosion-Limited Conditions. *Journal of Physical Oceanography*, 48(8):1629–1650.

Calbet, A. and Landry, M. R. (2004). Phytoplankton growth, microzooplankton grazing, and carbon cycling in marine systems. *Limnology and Oceanography*, 49(1):51–57.

Chambord, S., Maris, T., Colas, F., Van Engeland, T., Sossou, A. C., Azémar, F., Le Coz, M., Cox, T., Buisson, L., Souissi, S., Meire, P., and Tackx, M. (2016). Mesozooplankton affinities in a recovering freshwater estuary. *Estuarine, Coastal and Shelf Science*, 177:47–59.

Cira, E. K., Paerl, H. W., and Wetz, M. S. (2016). Effects of Nitrogen Availability and Form on Phytoplankton Growth in a Eutrophied Estuary (Neuse River Estuary, NC, USA). *PLOS ONE*, 11(8).

Cox, T. J., Maris, T., Soetaert, K., Conley, D. J., Van Damme, S., Meire, P., Middelburg, J. J., Vos, M., and Struyf, E. (2009). A macro-tidal freshwater ecosystem recovering from hypereutrophication: The Schelde case study. *Biogeosciences*, 6(12):2935–2948.

Cox, T. J. S., Maris, T., Van Engeland, T., Soetaert, K., and Meire, P. (2019). Critical transitions in suspended sediment dynamics in a temperate meso-tidal estuary. *Scientific Reports*, 9(1):12745.

Denman, K. L. and Pea, M. A. (2002). The response of two coupled one-dimensional mixed layer/planktonic ecosystem models to climate change in the NE subarctic Pacific Ocean. *Deep-Sea Research Part II: Topical Studies in Oceanography*, 49(24-25):5739–5757.

Desmit, X., Vanderborght, J. P., Regnier, P., and Wollast, R. (2005). Control of phytoplankton production by physical forcing in a strongly tidal, well-mixed estuary. *Biogeosciences*, 2(2):205–218.

Dijkstra, Y. M., Brouwer, R. L., Schuttelaars, H. M., and Schramkowski, G. P. (2017). The iFlow modelling framework v2.4: a modular idealized process-based model for flow and transport in estuaries. *Geoscientific Model Development*, 10(7):2691–2713.

Dijkstra, Y. M., Chant, R. J., and Reinfelder, J. R. (2019a). Factors Controlling Seasonal Phytoplankton Dynamics in the Delaware River Estuary: an Idealized Model Study. *Estuaries and Coasts*, 42(7):1839–1857.

Dijkstra, Y. M., Schuttelaars, H. M., and Schramkowski, G. P. (2019b). Can the Scheldt River Estuary become hyperturbid? A model analysis of suspended sediment concentrations and transport in response to channel deepening. *Ocean Dynamics*, 69(7):809–827.

Dijkstra, Y. M., Schuttelaars, H. M., Schramkowski, G. P., and Brouwer, R. L. (2019c). Modeling the Transition to High Sediment Concentrations as a Response to Channel Deepening in the Ems River Estuary. *Journal of Geophysical Research-Oceans*.

Eilers, P. H. C. and Peeters, J. C. H. (1988). A Model for the Relationship Between Light-Intensity and the Rate of Photosynthesis in Phytoplankton. *Ecological Modelling*, 42(3-4):199–215.

Eppley, R. W. (1972). Temperature and phytoplankton growth in the sea. *Fish. bull*, 70(4):1063–1085.

Filardo, M. J. and Dunstan, W. M. (1985). Hydrodynamic control of phytoplankton in low salinity waters of the James River estuary, Virginia, U.S.A. *Estuarine, Coastal and Shelf Science*, 21(5):653–667.

Franks, P. J. S. (2009). Planktonic ecosystem models: perplexing parameterizations and a failure to fail. *Journal of Plankton Research*, 31(11):1299–1306.

Friedrichs, M. A., Dusenberry, J. A., Anderson, L. A., Armstrong, R. A., Chai, F., Christian, J. R., Doney, S. C., Dunne, J., Fujii, M., Hood, R., McGillicuddy, D. J., Moore, J. K., Schartau, M., Spitz, Y. H., and Wiggert, J. D. (2007). Assessment of skill and portability in regional marine biogeochemical models: Role of multiple planktonic groups. *Journal of Geophysical Research: Oceans*, 112(8).

Friedrichs, M. A., Hood, R. R., and Wiggert, J. D. (2006). Ecosystem model complexity versus physical forcing: Quantification of their relative impact with assimilated Arabian Sea data. *Deep-Sea Research Part II: Topical Studies in Oceanography*, 53(5-7):576–600.

Gypens, N., Delhez, E., Vanhoutte-Brunier, A., Burton, S., Thieu, V., Passy, P., Liu, Y., Callens, J., Rousseau, V., and Lancelot, C. (2013). Modelling phytoplankton succession and nutrient transfer along the Scheldt estuary (Belgium, The Netherlands). *Journal of Marine Systems*, 128:89–105.

Horemans, D. M. L., Dijkstra, Y. M., Schuttelaars, H. M., Meire, P., and Cox, T. J. S. (2020a). Unraveling the essential effects of flocculation on large-scale sediment transport patterns in a tide-dominated estuary. *Journal of Physical Oceanography*, 50(7):1957–1981.

Horemans, D. M. L., Dijkstra, Y. M., Schuttelaars, H. M., Sabbe, K., Vyverman, W., Meire, P., and Cox, T. J. S. (2021). Seasonal variations in flocculation and erosion affecting the large-scale suspended sediment distribution in the Scheldt estuary: the importance of biotic effects. *Journal of Geophysical Research: Oceans*, pages 1–20.

Horemans, D. M. L., Meire, P., and Cox, T. J. S. (2020b). The impact of temporal variability in light-climate on time-averaged primary production and a phytoplankton bloom in a well-mixed estuary. *Ecological Modelling*, 436:109287.

Kromkamp, J. and Peene, J. (1995). Possibility of net phytoplankton primary production in the turbid Schelde Estuary (SW Netherlands). *Marine Ecology Progress Series*, 121:249–259.

Lancelot, C., Spitz, Y., Gypens, N., Ruddick, K., Becquevort, S., Rousseau, V., Lacroix, G., and Billen, G. (2005). Modelling diatom and Phaeocystis blooms and nutrient cycles in the Southern Bight of the North Sea: The MIRO model. *Marine Ecology Progress Series*, 289(June 2014):63–78.

Le Coz, M., Chambord, S., Meire, P., Maris, T., Azémar, F., Ovaert, J., Buffan-Dubau, E., Kromkamp, J. C., Sossou, A. C., Prygiel, J., Spronk, G., Lamothe, S., Ouddane, B., Rabodonirina, S., Net, S., Dumoulin, D., Peene, J., Souissi, S., and Tackx, M. (2017). Test of some ecological concepts on the longitudinal distribution of zooplankton along a lowland water course. *Hydrobiologia*, 802(1):175–198.

Lionard, M., Azémar, F., Boulêtreau, S., Muylaert, K., Tackx, M., and Vyverman, W. (2005). Grazing by meso- and microzooplankton on phytoplankton in the upper reaches of the Schelde estuary (Belgium/The Netherlands). *Estuarine, Coastal and Shelf Science*, 64(4):764–774.

Liu, B. and de Swart, H. E. (2015). Impact of river discharge on phytoplankton bloom dynamics in eutrophic estuaries: A model study. *Journal of Marine Systems*, 152:64–74.

Lucas, L. V., Cloern, J. E., Koseff, J. R., Monismith, S. G., and Thompson, J. K. (1998). Does the Sverdrup critical depth model explain bloom dynamics in estuaries? *Journal of Marine Research*, 56(2):375–415.

Maris, T.and Oosterlee, L. and Meire, P. (2013). Onderzoek naar de gevolgen van het Sigmaplan, baggeractiviteiten en havenuitbreiding in de Zeeschelde op het milieu. Geïntegreerd eindverslag van het onderzoek verricht in 2011. Technical Report Report Ecosystem Management Research Group ECOBE, 013-R155, University of Antwerp, Antwerp, Belgium.

Maris, T.and Van Damme, S. and Meire, P. (2007). Onderzoek naar de gevolgen van het Sigmaplan, baggeractiviteiten en havenuitbreiding in de zeeschelde op het milieu. Geïntegreerd eindverslag van het onderzoek verricht in 2006-2007. Technical Report Report Ecosystem Management Research Group ECOBE, 07-107, University of Antwerp, Antwerp, Belgium.

Maris, T.and Van Damme, S. and Meire, P. (2009). Onderzoek naar de gevolgen van het Sigmaplan, baggeractiviteiten en havenuitbreiding in de zeeschelde op het milieu. Geïntegreerd eindverslag van het onderzoek verricht in 2008-2009. Technical Report Report Ecosystem Management Research Group ECOBE, 010-R124, University of Antwerp, Antwerp, Belgium.

Maris, T. and Meire, P. (2017). Omes rapport 2016. Onderzoek naar de gevolgen van het Sigmaplan, baggeractiviteiten en havenuitbreiding in de Zeeschelde op het milieu. Technical Report Report Ecosystem Management Research Group ECOBE, 017-R206, University of Antwerp, Antwerp, Belgium.

Meire, P., Ysebaert, T., Van Damme, S., Van den Bergh, E., Maris, T., and Struyf, E. (2005). The Scheldt estuary: a description of a changing ecosystem. *Hydrobiologia*, 540(1-3):1–11.

Mialet, B., Azémar, F., Maris, T., Sossou, C., Ruiz, P., Lionard, M., Van Damme, S., Lecerf, A., Muylaert, K., Toumi, N., Meire, P., and Tackx, M. (2010). Spatial spring distribution of the copepod Eurytemora affinis (Copepoda, Calanoida) in a restoring estuary, the Scheldt (Belgium). *Estuarine, Coastal and Shelf Science*, 88(1):116–124.

Mialet, B., Gouzou, J., Azémar, F., Maris, T., Sossou, C., Toumi, N., Van Damme, S., Meire, P., and Tackx, M. (2011). Response of zooplankton to improving water quality in the Scheldt estuary (Belgium). *Estuarine, Coastal and Shelf Science*, 93(1):47–57.

Muylaert, K., Sabbe, K., and Vyverman, W. (2009). Changes in phytoplankton diversity and community composition along the salinity gradient of the Schelde estuary (Belgium/The Netherlands). *Estuarine, Coastal and Shelf Science*, 82(2):335–340.

Naithani, J., de Brye, B., Buyze, E., Vyverman, W., Legat, V., and Deleersnijder, E. (2016). An ecological model for the Scheldt estuary and tidal rivers ecosystem: spatial and temporal variability of plankton. *Hydrobiologia*, 775(1):51–67.

Oreskes, N., Shrader-Frechette, K., and Belitz, K. (1994). Verification, validation, and confirmation of numerical models in the earth sciences. *Science*, 263(5147):641–646.

Pennock, J. R. and Sharp, J. H. (1994). Temporal alternation between light-limitation and nutrient-limitation of phytoplankton production in a coastal plain estuary. *Marine Ecology Progress Series*, 111(3):275–288.

Perkin, R. G. and Lewis, E. L. (1980). The Practical Salinity Scale 1978: Fitting the Data. *IEEE Journal of Oceanic Engineering*, 5(1):9–16.

Regnier, P., Wollast, R., and Steefel, C. I. (1997). Long-term fluxes of reactive species in macrotidal estuaries: Estimates from a fully transient, multicomponent reaction-transport model. *Marine Chemistry*, 58(1-2):127–145.

Rice, E. W., Baird, R. B., Eaton, A. D., and editors (2017). *Standard Methods for the Examination of Water and Wastewater*. American Public Health Association, American Water Works Association, and Water Environment Federation, 23rd edition.

Rijkswaterstaat (2020). Rijkswaterstaat official website.

Roubeix, V., Rousseau, V., and Lancelot, C. (2008). Diatom succession and silicon removal from freshwater in estuarine mixing zones: From experiment to modelling. *Estuarine, Coastal and Shelf Science*, 78(1):14–26.

Sarthou, G., Timmermans, K. R., Blain, S., and Tréguer, P. (2005). Growth physiology and fate of diatoms in the ocean: A review. *Journal of Sea Research*, 53(1-2 SPEC. ISS.):25–42.

Steele, J. H. and Henderson, E. W. (1992). The role of predation in plankton models. *Journal of Plankton Research*, 14(1):157–172.

Sverdrup, H. U. (1953). On Conditions for the Vernal Blooming of Phytoplankton. *ICES Journal of Marine Science*, 18(3):287–295.

Tilman, D., Kilham, S. S., and Kilham, P. (1982). Phytoplankton Community Ecology: The Role of Limiting Nutrients. *Annual Review of Ecology and Systematics*, 13(1):349–372.

van Maren, D. S. and Cronin, K. (2016). Uncertainty in complex three-dimensional sediment transport models: equifinality in a model application of the Ems Estuary, the Netherlands. *Ocean Dynamics*, 66(12):1665–1679.

Vegter, F. and De Visscher, P. R. M. (1984). Phytoplankton primary production in Brackish Lake Grevelingen (SW Netherlands) during 1976-1981. *Netherlands Journal of Sea Research*, 18(3-4):246–259.

Warner, J. C., Geyer, W. R., and Lerczak, J. A. (2005). Numerical modeling of an estuary: A comprehensive skill assessment. *Journal of Geophysical Research: Oceans*, 110(C5):1–13.

Waterinfo.be (cited 2019). Measurements and predictions of Waterinfo.be [data]. [Available online at `https://www.waterinfo.be/`].

Winkler, G., Dodson, J. J., Bertrand, N., Thivierge, D., and Vincent, W. F. (2003). Trophic coupling across the St. Lawrence river estuarine transition zone. *Marine Ecology Progress Series*, 251:59–73.

Winterwerp, J. C. (2002). On the flocculation and settling velocity of estuarine mud. *Continental Shelf Research*, 22(9):1339–1360.

Winterwerp, J. C. and Wang, Z. B. (2013). Man-induced regime shifts in small estuaries—I: theory. *Ocean Dynamics*, 63(11-12):1279–1292.

Chapter 6

Conclusions

In this chapter, we first conclude this thesis by answering the four main research questions we presented in Chapter 1. Next, we suggest further research opportunities that would naturally follow from our results.

6.1 Conclusions for our research questions

In this thesis, we studied the interconnection of SPM and phytoplankton on the large temporal- and spatial scale. We focused on a turbid, tide-dominated, and nutrient-rich estuary, being the Scheldt estuary. We combined the analysis of long-term observations covering the entire domain of the Scheldt estuary and a modeling approach. In Fig. 6.1, we repeat the outline of this thesis and present brief answers to our four main research questions corresponding to each chapter.

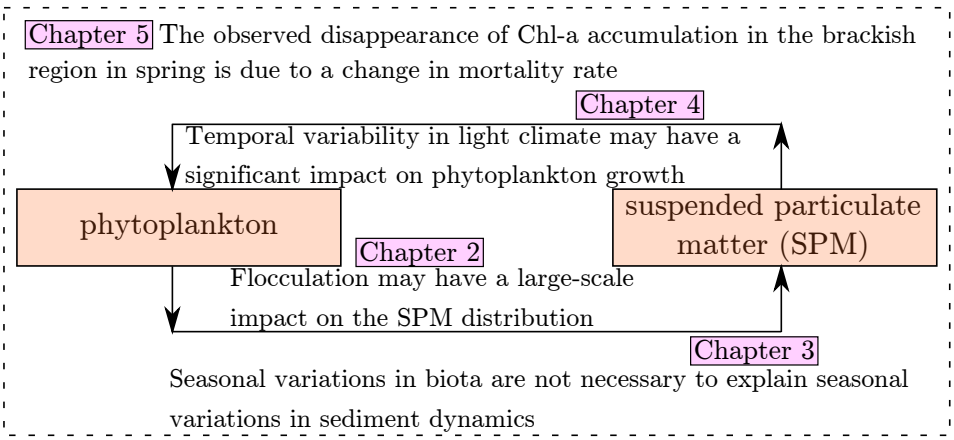

Figure 6.1: Illustration of the interconnection between SPM and phytoplankton studied in this thesis, the corresponding chapters, and a brief answer to the four main research questions. SPM limits phytoplankton growth by deteriorating the light climate in the water column. Phytoplankton may affect SPM dynamics by altering the floc size and structure of flocs and excreting sticky substances that stimulate flocculation of SPM. In Chapter 2, we studied the impact of flocculation on SPM. In Chapter 3, we focused on the importance of biotically-induced flocculation on SPM. In Chapter 4, we analyzed the impact of temporal variability in light climate (cf. SPM) on phytoplankton. We combined all results and studied a specific case in the Scheldt estuary in Chapter 5.

- What is the impact of flocculation on the large-scale SPM dynamics?

In Chapter 2, we determined whether the small-scale flocculation process may impact the

estuary-scale formation of estuarine turbidity maxima (ETM). To this end, we extended the idealized, width-averaged hydro-sediment transport model known as iFlow by a flocculation model and applied the model to the Scheldt estuary in winter conditions. We showed that spatial and temporal variations in settling velocity caused by flocculation are necessary to capture the observed magnitude of the SPM concentrations. More specifically, a mechanism caused by the temporal interaction between the longitudinal water flow velocity and settling velocity prevents flushing out of the ETM at large river discharges. Additionally, it promotes land-inward sediment transport and may cause the formation of additional ETM. It may also promote downstream net sediment transport, which depends on the phase between the longitudinal water flow velocity and the M2 tidal signal in the settling velocity and can thus differ for various estuaries. To conclude, the small-scale flocculation process may have an estuary-scale impact on the SPM distribution.

- Can we detect a seasonal biotic impact on the SPM dynamics through flocculation and erosion?

In Chapter 3, we applied the modeling framework from Chapter 2 to study the importance of biotically-induced seasonality in flocculation and erosion on seasonality in ETM formation. Here, we again focused on the Scheldt estuary. By calibrating the biotically-affected model parameters to long-term, in situ turbidity observations, we showed that we do not require seasonality in biotically-affected flocculation and erosion parameters to reproduce the seasonality in ETM formation. The mechanism resulting in the seasonality in ETM formation is the seasonality in freshwater discharge; the higher discharges in winter flush out the upstream ETM observed in summer. Additionally, they increase the shear rate in the upstream region, which promotes break-up and thereby decreases the land-inward sediment transport caused by flocculation. Our conclusion was supported by long-term, in situ observations of turbidity, floc size, Chl-a, and sticky substances excreted by phytoplankton; the abiotic observations show seasonality, while seasonality in the sticky substances is absent on the estuary and seasonal scale. To conclude, we cannot detect an important seasonal biotic impact through flocculation and erosion on the seasonal estuary-scale SPM dynamics.

- Can we construct a model to easily assess the relative impact of temporal fluctuations in SPM on phytoplankton growth?

In Chapter 4, before using our results from Chapters 2 and 3 to construct a phytoplankton-SPM model, we developed a tool to locally study the impact of temporal variability in light climate on primary production without solving the complex SPM dynamics explicitly. The tool allowed us to determine the relative impact of temporal variability in the SPM dynamics without a priori assumptions regarding these dynamics. We aimed to know whether we may neglect temporal variations in these parameters and, if not, how we can correct for the introduced error by excluding this temporal variability. We focused on three factors affecting phytoplankton growth through light availability: solar irradiance at the water surface, exponential light extinction in the water column, and water depth

(cf. ratio between euphotic/mixing depth). We again applied the tool to the Scheldt estuary. More specifically, we studied a phytoplankton bloom in spring and gross primary production in equilibrium conditions in summer and winter. We showed that our conceptual model correctly predicts the magnitude and sign of the introduced error. Moreover, we revealed that variability in solar irradiance has the largest impact on time-averaged primary production (PP) in dynamic equilibrium, resulting in a 30 % decrease compared to time-invariant PP. Caused by this decrease, temporal fluctuations in solar irradiance may also result in a significant decrease of unbounded exponential phytoplankton growth and may delay the onset of a phytoplankton bloom by ~ 2 weeks. Our case study showed that temporal variability in light extinction coefficient and water depth has a less significant influence on phytoplankton growth. The reason is that temporal variability is relatively small compared to its time average for these two parameters. We showed that the effect of temporal fluctuations in light extinction is more extensive in winter than in summer because of the larger temporal variations in winter. The relative importance of temporal variability in the parameters is thus season- and system-dependent. To conclude, we constructed a conceptual model that allowed us to easily assess the relative impact of temporal fluctuations in SPM on phytoplankton growth. The tool can be easily implemented in models that explicitly resolve the SPM-phytoplankton dynamics, as done in Chapter 5.

- Can we link the disappearance of the spring-bloom in the brackish region in the Scheldt estuary between 2004-2018 to multi-annual changes of processes impacting phytoplankton growth and their corresponding model parameters?

In Chapter 5, we combined our previous results to construct a phytoplankton-sediment transport model. To show its applicability, we applied the model to investigate the multi-annual evolution of the estuary-scale phytoplankton distribution in spring in the brackish region in the Scheldt estuary. More specifically, we determined what change in factors affecting phytoplankton growth may have dominantly contributed to the appearance and disappearance of a spring phytoplankton bloom in the Scheldt estuary between 2004-2018. To this end, we combined field observations and a modeling approach in which we applied an extensive sensitivity analysis and focused on the effects of individual model parameters. Our results suggest that the observed change in SPM alone cannot explain the multi-annual evolution in phytoplankton blooms in spring. Instead, a multi-annual change in phytoplankton mortality rate, grazing by zooplankton, and phytoplankton community characteristics may result in this multi-annual estuary-scale evolution of phytoplankton abundance. On the one hand, the combined effect of a land-inward shift of the zooplankton distribution and a change in grazing characteristics may explain the occurrence of a spring bloom of phytoplankton in the brackish region in 2008-2014. On the other hand, we can attribute this temporary spring bloom to multi-annual alterations in the phytoplankton community characteristics and the resulting different mortality caused by, for example, salinity stress. We thus found different model input parameter choices leading to similar model results, which is known as equifinality. Additional observations of grazing and mortality rates for various phytoplankton taxa in the Scheldt estuary are required to constrain further which multi-annual change in model parameters may have resulted in the multi-annual change in phytoplankton accumulation.

6.2 General conclusion

We combined a model approach and analysis of long-term observations in the Scheldt estuary to study the coupled SPM-phytoplankton dynamics on the large spatial and temporal scale. First, we extended a hydro-sediment transport model by a flocculation model and showed that flocculation may have a drastic impact on the estuary-scale SPM distribution. Next, we applied the model to study the impact of biotically-induced flocculation on the estuary-scale seasonality in the SPM distribution. Here, we showed that biotically-induced seasonality in flocculation and erosion only has a minor impact on the seasonality in SPM on the estuary scale; the observed seasonality in SPM can be explained through seasonality in freshwater discharge. Next, before constructing a model that explicitly resolves the phytoplankton-SPM dynamics, we constructed a conceptual model to assess the relative impact of temporal variability in light climate (cf. SPM) on phytoplankton growth. We found that temporal fluctuations in light climate may reduce time-averaged PP and unbounded exponential phytoplankton growth and delay the onset of a spring bloom by ~ 2 weeks. Finally, we implemented this conceptual model and our previous results to construct a phytoplankton-sediment transport model. We applied the model to determine what processes may explain the multi-annual appearance and disappearance of phytoplankton accumulation in the brackish region in spring in the Scheldt estuary in 2004-2018. We showed that a change in mortality rate may explain this multi-annual trend. Additionally, we showed that the change in mortality rate may be caused by changes in grazing by zooplankton or phytoplankton community characteristics. Although we used our framework to study the Scheldt estuary, it may also be applied to other turbid, tide-dominated, and nutrient-rich estuaries.

6.3 Implication for the Scheldt estuary

In this section, we list some examples of potential implications of our results for the Scheldt estuary.

6.3.1 Management

In Chapter 4, we showed that temporal variability in water depth might increase phytoplankton growth. Intertidal areas are regions in which the relative contribution of temporal variability in water depth is expected to be significant as they are shallow and tidally-rewetted. Therefore, intertidal areas may positively affect phytoplankton growth based on our results. This may be important for managing the estuary; expanding the Scheldt estuary by reclaiming and reflooding land may result in an overall increase of phytoplankton growth, which is a crucial indicator for the ecological state of the estuary set by the European Water Framework Directive.

6.3.2 Holistic approach

We illustrated the potential importance of bio-physical-chemical interactions when studying SPM dynamics. More specifically, we showed that flocculation, which may be impacted by biochemical activity, could significantly affect ETM formation in Chapter 2. It may result in additional ETM and prevent flushing of the ETM at large freshwater discharges. These conclusions may be relevant for the Scheldt estuary because Cox et al. (2019) reported an overall increase in SPM concentrations over the last two decades. Although we showed that biotically-induced flocculation and erosion have a limited impact on the seasonality in ETM formation, this may not be true when focusing on multi-annual changes in the SPM distribution. Differently put, it may be that the reported overall increase in SPM in the Scheldt estuary over the last two decades is caused by multi-annual changes in the flocculation characteristics. This shows the importance of a holistic and interdisciplinary approach when studying multi-annual shifts in the SPM distribution.

6.3.3 Monitoring

In this thesis, we demonstrated that combining field observations (cf. monitoring) and modeling may result in valuable insights into the functioning of the SPM and phytoplankton dynamics. Monitoring programs may thus deliver important modeling insights. Conversely, model results may also impact and optimize monitoring programs. For example, we constrained the multi-annual appearance and disappearance of phytoplankton blooms in spring in the brackish region in the Scheldt estuary to a limited number of calibration parameters in Chapter 5. These modeling insights may adjust monitoring programs by focusing on these constrained parameters in the future. The coherence between monitoring and modeling insights is crucial when studying a dynamic and complex system as the Scheldt estuary, which is continuously changing.

6.4 Opportunities for further research

In this section, we suggest ideas for further research that naturally follow from our results and would extend the research scope of this thesis.

6.4.1 Application to other estuarine systems

Given the complexity of estuarine SPM dynamics, their dominant processes may be highly system-dependent. Therefore, various authors applied an intercomparison study of different estuaries to understand their complex dynamics. In this thesis, we focused on the Scheldt estuary. However, the iFlow model without flocculation has also been applied to the Ems estuary (Dijkstra et al., 2019b), Delaware river estuary (Dijkstra et al., 2019a),

and the Garonne tidal river (Jalón-Rojas et al., 2021). To study the individual impact of flocculation, our model can thus be employed to these estuaries and other estuaries with similar characteristics, such as the Seine, Gironde, and Loire estuary. By doing so, we may reach different conclusions than found for the Scheldt estuary in Chapter 3: we may discover systems in which the aggregated effect of biotically-induced flocculation and erosion may have a significant impact on the seasonality of the estuary-scale SPM distribution or in which flocculation promotes net SPM export, which we calculated to be possible in Chapter 2.

6.4.2 Alternative model applications

Numerical models are a form of complex scientific hypotheses as they come with a list of assumptions (Oreskes et al., 1994). As explained by Franks (2009), the choice of an appropriate modeling approach depends on the research questions and data availability. Alternative model applications with different model assumptions are helpful to validate the model or hypothesis or answer additional research questions. For example, in an earlier iFlow model version, the settling velocity was considered constant. As we were interested in the effects of flocculation on the SPM dynamics and measurements of floc characteristics that have recently been included in the OMES monitoring program, we considered flocculation in the model. This resulted in a spatially and temporally varying settling velocity and valuable insight into the relative impact of flocculation on ETM formation on the estuary scale (Chapters 2-3). In future research, alternative model extensions that come with different assumptions can be applied to, for example, capture local processes such as the effects of intertidal areas on the SPM dynamics.

6.4.3 The link between TEP, stickiness, and Chl-a

The link between TEP, stickiness, and Chl-a is ambiguous; various estuaries and seasons show different correlations. The reason is that, firstly, the TEP concentrations are often estimated using the colorimetric method described in Claquin et al. (2008). A disadvantage of this method is that TEP is not well-defined from a chemical-physical perspective because it has various sub-fractions and components. Consequently, translating TEP to stickiness (i.e., a physical and chemical characteristic) may be very challenging.

Secondly, as opposed to some results found in the literature, a clear link between Chl-a and TEP was absent in the Scheldt estuary. We may attribute this discrepancy to the complex interplay between various bio-physical-chemical processes that result in TEP production. Various authors linked TEP concentrations to environmental conditions such as SPM concentration (Malpezzi et al., 2013), salinity (Alldredge et al., 1993; Bar-Zeev et al., 2015), turbulence (Beauvais et al., 2006), and nutrient depletion (Corzo et al., 2000; Passow, 2002). Additionally, the TEP concentration also depends on phytoplankton age and mortality (Liu and Buskey, 2000; Ramaiah et al., 2001; Morelle et al., 2017), and the community composition and phytoplankton and bacteria species interactions (Alldredge

et al., 1993; Ramaiah and Furuya, 2002; Grossart and Simon, 2007; Claquin et al., 2008).

Therefore, additional laboratory experiments may be set up in future research to study the impact of various phytoplankton taxa and environmental conditions on TEP production and its corresponding stickiness.

6.4.4 Refinement of the boundary conditions

We showed that the boundary conditions may significantly impact the phytoplankton and SPM concentrations. For example, an increased phytoplankton concentration at the up- and downstream boundary resulted in higher phytoplankton concentrations further away from its boundaries (Chapter 5). We also concluded that changes in phytoplankton community characteristics, which depend on the boundary conditions because marine and freshwater diatoms are imported from the down- and upstream boundaries, may have resulted in the multi-annual appearance and disappearance of the phytoplankton bloom in spring in the brackish region. This illustrates the importance of boundary conditions, which are in the current model version data-driven and not explicitly resolved. In future research, it may thus be interesting to refine the boundary conditions by, for example, extending our framework with a model that resolves the phytoplankton dynamics in the coastal region. This may result in valuable insights into the coastal-estuarine coupling.

6.4.5 Explicitly resolve the zooplankton dynamics

Various zooplankton-phytoplankton models have been applied in the literature, which showed that specific parameter choices may result in bifurcations and limit cycles (Steele and Henderson, 1992). Therefore, the zooplankton-phytoplankton coupling may also result in the appearance and disappearance of phytoplankton abundance, which we studied in Chapter 5. Because we aimed to eliminate the uncertainty of a dynamic zooplankton model and the temporal resolution of our field observations was relatively low (biweekly-monthly sampling), we used the observations of zooplankton concentrations directly in the model. We implemented the effect of grazing of phytoplankton by zooplankton parametrically, assuming equilibrium conditions. In future research, zooplankton-phytoplankton dynamics may be resolved explicitly. This may provide valuable insights into the dynamics on a smaller temporal scale ($\sim$ days-weeks), parameter stability, bifurcations, and limit cycles caused by the zooplankton-phytoplankton coupling.

6.4.6 Experimental validation of the calibrated model parameters

In Chapter 5, we concluded that the multi-annual appearance and disappearance of phytoplankton growth in the brackish region in spring in the Scheldt estuary may be caused by a change in both grazing by zooplankton and phytoplankton community characteristics. Also, in Chapter 3, we showed that both changes in primary particle density and floc

aggregation and break-up characteristics may result in a similar land-inward shift of the ETM. We thus found different model input parameter choices leading to similar model results, which is known as equifinality. To further constrain these parameters, additional experimental data is required. Therefore, given the potential importance of these parameters, our results can inspire and motivate experimental scientists to validate our model parameter values.

Bibliography

Alldredge, A. L., Passow, U., and Logan, B. E. (1993). The abundance and significance of a class of large, transparent organic particles in the ocean. *Deep Sea Research Part I: Oceanographic Research Papers*, 40(6):1131–1140.

Bar-Zeev, E., Passow, U., Romero-Vargas Castrillón, S., and Elimelech, M. (2015). Transparent Exopolymer Particles: From Aquatic Environments and Engineered Systems to Membrane Biofouling. *Environmental Science & Technology*, 49(2):691–707.

Beauvais, S., Pedrotti, M., Egge, J., Iversen, K., and Marrasé, C. (2006). Effects of turbulence on TEP dynamics under contrasting nutrient conditions: implications for aggregation and sedimentation processes. *Marine Ecology Progress Series*, 323:47–57.

Claquin, P., Probert, I., Lefebvre, S., and Veron, B. (2008). Effects of temperature on photosynthetic parameters and TEP production in eight species of marine microalgae. *Aquatic Microbial Ecology*, 51(1):1–11.

Corzo, A., Morillo, J., and Rodríguez, S. (2000). Production of transparent exopolymer particles (TEP) in cultures of Chaetoceros calcitrans under nitrogen limitation. *Aquatic Microbial Ecology*, 23(1):63–72.

Cox, T. J. S., Maris, T., Van Engeland, T., Soetaert, K., and Meire, P. (2019). Critical transitions in suspended sediment dynamics in a temperate meso-tidal estuary. *Scientific Reports*, 9(1):12745.

Dijkstra, Y. M., Chant, R. J., and Reinfelder, J. R. (2019a). Factors Controlling Seasonal Phytoplankton Dynamics in the Delaware River Estuary: an Idealized Model Study. *Estuaries and Coasts*, 42(7):1839–1857.

Dijkstra, Y. M., Schuttelaars, H. M., Schramkowski, G. P., and Brouwer, R. L. (2019b). Modeling the Transition to High Sediment Concentrations as a Response to Channel Deepening in the Ems River Estuary. *Journal of Geophysical Research-Oceans*.

Franks, P. J. S. (2009). Planktonic ecosystem models: perplexing parameterizations and a failure to fail. *Journal of Plankton Research*, 31(11):1299–1306.

Grossart, H. P. and Simon, M. (2007). Interactions of planktonic algae and bacteria: Effects on algal growth and organic matter dynamics. *Aquatic Microbial Ecology*, 47(2):163–176.

Jalón-Rojas, I., Dijkstra, Y. M., Schuttelaars, H. M., Brouwer, R. L., Schmidt, S., and Sottolichio, A. (2021). Multidecadal Evolution of the Turbidity Maximum Zone in a Macrotidal River Under Climate and Anthropogenic Pressures. *Journal of Geophysical Research: Oceans*, 126(5):e2020JC016273.

Liu, H. and Buskey, E. J. (2000). Hypersalinity enhances the production of extracellular polymeric substance (eps) in the texas brown tide alga, *aureoumbra lagunensis* (PELAGOPHYCEAE). *Journal of Phycology*, 36(1):71–77.

Malpezzi, M., Sanford, L., and Crump, B. (2013). Abundance and distribution of transparent exopolymer particles in the estuarine turbidity maximum of Chesapeake Bay. *Marine Ecology Progress Series*, 486:23–35.

Morelle, J., Schapira, M., and Claquin, P. (2017). Dynamics of phytoplankton productivity and exopolysaccharides (EPS and TEP) pools in the Seine Estuary (France, Normandy) over tidal cycles and over two contrasting seasons. *Marine Environmental Research*, 131:162–176.

Oreskes, N., Shrader-Frechette, K., and Belitz, K. (1994). Verification, validation, and confirmation of numerical models in the earth sciences. *Science*, 263(5147):641–646.

Passow, U. (2002). Transparent exopolymer particles (TEP) in aquatic environments. *Progress in Oceanography*, 55(3-4):287–333.

Ramaiah, N. and Furuya, K. (2002). Seasonal variations in phytoplankton composition and transparent exopolymer particles in a eutrophicated coastal environment. *Aquatic Microbial Ecology*, 30(1):69–82.

Ramaiah, N., Yoshikawa, T., and Furuya, K. (2001). Temporal variations in transparent exopolymer particles (TEP) associated with a diatom spring bloom in a subarctic ria in Japan. *Marine Ecology Progress Series*, 212:79–88.

Steele, J. H. and Henderson, E. W. (1992). The role of predation in plankton models. *Journal of Plankton Research*, 14(1):157–172.

Model and data availability

The iFlow code is open source and licensed under LGPL (GNU Lesser General Public License), which means that it may be used freely for non-commercial and commercial purposes. The version 2.9 code with the flocculation extension and an input file example are available through `https://doi.org/10.5281/zenodo.4560637`.

The data presented in this thesis in the Belgian and Dutch region of the Scheldt estuary is third-party data and was accessed through `http://www.omes-monitoring.be/en/data` and `https://waterinfo.rws.nl/`, respectively.

The turbidity, floc size, primary particle size, Chl-a, and TEP data set presented in Chapter 3 can be accessed through `https://doi.org/10.14284/450`, `https://doi.org/10.14284/451`, `https://doi.org/10.14284/452`, `https://doi.org/10.14284/449`, and `https://doi.org/10.14284/453`, respectively.

We sincerely thank T. Maris and De Vlaamse Waterweg NV for providing the OMES data, IMDC for providing the floc size data set, Flanders Marine Institute (VLIZ) for lending us the LISST 200x instrument, T. Van Engeland for the approval to use the ScheldeData package to generate the illustration of the Scheldt estuary (e.g., Fig. 1.2), and F. Azémar and C. A. Sossou for their contribution to the zooplankton data set. The main author is an SB Ph.D. fellow at FWO (1S36518N).

Acknowledgments

My Ph.D. would not have been possible without the support of others. Below, I would like to acknowledge some who particularly helped and inspired me during my Ph.D.

In March 2017, I started my Ph.D. at Ecosystem Management Research Group (Ecobe) at the University of Antwerp. First, my Ph.D. was financed by the Flemish-Dutch Scheldt Committee (VNSC) to work on turbidity and phytoplankton dynamics. I want to thank Kerst Buis, Tom Cox, and Patrick Meire for their trust and help with my FWO grant application. Without this, my Ph.D. would not have been possible.

In spring 2018, I went on a first research stay at Delft University of Technology. There, I was supervised by Yoeri Dijkstra and Henk Schuttelaars, two inspiring scientists who would become very important throughout my Ph.D. I am very grateful for your enthusiasm and support. The many detailed reviews of manuscript drafts and video calls challenged me to improve my work.

Furthermore, I thank my colleagues at Ecobe for the interesting discussions and beautiful moments. I want to thank a few in particular. Alison Govaerts, when you told me you were the successful candidate to do a Ph.D. in Germany, I felt conflicted; I really enjoyed our coffee-break talks, but I wish you all the best in your new adventure. Heleen Keirsebelik, thank you for all the laughter we shared. I still believe our team will one day become foosball champion. Steven Jacobs, your orchid trips were legendary. Our discussions tended to be lengthy, but your opinion was always inspiring. I (and many others) will never forget our DJ-session at a workshop in Hingene. Pali Gelsomini, I am glad to have had you share the office with me. Although our discussions were not always good for our productivity, they inspired us in other ways. Dorian Bas, Roos Carpentier, Ken Schoutens, and Niels Van Putte, our trip to a workshop in Wales and the subsequent holiday we spent there were not only interesting but also adventurous and exciting.

Finally, I am very grateful to my friends and family. Especially to my wife and best friend, Emma Boegborn, thank you for the many hours you listened to my work-related stories during challenging times throughout my Ph.D. I truly admire your patience. Also, a special thank you to my very good friend Laura van Evelingen for making the cover. It is almost too pretty to open and read this thesis.

List of publications

A1

- Horemans, D. M. L., Dijkstra, Y. M., Schuttelaars, H. M., Sabbe, K., Vyverman, W., Meire, P., & Cox, T. J. S. (2021). Seasonal variations in flocculation and erosion affecting the large-scale suspended sediment distribution in the Scheldt estuary: the importance of biotic effects. Journal of Geophysical Research: Oceans, 126, e2020JC016805. https://doi.org/10.1029/2020JC016805.

- Horemans, D. M. L., Meire, P., & Cox, T. J. S. (2020). The impact of temporal variability in light-climate on time-averaged primary production and a phytoplankton bloom in a well-mixed estuary. Ecological Modelling, 436, 109287. https://doi.org/10.1016/j.ecolmodel.2020.109287

- Horemans, D. M. L., Dijkstra, Y. M., Schuttelaars, H. M., Meire, P., & Cox, T. J. S. (2020). Unraveling the essential effects of flocculation on large-scale sediment transport patterns in a tide-dominated estuary. Journal of Physical Oceanography, 50(7). https://doi.org/10.1175/JPO-D-19-0232.1

- Schoelynck, J., Wolters, J. W., Teuchies, J., Brion, N., Puijalon, S., Horemans, D. M. L., ... Meire, P.(2019). Experimental evidence for the decline of submerged vegetation in freshwater ecosystems by the invasive Chinese mitten crab (Eriocheir sinensis). Biological Invasions. https://doi.org/10.1007/s10530-019-02118-2

Reports

- Meire, P., Plancke, Y., Govaerts, A., Cox, T., Gelsomi, P., Horemans, D., Meire, D., Meire, L., Zetsche, E. and Maris, T. (2021). Synthesis note: SPM dynamics and trends in the Scheldt estuary. ECOBE Report 021-R267 Universiteit Antwerpen, Antwerpen.

- Maris, T., P. Gelsomini, D. M. L. Horemans and P. Meire, 2020. Onderzoek naar de gevolgen van het Sigmaplan, baggeractiviteiten en havenuitbreiding in de Zeeschelde op het milieu. Geïntegreerd eindverslag van het onderzoek verricht in 2019. ECOBE 020-R265. Universiteit Antwerpen, Antwerpen.

- Maris, T., Horemans, D. M. L., Meire, P., 2019. OMES rapport 2018. Onderzoek naar de gevolgen van het Sigmaplan, baggeractiviteiten en havenuitbreiding in de Zeeschelde op het milieu. Technical Report. University of Antwerp.

- Cox, T. J. S., Horemans, D. M. L., De Mulder, T., Meire, P. (2017). Hoogfrequente in-situ metingen van de interactie tussen SPM- en zuurstofdynamiek in het Schelde-estuarium. Deelrapport 1. Metingen nabij het oppervlak. Universiteit Antwerpen, onderzoeksgroep Ecosysteembeheer en Universiteit Gent, laboratorium voor Hydraulica. ECOBE 018-R215.

Software

- Expansion of the width-averaged, hydrodynamics and sediment transport model called iFlow to include flocculation processes (2020):
`https://github.com/YoeriDijkstra/iFlow`
- Model to analyze the impact of temporal variability in light availability on primary production (2020):
`https://ars.els-cdn.com/content/image/1-s2.0-S0304380020303574-mmc1.zip`